May 2019

Processing and Properties of New Anisotropic and Mechanically Active Polymeric Composites

Matthew M. Ali
Syracuse University

Recommended Citation

Ali, Matthew M., "Processing and Properties of New Anisotropic and Mechanically Active Polymeric Composites" (2019). *Dissertations - ALL*. 1047.
https://surface.syr.edu/etd/1047

Abstract

Electrospinning is a versatile and inexpensive method to fabricate micron-sized polymer fibers, and it has been employed in this work to develop highly anisotropic fibrous composites. Previous work has detailed the properties of using electrospinning to fabricate fibrous anisotropic composites that was achieved by embedding stiff fibers in an elastomeric matrix. The goal of this work is to achieve anisotropic composites through creating a layering of rigid and elastic fibers in a laminate structure using primarily electrospinning in the fabrication. The composite produced has a unique deformation pattern when strained perpendicularly. The rigid fibers experienced no entanglement with each other and were able to separate from each other without hindrance. This allows a large differential in the stiffness in different directions. Through changes of the composite variables like polymer fiber diameter, and the percentage of the elastic polymer in the laminate, an optimization of anisotropy was determined.

Shape memory induced optical change in a new sensing materials was investigated using a thermomechanically active polymeric film incorporating dispersed silica nanoparticles. This was an improvement upon prior research where a similar effect was achieved using an elastomeric matrix. The advantage to using a shape memory polymer is that the actuation and optical change of the material can occur at a moment triggered by environmental thermal stimulus. Through a thermal change, the material recovers programmed strain and returns from a temporarily opaque state to with base state of optical clarity. This idea was expanded upon by incorporating the process of functional grading to the polymerization process. This is a method to spatially grade the material's glass transition temperature using a post cure heating stage. The staged recovery of this material has been demonstrated with a change in its optical translucency following the same recovery.

Processing and Properties of New Anisotropic and Mechanically Active Polymeric Composites

By
Matthew M. Ali
B.S. SUNY College of Environmental Science and Forestry, degree was earned, 2010
M.S. SUNY College of Environmental Science and Forestry, degree was earned, 2013

Dissertation
Submitted in partial fulfillment of the requirements for the degree of
Doctor of Philosophy in Chemical Engineering

Syracuse University
May 2019

Acknowledgements

First and foremost I must thank my advisor, Dr. Patrick Mather for all of his support, and guidance throughout my time at Syracuse & Bucknell Universities. During my time at the Syracuse Biomaterials Institute (SBI), Dr. Mather became the Dean of Engineering at Bucknell University. I was excited and deeply honored that he requested my assistance in creating his research lab at the new university. The position came with many challenges, but I was able to learn and grow, as well as make lifelong friendships there, and for that I am greatly appreciative.

I would like to express my gratitude to my thesis committee members, Drs. Ian Hosein, Jesse Bond, Pranav Soman, Julie Hasenwinkel and Teng Zhang. Their time and helpful remarks are always greatly appreciated.

I would like to thank the members of the Bucknell community that I have come to call not only colleagues, but friends, specifically Drs. Brandon Vogel, Katsuyuki Wakabayashi, Benjamin Wheatley and Kenny Mineart. They had made me feel warmly welcomed to Bucknell and treated me as a peer, to which I couldn't have asked for better. Amy Downs, Dan Johnson, Tom Thul and Diane Hall all selflessly assisted me whenever I was in need. They were pivotal to my success and I thank them. Of course I can't forget all the great undergraduate researchers I had the good fortune to know. They all helped me learn and grow as a mentor, and through many trips to Starbucks, became my friends as well. I would like to give special thanks to Emily Sharp, who contributed significantly to my success. She has a bright future ahead of her and I wish her the best!

I would like to thank all my friends and family for the support and patience they have provided me over the years. You all have help ease the pain of this process and for that I am truly grateful.

Finally, I would like to give special thanks to my wife, Alyssa. The patience she has exhibited throughout this process has rivaled saint-hood. This has been a lifelong goal of mine, and without her by my side I am certain I wouldn’t have been able to achieve it. I am deeply appreciative to have such a great companion. Simply put, thank you for everything.

Table of Contents

List of Schemes

List of Figures

with 20wt. % solution concentration of poly(methyl methacrylate) 0°, (d) trilayer with 20wt. % solution concentration of poly(methyl methacrylate) 90°.

Figure 2-32: Resulting mechanical properties of electrospun trilayer of 15wt. % solution concentration of poly(methyl methacrylate) from tensile testing as a function of the fiber orientation angle. (a) Young's modulus, (b) magnified view of Young's modulus, (c) tensile strength, (d) toughness and (e) strain-to-failure. All data points are an average of $n = 5$.

Figure 2-33: Resulting mechanical properties of electrospun trilayer of 20wt. % solution concentration of poly(methyl methacrylate) from tensile testing as a function of the fiber orientation angle. (a) Young's modulus, (b) magnified view of Young's modulus, (c) tensile strength, (d) toughness and (e) strain-to-failure. All data points are an average of $n = 5$.

Figure 2-34: Dynamic mechanical analysis of (a) storage and (b) loss modulus for $\theta = 0°$ and (c) storage and (d) loss modulus for $\theta = 90°$ of electrospun (i) Pellethane, (ii) 10wt. % sol. concentration poly(methyl methacrylate), (iii) 15wt. % sol. concentration poly(methyl methacrylate) and (iv) 20wt. % sol. concentration poly(methyl methacrylate).

Figure 2-35: Dynamic mechanical analysis of (a) storage and (b) loss modulus for $\theta = 0°$ and (c) storage and (d) loss modulus for $\theta = 90°$ of electrospun (i) trilayer with 10wt. % sol. concentration poly(methyl methacrylate), (ii) trilayer with 15wt. % sol. concentration poly(methyl methacrylate) and (iii) trilayer with 20wt. % sol. concentration poly(methyl methacrylate).

Figure 2-36: Dynamic mechanical analysis of 0° fiber orientation (solid) and 90° fiber orientation (dashed) for (a) electrospun trilayer of 10wt. % solution concentration of poly(methyl methacrylate), (b) electrospun trilayer of 15wt. % solution concentration of poly(methyl methacrylate) and (c) electrospun trilayer of 20wt. % solution concentration of poly(methyl methacrylate).

Figure 2-37: SEM micrographs of electrospun trilayer of anisotropic poly(methyl methacrylate) 20wt. % sol. concentration and $9.8\text{x}10^{-3}$ g/cm^2 of Pellethane fibers.

Figure 2-38: SEM micrographs of electrospun trilayer of anisotropic poly(methyl methacrylate) 20wt. % sol. concentration and $3.9\text{x}10^{-2}$ g/cm^2 of Pellethane fibers.

Figure 2-39: Box and whisker plot of the thickness of the Pellethane layer as measured using scanning electron microscopy.

Figure 2-40: Plot of porosity (a) and web density (b) as a function of Pellethane thickness within each trilayer composite.

Figure 2-41: Bar charts of the measured apparent porosity (method 1) and porosity (method 2) for (a) trilayer with $9.8\text{x}10^{-3}$ g/cm^2 of Pellethane and (b) trilayer with $3.9\text{x}10^{-2}$ g/cm^2 of Pellethane.

Figure 2-42: Representative images showing the change in physical appearance between the as spun fiber sheet (top) and the melted film (bottom) for (a) trilayer with 9.8x10^{-3} g/cm^{2} of Pellethane and (b) trilayer with with 3.9x10^{-2} g/cm^{2} of Pellethane.

Figure 2-43: DSC of the second heat for electrospun (i) Pellethane, (ii) 9.8x10^{-3} g/cm^{2} of Pellethane in the trilayer, (iii) 1.9x10^{-2} g/cm^{2} of Pellethane in the trilayer, (iv) 3.9x10^{-2} g/cm^{2} of Pellethane in the trilayer and (v) electrospun poly(methyl methacrylate). The measured glass transition temperatures (T_g) for Pellethane is -10 °C and 125°C for poly(methyl methacrylate). Pellethane is a thermoplastic elastomer and has a small melt peak around 155 °C.

Figure 2-44: TGA of mass loss as a function of temperature for the (i) Pellethane, (ii) 9.8x10^{-3} g/cm^{2} of Pellethane in the trilayer, (iii) 1.9x10^{-2} g/cm^{2} of Pellethane in the trilayer, (iv) 3.9x10^{-2} g/cm^{2} of Pellethane in the trilayer and (v) electrospun poly(methyl methacrylate).

Figure 2-45: Representative stress strain curves (top) and magnified view of the elastic deformation (bottom) for (i) 9.8x10^{-3} g/cm^{2} of Pellethane in the trilayer, (ii) 1.9x10^{-2} g/cm^{2} of Pellethane in the trilayer, (iii) 3.9x10^{-2} g/cm^{2} of Pellethane in the trilayer. All samples are $\theta = 0°$ with n of 5.

Figure 2-46: Summation of mechanical properties of the trilayer samples with variable Pellethane thickness obtained through interpretation of the stress-strain curves for all samples with the fiber orientation angle $\theta = 0°$. (a) Young's modulus, (b) tensile strength, (c) toughness and (d) strain-to-failure. All data points are an average of n = 5.

Figure 2-47: Representative stress strain curves (top) and magnified view of the elastic deformation (bottom) for (i) 9.8x10^{-3} g/cm^{2} of Pellethane in the trilayer, (ii) 1.9x10^{-2} g/cm^{2} of Pellethane in the trilayer, (iii) 3.9x10^{-2} g/cm^{2} of Pellethane in the trilayer. Noise of the samples in the magnified view is due to the sensitivity limitation of the Instron force gauge. All samples are $\theta = 90°$ with n of 5.

Figure 2-48: Summation of mechanical properties of the trilayer samples with variable Pellethane thickness obtained through interpretation of the stress-strain curves for all samples with the fiber orientation angle $\theta = 90°$. (a) Young's modulus, (b) tensile strength, (c) toughness and (d) strain-to-failure. All data points are an average of n = 5.

Figure 2-49: Representative stress-strain curves for (a) trilayer with 9.8x10^{-3} g/cm^{2} of Pellethane (b) magnified view of trilayer with 9.8x10^{-3} g/cm^{2} of Pellethane (c) trilayer with 3.9x10^{-2} g/cm^{2} of Pellethane and (d) magnified view of trilayer with 3.9x10^{-2} g/cm^{2} of Pellethane. Each graph shows seven distinct fiber orientation angles ($\Delta\theta$) of 0° (black), 15° (blue), 30° (green) 45°(purple), 60° (turquoise), 75° (red) and 90° (brown). All sample curves are an average of n = 5.

Figure 2-50: Representative post tensile tested dog bones (right) with pre tensile tested dog bones (left) for (a) trilayer with 9.8x10^{-3} g/cm^{2} of Pellethane 0°, (b) trilayer with 9.8x10^{-3} g/cm^{2} of Pellethane 90°, (c) trilayer with 3.9x10^{-2} g/cm^{2} of Pellethane 0°and (d) trilayer with 3.9x10^{-2} g/cm^{2} of Pellethane 90°.

Figure 2-51: Resulting mechanical properties of electrospun trilayer with $9.8\text{x}10^{-3}$ g/cm^2 of Pellethane from tensile testing as a function of the fiber orientation angle. (a) Young's modulus, (b) magnified view of Young's modulus, (c) tensile strength, (d) toughness and (e) strain-to-failure. All data points are an average of n = 5.

Figure 2-52: Resulting mechanical properties of electrospun trilayer with $3.9\text{x}10^{-2}$ g/cm^2 of Pellethane from tensile testing as a function of the fiber orientation angle. (a) Young's modulus, (b) magnified view of Young's modulus, (c) tensile strength, (d) toughness and (e) strain-to-failure. All data points are an average of n = 5.

Figure 2-53: Dynamic mechanical analysis of (a) storage and (b) loss modulus for $\theta = 0°$ and (c) storage and (d) loss modulus for $\theta = 90°$ of electrospun (i) trilayer with $9.8\text{x}10^{-3}$ g/cm^2 of Pellethane (ii) trilayer with $1.9\text{x}10^{-2}$ g/cm^2 of Pellethane and (iii) trilayer with $3.9\text{x}10^{-2}$ g/cm^2 of Pellethane.

Figure 2- 54: Dynamic mechanical analysis of 0° fiber orientation (solid) and 90° fiber orientation (dashed) for (a) electrospun trilayer with $9.8\text{x}10^{-3}$ g/cm^2 of Pellethane and (b) electrospun trilayer with $3.9\text{x}10^{-2}$ g/cm^2 of Pellethane.

Figure 2-55: Finite element analysis performed by Dr. Benjamin Wheatley[1] to calculate the correction factor for incorrect ASTM dog bones used. The strain multiplier is correlated with Poisson's ratio.

Figure 3-1: TGA mass loss curve as a function of temperature for poly(*tert*-butyl acrylate).

Figure 3-2: DSC of the second heating curve for poly(*tert*-butyl acrylate). The measured glass transition temperature (T_g) is 45 °C.

Figure 3-3: Conventional one way shape memory (1WSM) testing of poly(*tert*-butyl acrylate) showing four distinct steps. The 1WSM method involved equilibrating the temperature to 90.00 °C, isothermal for 5 min, then (i) ramped force at 0.0500 N/min to 0.25 N, isothermal for 2 min, (ii) ramped 2 °C/min to 0 °C, isothermal for 2 min, (iii) ramped force 0.2000 N/min to 0.0010 N, isothermal for 2 min and ramped 2 °C/min to 90.00 °C, isothermal for 2 min to complete cycle.

Figure 3-4: Manual stretcher custom made by the machine shop at Syracuse University.

Figure 3-5: Series of images of showing the combinations used to achieve high stretched opacity. Each combination was cured (original), heated above the T_g, stretched and then cooled under constraint (stretched 40%) and finally heated above the T_g and allowed to recover (recovered).

Figure 3-6: Sample graphs of intensity vs wavelength for the (a) light reference, (b) the dark reference, (c) the poly*(tert*-butyl acrylate) sample clear, (d) the poly(*tert*-butyl acrylate) sample opaque.

---

[1] . Collaboration with Dr. Benjamin Wheatley (Bucknell University, Mechanical Engineering) 2018

Figure 3-7: Translucency measured for each of the former combinations of poly(*tert*-butyl acrylate). The samples are (a) 1 wt. % silica dissolved in poly(*tert*-butyl acrylate), (b) 3 wt. % silica dissolved in poly(*tert*-butyl acrylate), (c) 5 wt. % silica dissolved in poly(*tert*-butyl acrylate), (d) 10 wt. % silica layered in poly(*tert*-butyl acrylate), (e) electrospun polylactic acid cured with poly(*tert*-butyl acrylate) and (f) electrospun poly(ε-caprolactone) cured with poly(*tert*-butyl acrylate).

Figure 3-8: SEM images of (a) poly(*tert*-butyl acrylate) with silica nanoparticles as cured and (b) stretched poly(t-butyl acrylate) showing the void spaces created.

Figure 3-9: Saw-tooth graph showing the measured translucency of 3 wt. % silica nanoparticles in poly(*tert*-butyl acrylate) undergoing a shape memory cycle five times, both in the stretched and recovered states.

Figure 3-10: Saw-tooth graph showing the measured translucency of 3 wt. % silica nanoparticles in poly(*tert*-butyl acrylate) undergoing a shape memory cycle five times were the amount of strain used is systematically increased, both in the stretched and recovered states.

Figure 3-11: Schematic of temperature gradient stage[8] as shown by DiOrio et. al. The same temperature stage was used for this research with the exception of having a solid aluminum top plate.

Figure 3-12: Pictures of the (a) setup used to functionally grade the poly(*tert*-butyl acrylate) with 3 wt. % silica nanoparticles (b) thermal image, and (c) thermal image of just the gradient stage.

Figure 3-13: Temperature measurements of the functional gradient stage, the glass slide, polymer T_g as measured using DSC without silica and the polymer T_g as measured using DSC with silica.

Figure 3-14: Image series showing the progression of shape memory recovery of the stretched poly(*tert*-butyl acrylate) with 3 wt. % silica particles. The sample has a glass transition temperature gradient through the length of the sample, which is increasing from right to left. The farthest left of the sample was intentionally held clear as a method to track recovery progress. Samples where heated using the Peltier plate for the AR-G2 TA rheometer, because it has a precise temperature control, within 0.1 °C and each temperature increment was confirmed using a thermocouple. The sample was allowed to equilibrate at each temperature increment for 5 min.

Figure 3-15: Series of graphs showing the translucency measurements of the functionally graded poly(*tert*-butyl acrylate) polymer with 3 wt. % silica nanoparticles. The sequence is quantifying how the sample in **Figure 3-14** is being recovered. The polymer has an increasing glass transition temperature from right to left. As the sample recovers, it also decreases in length, but generally the trend observed is the increasing of optical translucency from right to left as the temperature increase.

List of Tables

Table 2-13: Anisotropy of the electrospun fiber samples quantified as a function of Young's modulus in a ratio of the 0° / 90° fiber orientation angles obtained through interpreting the stress-strain curves.

Table 2-14: Average Young's modulus, toughness, tensile strength and strain to failure for all fiber orientation angles ($\Delta\theta$) interpreted from the stress strain curves of the electrospun trilayer of 15wt. % solution concentration of poly(methyl methacrylate).

Table 2-15: Average Young's modulus, toughness, tensile strength and strain to failure for all fiber orientation angles ($\Delta\theta$) interpreted from the stress strain curves of the electrospun trilayer of 20wt. % solution concentration of poly(methyl methacrylate).

Table 2-16: Anisotropy of the electrospun fiber samples quantified as a function of storage modulus in a ratio of the 0° / 90° fiber orientation angles obtained through interpreting the stress-strain curves.

Table 2-17: Average thickness as measured using SEM of the middle Pellethane layer thickness and the thickness of the poly(methyl methacrylate) layer for each composite.

Table 2-18: Unpaired t-test comparing the thickness of Pellethane of each composite with each other, showing there is a statistical difference between the total thickness of each composite and the middle Pellethane layer. Statistical difference $h = 1$.

Table 2-19: Char yield of trilayer composites in relation to the amount of Pellethane present based on TGA and DSC analysis. The thin, medium and thick layer of Pellethane trilayers have $9.8\text{x}10^{-3}$ g/cm^2, $1.9\text{x}10^{-2}$ g/cm^2 and $3.9\text{x}10^{-2}$ g/cm^2 of Pellethane respectively.

Table 2-20: Unpaired t-test comparing the mechanical properties of the variable thickness Pellethane trilayers with each other, showing there is no statistical difference between them $\theta = 0°$. Statistical difference $h = 1$.

Table 2-21: Unpaired t-test comparing the mechanical properties of the variable thickness Pellethane trilayers with each other, showing statistical difference between them $\theta = 90°$. Statistical difference $h = 1$.

Table 2-22: Anisotropy of the electrospun fiber samples quantified as a function of Young's modulus in a ratio of the 0° / 90° fiber orientation angles obtained through interpreting the stress-strain curves.

Table 2-24: Average Young's modulus, toughness, tensile strength and strain to failure for all fiber orientation angles ($\Delta\theta$) interpreted from the stress strain curves of the electrospun trilayer with $9.8\text{x}10^{-3}$ g/cm^2 of Pellethane.

Table 2-25: Average Young's modulus, toughness, tensile strength and strain to failure for all fiber orientation angles ($\Delta\theta$) interpreted from the stress strain curves of the electrospun trilayer with $3.9\text{x}10^{-2}$ g/cm^2 of Pellethane.

Chapter 1: Introduction

1.1 Inspiration

Polymeric materials are a serious driving force in today's markets; many nations, both in developed areas, as well as areas that are growing, have necessity for their versatility[1–3]. This drives a large demand for new technology that is polymer-based[4–6]. Specifically, polymer-based materials that have strength and durability that rival more expensive alternatives, as well as being environmentally[7–9] and biologically compatible,[10,11] are desired. These needs, which emanate from the end users of these products have continually set their expectations high and desire more. These factors lead to corporations as well as academia rushing in to meet these market demands[12,13]. In what follows, focus is placed on three specific niches that have application that have inspired the research of this dissertation.

Biomedical devices[14,15] are replete with highly engineered polymers. A great deal of research has gone into devices that interface with the human body with specific inquiry on how to improve upon them. Polymeric webs (sometimes referred to as "non-wovens") that can be triggered to actuate is a concept being used currently in systems like medical stents[16], drug delivery[17], and DNA scaffolds[18,19]. Incorporating a polymer into the design that can actuate[20] under controlled stimuli is the method generally used to achieve this. However, improvement can be made through using stimuli triggers[21–29] that are non-thermal and potentially have reversible actuation.

Biomimetic materials[30–32] are another such area where highly engineered polymers can show their superiority. Specifically, soft laminates[33] have shown strongly anisotropic[34] mechanical properties. This is done through the incorporation of elastomers into a more rigid polymer laminate. When these components are incorporated effectively the resulting material can be rigid in one direction and elastically compliant in another. Such a material would be ideal for mimicking naturally occurring membranes that have similar requirements, such as bat wings,[35,36] or fish fins[37,38]. Effectively mimicking these materials would allow vast improvement in personal or vehicular locomotion through either the medium of air or water.

Finally, the pharmaceutical packaging[39] business has highly specific design constraints stemming from customer interfacing. The packaging that drugs are stored and shipped in can add beneficially to both the producer and consumer[40,41]. As a practical example, this concept has been used to keep the packages from discoloring, which would otherwise give the customers a negative connotation about the product. The safety of end-usage is something that is always kept in the forefront, and is an area that can be improved upon. One such way that the packaging can aid in customer safety is creating a material which can give a visual cue that the product has exceeded, for instance, an unsafe temperature.

1.2 Active Polymers

Active polymers are an expanding catalog of materials that have the ability to actuate or change shape in response to a wide variety of external stimuli. Within this diverse group of polymers, shape memory polymers (SMPs) will be of specific interest in regard to the research contained within this dissertation. These materials, in general, are classified by the macromolecular mechanisms associated with a two-step process. The first step is their ability to be fixed into a temporary shape, with the second step specific to the polymers ability to recover to its original shape. There is a broad range of stimuli that has been used to activate this recovery notably temperature[42,43], solvent[44–46], enzymes[47], pH[48], light[49], electrical current[25], and magnetic fields[50].

Thermally responsive SMPs[51] are specifically the polymers that use temperature as the stimuli to initiate shape change in both programming and recovery. The general macroscopic process for observing the shape memory ability of a polymer network follows a five step process. The process is as follows: (1) heating, (2) deforming, (3) cooling in the deformed shape, (4) unloading of the deformation stress, and (5) heating to recover initial shape. The initial heating stage is done through a transition temperature such as the glass transition (T_g) or melting (T_m) temperatures, which are specific to each polymer. The heated polymer network can now be deformed into a secondary shape, which can be achieved through compression or elongation. In order to fix this temporary shape the polymer network will need to undergo a cooling below the transition temperature while in its deformed shape. To complete the final phase of the process and recover the initial shape, the polymer network need only to be heated again through the transition temperature. The schematic **Scheme 1-1** depicts the aforementioned shape memory cycle. Another method to visualize the process can be depicted through a 3D plot **Figure 1-1** of stress, strain and temperature, here shown for a semicrystalline network wherein crystallization-induced elongation under stress is evident between points (i) and (ii). A quantitative assessment of the polymer shape memory capabilities can be done using this method.

The shape memory process involves specifically two independent mechanisms, which are used to quantify the shape memory of a polymer network. These mechanisms take place at the nanoscale where polymer physics take control. The first mechanism is the shape fixing of the polymer network. In order for the overall polymer network to hold a temporary shape it needs to have immobility from polymer chain to polymer chain. In specific to thermally triggered SMPs, this polymer immobility is obtained through cooling the network through the transition temperatures. In crystalline and semi-crystalline polymers this can be the melt temperature (T_m).

In these crystalline regions the polymer network forms highly ordered arrangements of polymer chains, which are able to tightly pack together. These crystalline regions will act as physical crosslinks that will hold the polymer network in a temporary shape. In the case of amorphous polymers the important transition is vitrification, where the polymer network cools below the glass transition temperature. At this stage the polymer chains no longer have enough thermal or kinetic energy to move about. The polymer chain entanglements are now more of a physical barrier to chain motion, which reduces the overall free volume and an overall thermal contraction occurs. It is important to note that in this state, local polymer chain motion can still occur. This process is referred to as physical aging[52], and or creep, if there is an externally applied stress. This will not be considered for the scope of this dissertation because all samples made were tested consecutively, not allowing for these long time scale changes to occur. The most robust method for quantifying how well a polymer network is able to stay in a temporary shape is defined as the fixing ratio, R_f, and is shown in **Eq. (1-1)**

$$R_f(\%) = \frac{\varepsilon_f - \varepsilon_i}{\varepsilon_d - \varepsilon_i} * 100 \tag{1-1}$$

In the equation above ε_f is the fixed strain, which is specifically the strain after the stress has been removed. The initial strain before any deformation is ε_i and ε_d is the strain in the polymer after deformation but before the stress is released. The **Figure 1-1** can also show approximately how well the polymer has fixed through the slope of the curve at step 4. In general, the more flat the line, the better the polymer has held a secondary shape.

The other important mechanism involved is the shape recovery[53,54]. This is how well the polymer network is able to return to its original conformation. The polymer network's initial shape is obtained through crosslinking of the polymer chains. In general, the polymer can be physically crosslinked, which can occur through two polymer chains being entangled with each other as well as a region of crystallinity[55]. The polymer chains can also be chemically crosslinked which occurs through covalent and or hydrogen bonding[56]. During deformation the chemical bonds between atoms, or functional groups, are altered away from their lowest energy conformation. This new high energy state is maintained, until heating through a transition temperature which allows reorientation of the chemical bonds. The additive effect resulting from the reorientation of these bonds is what ultimately changes the macrostructure of the polymer network to its original low energy conformation. In so doing the polymer network has macroscopically appeared to remember its first shape. The method for quantifying the recovery of the polymer network is calculated below **Eq. (1-2)**

$$R_r(\%) = \frac{\varepsilon_f - \varepsilon_r}{\varepsilon_f - \varepsilon_i} * 100 \tag{1-2}$$

Rr is defined as the recovery ratio and is calculated very similarly to Rf, where all similar variables maintain their meaning. In this new equation ε_r is the strain of the polymer network after it has fully recovered, or in **Figure 1-1** the end of step 5.

1.3 Hydration-Triggered Shape Memory Polymers

As briefly touched upon, the shape memory affect can be exploited from polymer networks that use a non-thermal trigger to initiate the shape change. The exact mechanism is different than the thermally triggered SMPs discussed above. Specific to this dissertation, water triggered shape memory will be further exploited. In this, the transition temperature of T_g will be affected through the application of water. The water molecules diffuse into the network of polymer chains and disrupt the normal structure, particularly the free volume. This can cause a local swelling of the polymer to accommodate the excess water. This water acts as a plasticizer, where it liberates motion between the polymer chains, subsequently reducing the T_g of the affected area. This locally controlled reduction of the polymer T_g can be used to trigger the recovery of an SMP. This effect can also be used for semi-crystalline polymers, where the water is able to disassociate the crystalline regions. The speed of recovery in these polymers can be affected through adjusting the main contributing factors. Increasing the porosity of the polymer web would allow faster diffusion, and decrease the overall recovery time.

1.4 Fabrication of Polymer Composites

The mechanical properties of a singular polymeric systems (single component) are often times not able to meet the demands required for a specific purpose. One method that has been used to address this limitation has been to incorporate another polymer that can make up for the mechanical short fall. There are many methods for incorporating two polymers together to synergize their mechanical properties, however the scope of this dissertation will focus on using electrospinning as the main fabrication methodology.

Electrospinning[57] is simplistic in concept as well as application, and it has proven itself to be a valuable method for producing polymeric materials in non-woven, micro/nanoporous form. The method has many features[58] that are worth consideration such as price[59], ease of use, and variability. A salient attribute that makes electrospinning so intriguing is that it is capable of producing micro[60] and nano-sized polymer fibers[61–64]. Generating fibers of this fine scale allows characteristics such as a large surface area to volume ratio as well as improved stiffness and tensile strength[65], when compared to other processing forms of the same materials. When adding to this the ability to incorporate different polymers, different fiber morphologies or a variable compositional makeup, the sheer number of different materials that can be made are seemingly endless. Incorporating polymers together with vastly different attributes would allow the engineering of highly complex composites that could fit tightly specialized needs. A schematic of the electrospinning setup is shown in **Scheme 1-2**, described in details below.

Electrospinning as a process requires first, a polymer solution, which is usually a pelletized polymer dissolved in particular solvent(s). The solvents selected, aside from having the correct solubility for this use, should also have an adequate electrical properties, particularly a sufficiently high dielectric constant. The volatility of the solvent is also a major factor in ultimately forming a good fibrous sheet. If the solvent used is too volatile, it will evaporate too quickly causing gelation at the needle tip and decreasing the overall amount of polymer reaching the collector. If the solvent is not volatile enough, the fibers will have trapped solvent in the web and that will alter the desired morphology of the web. Using a ratio of miscible volatile and nonvolatile solvents for the solution can obviate these issues. These polymer solutions are placed in a syringe and dispensed using a syringe pump to precisely control the volumetric flow rate. A voltage source is applied to a metallic needle tip and at the liquid-air interface the polymer solution transforms in shape from a hemispherical meniscus to a Taylor cone. This comes about through a balance between the electrostatic repulsion created by the high voltage and the surface tension of the polymer solution. The electrostatic force overcomes the surface tension and a stream of fluid is pulled toward an electrical ground, or “collector” which is either maintained at electrical ground or with an oppositely charged potential. The amount and forcefulness that the polymer is pulled toward the collector can be adjusted through adjusting the needle tip voltage; e.g., the more voltage the more electrostatic force and the smaller the resulting Taylor cone. However, as the voltage is increased, if the surface charge density exceeds a particular threshold the resulting jet can split into multiple smaller jets. Before the polymer fluid stream reaches the collector, an instability arises and causes an erratic whipping of the polymer stream. In this regime, the polymer stream experiences a strong elongational force, which stretches the polymer to its desired micro/nano diameter as well as efficiently releases the solvent from the solution, helping to solidify the resulting fiber. Controlling the concentration of polymer in solution can affect the resulting fiber diameter. Reducing the amount of polymer in solution will cause smaller and smaller fiber diameter directly through mass transfer considerations and indirectly through the effect of concentration on viscosity. Considering mass transfer, in particular, less polymer (relative to solvent) flowing through a cross section of the needle tip per unit time will result in smaller diameters after solvent evaporation. There is a critical value of polymer concentration in solution that is required in order to make fibers as opposed to droplets or beaded fibers. Below this threshold the polymer surface tension will be too large and cause the resulting process to form beads. This process can be taken advantage of for making micro/nano particles and is referred to as electrospraying. That will not be further considered for the scope of this dissertation. The final step in the process is where the polymer fibers are being collected. Using a spinning mandrel allows you the ability to align the polymer fibers. In general, the faster the mandrel is rotating the more anisotropy you can observe.

The final method for polymer fabrication in this dissertation will focus on the development of a polymeric network based on *t*-butyl acrylate monomer. The polymerization of acrylate monomers[66] shown in **Scheme 1-3** occurs when it is mixed with a photo-initiator and cross linking agent. This process is started through the exposure to UV light, 200-400nm wavelength, and is propagated through a process of radical polymerization[67]. The photo-initiator absorbs the UV light decomposes to generate the required free radicals. These subsequent free radicals will attack the double bonds of the acrylate causing them to link together with other monomers forming a polymer. When a crosslinking agent is used, the free radicals will attack both the acrylate monomer and the crosslinking molecule (two or more monomers linked together), yielding a branched and, eventually crosslinked macromolecule. For the particular chemistry indicated, a glassy network results after full conversation of monomers to polymer. The benefit of using this particular system is its thermal responsiveness. The material begins optically clear, upon exposure to a temperature increase and the material will become optically opaque. Additions of catalytic compounds into this schematic had been briefly attempted. The effects of the catalysis[68] allowed polymerization of the material in significantly reduced reaction times. However, quantifying the effect of the previously uninvestigated compounds in this material was largely outside the scope of this research.

1.5 Scope of Dissertation

The research enclosed within seeks to take advantage of the attributes from electrospinning. Mainly, the ability to accurately incorporate two polymer fibers together with precision to control their individual distribution in the resulting composite. Doing so we seek to create novel polymeric material that will display mechanical properties that maximize the synergy of both components. **Chapter 2** The goal is to combine a rigid glassy polymer with an elastomer in a unique form that maximizes mechanical anisotropy. This chapter will detail how the exact distribution of these two materials will result in drastically different mechanical properties. **Chapter 3** The goal is to combine poly(*t*-butyl acrylate) with silica nano-particles so that the resulting composite can change its optical transparency.. This represents a significant extension of the research done by Dengteng et. al[69]. where we will create a thermally sensitive matrix polymer with silica nanoparticles distributed throughout. Using a shape memory effect, we will demonstrate the same effect Dengteng was able to achieve, but through the use of thermal actuation to trigger the optical response. Continuing, we will use a method to functionally grade the material, so as to cause the thermal actuation in stages through the material.

Throughout the research, specific focus will be placed on the material properties of each composite material. The careful probing of these properties is critical for understanding the role that they play in the resulting material. Elucidating the material properties is then essential for creating more complex devices using that material. A brief discussion for potential applications of each material will be given for further context on development and design constraints.

1.6 References

1. Bakis C. E. *et al.* Fiber-Reinforced Polymer Composites for Construction—State-of-the-Art Review. *J. Compos. Constr.* **6,** 73–87 (2002).

2. Siracusa, V., Rocculi, P., Romani, S. & Rosa, M. D. Biodegradable polymers for food packaging: a review. *Trends Food Sci. Technol.* **19,** 634–643 (2008).

3. Heeger, A. J. Semiconducting and metallic polymers: the fourth generation of polymeric materials. *Synth. Met.* **125,** 23–42 (2001).

4. Geyer, R., Jambeck, J. R. & Law, K. L. Production, use, and fate of all plastics ever made. *Sci. Adv.* **3,** e1700782 (2017).

5. Galaev, I. Y. & Mattiasson, B. ‘Smart’ polymers and what they could do in biotechnology and medicine. *Trends Biotechnol.* **17,** 335–340 (1999).

6. Kumar, A., Srivastava, A., Galaev, I. Y. & Mattiasson, B. Smart polymers: Physical forms and bioengineering applications. *Prog. Polym. Sci.* **32,** 1205–1237 (2007).

7. Hatakeyama, H. Thermal analysis of environmentally compatible polymers containing plant components in the main chain. *J. Therm. Anal. Calorim.* **70,** 755–795 (2002).

8. Monteiro, S. N., Lopes, F. P. D., Ferreira, A. S. & Nascimento, D. C. O. Natural-Fiber Polymer-Matrix Composites: Cheaper, Tougher, and Environmentally Friendly. *JOM N. Y.* **61,** 17–22 (2009).

9. Janaki, V. *et al.* Polyaniline/chitosan composite: An eco-friendly polymer for enhanced removal of dyes from aqueous solution. *Synth. Met.* **162,** 974–980 (2012).

10. Elbert, D. L. & Hubbell, J. A. Surface Treatments of Polymers for Biocompatibility. *Annu. Rev. Mater. Sci.* **26,** 365–394 (1996).

11. Shah, A. A., Hasan, F., Hameed, A. & Ahmed, S. Biological degradation of plastics: A comprehensive review. *Biotechnol. Adv.* **26,** 246–265 (2008).

12. Harun, R., Singh, M., Forde, G. M. & Danquah, M. K. Bioprocess engineering of microalgae to produce a variety of consumer products. *Renew. Sustain. Energy Rev.* **14,** 1037–1047 (2010).

13. Schettler, T. Human exposure to phthalates via consumer products. *Int. J. Androl.* **29,** 134–139 (2006).

14. Middleton, J. C. & Tipton, A. J. Synthetic biodegradable polymers as orthopedic devices. *Biomaterials* **21,** 2335–2346 (2000).

15. Chaterji, S., Kwon, I. K. & Park, K. Smart polymeric gels: Redefining the limits of biomedical devices. *Prog. Polym. Sci.* **32,** 1083–1122 (2007).

16. Kuribayashi, K. *et al.* Self-deployable origami stent grafts as a biomedical application of Ni-rich TiNi shape memory alloy foil. *Mater. Sci. Eng. A* **419,** 131–137 (2006).

17. Fernandes, R. & Gracias, D. H. Self-folding polymeric containers for encapsulation and delivery of drugs. *Adv. Drug Deliv. Rev.* **64,** 1579–1589 (2012).

18. Rothemund, P. W. K. Folding DNA to create nanoscale shapes and patterns. *Nature* **440,** 297–302 (2006).

19. Douglas, S. M. *et al.* Self-assembly of DNA into nanoscale three-dimensional shapes. *Nature* **459,** 414–418 (2009).

20. Prior, C., Moussou, J., Chakrabarti, B., Jensen, O. E. & Juel, A. Ribbon curling via stress relaxation in thin polymer films. *Proc. Natl. Acad. Sci. U. S. A.* **113,** 1719–1724 (2016).

21. Torbati, A. H., Nejad, H. B., Ponce, M., Sutton, J. P. & Mather, P. T. Properties of triple shape memory composites prepared via polymerization-induced phase separation. *Soft Matter* **10,** 3112–3121 (2014).

22. Nejad, H. B., Baker, R. M. & Mather, P. T. Preparation and characterization of triple shape memory composite foams. *Soft Matter* **10,** 8066–8074 (2014).

23. Lendlein, A., Jiang, H., Jünger, O. & Langer, R. Light-induced shape-memory polymers. *Nature* **434,** 879–882 (2005).

24. Lee, K. M., Koerner, H., Vaia, R. A., Bunning, T. J. & White, T. J. Light-activated shape memory of glassy, azobenzene liquid crystalline polymer networks. *Soft Matter* **7,** 4318–4324 (2011).

25. Luo, X. & T. Mather, P. Conductive shape memory nanocomposites for high speed electrical actuation. *Soft Matter* **6,** 2146–2149 (2010).

26. Leng, J. S. *et al.* Electrical conductivity of thermoresponsive shape-memory polymer with embedded micron sized Ni powder chains. *Appl. Phys. Lett.* (20080107).

27. Schmidt, A. M. Electromagnetic Activation of Shape Memory Polymer Networks Containing Magnetic Nanoparticles. *Macromol. Rapid Commun.* **27,** 1168–1172 (2006).

28. Mohr, R. *et al.* Initiation of shape-memory effect by inductive heating of magnetic nanoparticles in thermoplastic polymers. *Proc. Natl. Acad. Sci. U. S. A.* **103,** 3540–3545 (2006).

29. Chen, H. *et al.* Highly pH-sensitive polyurethane exhibiting shape memory and drug release. *Polym. Chem.* **5,** 5168–5174 (2014).

30. Drotleff, S. *et al.* Biomimetic polymers in pharmaceutical and biomedical sciences. *Eur. J. Pharm. Biopharm.* **58,** 385–407 (2004).

31. Ma, P. X. Biomimetic materials for tissue engineering. *Adv. Drug Deliv. Rev.* **60,** 184–198 (2008).

32. Duncan, R. The dawning era of polymer therapeutics. *Nat. Rev. Drug Discov.* **2,** nrd1088 (2003).

33. Mouritz, A. P. Review of z-pinned composite laminates. *Compos. Part Appl. Sci. Manuf.* **38,** 2383–2397 (2007).

34. Mathieu, L. M. *et al.* Architecture and properties of anisotropic polymer composite scaffolds for bone tissue engineering. *Biomaterials* **27,** 905–916 (2006).

35. Cheney, J. A. *et al.* Membrane muscle function in the compliant wings of bats. *Bioinspir. Biomim.* **9,** 025007 (2014).

36. Furst, S. J., Bunget, G. & Seelecke, S. Design and fabrication of a bat-inspired flapping-flight platform using shape memory alloy muscles and joints. *Smart Mater. Struct.* **22,** 014011 (2012).

37. Lauder, G. V. & Drucker, E. G. Morphology and experimental hydrodynamics of fish fin control surfaces. *IEEE J. Ocean. Eng.* **29,** 556–571 (2004).

38. Ono, N., Kusaka, M., Taya, M. & Wang, C. Design of fish fin actuators using shape memory alloy composites. in *Smart Structures and Materials 2004: Industrial and Commercial Applications of Smart Structures Technologies* **5388,** 305–313 (International Society for Optics and Photonics, 2004).

39. Karbowiak, T., Debeaufort, F. & Voilley, A. Importance of Surface Tension Characterization for Food, Pharmaceutical and Packaging Products: A Review. *Crit. Rev. Food Sci. Nutr.* (2007). doi:10.1080/10408390591000884

40. Piringer, O. G. & Baner, A. L. *Plastic Packaging: Interactions with Food and Pharmaceuticals*. (John Wiley & Sons, 2008).

41. Farris, S., Schaich, K. M., Liu, L., Piergiovanni, L. & Yam, K. L. Development of polyion-complex hydrogels as an alternative approach for the production of bio-based polymers for food packaging applications: a review. *Trends Food Sci. Technol.* **20,** 316–332 (2009).

42. Santiago, D., Ferrando, F. & Flor, S. D. la. Influence of Holding Time on Shape Recovery in a Polyurethane Shape-Memory Polymer. *J. Mater. Eng. Perform.* **23,** 2567–2573 (2014).

43. Westbrook, K. K. *et al.* Two-way reversible shape memory effects in a free-standing polymer composite. *Smart Mater. Struct.* **20,** 065010 (2011).

44. Gu, X. & Mather, P. T. Water-triggered shape memory of multiblock thermoplastic polyurethanes (TPUs). *RSC Adv.* **3,** 15783–15791 (2013).

45. Huang, W. M., Yang, B., An, L., Li, C. & Chan, Y. S. Water-driven programmable polyurethane shape memory polymer: Demonstration and mechanism. *Appl. Phys. Lett.* **86,** 114105 (2005).

46. Lv, H., Leng, J., Liu, Y. & Du, S. Shape-Memory Polymer in Response to Solution. *Adv. Eng. Mater.* **10,** 592–595 (2008).

47. Toledano, S., Williams, R. J., Jayawarna, V. & Ulijn, R. V. Enzyme-Triggered Self-Assembly of Peptide Hydrogels via Reversed Hydrolysis. *J. Am. Chem. Soc.* **128,** 1070–1071 (2006).

48. Han, X.-J. *et al.* pH-Induced Shape-Memory Polymers. *Macromol. Rapid Commun.* **33,** 1055–1060 (2012).

49. Long, K. N., Scott, T. F., Jerry Qi, H., Bowman, C. N. & Dunn, M. L. Photomechanics of light-activated polymers. *J. Mech. Phys. Solids* **57,** 1103–1121 (2009).

50. Buckley, P. R. *et al.* Inductively Heated Shape Memory Polymer for the Magnetic Actuation of Medical Devices. *IEEE Trans. Biomed. Eng.* **53,** 2075–2083 (2006).

51. Mather, P. T., Luo, X. & Rousseau, I. A. Shape Memory Polymer Research. *Annu. Rev. Mater. Res.* **39,** 445–471 (2009).

52. Eulate, N. G. P.-D. & Cangialosi, D. The very long-term physical aging of glassy polymers. *Phys. Chem. Chem. Phys.* (2018). doi:10.1039/C8CP01940A

53. Liu, C., Qin, H. & Mather, P. T. Review of progress in shape-memory polymers. *J. Mater. Chem.* **17,** 1543–1558 (2007).

54. Rousseau, I. A. Challenges of shape memory polymers: A review of the progress toward overcoming SMP's limitations. *Polym. Eng. Amp Sci.* **48,** 2075–2089 (2008).

55. Yang, F., Zhang, S. & Li, J. C. M. Impression recovery of amorphous polymers. *J. Electron. Mater.* **26,** 859 (1997).

56. Liu, C. *et al.* Chemically Cross-Linked Polycyclooctene: Synthesis, Characterization, and Shape Memory Behavior. *Macromolecules* **35,** 9868–9874 (2002).

57. Greiner, A. & Wendorff, J. H. Electrospinning: A Fascinating Method for the Preparation of Ultrathin Fibers. *Angew. Chem. Int. Ed.* **46,** 5670–5703 (2007).

58. Mercante, L. A., Scagion, V. P., Migliorini, F. L., Mattoso, L. H. C. & Correa, D. S. Electrospinning-based (bio)sensors for food and agricultural applications: A review. *TrAC Trends Anal. Chem.* **91,** 91–103 (2017).

59. Persano, L., Camposeo, A., Tekmen, C. & Pisignano, D. Industrial Upscaling of Electrospinning and Applications of Polymer Nanofibers: A Review. *Macromol. Mater. Eng.* **298,** 504–520 (2013).

60. Jaworek, A. Micro- and nanoparticle production by electrospraying. *Powder Technol.* **176,** 18–35 (2007).

61. Deitzel, J. M., Kleinmeyer, J., Harris, D. & Beck Tan, N. C. The effect of processing variables on the morphology of electrospun nanofibers and textiles. *Polymer* **42,** 261–272 (2001).

62. Fong, H., Chun, I. & Reneker, D. H. Beaded nanofibers formed during electrospinning. *Polymer* **40,** 4585–4592 (1999).

63. Huang, Z.-M., Zhang, Y.-Z., Kotaki, M. & Ramakrishna, S. A review on polymer nanofibers by electrospinning and their applications in nanocomposites. *Compos. Sci. Technol.* **63,** 2223–2253 (2003).

64. Rutledge, G. C. & Fridrikh, S. V. Formation of fibers by electrospinning. *Adv. Drug Deliv. Rev.* **59,** 1384–1391 (2007).

65. Shenoy, S. L., Bates, W. D., Frisch, H. L. & Wnek, G. E. Role of chain entanglements on fiber formation during electrospinning of polymer solutions: good solvent, non-specific polymer–polymer interaction limit. *Polymer* **46,** 3372–3384 (2005).

66. Page, Z. A. *et al.* A di-tert-butyl acrylate monomer for controlled radical photopolymerization. *J. Polym. Sci. Part Polym. Chem.* **55,** 801–807 (2017).

67. Matyjaszewski, K., Nakagawa, Y. & Jasieczek, C. B. Polymerization of n-Butyl Acrylate by Atom Transfer Radical Polymerization. Remarkable Effect of Ethylene Carbonate and Other Solvents. *Macromolecules* **31,** 1535–1541 (1998).

68. Avar, S., Mortazavi, S. M. M., Ahmadjo, S. & Zohuri, G. H. α-Diimine nickel catalyst for copolymerization of hexene and acrylate monomers activated by different cocatalysts. *Appl. Organomet. Chem.* **32,** e4238 (2018).

69. Ge, D. *et al.* A Robust Smart Window: Reversibly Switching from High Transparency to Angle-Independent Structural Color Display. *Adv. Mater.* **27**, 2489–2495 (2015).

1.6 Figures, Schemes and Tables

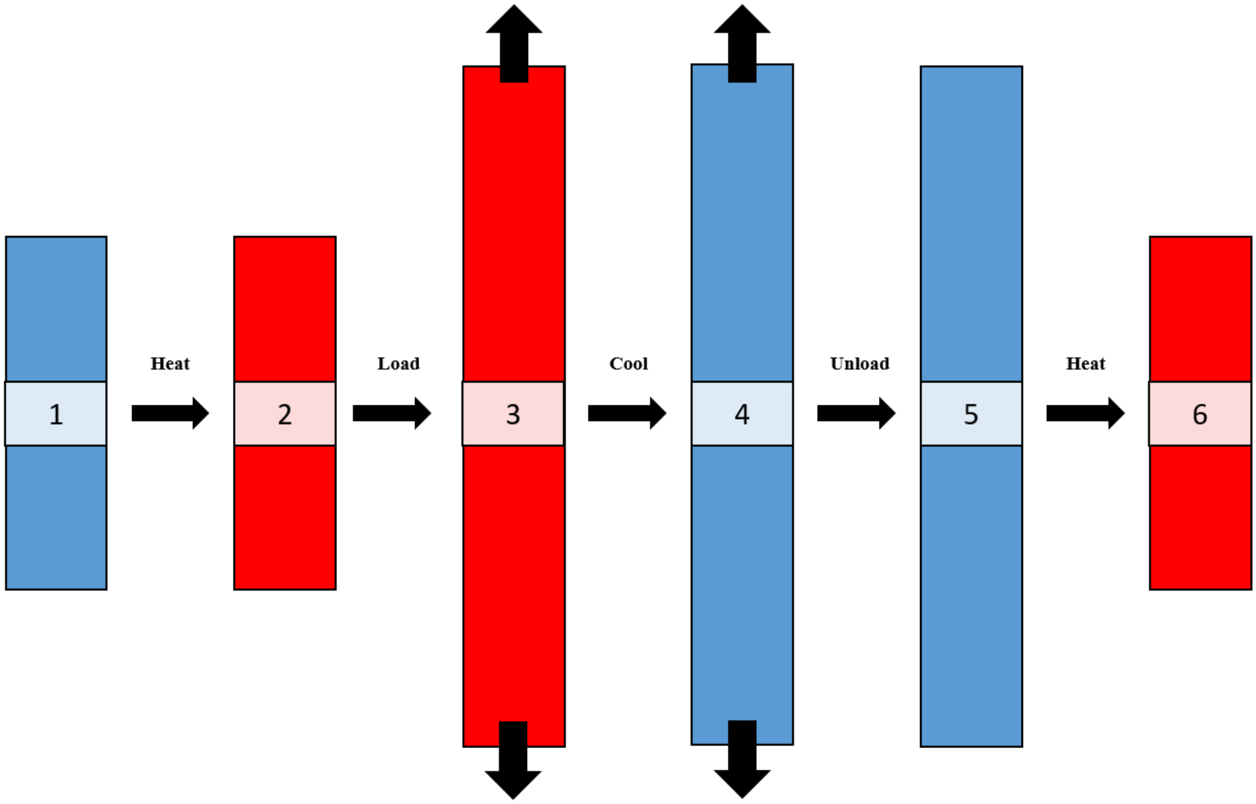

Scheme 1-1 A general shape memory cycle for a thermally triggered shape memory polymer. The polymer (1) is heated above the transition temperature (2) and then deformed through applying a load (3). While maintaining the deformation the sample is cooled below the same transition temperature (4) and then the sample is unloaded (5). The sample is heated above the transition temperature again (6) to recover the fixed strain in the sample, and it will return to its original shape.

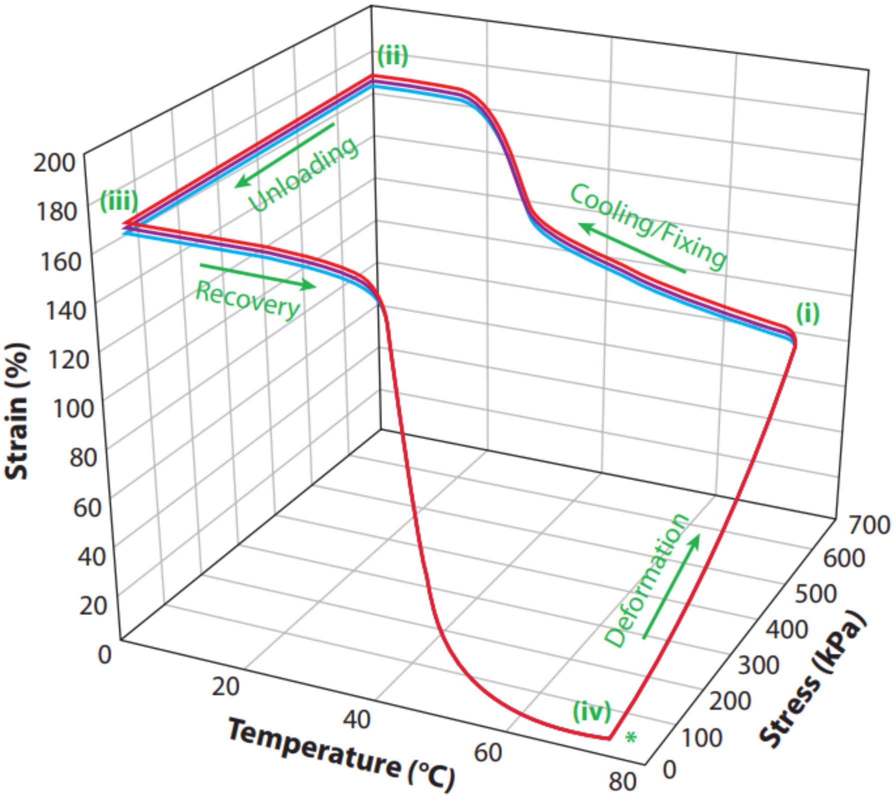

Figure 1-1 A general shape memory cycle as depicted in a 3D graph[51] of stress, strain and temperature for a thermally triggered SMP. The steps of the cycle and their corresponding positions on the graph are (i) deformation after heating above transition temperature, (ii) shape fixing, (iii) unloading and (iv) heating to obtain shape recovery. The polymer used to demonstrate this is cross-linked poly(cyclooctene)

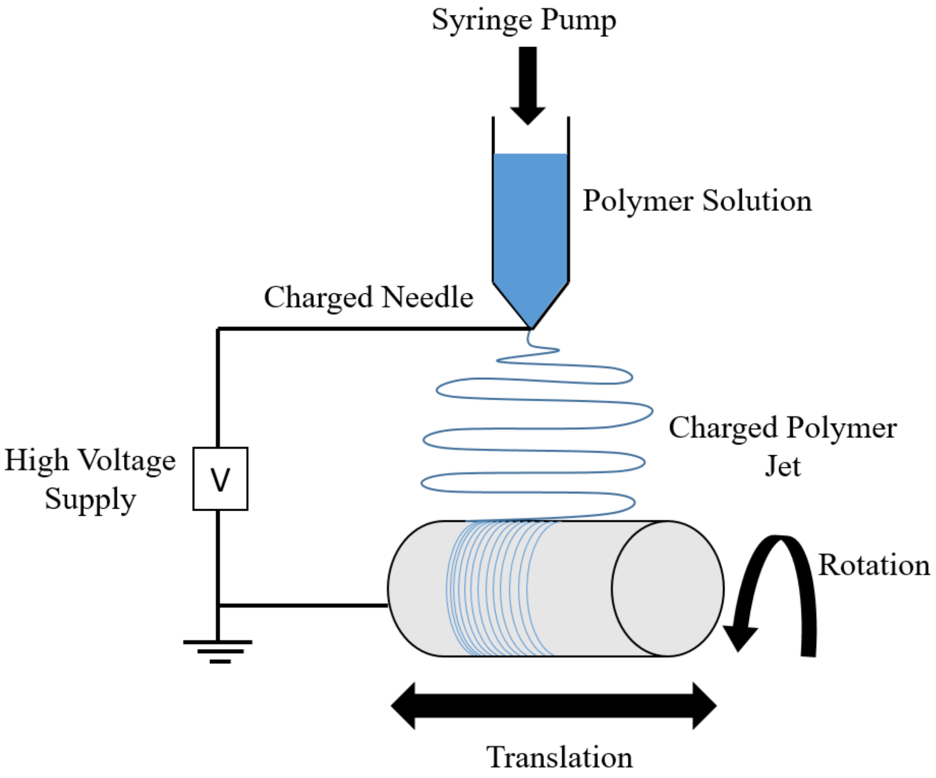

Scheme 1-2 A general electrospinning setup used to fabricate anisotropic/isotropic fibers

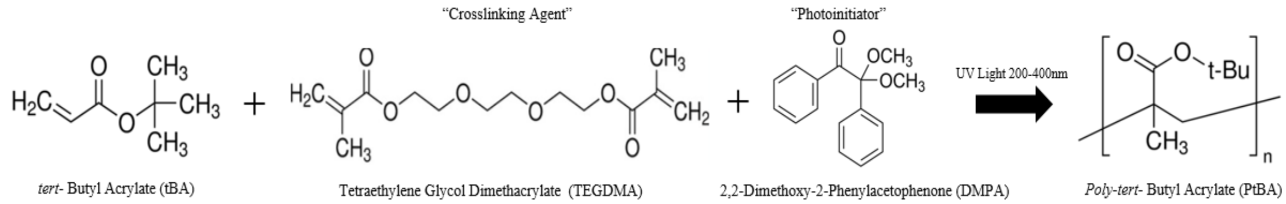

Scheme 1-3 A *tert*-butyl acrylate monomer being combined with TEGDMA, as crosslinking agent and DMPA a photo initiator to be cured under ultraviolet light to form the polymer film.

Chapter 2. Design, Processing, and Characterization of New Anisotropic Electrospun Polymer Composites.

2.1 Synopsis

This chapter aims to design, fabricate, and characterize new highly anisotropic polymeric composites. Previous attempts showed that achieving anisotropy can be done through incorporating electrospun fibers into a matrix material. Building upon that, the current research will use specifically poly(methyl methacrylate) and Pellethane 5863-80A (hereafter "Pellethane"); both polymers will be electrospun in layers to create a laminated structure designed to yield the desired anisotropy. In this chapter, the relative thickness of Pellethane, as well as differences in the specific laminate structures will be investigated in order to determine the optimal anisotropy.

2.2 Introduction

Rigid anisotropic materials have been widely researched and developed for use in industries from automotive to aeronautics. The usefulness of these materials is multifaceted, with a noteworthy contribution being improved damage tolerance through highly directional fracture toughness[1]. The overall damage tolerance of any material will be dependent on variables like strength, ductility, and the overall microstructure. For instance, crack propagation through a material can be arrested through incorporation of highly oriented fibers[2]. Broadly, anisotropic materials have another noteworthy contribution which is they can exhibit rigid strength directionally, while also employing a high yield stress. Development of a material that displays these characteristics is the focus of this chapter.

Building upon the material knowledge developed for rigid, load-bearing composite materials, a need has emerged for polymer-based anisotropic materials for applications in "soft[3] industries" like medicine and biological mimicry. Soft material anisotropy can be used for developing a range of biomimetic materials from artificial myocardium[4,5] to artificial extracellular matrix material[6,7]. More specifically, advancements in biomimicry for potential technological application is the impetus for the research contained within. Replication of natural anisotropic biological materials such as bat wings[8,9] or fish fins has applications in autonomous robotics for both private-sector and military purposes. Replicating a bat wing has specific design constraints, where the material needs to be stiff in the airfoil (cord) direction but also collapsible in the span direction. A bat wing is structurally a membrane that is comprised of a collagen and elastin fiber bundle network. Each of these biological inspiring materials is mechanically distinctive and provides the membranes overall anisotropy using various fiber orientations. There is speculation that these two materials play a critical role to effectively transmit aerodynamic forces from the wing membrane to the skeleton[9].

Development of soft anisotropic materials has been approached from several different angles. Extrusion has been a fabrication approach used to improve anisotropy in polymeric materials. Burt et al.[10] used a method of multilayer co-extrusion of Polystyrene (PS) and Polystyrene-block-polyethylene / polypropylene-block-polystyrene (SEPS) to get shear banded separation of the two polymer blends yielding a multilayer material. They found that the yielding behavior (plastic deformation) in the cylindrical direction was far different than in the extrusion direction. They postulate through precise control of the thickness of the given layers they could tune the material properties from brittle to ductile. Li et al.[11] used a method of melt blending cylinder-forming poly (styrene-b-butadiene-co-butylene-b-styrene) (SBBS) and a liquid crystal polymer (LCP). Injection molding of this material allows the LCP to form highly ordered fibers in the SBBS matrix. They were able to achieve excellent anisotropic properties with the modulus parallel to the injection direction 47 times higher than in the transverse direction, with a 56 times smaller elongation at break. One potential downside to the extrusion method is in the limitation of the materials that can be effectively mixed together. Another potential downside is that the overall structure of the resulting material is a film. Having versatility to fabricate film / fiber networks would be more desirable.

Electrospinning, as a fabrication technique, would be able to overcome the limitations of extrusion while having the advantage of incorporating a wide variety of polymeric materials together. This method can also be used to make anisotropic materials shown from work done by Neisiany et al.[12]. They used electrospun styrene acrylonitrile (SAN) nanofibers to improve the impact properties of conventional carbon fiber/ epoxy composites. This research group found that when these fibers were embedded into the carbon fiber/epoxy material there was a significant increase in several of the material properties such as flexural strength, flexural work to fracture, interlaminar shear strength, and impact absorption energy. This improvement made a new material which had a much tougher fracture, during breakage. Incorporating polymeric fibers into a matrix material is an appealing method for developing highly anisotropic materials.

Building upon the idea of embedding electrospun fibers into a matrix material, Rodriguez et al.[13] used electrospun polyvinyl acetate (PVAc) to reinforce a crosslinked PDMS matrix. What they found was good anisotropy in terms of the materials modulus, when comparing the 0° fiber direction to the perpendicular, or 90° fiber direction. However, the more interesting adaptation of this research was using shape memory polymers to do so. Rodriguez was able to add the functionality of thermally triggered shape memory into an anisotropic material[14].

All the prior research suggests that a high degree of anisotropy in a polymeric material is best achieved using a fiber-based composite approach. Specifically, the method that seems to take advantage of both the prior fabrication methods is to create an electrospun laminated structure. Kousaalya et al.[15] used an alternate film stacking technique of poly (lactic acid) (PLA) and areca fibers as a bio-based laminate to the popular alternative of thermoplastic polyolefins. They found that a 6% by weight increase in the amount of areca fibers in the composite can lead to a 50% increase in the crystallinity of PLA. Similarly Zarabadi et al.[16] were also interested in using a laminated structure of electrospun nylon-6 with oat based protein to make more environmentally friendly biodegradable film. They found that through incorporating these fibers in as little as 0.5% (wt/wt) that the water permeability decreased while the oxygen and water vapor permeability as well as the films mechanical properties all increased. The real upside to their approach was that the incorporation of these fibers did not alter the optical properties of the composites produced. The laminated structure can also work well with epoxy resins as shown from Ognibene et al.[17]. They found that using a laminated structure of epoxy resin with fiber reinforced veils had the effect of lowering the curing times, as well as showed that the solution had complex viscoelastic properties.

Poly(methyl methacrylate) (PMMA) has been broadly applied in various polymeric products because of its competitive material characteristics. PMMA is a strong and tough material[18] that is also lightweight and easily processed, allowing development of commercial products, such as Plexiglas™. These characteristics make it an excellent candidate for making composite laminate materials[19] via electrospinning[20].

The aim within this chapter is to incorporate poly(methyl methacrylate) with a thermoplastic elastomer, Pellethane® using a laminated structure. The purpose for doing so is to optimize the resulting material's mechanical anisotropy. We will use the fabrication technique of electrospinning to sequentially layer oriented, nonwoven fibrous sheet of PMMA and Pellethane. Electrospinning each polymer in alternating layers directly on top of the last will be the method for obtaining an overall laminate structure. The differences in the stiffness and elasticity of the two polymers used were anticipated to yield highly anisotropic properties in the resulting laminated nonwoven films.

2.3 Experimental

2.3.1 Materials

Pellethane® (5863-80A) (hereafter, “Pellethane”; a polyether-based thermoplastic polyurethane elastomer) pellets were supplied from the Lubrizol Corporation. Poly(methyl methacrylate) (PMMA) (Mw = 550,000 g/mol) pellets was purchased from Sigma-Aldrich. Chloroform ($CHCl_3$) and N,N- dimethylformamide (DMF) were also purchased from Sigma-Aldrich, the Tetrahydrofuran (THF) was purchased from VWR International. All solvents and pellets were used as received.

2.3.2 Electrospinning Solutions

The electrospinning solution of Pellethane contained 11% w/v and was dissolved in a solution of DMF and THF in a 1:1.5 ratio which is a modified method from Robertson et al[21]. The poly(methyl methacrylate) solution contained 20%, 15%, or 10% w/v for each respective composite and was dissolved in a DMF and $CHCl_3$ solution in a 1:4 ratio, which is a modified method from Luo et al[22]. Both solutions were stirred continuously for 24 - 36 h at room temperature to ensure the polymers were completely dissolved and the solution was distributed evenly.

2.3.3 Electrospinning Equipment

All composites contained within were fabricated using the Spraybase® electrospinning syringe pumps and voltage sources which were integrated into the rotating drum collector with a multi-head emitter as shown in **Scheme 1-2**. For the purposes of this research only 2 emitters were used. The metallic mandrel is 300 mm in width and 95.6 mm in diameter. The tubing used to connect the syringe pump to the emitter is 1 mm in diameter and 18 gauge emitters were used for both solutions. The collector mandrel was set to -1000 V and to a rotational speed of 2000 rpm. Both of the emitter tips were translated across the width of the mandrel from 60 mm to 190 mm and were held at a large positive electrical potential in the range of 12 to 13 kV.

2.3.4 Anisotropic Composite Fabrication

2.3.4.1 Singular Component Fabrication

Both poly(methyl methacrylate) and Pellethane were electrospun into individually formed fiber mats. A 10wt. % solution concentration of poly(methyl methacrylate) and an 11wt. % solution concentration of Pellethane was used. The flow rate of 8 mL/h for 2 h and the flow rate of 10 mL/h for 2h was used for Pellethane and poly(methyl methacrylate) respectively.

2.3.4.2 Dual Electrospun Composite Fabrication

A dual electrospinning setup was used to simultaneously electrospun both the polymers for this composite. Both polymer solutions were spun and collected on the same mandrel rotating at 2000 rpm. The two syringes containing the polymer solutions were connected to the electrospinner via a 1mm ID tubing and were positioned on opposite sides of the mandrel. The needle tip to the mandrel distance was kept constant for both polymer streams at approximately 8 cm. The flow rates for the syringes were controlled by separate pumps and could be programmed independent of each other, which allowed control over the relative weight fraction of each polymer in the composite fiber mat.

2.3.4.3 Trilayer Composite Fabrication

The trilayer composites were prepared by first, electrospinning the poly(methyl methacrylate) solution onto a rotating drum at 2000 rpm. Immediately following that, Pellethane was electrospun directly on top of the poly(methyl methacrylate) fiber sheet. Finally, the same poly(methyl methacrylate) solution was electrospun directly on top of the Pellethane.

2.3.4.4 Trilayer with Variable Poly(methyl methacrylate) sol. Wt. %

Three separate trilayer composites were fabricated by systematically increasing the poly(methyl methacrylate) solution concentration from 10wt. % to 20wt. %. There was a subsequent increase in the needle tip voltage to accommodate the increased solution concentration, which would vary from 9 to 11.5 kV. The overall amount of poly(methyl methacrylate) in the composite was held constant and all other electrospinning variables were held constant.

2.3.4.5 Trilayer with Variable Pellethane Layer Thickness

Three individual trilayer composites were fabricated by systematic variation in the thickness of the Pellethane layer electrospun into the middle of each composite. The three composites contained 9.8×10^{-3}, 1.9×10^{-2} and 3.9×10^{-2} g/cm^2 areal density of Pellethane respectively. This was achieved by pumping at the same rate and the same solution wt. % of Pellethane as was used prior, but allowing it to run for progressively longer time intervals. All other electrospinning variables were held constant.

2.3.5 Thermal Analysis and Pellethane Content Calculation

Thermal Gravimetric Analysis (TGA) (SDT-Q600) was used to observe changes in the degradation profiles of the poly(methyl methacrylate) /Pellethane composites. The heating rate of 10 °C min^{-1} was used to best determine the degradation events of each individual polymer.

Differential Scanning Calorimetry (DSC) (TA Q2000) was used to measure the glass transition and the heat capacity of the neat Pellethane in all the subsequent composites. The process used two heating cycles where the sample is heated at a rate of 5 °C min^{-1} to 200 °C, cooled at 10 °C/min to -50 °C and then heated at 5 °C min^{-1} to 200 °C. The Pellethane content in the neat and composite materials was calculated using the same assumptions and process from Tumbic et al[23]. The following equation was used to calculate all Pellethane content in the composites **Eq. (2-1)**:

$$w = \left(\frac{\Delta C_p}{\Delta C_{p,neat}}\right) * 100 \tag{2-1}$$

where w is the weight percent of the Pellethane in the composite, ΔC_p is the step change in heat capacity at T_g of the Pellethane in the composite, and $\Delta C_{p,neat}$ is the heat capacity of the neat electrospun Pellethane[21,24]. All heat capacity values were used from the second heating cycle to ensure all samples had equal thermal history.

2.3.6 Scanning Electron Microscopy

Surface topography of all samples was assessed using the SEM (Jeol JSM-6390LV). All samples were prepared by cutting out a square and adhering it to an SEM stub using carbon tape. All samples were gold-sputter coated for 120 sin a Denton Vacuum desk IV. The working distance was 10 mm with an accelerating voltage of 10-15 kV.

2.3.7 Mechanical Testing

To determine the Young's modulus, toughness, strain-to-failure, and tensile strength (and anisotropy thereof) of the trilayer composites, dog bones (ASTM D1708) with gauge length of 22 mm and width of 5 mm, were cut from each sample. The dog bones were cut with θ = 0°, 15°, 30°, 45°, 60°, 75° and 90° with these angles corresponding to the angle between the direction parallel to the fibers and the loading direction. The samples were stretched at 25 °C using an Instron 5965 dual column table frame tensile tester at 33 µm s^{-1} (0.15%/s) until failure. The Instron tester measures, among other things, the force required to stretch the sample and the distance the sample has been stretched. From this data, a stress-strain curve can be generated. The engineering stress was calculated using **Eq. (2-2):**

$$\sigma = \frac{F}{A} \tag{2-2}$$

Where σ is the engineering stress (MPa), F is the force (N), and A is the cross sectional area of the sample prior to stretching (mm^2). The engineering strain was calculated using **Eq. (2-3):**

$$\varepsilon = \frac{\Delta L}{L} * 100 \tag{2-3}$$

Where ε is the engineering strain (%), ΔL is the distance the sample has been stretched (mm), and L is the initial length of the sample prior to stretching (mm). The Young's modulus was measured as the slope of the stress-strain curve in the linear, elastic region. The toughness is measured as the area under the stress-strain curve. The tensile strength is the ultimate stress reached and strain-to-failure being to ultimate strain reached.

2.3.8 Dynamic Mechanical Analysis

Quantifying the anisotropy obtained in each composite was determined using a Q800 TA Dynamic Mechanical Analyzer (DMA). Strips were cut from each sample in both the 0° and 90° fiber directions. A regular DMA program was used to determine what the storage modulus of the material was, for the given fiber orientation, at 20 °C. The material was tested using the DMA multi-frequency strain program with the rectangular sample geometry. While holding a 20 µm amplitude, 0.5% strain, 0.01N preload force and 108% force track the sample was first cooled to -50 °C, held there for 10 min and then heated to 150 °C.

2.3.9 Porosity Testing

Determination of how densely pack the fibers are in each composite was calculated using density measurements in as-processed and compacted forms of the films. First, precisely measuring the thickness of the sheet as well as the mass, the density of the composite is obtained. Through doing the same for the composite film (compacted in a hot press at 230 ºC for 50 min), a ratio of the two will reveal the porosity using **Eq. (2-4):**

$$Porosity = 1 - \frac{\rho_{web}}{\rho_{film}} \tag{2-4}$$

Where ρ_{web} is the density as measured for the electrospun composite and ρ_{film} is the density of the composite film, where all porosity has been removed through heating.

2.3.10 Statistical Analysis

Where data points from the composites appeared to be similar, differences were determined using the unpaired 2 sample t-test **(Eq. 2-5)** to validate if there were statistical differences between them, for the variable in question. A *p*-value greater than 0.05 means the null hypothesis must not be rejected, whereas *p*-values less than 0.05 means the null hypothesis is rejected.

$$t = \frac{m_1 - m_2}{\sqrt{s^2\left(\frac{1}{n_1} + \frac{1}{n_2}\right)}} \tag{2-5}$$

The *m* variable is the individual sample means the *s* variable is the pooled sample variance and the *n* variable is the sample size of each population.

2.4 Results

Anisotropic electrospun composites of poly(methyl methacrylate) and Pellethane were fabricated using the methods described in the experimental section (**Section 2.3**). Three distinct categories of electrospun materials were fabricated and tested for the purpose of maximizing the resulting materials anisotropy. The first category of material was used to determine which integration technique would create the highest anisotropy i.e. dual electrospinning opposed to a layering method. The second category of materials systematically altered the apparent fiber diameter of the poly(methyl methacrylate) fibers in the trilayer composites. The last category of materials systematically increased the Pellethane layer thickness in the trilayer composites. All fiber mats were analyzed at the various fiber orientation angles (θ = 0°, 15°, 30°, 45°, 60°, 75° and 90°).

2.4.1 Determination of Composite Structure for Maximizing Anisotropy

The **Scheme 2-1** is an artistic interpretation to visually clarify the difference between the materials fabricated within this category. The larger block-like images are the poly(methyl methacrylate) fibers, which are used to show the relative size difference between them and the Pellethane fibers. The visual guide shows the fundamental difference between the materials made through dual electrospinning (3) and a layering technique (4) where the poly(methyl methacrylate) fibers are on the outer edges. The dual electrospinning integrates the two fibers together in a homogenous sheet, where the large poly(methyl methacrylate) fibers and small Pellethane fibers are dispersed randomly amongst each other. The trilayer has three clear delineations, or “layers” of fibers, where there is no significant presence of a poly(methyl methacrylate) fiber in the Pellethane layer, and vice versa.

The fabrication technique used for all of the subsequent materials discussed in this chapter was electrospinning. An artistic interpretation of this technique can be seen in the **Scheme 2-2 – 2-4**. Fibrous mats of the pure poly(methyl methacrylate) and Pellethane being electrospun are shown in **Scheme 2.2**. The pure materials are visually differentiated by the different color, and the usage of the larger block-like fibers for poly(methyl methacrylate) and the smaller “wavy” fibers for Pellethane. The usage of a spinning mandrel during electrospinning aligns the polymer fibers. The depiction of the Pellethane fibers was done to accentuate the difference between them and the poly(methyl methacrylate), which sacrificed visual accuracy. In **Scheme 2-3** an interpretation of the dual electrospinning process can be seen. This method shows both polymers, differentiated by color, being electrospun on a spinning mandrel simultaneously. The **Scheme 2-4** is an interpretation of a layering technique used to create the resulting trilayer material. Using the color difference for visual guidance of the process, the poly(methyl methacrylate) fibers are electrospun first, as a layer. Switching syringes and polymers the Pellethane is electrospun directly on top of the poly(methyl methacrylate) fibers. Finally switching syringes and polymers again, for the poly(methyl methacrylate) fibers are electrospun directly on top of the previous two layers, completing the trilayer.

2.4.1.1 Image Analysis

Scanning Electron Microscopy (SEM) was used to assess the individual fiber morphology and diameter as well as the structure of the fibrous mats in the composites. As can be seen in **Figure 2-1a & b** the pure electrospun poly(methyl methacrylate) fibers are large and exhibit a high degree of alignment. This alignment can be attributed to the orientation induced through electrospinning onto a rotating mandrel, as well as the size and stiffness of the poly(methyl methacrylate) fibers causing them to be less susceptible to un-orienting factors experienced during fabrication. The electrospun Pellethane fibers as shown in **Figure 2-1c & d** show that there is alignment of the fibers, but qualitatively less so as compared to the poly(methyl methacrylate) fibers. The same rationale used to explain the alignment of poly(methyl methacrylate) fibers can be used to explain this phenomenon. The smaller elastic fibers are more susceptible to the un-orienting factors of, for example, stray air currents and random electrical charging of surrounding areas. Dual electrospinning produced the composite seen in **Figure 2-1e & f** where the visually predominate fibers are the poly(methyl methacrylate) with the small “string-like” Pellethane fibers askew across them. These images show that the fibers in this composite are not spatially close together, as observed in other dual electrospun blends, or the pure electrospun materials. This behavior can be explained through closely observing the simultaneous deposition of the fibers onto the mandrel. The assumption made for explaining this composite structure is the poly(methyl methacrylate) fibers are physically restricting the Pellethane fibers from forming a web. The size and stiffness difference between the two polymers are, in this case, causing non homogeneity of the fibers distribution in the mat. Finally the trilayer structure can be seen in **Figure 2-1g & h**. The main visual difference between the former composite and the trilayer is the spatial arrangement of the polymer fibers. In the trilayer both the poly(methyl methacrylate) and the Pellethane fibers are able to form a homogenously packed web, in a segregated layer. This spatial arrangement visually appears to overcome the fiber packing issue seen in the dual electrospun composite.

2.4.1.2 Porosity Analysis

The porosity of the all the electrospun fiber mats was assessed using a comparison of the web density and the density of a film formed from the same sheet as shown in **Scheme 2-5** method 2 and calculated using **Eq. (2-4)**. Images of samples taken both before and after this process can be seen in **Figure 2-2** where the samples as spun are white and opaque and after being heated and compressed become clear and translucent. This visual change can be attributed to the melting of the polymer fibers, which removes the porosity in the sheet. The measurements of each composite’s porosity can be seen in **Figure 2-3** showing the difference in porosity obtained from the oil immersion (method 1) and creating a film (method 2). The oil immersion method used to measure the porosity had low replicability, therefore it was used as supplementary to the preferred method, method 2. The comparison of all composite porosities is shown in **Figure 2-4**. The porosity of the pure Pellethane is the highest, which is expected due to the size and packing of its fibers in a mat. The poly(methyl methacrylate) fibers show the lowest porosity for a similar reason. The dual electrospun composite shows a higher porosity than the trilayer composite. The interaction of the fibers and the structure of the web which control the porosity can be observed on the SEM micrographs, where the dual spun composite formed a web loosely held together.

2.4.1.3 Thermal Analysis

Differential scanning calorimetry (DSC) as seen in **Figure 2-5**, was used to determine the mass ratio of Pellethane in the composites, following **Eq. (2-1)**. The second heat was used to remove thermal history in the composites and to obtain accurate glass transition temperatures for each polymer. Poly(methyl methacrylate) glass transition temperature and Pellethane's melt temperature occur around 125 °C. This obscures the ΔC_p of poly(methyl methacrylate) in the composite, and lead to an incorrect calculation of its mass ratio. For this reason the poly(methyl methacrylate) mass ratio was not measured directly. Direct measurement of Pellethane's ΔC_p was done and in all composites it was used to calculate the mass ratio for both polymers.

Thermogravimetric analysis (TGA) as seen in **Figure 2-6**, was used to compare the thermal stability of the different electrospun composites. Ideally the degradation events of the constituents would occur at different temperatures, with one component completely degrading before the other. However the degradation is complex and there is significant overlap of degradation events, therefore it was not used to estimate the constituent mass ratios in the composite.

In **Table 2-1** the char yield is reported as a function of the amount of both constituent polymers present. The trend observed is, in general the more Pellethane present, the more char yield. This is hypothesized to be related to the web density of the Pellethane fibers. The tightly bundled fibers have a higher resistance to flashing off at high temperatures. The dual electrospun had lower char yield than the trilayer. The density of the Pellethane fibers in these composites are different. The dual electrospun composite having loosely packed Pellethane fibers is not able to resist the flash off at high temperatures, whereas the Pellethane fibers in the trilayer are able to.

2.4.1.4 Mechanical Analysis

2.4.1.4.1 Tensile Testing

Quantifying the amount of anisotropy achieved in the composites was assessed using the Young's modulus as measured using the Instron 5965 dual column table frame tensile tester. Dog bones were cut from each composite with the fiber orientation angle ranging from 0° to 90° in 15° increments as shown in **Scheme 2-6**. The representative stress strain curves form which the Young's modulus was determined can be seen in **Figure 2-7** and summarized in **Figure 2-8** for the 0° fiber orientation angle and **Figure 2-9** for the 90° fiber orientation angle. The trilayer structure was able to perform better than the dual spun composite on the metrics of Young's modulus, tensile strength, toughness and strain to failure. Quantifying for comparison of the anisotropy for the composites was done in **Table 2-2**. The Young's modulus of the composites at the 0° fiber orientation angle can be attributed to the aligned poly(methyl methacrylate) present. The Young's modulus of the composites at the 90° fiber orientation angle show the important difference between the composites stiffness. The trilayer structure is able to show the highest stiffness in the 0° fiber orientation angle and the lowest stiffness in the 90° fiber orientation angle. In terms of the composite anisotropy this makes the trilayer structure the most anisotropic composite that was made and tested. In these composites the low stiffness in the 90° fiber orientation angle is dependent on how the poly(methyl methacrylate) fibers interact with each other. The layering of poly(methyl methacrylate) into a laminate allows them to separate from each other with less obstruction than in the dual spun composite.

The representative stress strain curves of the individual polymers, poly(methyl methacrylate) and Pellethane as well as the composites, dual spun and trilayer are shown in **Figure 2-10**. In general for all samples the stiffness decreased as the fiber orientation angle increased from $\theta = 0°$ to $\theta = 90°$ due to the fibers reduced capacity to bear the load for $\theta > 0°$. The trilayer composite showed the most dramatic change in stress strain curve from 0° fiber orientation angle to the 90° fiber orientation angle. This change suggests that there are two distinct mechanical behaviors of this material when tested directionally. The integrating of the stiff polymer poly(methyl methacrylate) and the elastic polymer Pellethane in the trilayer configuration is able to use both components advantageously to overall material anisotropy.

The material's behavior during fracture as seen in **Figure 2-11** shows the fundamental difference between the pure materials as well as between the composites. The fracture of the dual spun composite (**e**) (**f**) shows a brittle fracture for both the 0° and the 90° fiber orientation angle. The trilayer fracture (**g**) (**h**) shows a clear difference between the two fiber orientation angles. The composite shows a brittle fracture of the poly(methyl methacrylate) fibers in the 0° fiber orientation angle (**g**) and a quasi-ductile failure (**h**). This failure pattern confirms that the trilayer composite displays material anisotropy.

Graphically summarizing the electrospun materials mechanical behavior, as quantified from there stress strain curves, for specifically four properties is shown in **Figure 2-12** through

2-15 and numerically summarized in **Table 2-3** through **2-6**. In general the Young's modulus and tensile strength of the composites show precipitous drops as the θ > 0°. These trends suggests that there is good overall fiber alignment and that anisotropy can be seen and quantified using these properties. The largest drop in stiffness occurs in the trilayer composite from the 0° fiber orientation angle to the 90° fiber orientation angle. This shows that the poly(methyl methacrylate) fibers bear none of the tensile load when it is applied at θ > 0°. The properties of toughness and strain-to-failure don't follow as clear of a trend when the fiber orientation angle is increased. In general all materials tested are able to elongate to a higher degree at a 90° fiber orientation angle as compared to the 0° fiber orientation angle. There is a minima of toughness and elongation for the poly(methyl methacrylate) and dual spun composite. A fibrous sheet with low toughness and elongation is an unexpected result and atypical for other electrospun fiber mats. The trilayer composite shows the ability to elongate the most at the 90° fiber orientation angle.

Comparison of the four mechanical properties of each electrospun composite shows that the trilayer configuration is the preferred method of integrating the poly(methyl methacrylate) and the Pellethane polymers. The trilayer structure is able to take advantage of the poly(methyl methacrylate)'s strength and the Pellethane's elasticity simultaneously.

2.4.2 Trilayer Composites with Variable Poly(methyl methacrylate) Fiber Diameter

The **Scheme 2-7** is an artistic interpretation used clarify the difference between the electrospun trilayer materials fabricated within this category. The trilayer composite, which was determined to display the most anisotropy, is further investigated in this section. The diameter of the electrospun poly(methyl methacrylate) fibers are systematically increased to observe the relationship of anisotropy to poly(methyl methacrylate) fiber size.

2.4.2.1 Image Analysis

A complex fiber nanostructure of the smallest poly(methyl methacrylate) fibers on the electrospun trilayer are shown in **Figure 2-16**. The poly(methyl methacrylate) fiber diameter was increased, using the same trilayer structure shown in **Figure 2-17**. The nanostructure of the medium sized poly(methyl methacrylate) fibers are less complex and the lack of complexity appears to make the fibers more dense. A fundamental structural change of the poly(methyl methacrylate) fibers occurs as the fiber diameter was increased. This structural change appears to affect the way in which the poly(methyl methacrylate) fibers interact with each other on the composite. The poly(methyl methacrylate) fibers in **Figure 2-17** appear to adhere to each other, forming a quasi-film coating on the trilayer. The largest poly(methyl methacrylate) fibers, shown in **Figure 2-18**, visually display another structural change from the previous fiber size. The complexity of the nanostructure stays constant; however, the fiber to fiber interaction appears to change. The largest fibers of poly(methyl methacrylate) qualitatively adhere less to each other, not forming the aforementioned quasi-film. The structural changes occurring between the poly(methyl methacrylate) fiber sizes and how they interact with one another will affect the resulting materials anisotropy. In general the less adhesion between them, the more anisotropic the material will be.

The poly(methyl methacrylate) fibers that were made can be put into three size classifications, which are small, medium and large. The sizes of the fibers were altered using an increase in the electrospinning parameter of poly(methyl methacrylate) solution wt. %. The poly(methyl methacrylate) fibers are not circular, therefor an equivalent fiber diameter was used and calculated by averaging the fibers' long axis and short axis dimensions. Approximately 100 measurements of each fiber size classification was done using SEM and a box and whisker plot was generated for the resulting size distributions as seen in **Figure 2-19**. In **Table 2-7** the statistical analysis of an unpaired t-test was applied to the measurement data, and used to confirm that there was a statistical difference between each size classification. The three equivalent fiber diameters of poly(methyl methacrylate) fibers were 6.21 ± 1.5, 22.71 ± 6.2 and 39.29 ± 11.7 µm respectively.

2.4.2.2 Porosity Analysis

The porosity and web density of each individual poly(methyl methacrylate) fiber size and Pellethane was assessed using the same method described in section 2.4.1.2. The porosity in **Figure 2-20** (**a**) shows the expected trend with respect to increasing fiber size. The porosity increases as the fiber size increases, with the largest increase in porosity being from Pellethane to poly(methyl methacrylate). The web density shows another expected trend that can be seen in (**b**) where the electrospun web becomes less dense as the fiber size increases. Use of the unpaired t-test, as shown in **Table 2-8** determined that there was not a statistically significant difference in the porosity nor web density between the different equivalent poly(methyl methacrylate) fiber diameters. There was a statistically significant difference between the Pellethane and all the poly(methyl methacrylate) fibers.

The porosity and web density of the three trilayer composites using each equivalent poly(methyl methacrylate) fiber diameter was measured. In **Figure 2-21** (**a**) the porosity of the trilayers varies greatly and in an unexpected trend from the pure material. The porosity goes through a minimum at the 22.71 µm equivalent poly(methyl methacrylate) fiber diameter. The porosity decreasing at this fiber size confirms the visual inspection in section 2.4.2.1. The quasi-film behavior of this trilayer material shows a lower porosity then would otherwise be expected. The porosity trending upward for the largest equivalent poly(methyl methacrylate) fiber diameter also agrees with the visual inspection. The fundamental change in fiber morphology of the poly(methyl methacrylate) fibers at this size can be seen in the porosity change. The web density of the trilayers as in seen in (**b**) shows the same trend as the porosity. The medium sized poly(methyl methacrylate) fibers show an inflection point and because of this the web density does not follow a trend that is expected. The statistical analysis of these measurements as seen in **Table 2-9**, shows that there is a difference between the 22.71 µm equivalent poly(methyl methacrylate) fiber diameter and the 39.36 µm equivalent poly(methyl methacrylate) fiber diameter in terms of web density. There is also a statistical difference between the 6.21 µm equivalent poly(methyl methacrylate) fiber diameter and the others in terms of porosity. This suggests that there is important changes to the topography of these composites as fiber diameter is increase.

The individual porosity measurements, as measured using the same method as in section 2.4.1.2, for the trilayer composite with the 22.71 µm equivalent poly(methyl methacrylate) fiber diameter shown in **Figure 2-22** (**a**) with the 39.29 µm equivalent poly(methyl methacrylate) fiber diameter in (**b**). For both trilayer composites the film method for measurement is lower and is preferred for its replicability. Samples taken from this method can be seen in **Figure 2-23** (**a**) & (**b**) where the top opaque samples are the as spun porous trilayers, and the bottom clear samples are the non-porous films.

2.4.2.3 Thermal Analysis

DSC analysis as shown in **Figure 2-24** was used to determine the mass ratios of Pellethane in each trilayer composite, as was used in section 2.4.1.3. For reference Pellethane shown as the blue line (i) shows a glass transition temperature around -10 °C and the poly(methyl methacrylate) shown as the red line (v) shows it’s glass transition temperature around 125 °C. All three trilayer composites (ii) (iii) and (iv) display both Pellethane and poly(methyl methacrylate) glass transition temperatures, which is expected for specifically these composites.

TGA as seen in **Figure 2-25** was conducted to observe the thermal stability of the three trilayer composites according to section 2.4.1.3. The electrospun Pellethane as shown as a blue line (i) and electrospun poly(methyl methacrylate) as shown as a red line (v) both thermally decay non-monotonically. The three trilayer samples (ii) (iii) and (iv) thermally decay similarly, which indicated that the change in equivalent poly(methyl methacrylate) fiber diameter does not affect its thermal stability.

The summarizing of both thermal analyses are shown in **Table 2-10** where the amount of Pellethane present in each trilayer, as confirmed via DSC, is approximately the same given a 5% tolerance for the measurement. The similar char yield also suggests that there is similar amount of Pellethane present in each composite. This was an important consideration for fabricating the trilayer composites, so as to have only one variable present i.e. the equivalent poly(methyl methacrylate) fiber diameter.

2.4.2.4 Mechanical Analysis

2.4.2.4.1 Tensile Testing

Quantifying the anisotropy of the trilayer composites was done the same as in section 2.4.1.4.1 and the representative stress strain curves for the fiber orientation angle of 0° are shown in **Figure 2-26**. Electrospun Pellethane as shown by the blue line (i) and electrospun poly(methyl methacrylate) as shown by the red line (v) have distinctly different mechanical behavior. Pellethane shows a low stiffness, but high elongation while the poly(methyl methacrylate) shows a high stiffness and short elongation, as is expect for these polymers. The trilayer composites show a hybrid mechanical behavior of the two component polymers. In general the smallest equivalent poly(methyl methacrylate) fiber diameter of 6.21 µm as shown as a purple line (ii) and the largest of 39.29 µm as shown as the green line (iv) both show a relatively high stiffness and then a high elongation. The black line (iii) of the 22.71 µm equivalent poly(methyl methacrylate) fiber diameter trilayer, only displays a high stiffness with no elongation. The summarization of the same four mechanical properties described in section 2.4.1.4.1 are shown in **Figure 2-27**. In general for the 0° fiber orientation angle the 39.29 µm equivalent poly(methyl methacrylate) fiber diameter shows the highest mechanical properties, but also shows the highest variability amongst them. The statistical analysis of the experimental data for these mechanical properties as seen in **Table 2-11** shows that there is not a significant difference between the trilayer samples for the mechanical properties. This is an unexpected result because in the three trilayer composites tested, for this fiber orientation angle the poly(methyl methacrylate) is providing the load bearing, and we would expect to see a significant increase with all properties as the poly(methyl methacrylate) fiber diameter is increased.

Representative stress strain curves for the fiber orientation angle of 90° are shown in **Figure 2-28**. Electrospun Pellethane as shown by the blue line (i) and electrospun poly(methyl methacrylate) as shown by the red line (v) have similar mechanical behavior in this orientation. Both polymers are less stiff than in the 0° fiber orientation angle and elongate more. The trilayer composites show distinctly different mechanical behavior from the 0° fiber orientation angle. The trilayer composites no longer display a high stiffness. This is indicative of the poly(methyl methacrylate) fibers not bearing any of the applied load. The summary of the mechanical properties in the 90° fiber orientation angle are shown in **Figure 2-29**. The 39.29 µm equivalent poly(methyl methacrylate) fiber diameter (prepared using a 20 wt.% solution) shows the highest mechanical properties for all but Young’s modulus which are all statistically significant differences from the other trilayers. The other two trilayers have no statistical differences between the mechanical properties, except for toughness as can be seen in **Table 2-12**.

The determination of the most anisotropic trilayer composite using the Young’s modulus for both fiber orientation angles can be seen in **Table 2-13**. The 22.71 µm and 39.29 µm equivalent poly(methyl methacrylate) diameter fibers were not able to be individually tested. The electrospun fibers at those sizes did not have enough structural rigidity to maintain a dogbone shape for tensile testing. The most anisotropic trilayer uses the largest equivalent poly(methyl methacrylate) fiber diameter of 39.29 µm and has a stiffness ratio of 902.8. The Young’s modulus in the 0° fiber orientation angle is the lowest of the trilayers. However the large anisotropy is derived from the Young’s modulus in the 90° fiber orientation angle, which is much lower than the others. This suggests that high anisotropy for the trilayer composites is dictated by how stiff the composites are in the 90° fiber orientation angle.

Representative stress strain curves for the 22.71 µm and 39.29 µm equivalent poly(methyl methacrylate) fiber diameter trilayers, for all fiber orientation angles tested, are shown in **Figure 2-30**. In general the 22.71 µm (**a**) and 39.29 µm (**c**) equivalent poly(methyl methacrylate) fiber diameter trilayers show similar mechanical behavior as the fiber orientation angle is increased. For fiber orientation angles greater the 15° the stiffness of the composites drop off precipitously. This suggests that for the higher fiber orientation angles the poly(methyl methacrylate) is bearing none of the applied load. The post tensile tested dogbones for these trilayers are shown in **Figure 2-31**. The fracture pattern for both trilayers, in both fiber orientation angles are qualitatively similar, as is expected. The main visual difference between the composites is the appearance of delamination of the layers in the large equivalent poly(methyl methacrylate) fiber diameter trilayer (**c**) when compared to the medium equivalent poly(methyl methacrylate) fiber diameter trilayer (**a**).

A summarization of the mechanical properties for the 22.71 µm equivalent poly(methyl methacrylate) fiber diameter trilayer, which are derived from the stress strain curves in graphical form, is shown in **Figure 2-32** and in tabular form in **Table 2-14**. A trend of exponential decay for the Young's modulus (**a**) and tensile strength (**c**) is observed as the fiber orientation angle is increased. The strain to failure (**e**) shows an exponential increase as fiber orientation angle is increased with an unexpected minima occurring at 15°, and with the toughness (**d**) showing no clear trend. A summarization of the mechanical properties for the 39.29 µm equivalent poly(methyl methacrylate) fiber diameter trilayer, which are derived from the stress strain curves in graphical form, is shown in **Figure 2-33** and in tabular form in **Table 2-15**. Similar to the former trilayer, the same trends of the same mechanical properties are seen for this trilayer.

2.4.2.4.2 Dynamic Mechanical Analysis

The storage and loss moduli of the electrospun materials, Pellethane and poly(methyl methacrylate) for the 0° fiber orientation angle can be seen in **Figure 2-34** (**a**) & (**b**) and the 90° fiber orientation angle in (**c**) & (**d**) respectively. As expected for the 0° fiber orientation angle (**a**) the three different poly(methyl methacrylate) fibers tested maintain a high storage moduli until it reaches its thermal transition temperature at approximately 125 °C, in which case the storage moduli decreases rapidly. This decrease is caused from the increased thermal motion of the polymer chains which begin to flow to alleviate the applied strain. Pellethane shows a distinctly different behavior, due to its thermal transition being much lower than the poly(methyl methacrylate). In the 90° fiber orientation angle (**c**) all the electrospun materials display the same trend as seen in (**a**), with the difference being at a lower magnitude. The largest poly(methyl methacrylate) equivalent fiber diameter sample was not able to be tested in this fiber orientation angle to do a lack of structural rigidity. The inability of this material to be tested shows an interesting morphological change in the poly(methyl methacrylate) fibers that occurs at the large fiber size. The anisotropy of this material, with minimal fiber to fiber interaction suggests it will be optimal for maximizing the trilayer composite anisotropy.

The three trilayer composite samples with increasing equivalent poly(methyl methacrylate) fiber diameters and their respective storage and loss moduli are shown in **Figure 2-35** (**a**) - (**d**). The 0° fiber orientation angle (**a**) shows a similar behavior for the trilayer samples as was seen in the pure poly(methyl methacrylate) materials **Figure 2-34** (**a**). This is an expected result, showing that for this fiber orientation angle the poly(methyl methacrylate) fibers are bearing all of the applied stress, and that the different equivalent fiber diameters do not drastically affect the mechanical behavior. For the 90° fiber orientation angle all three trilayers behave similarly to pure Pellethane, as seen in **Figure 2-34** (**c**). This finding strongly suggests that when a load is applied in the perpendicular direction to the fibers, the Pellethane bears the stress in the trilayer composites.

Quantification of the composites anisotropy using the ratio of 0° to 90° fiber orientation angle for each materials storage moduli at 25 °C is shown in **Table 2-16**. For the trilayers there is an inflection point occurring at the 22.71 µm equivalent poly(methyl methacrylate) fiber diameter. This inflection point can be explained through analysis of it topography and fiber to fiber interaction, which seems to be unique to this sized fiber diameter. The quasi-film formed at this size fiber diameter appears to assist in the moduli for the 0° fiber orientation angle. The largest equivalent poly(methyl methacrylate) fiber diameter of 39.29 µm shows the lowest storage moduli in the 90° fiber orientation angle. The storage moduli in the perpendicular direction to fiber orientation is the most crucial for creating a trilayer material with high anisotropy. In this case the trilayer using the 39.29 µm equivalent poly(methyl methacrylate) fiber diameter displays a storage moduli anisotropy of 4200.

The storage and loss moduli for each trilayer composite is shown in **Figure 2-36**. In general the trends amongst them are similar for both the storage and loss moduli as seen prior.

2.4.3 Trilayer Composites with Variable Pellethane Layer Thickness

The **Scheme 2-8** is an artistic interpretation used to show the difference between the electrospun trilayer materials fabricated within this category. The trilayer composite with the largest equivalent poly(methyl methacrylate) fiber diameter was determined to display the most anisotropy and it is further investigated in this section. Using the trilayer composite with the largest equivalent poly(methyl methacrylate) fiber diameter the center Pellethane layer thickness was systematically increased to observe the relationship of anisotropy to Pellethane thickness.

2.4.3.1 Image Analysis

SEM images of the trilayer with the thinnest layer of Pellethane in the center is shown in **Figure 2-37**. The large rigid stick like poly(methyl methacrylate) fibers are able to cover the smaller Pellethane fibers so they are not visually apparent. Contrasted with the thickest layer of Pellethane shown in **Figure 2-38**, where the smaller Pellethane fibers show predominately. A noteworthy observation is the high amount of Pellethane appears to make the previously rigid appearing poly(methyl methacrylate) fibers, now appear flexible as seen in (**a**). This apparent loss of rigidity will negatively affect the stiffness of this specific trilayer composite in the 0° fiber orientation angle.

Cross sections of each trilayer were used and approximately 100 measurements were taken to determine the thickness of the Pellethane layer in each trilayer composite. The analysis of the measurements taken, shown in **Figure 2-39** displays an upward trend of the means. The summarization of this data is shown in **Table 2-17** and agrees that the average of Pellethane layer thickness is increasing. The three distinct thicknesses of Pellethane used were 32.07 ± 7.8 µm, 54.9 ± 10.2 µm and 78.3 ± 14.96 µm respectively. The thickness of poly(methyl methacrylate) fibers was also measured, which shows a similar amount for each trilayer. This data was statistically analyzed using an unpaired t-test in **Table 2-18** and it shows that each trilayer composite has a significant difference in the thickness of Pellethane. Consequently the total thickness of each trilayer also increased significantly which was 250.96 ± 31.9 µm, 275.23 ± 30.6 µm and 304.16 ± 50.16 µm respectively. This was an unavoidable relationship for how the trilayers were constructed.

2.4.3.2 Porosity Analysis

The porosity and web density was assessed using the same method described in section 2.4.1.2 for the three trilayer composites with an increasing Pellethane layer thickness. The porosity in **Figure 2-40** (**a**) shows a decreasing trend the thicker the layer of Pellethane becomes. The web density (**b**) shows a sharply increasing trend as the layer of Pellethane increases in thickness. The Pellethane fiber size is maintained throughout the fabrication process therefor the explanation is the continue layering of small fibers into a web leads to a progressively denser web. There are upper limitations on this trend for this fabrication technique, which is mainly a change in electrical conductivity of the fiber mat, which in turn skews fibers away from the fiber mat.

The individual porosity measurements, as measured using the same method as in section 2.4.1.2, for the trilayer composites with the thinnest Pellethane layer of $9.8 \text{x} 10^{-3}$ g/cm^2 is shown in **Figure 2-41** (**a**) with the thickest Pellethane layer of $3.9 \text{x} 10^{-2}$ g/cm^2 in (**b**). For both trilayer composites the film method for measurement is preferred for its replicability. The Film method shows a higher porosity in (**b**) due to the Pellethane fibers ability to trap oil within the matrix from method1. This trend is seen in the pure Pellethane **Figure 2-3** (**b**). Trilayer samples can be seen in **Figure 2-42** (**a**) & (**b**) where the top opaque samples are the as spun porous trilayers, and the bottom clear samples are the non-porous films.

2.4.3.3 Thermal Analysis

DSC analysis as shown in **Figure 2-43** was used to determine the mass ratios of Pellethane in each trilayer composite, as was used in section 2.4.1.3. For reference Pellethane shown as the blue line (i) shows a glass transition temperature around -10 °C and the poly(methyl methacrylate) shown as the red line (v) shows it's glass transition temperature around 125 °C. All three trilayer composites (ii) (iii) and (iv) display both Pellethane and poly(methyl methacrylate) glass transition temperatures, which is expected for specifically these composites.

TGA as seen in **Figure 2-44** was conducted to observe the thermal stability of the three trilayer composites according to section 2.4.1.3. The electrospun Pellethane as shown as a blue line (i) and electrospun poly(methyl methacrylate) as shown as a red line (v) both thermally decay non-monotonically. The three trilayer samples (ii) (iii) and (iv) thermally decay differently, which indicated that there is a change in Pellethane fiber layer and it does affect its thermal stability. Generally the more Pellethane present in the trilayer, the more the thermal decay looks similar to the pure Pellethane (i).

The summarizing of both thermal analyses are shown in **Table 2-19** where the amount of Pellethane present in each trilayer, as confirmed via DSC, is approximately the same given a 5% tolerance for the measurement. The similar char yield also suggests that there is similar amount of Pellethane present in each composite. This was an important consideration for fabricating the trilayer composites, so as to have only one variable present i.e. the equivalent poly(methyl methacrylate) fiber diameter.

2.4.3.4 Mechanical Analysis

2.4.3.4.1 Tensile Testing

Quantifying the anisotropy of the trilayer composites was done the same as in section 2.4.1.4.1 and the representative stress strain curves for the fiber orientation angle of 0° are shown in **Figure 2-45**. The trilayers in this section behave similarly to the trilayers seen in the previous section 2.4.2.4.1. The trilayer composites display a high stiffness in the inelastic deformation region of the graph followed by a sharp decline, which is followed by elongation in the elastic deformation region on the graph. The thinnest Pellethane layer of 9.8×10^{-3} g/cm^2 shown as the purple line (i) and the thickest Pellethane layer of 3.9×10^{-2} g/cm^2 shown as the black line (iii) show similarity in their mechanical behavior. The intermediate Pellethane layer of 1.9×10^{-2} g/cm^2 shown as the green line (ii) displays both the highest stiffness and the most elongation. The summarization of the same four mechanical properties described in section 2.4.1.4.1 are shown in **Figure 2-46**. The 0° fiber orientation angle for the three trilayers tested don’t show a trend amongst them. The statistical analysis of the experimental data for these mechanical properties as seen in **Table 2-20** shows that there is not a significant difference between the trilayer samples for the mechanical properties. This result further suggests that in the 0° fiber orientation angle the Pellethane is not meaningfully contributing to the distribution of the applied load.

Representative stress strain curves for the fiber orientation angle of 90° are shown in **Figure 2-47**. In general the trilayer composites are less stiff than in the 0° fiber orientation angle and elongate more. The trilayers again show distinctly different mechanical behavior from the 0° fiber orientation angle. The summary of the mechanical properties in the 90° fiber orientation angle are shown in **Figure 2-48**. The trilayer composites, again show no trend with exception being the for the 9.8x10^{-3} g/cm^{2} layer of Pellethane showing a higher Young's modulus than the 1.9x10^{-2} g/cm^{2} layer of Pellethane. The other exception being the 9.8x10^{-3} g/cm^{2} layer of Pellethane showing a lower toughness than the 3.9x10^{-2} g/cm^{2} layer of Pellethane. Statistical analysis was applied to show that the only statistically significant difference in mechanical properties amongst the trilayer are the two prior.

The determination of the most anisotropic trilayer composite using the Young's modulus for both fiber orientation angles can be seen in **Table 2-22**. The most anisotropic trilayer uses the intermediate Pellethane layer of 1.9x10^{-2} g/cm^{2} showing an anisotropy of 902.8 for Young's modulus. The Young's modulus in the 0° fiber orientation angle is the highest amongst the trilayers as well as the 90° fiber orientation angle being the lowest.

Representative stress strain curves for the trilayers with a Pellethane layer of 9.8x10^{-3} g/cm^{2} (**a**) and the Pellethane layer of 3.9x10^{-2} g/cm^{2} (**b**) for all fiber orientation angles tested are shown in **Figure 2-49**. The trilayer with the Pellethane layer of 3.9x10^{-2} g/cm^{2} shows a gradual change as the fiber orientation angle is increased. This suggests that for the fiber orientation angles above 15° the Pellethane is showing a higher degree of stiffness than seen prior. The trilayer with the Pellethane layer of 9.8x10^{-3} g/cm^{2} shows a more pronounced change as the fiber orientation angle is increased above 15°. This would suggest that as seen prior, the poly(methyl methacrylate) fibers are not bearing the load, and the stiffness of the Pellethane is low. The post tensile tested dogbones for these trilayers are shown in **Figure 2-50**. The difference between the thin Pellethane layer (**a**) and the thickest Pellethane layer (**c**) display the affect that the increase in Pellethane has. The rigid fracture seen in (**a**) is more typical of the trilayer tensile fractures as seen prior. The ductile fracture shown in (**c**) is unique to this amount of Pellethane used in the trilayer fabrication.

A summarization of the mechanical properties for the 9.8x10^{-3} g/cm^{2} thick layer of Pellethane, which are derived from the stress strain curves in graphical form, is shown in **Figure 2-51** and in tabular form in **Table 2-24**. The trend of exponential decay for the Young's modulus (**a**), tensile strength (**c**) and toughness (**d**) is observed as the fiber orientation angle is increased. The strain to failure (**e**) shows an exponential increase as fiber orientation angle is increased with the exception of a drop shown between the 0° and 15° fiber orientation angles. A summarization of the mechanical properties for the 3.9x10^{-2} g/cm^{2} thick layer of Pellethane, which are derived from the stress strain curves in graphical form are shown in **Figure 2-52** and in tabular form in **Table 2-25**. Similar to the former trilayer, the same trends of the same mechanical properties are seen for this trilayer.

2.4.3.4.2 Dynamic Mechanical Analysis

The three trilayer composite samples with an increasing thickness of the Pellethane layer and their respective storage and loss moduli are shown in **Figure 2-53** (**a**) - (**d**). The 0° fiber orientation angle (**a**) shows a decline of the storage modulus in each trilayer as the amount of Pellethane was increased. The trilayer with the Pellethane layer of 3.9x10^{-2} g/cm^{2} shown as the black line (iii) shows a thermal transition of Pellethane, previously unseen for the 0° fiber orientation angle. This suggests that the Pellethane is bearing some of the cyclic stress being applied to the sample, which again has not been seen for any previous trilayer. For the 90° fiber orientation angle all three trilayers behave similarly to pure Pellethane, as seen in **Figure 2-34** (**c**). This finding suggests again, that when a load is applied in the perpendicular direction to the fibers, the Pellethane bears the stress in the trilayer composites.

Quantification of the composites anisotropy using the ratio of 0° to 90° fiber orientation angle for each materials storage moduli at 25 °C is shown in **Table 2-26**. The trilayers follow a trend of increasing anisotropy as the thickness of the Pellethane layer is decreased. The storage moduli of the trilayers in the 90° fiber orientation angle are similar. This is expected and can be understood through the earlier discussion of the poly(methyl methacrylate) fiber interaction. The trilayers in this section use the same poly(methyl methacrylate) fibers, which removes variability of storage moduli for the 90° fiber orientation angle. The storage moduli for the trilayers in the 0° fiber orientation follow the same trend as anisotropy. This is an unexpected result and would suggest that the increase in Pellethane negatively affects the storage moduli of the trilayer material in the 0° fiber orientation angle. As the layer or Pellethane is increased in the trilayer composite it will bear more of the cyclical stress being applied to the sample, creating a trend of lowering the storage moduli. The thinnest layer of Pellethane using $9.8\text{x}10^{-3}$ g/cm^2 shows the highest anisotropy in terms of storage moduli of 7010.

The storage and loss moduli for the two trilayer composites is shown in **Figure 2-54**. In general the trilayer with $9.8\text{x}10^{-3}$ g/cm^2 of Pellethane (**a**) has a storage moduli an order of magnitude higher than the trilayer with $3.9\text{x}10^{-2}$ g/cm^2 of Pellethane (**b**). In the storage moduli at the 0° fiber orientation angle a clear Pellethane thermal transition can also be seen in the trilayer with $3.9\text{x}10^{-2}$ g/cm^2 of Pellethane (**b**).

All tensile data was gathered using dog bones following the standard ASTM D1708, which is not appropriate, formally, for the calculation of elastic modulus. A finite element analysis was used to determine a correction factor for all elastic moduli as shown in **Figure 2-55**.

All the elastic moduli shown can be corrected by simply dividing through by 1.1 to get an accurate value; nevertheless, the trends observed are not affected by this correction.

2.5 Conclusions

A unique highly anisotropic electrospun composite was introduced. Achieving high anisotropy through electrospinning into a laminate structure, is atypical for electrospun composites. A salient point is the simplicity of fabrication for this composite. High anisotropy was achieved through placement of the polymers in specific structural distributions. The moduli dependence of the fiber orientation allows for high stiffness in one direction and high compliance in the perpendicular direction. The incorporation of two polymers with different material properties can be synergized through a mechanical method. This material, and the fabrication technique can be used as a platform to build more complex composites that effectively use polymers of different properties.

2.6 References

1. Mouritz, A. P. *Introduction to Aerospace Materials*. (Elsevier, 2012).

2. LeMaitre, J. *Handbook of Materials Behavior Models, Three-Volume Set: Nonlinear Models and Properties*. (Elsevier, 2001).

3. Mather, P. T. Responsive Materials: Soft answers for hard problems. *Nat. Mater.* **6**, 93–94 (2007).

4. Valderrábano, M. Influence of anisotropic conduction properties in the propagation of the cardiac action potential. *Prog. Biophys. Mol. Biol.* **94**, 144–168 (2007).

5. Deng, D. *et al.* Engineering human neo-tendon tissue in vitro with human dermal fibroblasts under static mechanical strain. *Biomaterials* **30**, 6724–6730 (2009).

6. Vaquette Cedryck, Sudheesh Kumar P. T., Petcu Eugen Bogdan & Ivanovski Saso. Combining electrospinning and cell sheet technology for the development of a multiscale tissue engineered ligament construct (TELC). *J. Biomed. Mater. Res. B Appl. Biomater.* **106**, 399–409 (2017).

7. Kim, G. H. Electrospun PCL nanofibers with anisotropic mechanical properties as a biomedical scaffold. *Biomed. Mater.* **3**, 025010 (2008).

8. Cheney, J. A. *et al.* Membrane muscle function in the compliant wings of bats. *Bioinspir. Biomim.* **9**, 025007 (2014).

9. Padian, K. & Rayner, J. M. V. The wings of pterosaurs. *Am. J. Sci.* **293**, 91–166 (1993).

10. Burt, T. M., Jordan, A. M. & Korley, L. T. J. Toward Anisotropic Materials via Forced Assembly Coextrusion. *ACS Appl. Mater. Interfaces* **4**, 5155–5161 (2012).

11. Li, Y., Iwakura, Y., Nakayama, K. & Shimizu, H. Highly anisotropic properties of thermoplastic elastomer composites with aligned hierarchical structures. *Compos. Sci. Technol.* **67**, 2886–2891 (2007).

12. Neisiany, R. E., Khorasani, S. N., Lee, J. K. Y., Naeimirad, M. & Ramakrishna, S. Interfacial toughening of carbon/epoxy composite by incorporating styrene acrylonitrile nanofibers. *Theor. Appl. Fract. Mech.* **95**, 242–247 (2018).

13. Rodriguez, E. D., Weed, D. C. & Mather, P. T. Anisotropic Shape-Memory Elastomeric Composites: Fabrication and Testing. *Macromol. Chem. Phys.* **214**, 1247–1257 (2013).

14. Robertson, J. M. *et al.* Mechanically programmed shape change in laminated elastomeric composites. *Soft Matter* **11**, 5754–5764 (2015).

15. Kousaalya Adhimoolam Bakthavachalam, Biddappa Bopaiah Ittira, Krumm Kelly, Pradeep Sai Aditya & Pilla Srikanth. Poly(lactic acid)/areca fiber laminate composites processed via film stacking technique. *J. Appl. Polym. Sci.* **135**, 45795 (2017).

16. Habibi Zarabadi Maryam, Kadivar Mahdi & Keramat Javad. Production and evaluation the properties of laminated oat protein film and electrospun nylon. *J. Food Process. Preserv.* **42**, e13513 (2017).

17. Ognibene, G., Mannino, S., Fragalà, M. E. & Cicala, G. Trifunctional Epoxy Resin Composites Modified by Soluble Electrospun Veils: Effect on the Viscoelastic and Morphological Properties. *Materials* **11**, 405 (2018).

18. Carrizales, C. *et al.* Thermal and mechanical properties of electrospun PMMA, PVC, Nylon 6, and Nylon 6,6. *Polym. Adv. Technol.* **19**, 124–130 (2008).

19. Ali, U., Karim, K. J. B. A. & Buang, N. A. A Review of the Properties and Applications of Poly (Methyl Methacrylate) (PMMA). *Polym. Rev.* (2015).

20. Matsuura, T., Tsuchiya, E., Fukui, Y. & Maruyama, T. Electrospun polymeric short microfibers with surface-selective functionalization. *Colloid Polym. Sci.* **296**, 239–244 (2018).

21. Robertson, J. M., Birjandi Nejad, H. & Mather, P. T. Dual-Spun Shape Memory Elastomeric Composites. *ACS Macro Lett.* **4**, 436–440 (2015).

22. Luo, X. & Mather, P. T. Triple-Shape Polymeric Composites (TSPCs). *Adv. Funct. Mater.* **20**, 2649–2656 (2010).

23. Tumbic, J., Romo-Uribe, A., Boden, M. & Mather, P. T. Hot-compacted interwoven webs of biodegradable polymers. *Polymer* **101**, 127–138 (2016).

24. Nejad, H. B., Robertson, J. M. & Mather, P. T. Interwoven polymer composites via dual-electrospinning with shape memory and self-healing properties. *MRS Commun.* **5**, 211–221 (2015).

2.7 Figures, Schemes and Tables

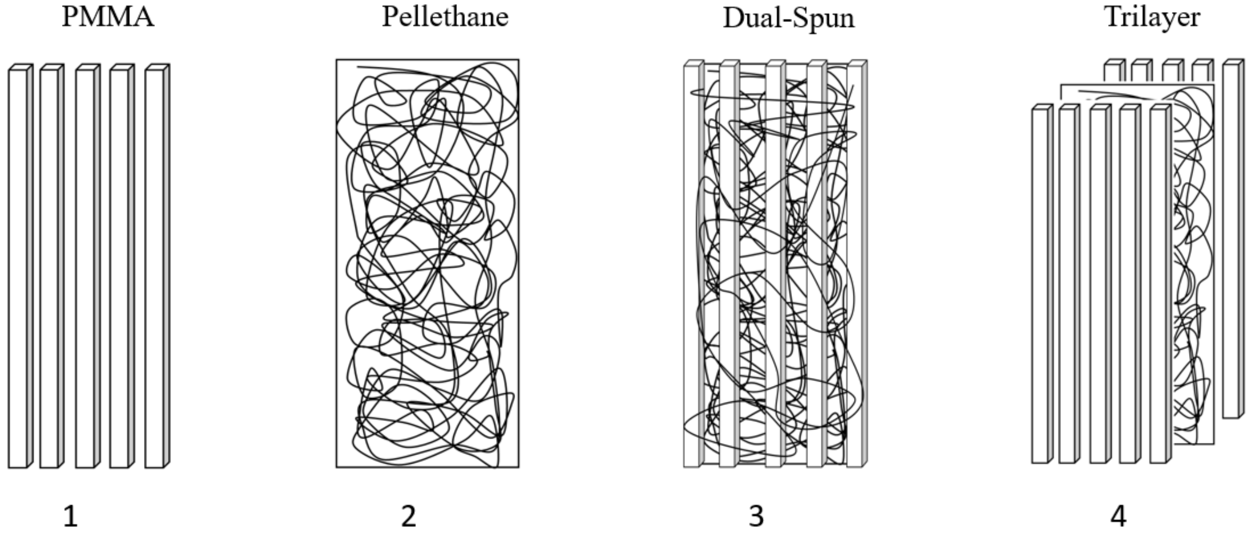

Scheme 2-1 A depiction of anisotropic electrospun materials fabricated and tested. From left to right, (1) poly(methyl methacrylate), (2) Pellethane, (3) dual electrospun poly(methyl methacrylate) with Pellethane and (4) trilayer composite with poly(methyl methacrylate) on the top and bottom with Pellethane in the middle.

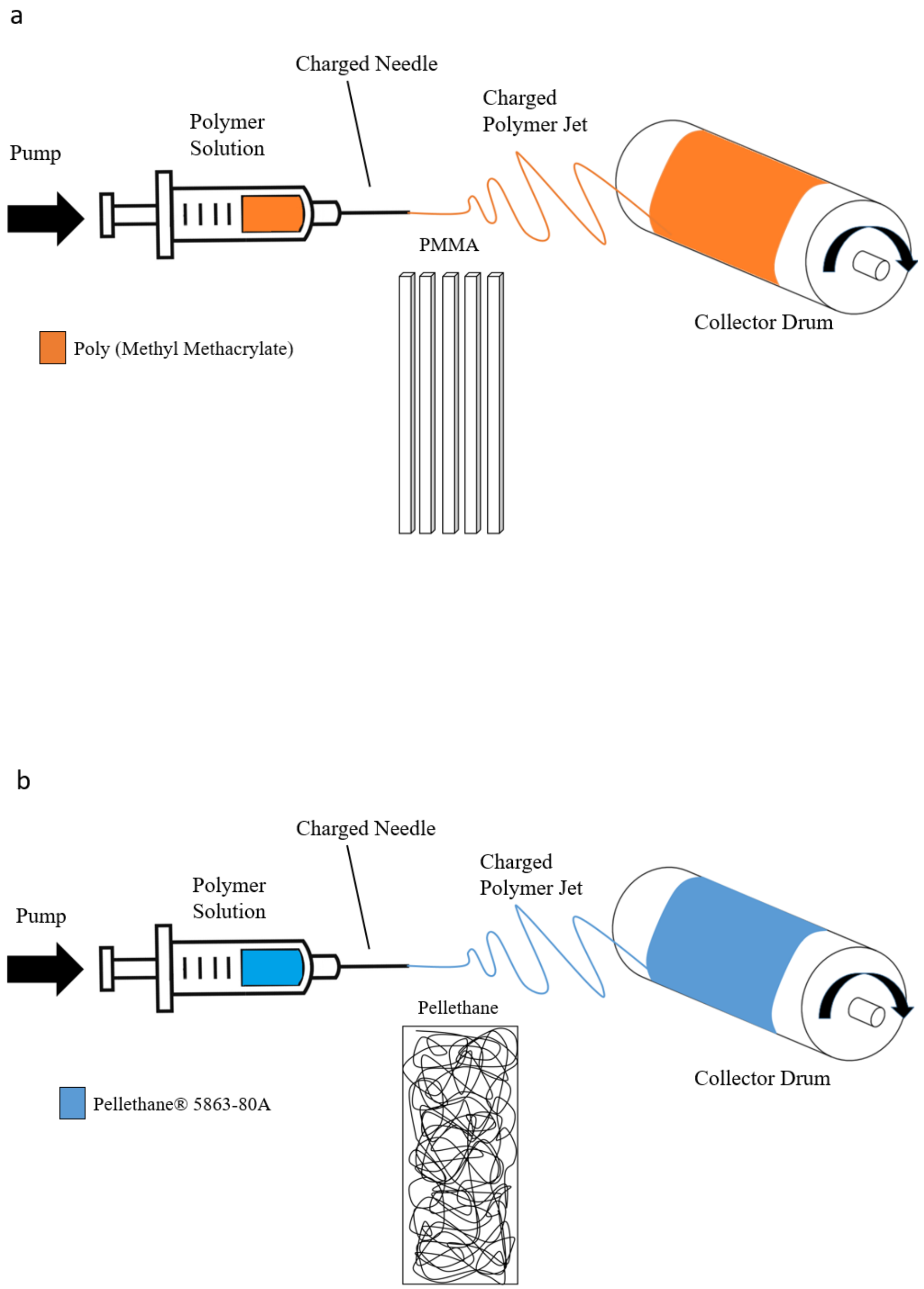

Scheme 2-2: Electrospinning setup used to electrospun aligned fiber mats of (a) poly(methyl methacrylate) and (b) Pellethane.

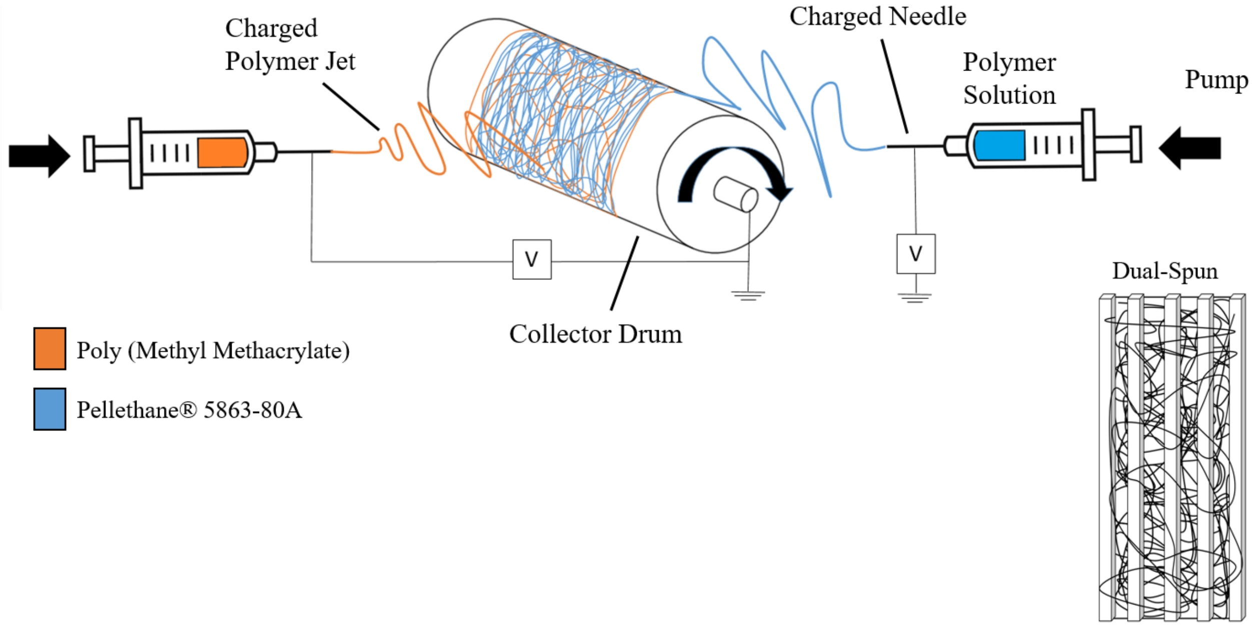

Scheme 2-3: Electrospinning setup used to dual electrospin aligned fiber mats of poly(methyl methacrylate) with Pellethane. Each polymer was pump simultaneously to cause a uniformly mixed fiber mat.

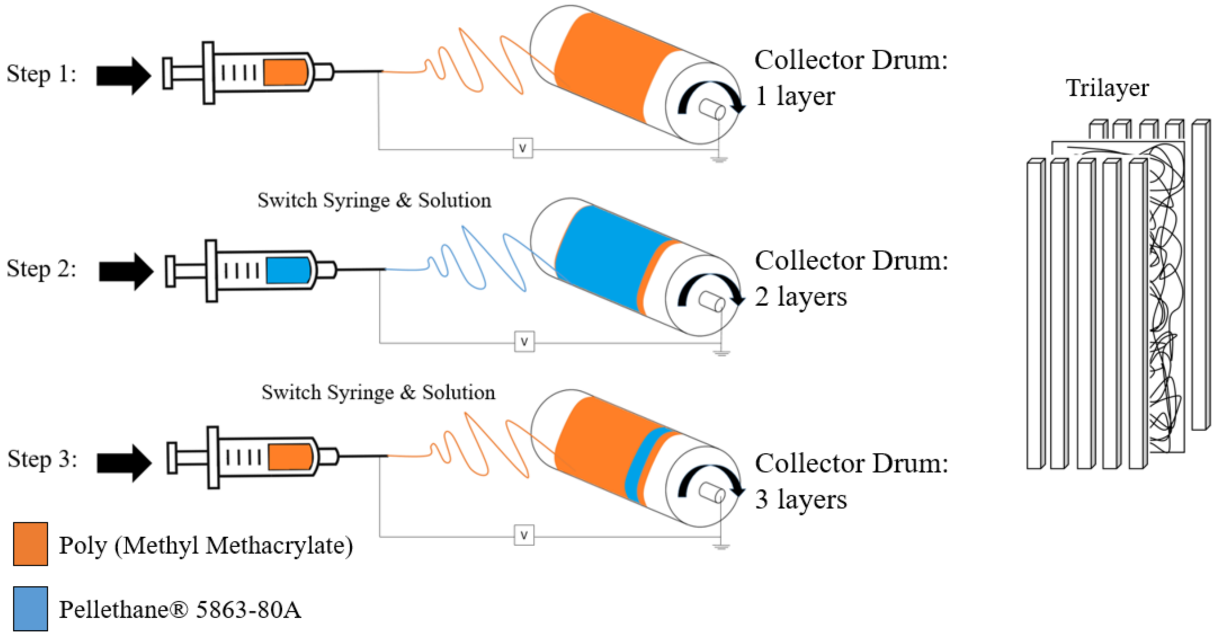

Scheme 2-4: Electrospinning setup used to electrospin aligned trilayer fiber mats of poly(methyl methacrylate) with Pellethane. Fabrication begins with electrospinning poly(methyl methacrylate) into a singular layer. Switching polymer solutions, the electrospinning is continued with the Pellethane directly on top of the pervious layer. Finishing off the composite by switching the polymer solution back to the previous poly(methyl methacrylate) and electrospinning directly on top of the previous two layers.

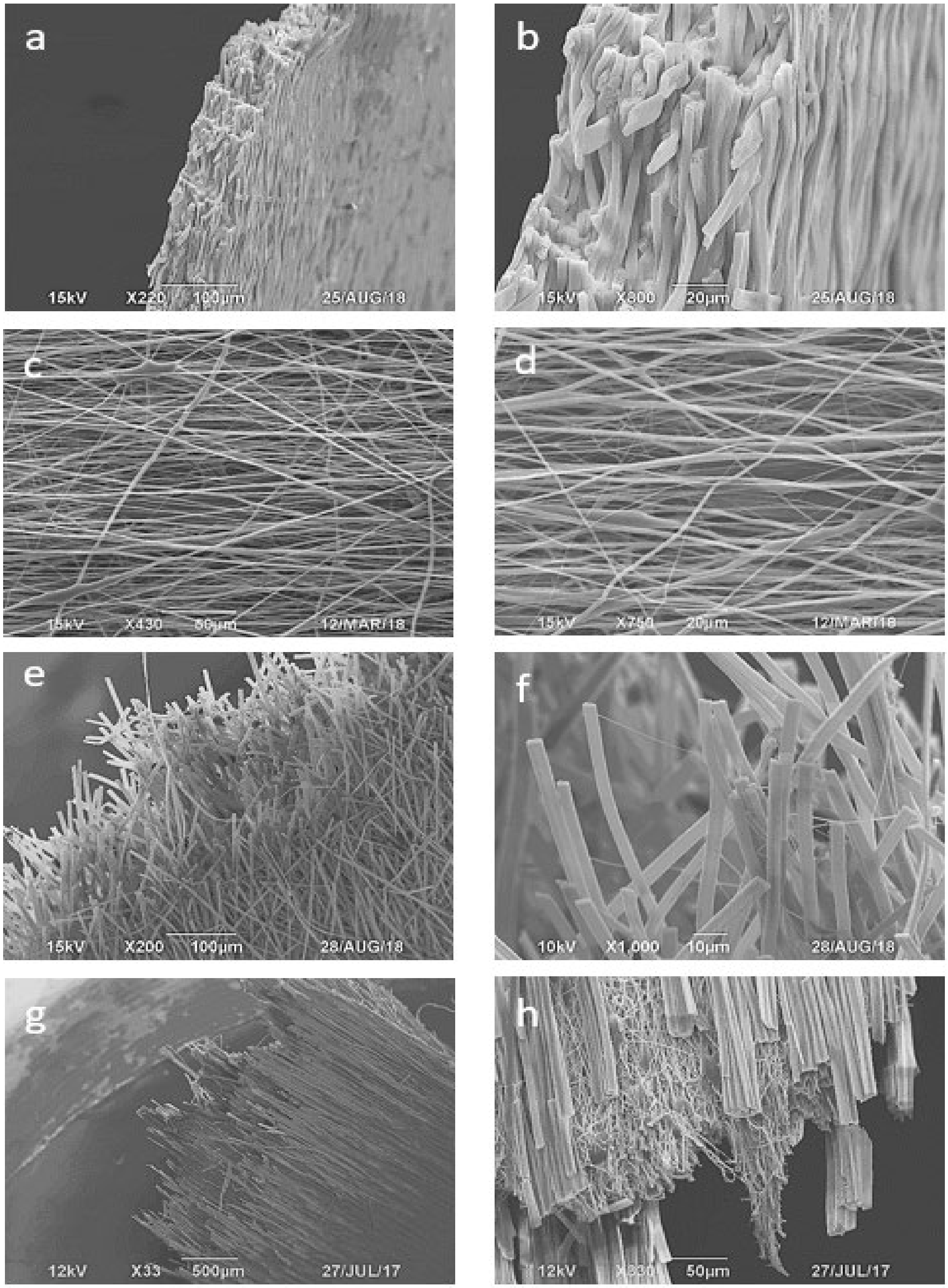

Figure 2-1: SEM Micrographs of electrospun (a),(b) anisotropic poly(methyl methacrylate) 10wt. % sol. concentration, (c),(d) anisotropic Pellethane, (e),(f) anisotropic dual electrospun poly(methyl methacrylate) with Pellethane and (g),(h) anisotropic trilayer of poly(methyl methacrylate) outer layers and Pellethane inner layer.

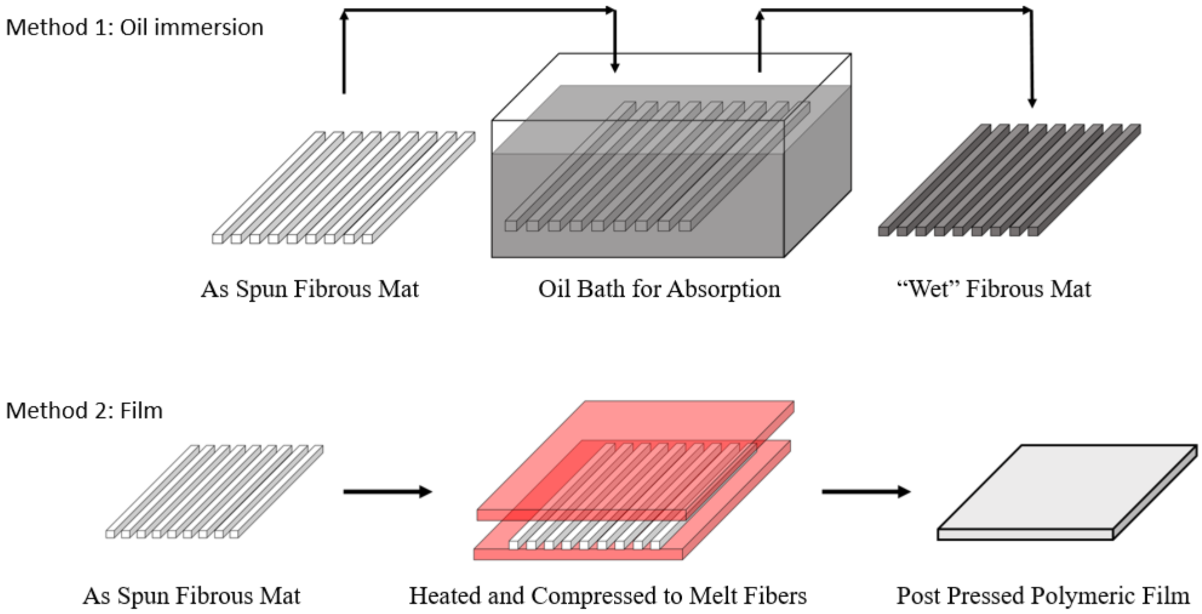

Scheme 2-5: Two complimentary methods used to determine the porosity of the resulting fiber mats. The oil immersion method (1) measured the as spun fiber mat density before applying oil of a known density at room temperature to the sheet for complete absorption. The wet density is measured and a ratio is taken to calculate apparent porosity. The film method (2) measures the as spun density before melting the polymer in a hot press creating a film. Measuring the film density and applying the previous ratio gives the sample porosity.

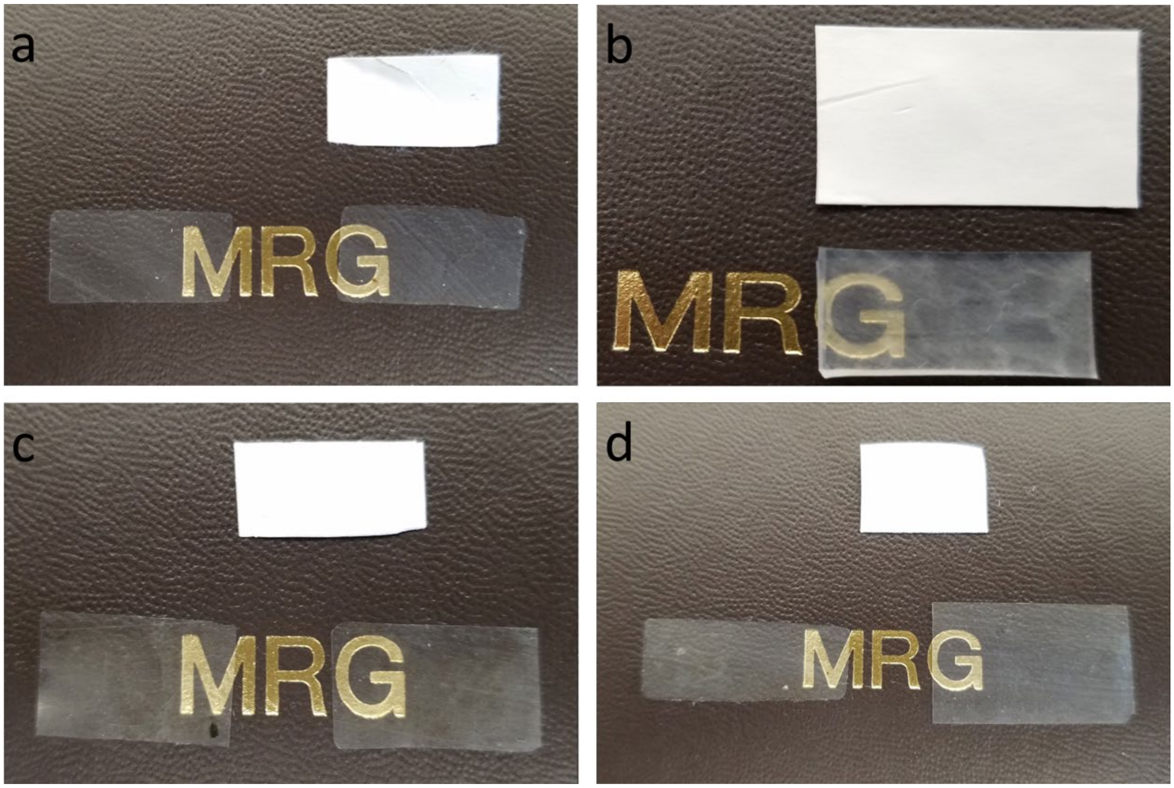

Figure 2-2: Representative images showing the change in physical appearance between the as spun fiber sheet (top) and the melted film (bottom) for (a) poly(methyl methacrylate), (b) Pellethane, (c) dual electrospun poly(methyl methacrylate) with Pellethane and (d) trilayer of poly(methyl methacrylate) with Pellethane.

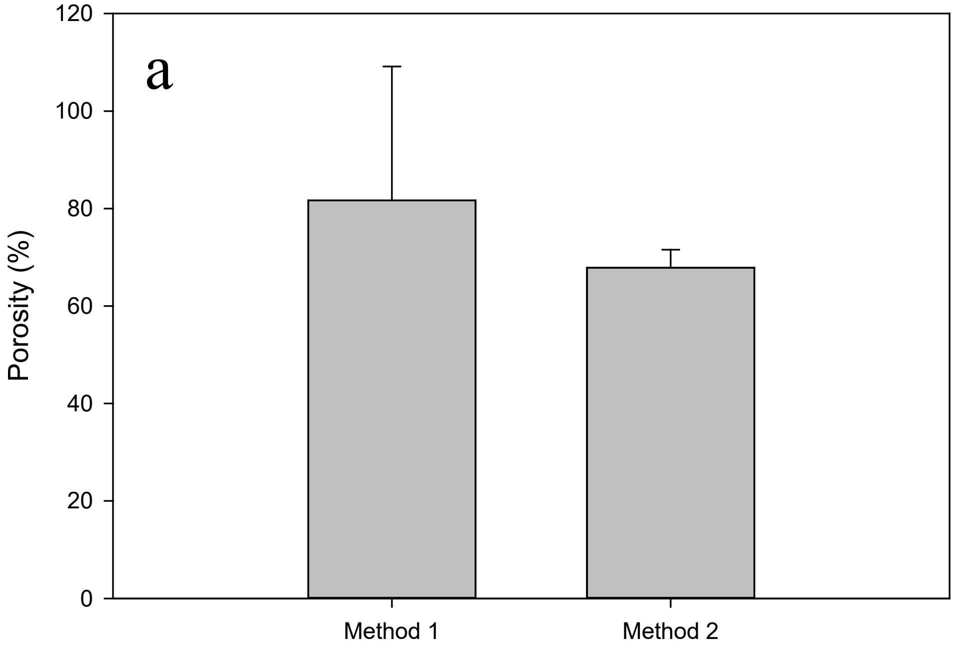
a
Porosity (%)
0
20
40
60
80
100
120
Method 1
Method 2

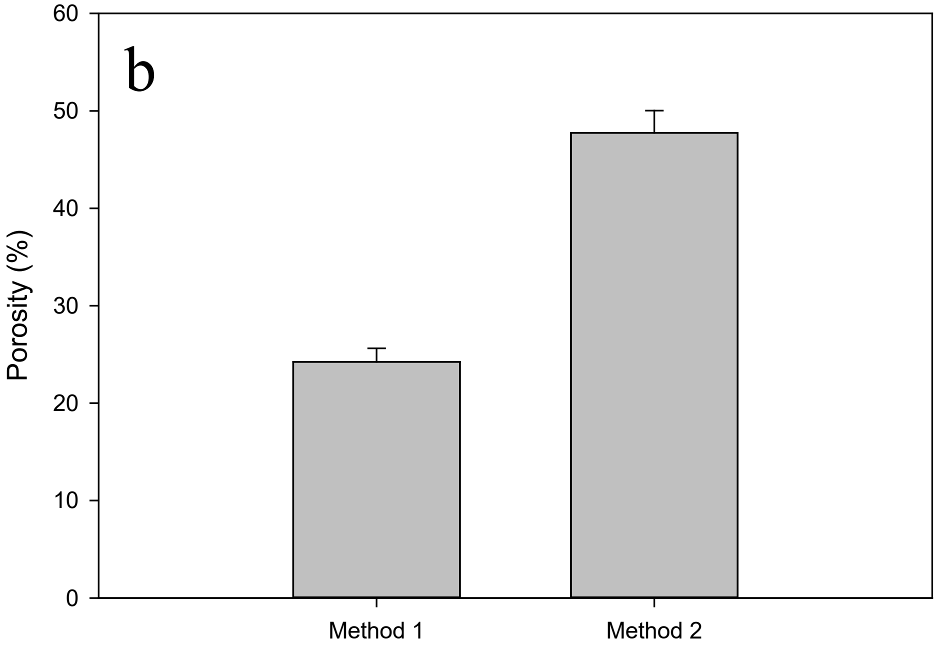
b
Porosity (%)
0
10
20
30
40
50
60
Method 1
Method 2

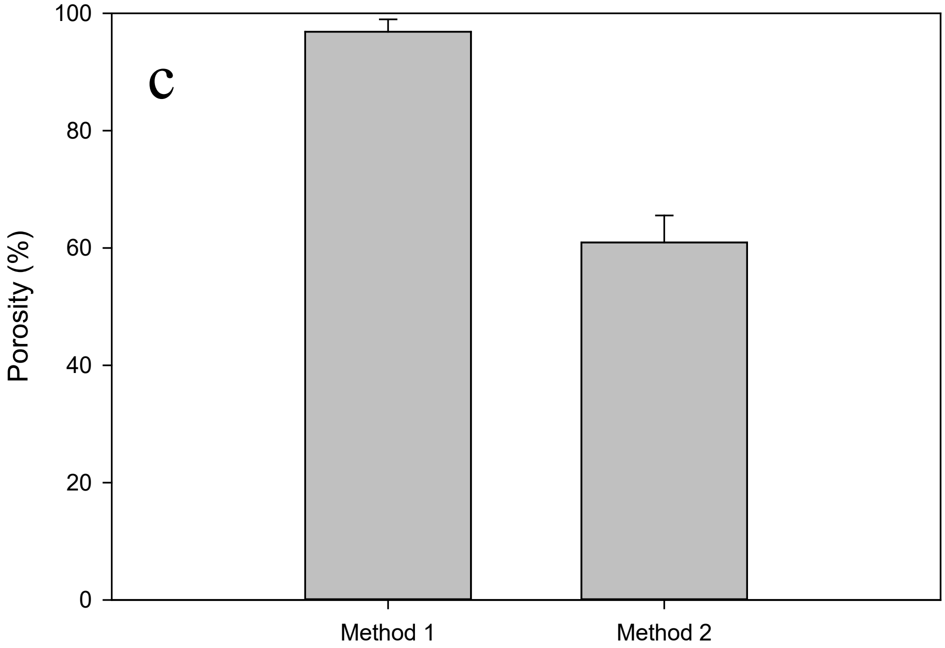

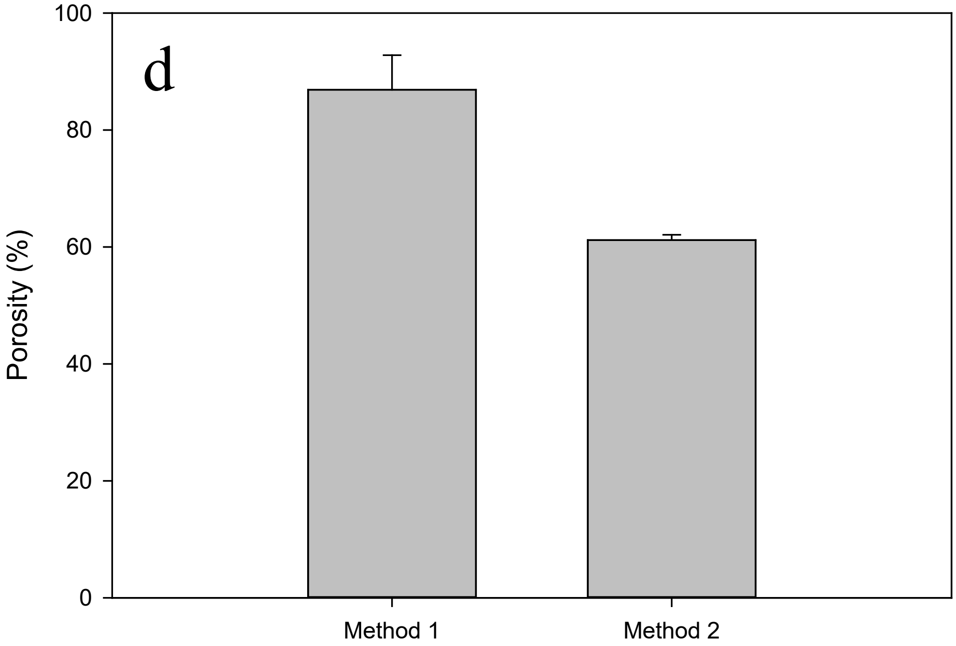

Figure 2-3: Bar charts of the measured apparent porosity (method 1) and porosity (method 2) for (a) poly(methyl methacrylate), (b) Pellethane, (c) dual electrospun poly(methyl methacrylate) with Pellethane and (d) trilayer of poly(methyl methacrylate) with Pellethane.

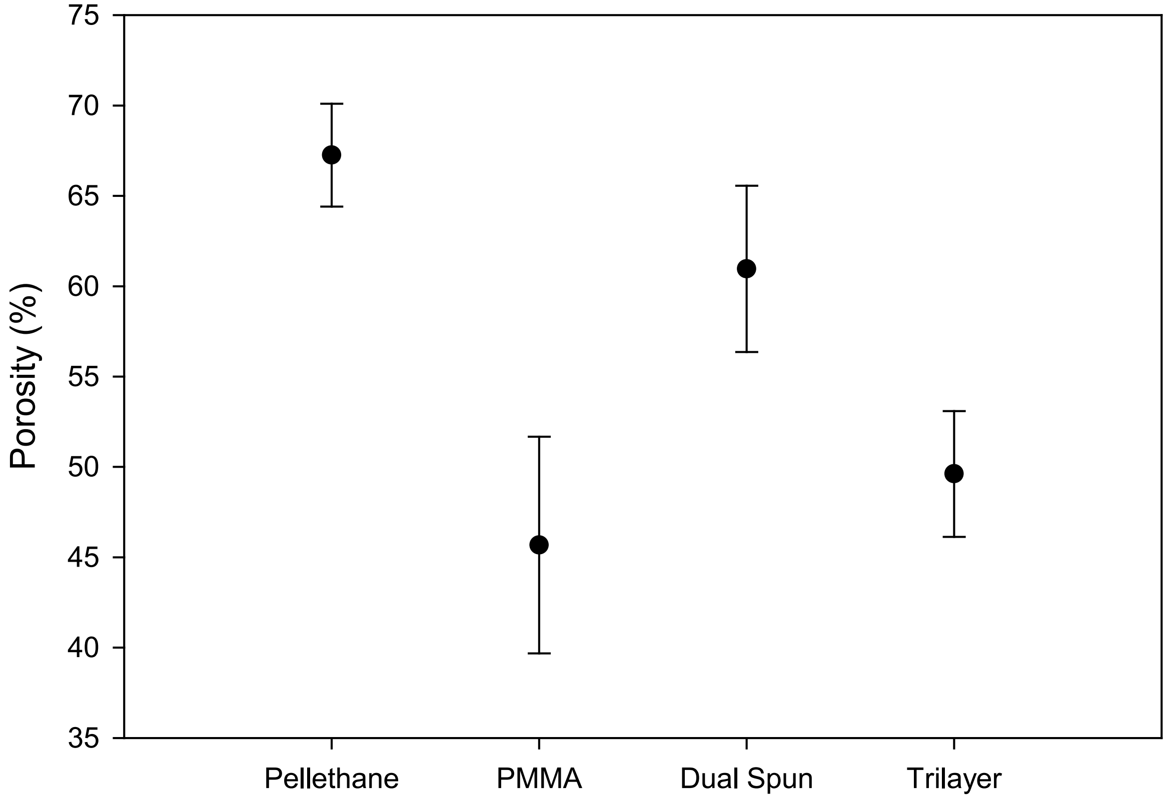

Figure 2-4: Scatter plot of the electrospun fiber mat porosities measured via the film method (method 2). Each data point is an average with n of 3.

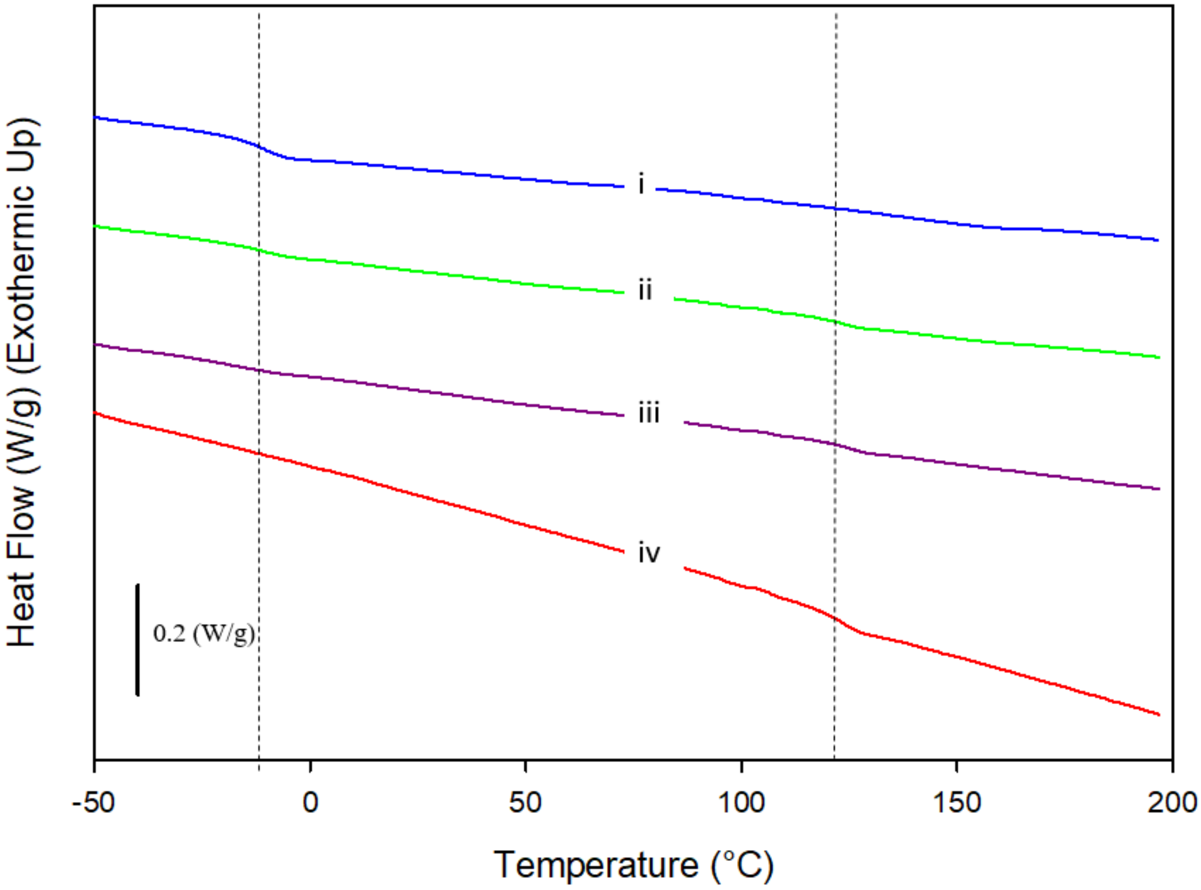

Figure 2-5: DSC of the second heating curves for (i) Pellethane, (ii) dual spun, (iii) trilayer and (iv) poly(methyl methacrylate). The measured glass transition temperatures (T_g) for Pellethane is -10 °C and 125°C for poly(methyl methacrylate). Pellethane is a thermoplastic elastomer and has a small melt peak around 155 °C.

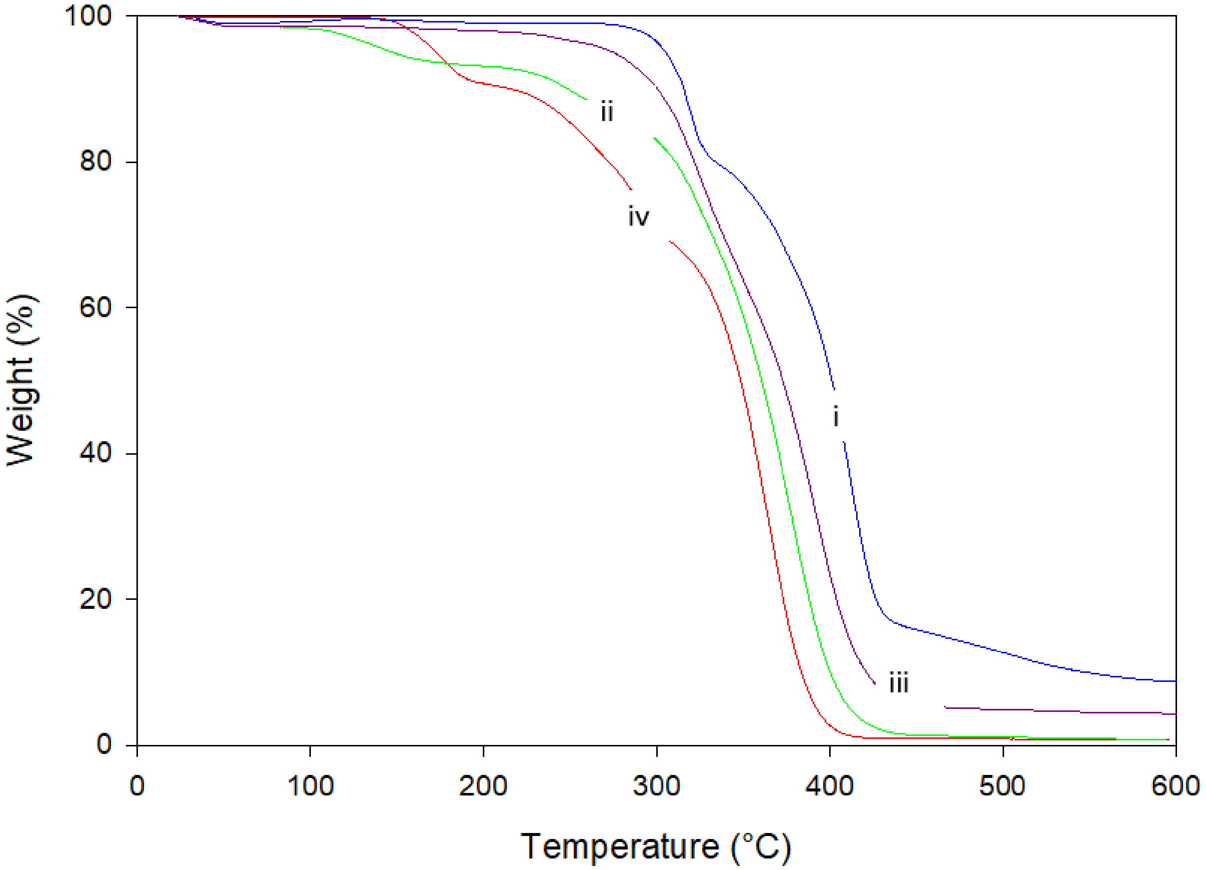

Figure 2-6: TGA mass loss curves as a function of temperature for (i) Pellethane, (ii) dual spun, (iii) trilayer and (iv) poly(methyl methacrylate).

Table 2-1: Char yield of composites in relation to the amount of poly(methyl methacrylate) and Pellethane present based on TGA and DSC analysis.

Electrospun Sample	PMMA Amount (%)	Pellethane Amount (%)	Char Yield (%)
PMMA	100	0	0.72
Dual	59.2	40.8	0.72
Trilayer	61.8	38.2	4.18
Pellethane	0	100	8.13

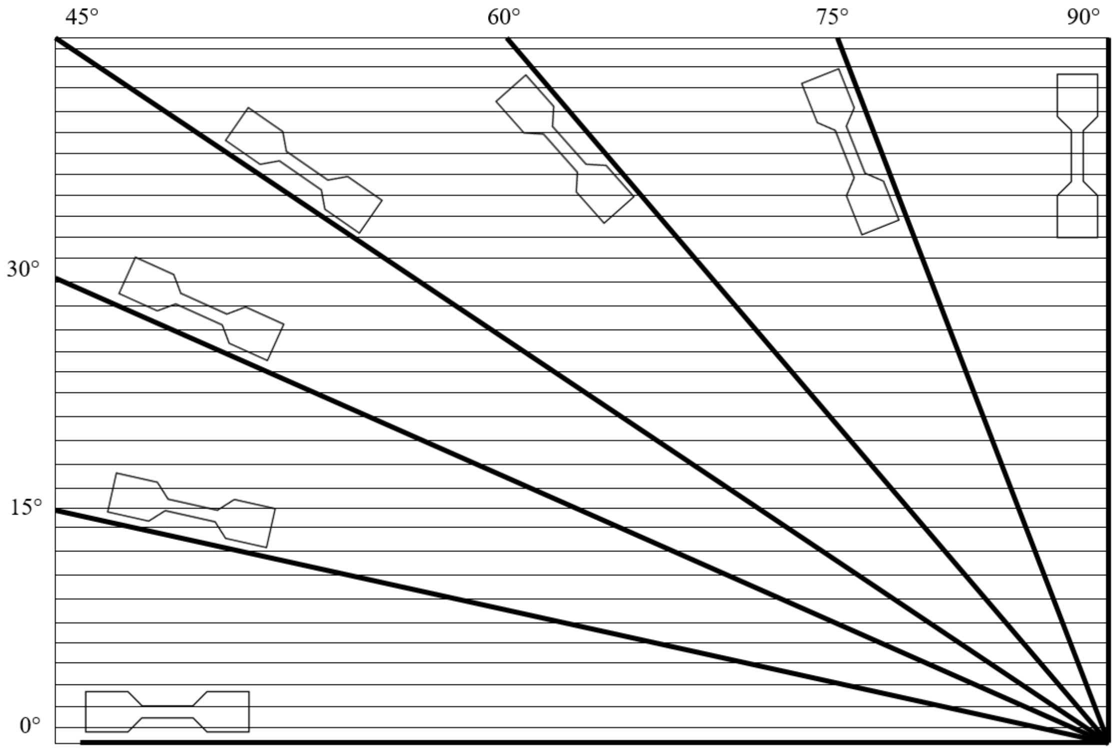

Scheme 2-6: Dog bone samples cut for tensile testing from each anisotropic fiber mat at seven different fiber orientation angles.

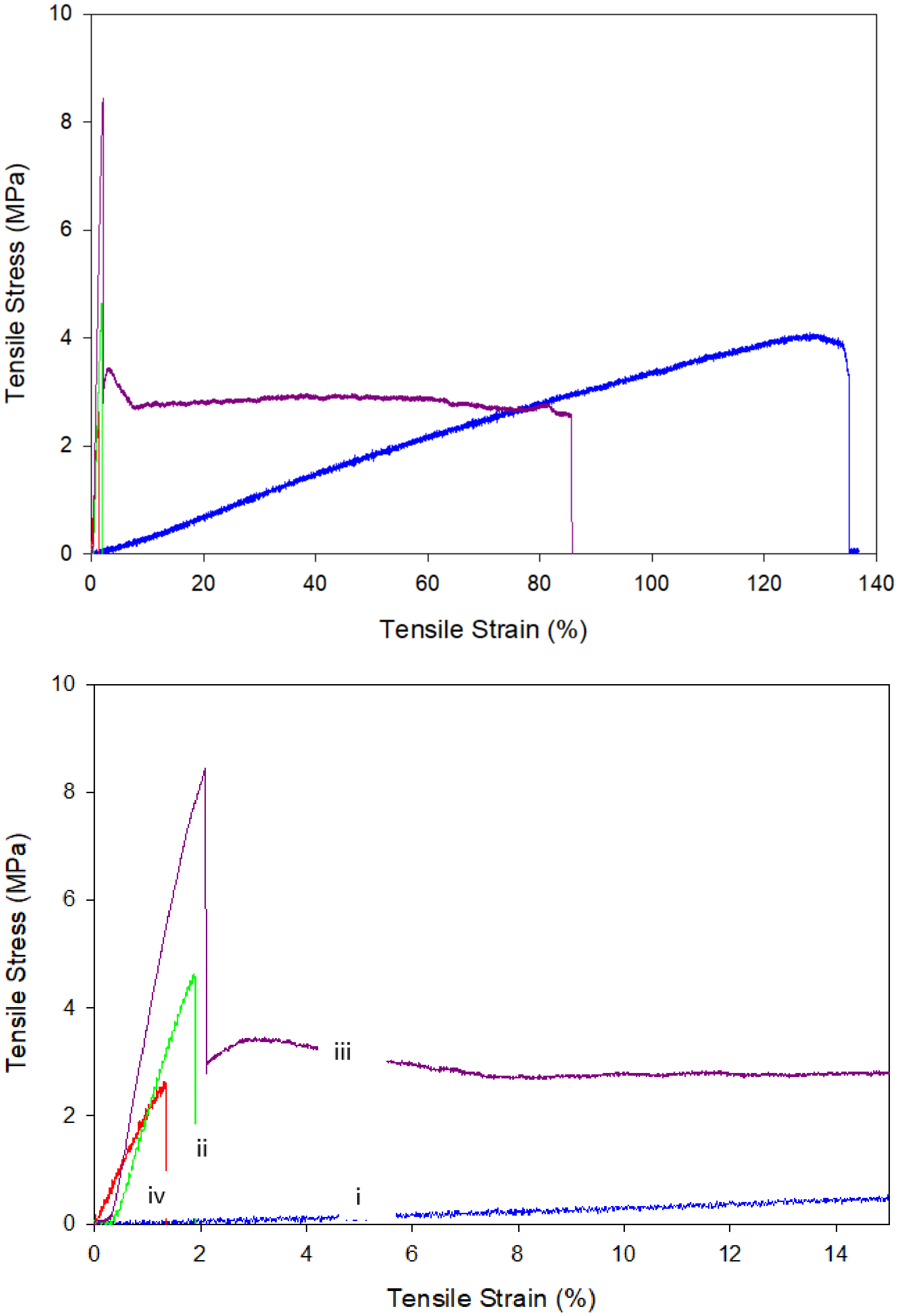

Figure 2-7: Combined representative stress-strain curves (top) and magnified view of the elastic deformation (bottom) for (i) Pellethane, (ii) dual spun, (iii) trilayer and (iv) poly(methyl methacrylate). All samples are θ = 0° with n of 5.

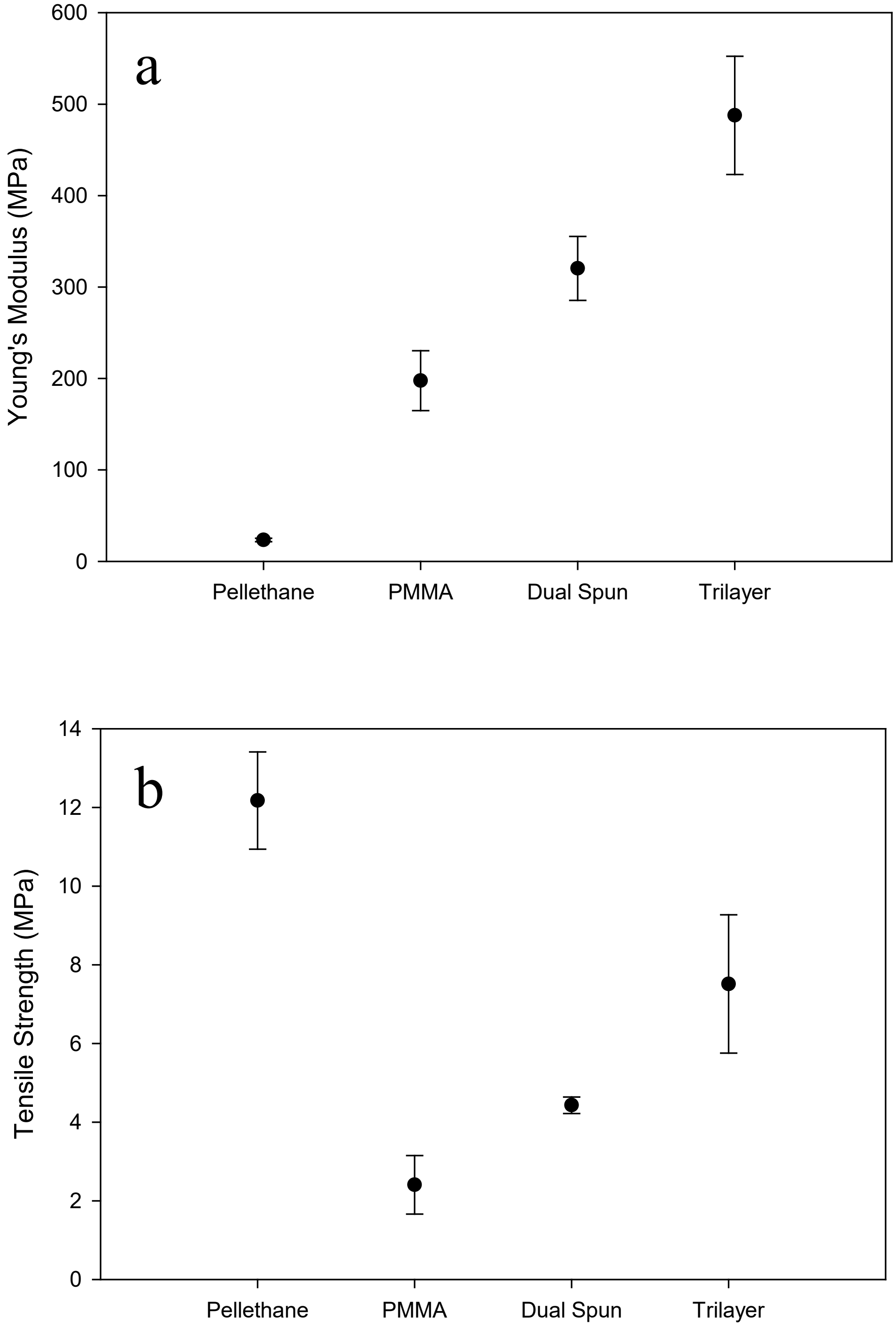
a
Young's Modulus (MPa)
0
100
200
300
400
500
600
Pellethane
PMMA
Dual Spun
Trilayer
b
Tensile Strength (MPa)
0
2
4
6
8
10
12
14
Pellethane
PMMA
Dual Spun
Trilayer

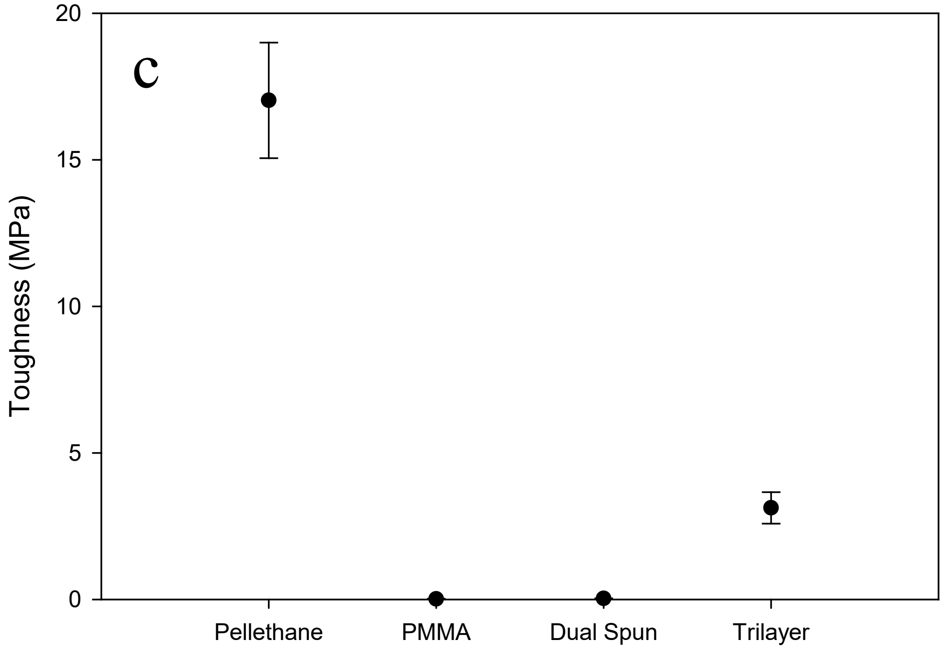
c
Toughness (MPa)
20
15
10
5
0
Pellethane
PMMA
Dual Spun
Trilayer

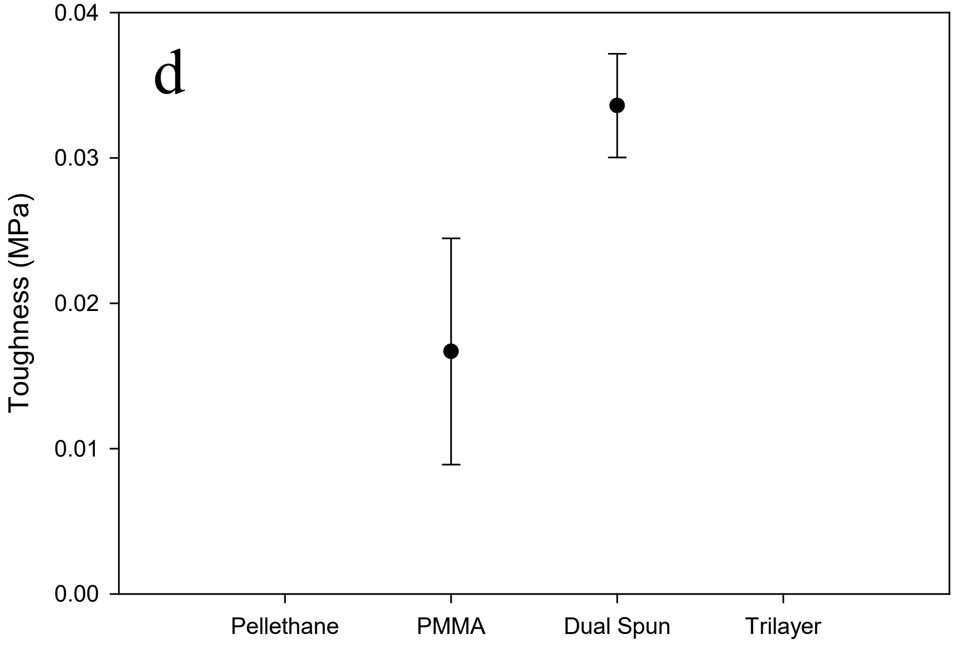
d
Toughness (MPa)
0.04
0.03
0.02
0.01
0.00
Pellethane
PMMA
Dual Spun
Trilayer

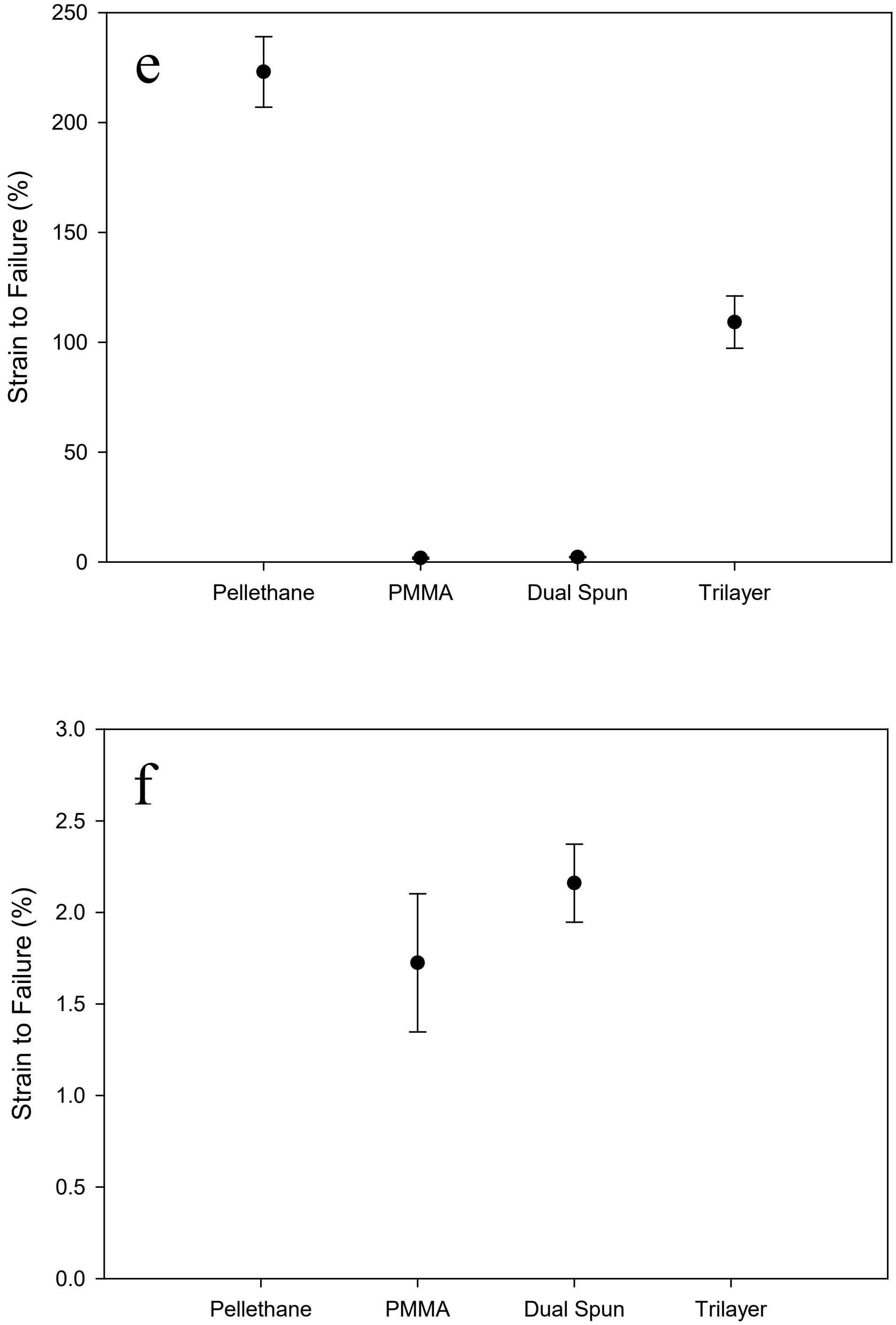

Figure 2-8: Summation of mechanical properties obtained through interpretation of the stress-strain curves for all samples with the fiber orientation angle θ = 0°. (a) Young's modulus, (b) tensile strength, (c) toughness, (d) magnified view of toughness, (e) strain-to-failure and (f) magnified view of strain-to-failure. All data points are an average of n = 5.

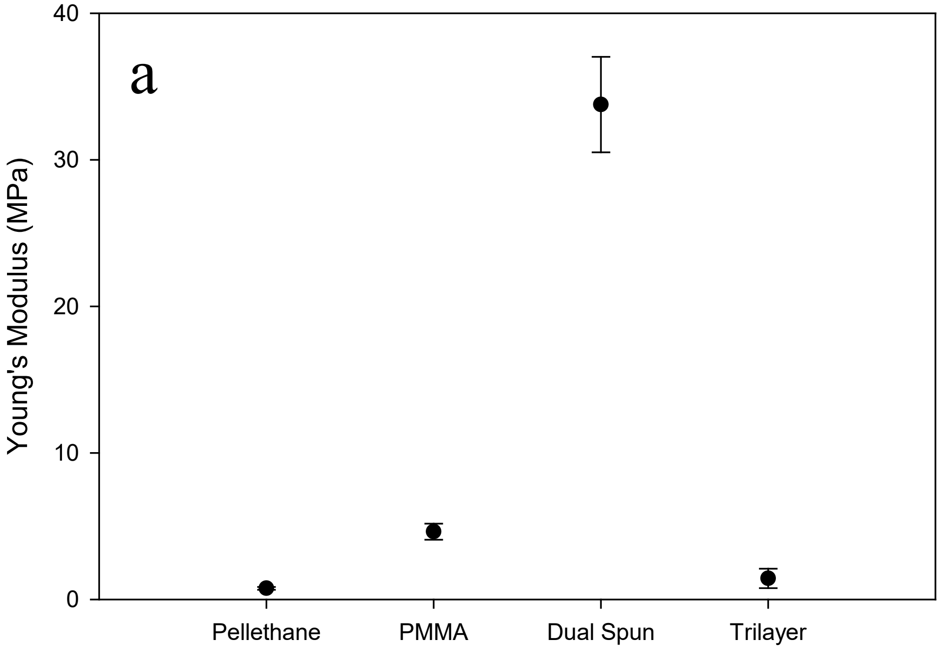
a
Young's Modulus (MPa)
0
10
20
30
40
Pellethane
PMMA
Dual Spun
Trilayer

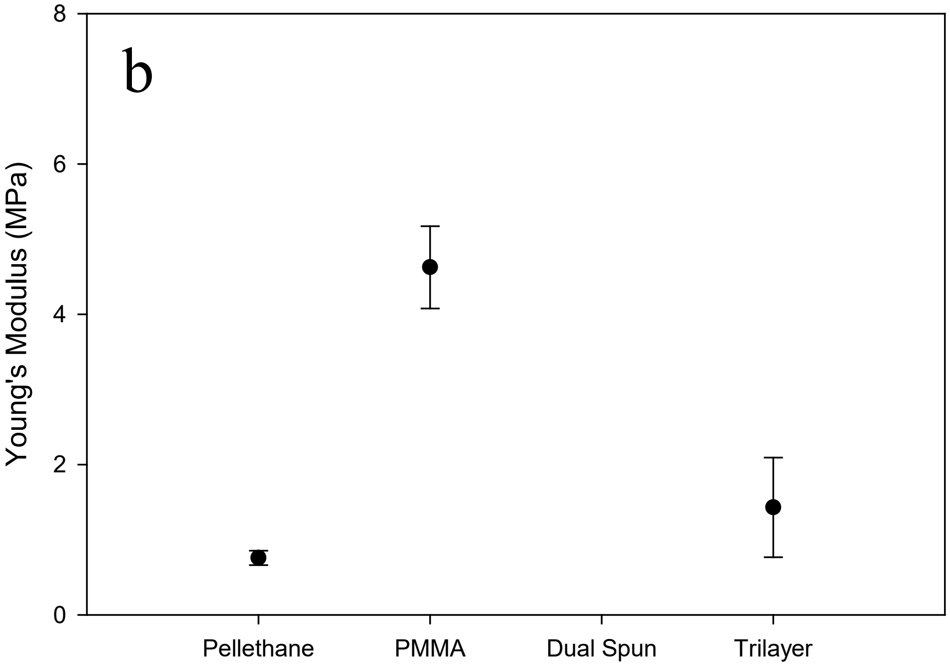
b
Young's Modulus (MPa)
0
2
4
6
8
Pellethane
PMMA
Dual Spun
Trilayer

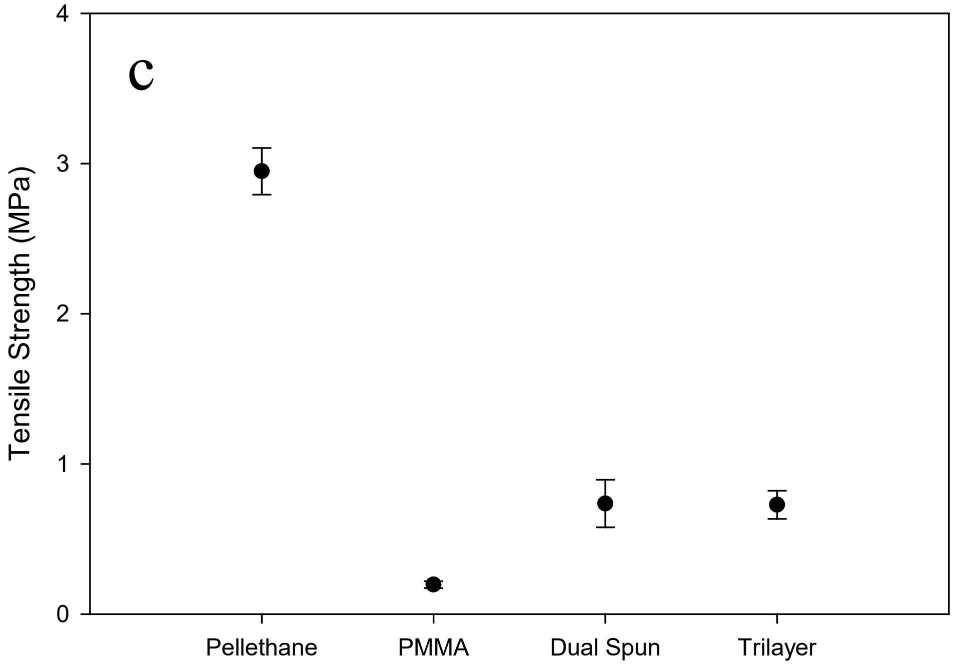
c
Tensile Strength (MPa)
4
3
2
1
0
Pellethane
PMMA
Dual Spun
Trilayer

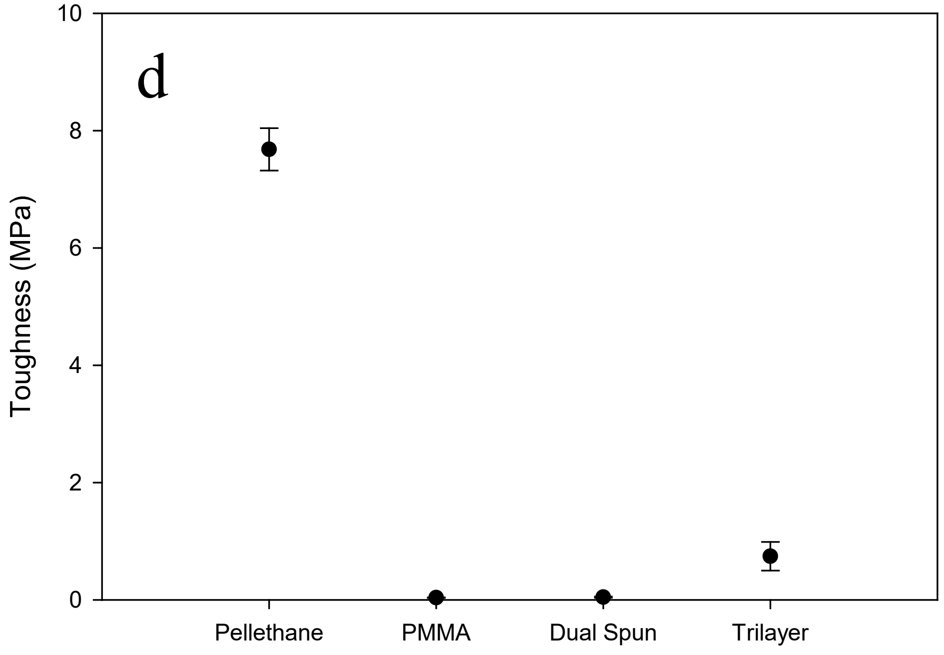
d
Toughness (MPa)
10
8
6
4
2
0
Pellethane
PMMA
Dual Spun
Trilayer

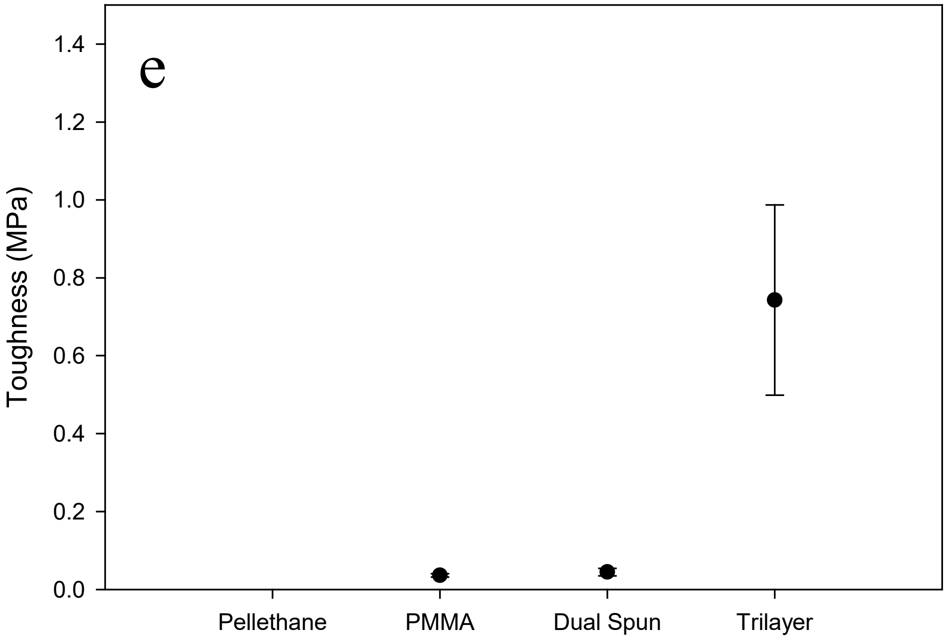

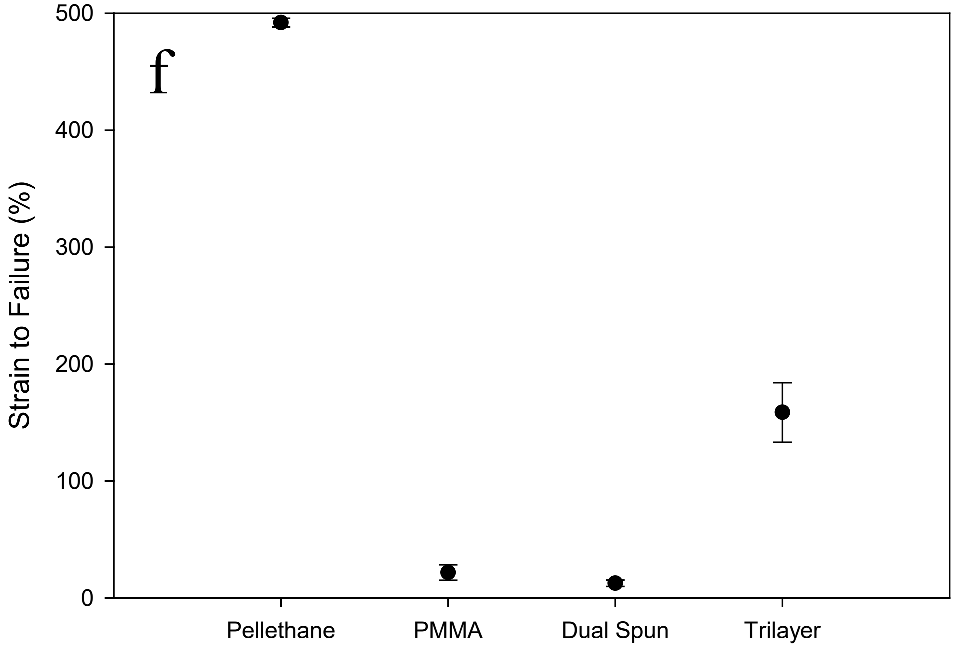

Figure 2-9: Summation of mechanical properties obtained through interpretation of the stress-strain curves for all samples with the fiber orientation angle θ = 90°. (a) Young's modulus, (b) magnified view of Young's modulus, (c) tensile strength, (d) toughness, (e) magnified view of toughness and (f) strain-to-failure. All data points are an average of n = 5.

Table 2-2: Anisotropy of the electrospun fiber samples quantified as a function of Young's modulus in a ratio of the 0° / 90° fiber orientation angles obtained through interpreting the stress-strain curves.

Electrospun Sample	Fiber Orientation Angle [°]	Youngs Modulus [MPa]	Anisotropy
PMMA	0°	197.62	42.68
	90°	4.63	
Pellethane	0°	23.4	30.79
	90°	0.76	
Dual Spun	0°	320.46	9.49
	90°	33.77	
Trilayer	0°	487.8	341.12
	90°	1.43	

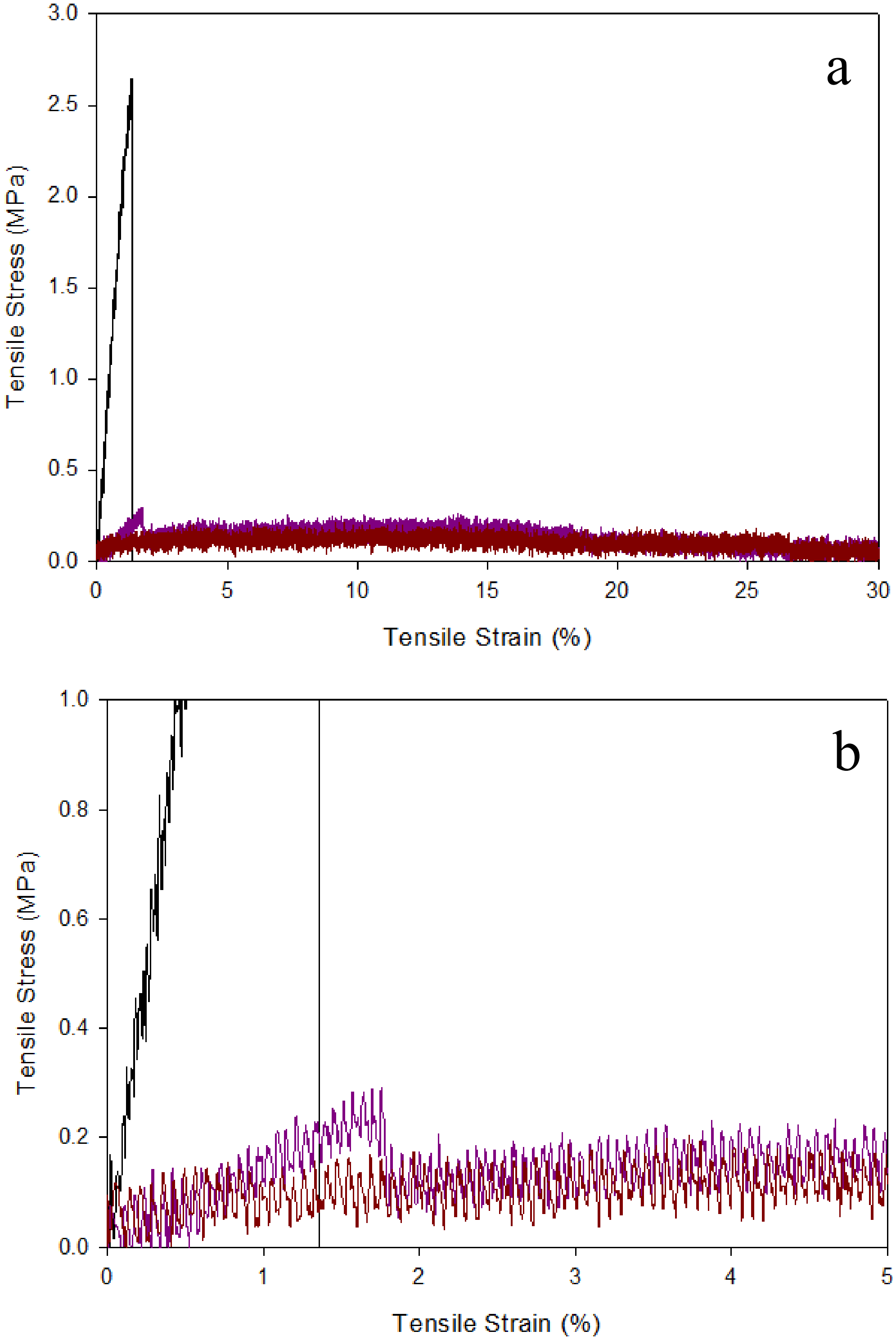
a
Tensile Stress (MPa)
3.0
2.5
2.0
1.5
1.0
0.5
0.0
0
5
10
15
20
25
30
Tensile Strain (%)
b
Tensile Stress (MPa)
1.0
0.8
0.6
0.4
0.2
0.0
0
1
2
3
4
5
Tensile Strain (%)

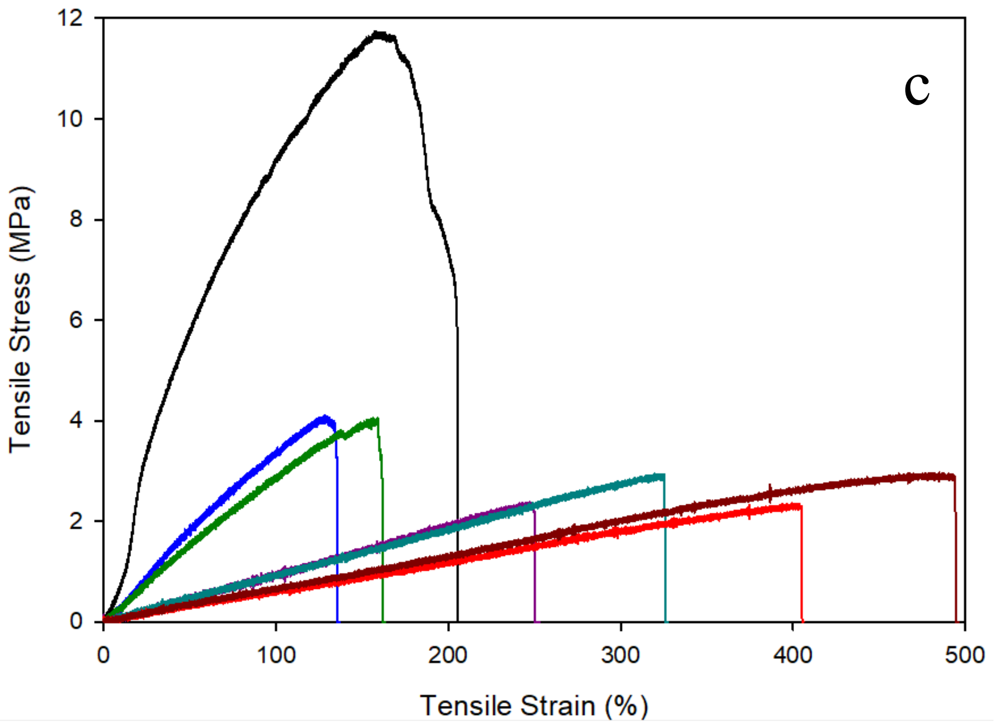
c
Tensile Stress (MPa)
Tensile Strain (%)
0
2
4
6
8
10
12
0
100
200
300
400
500

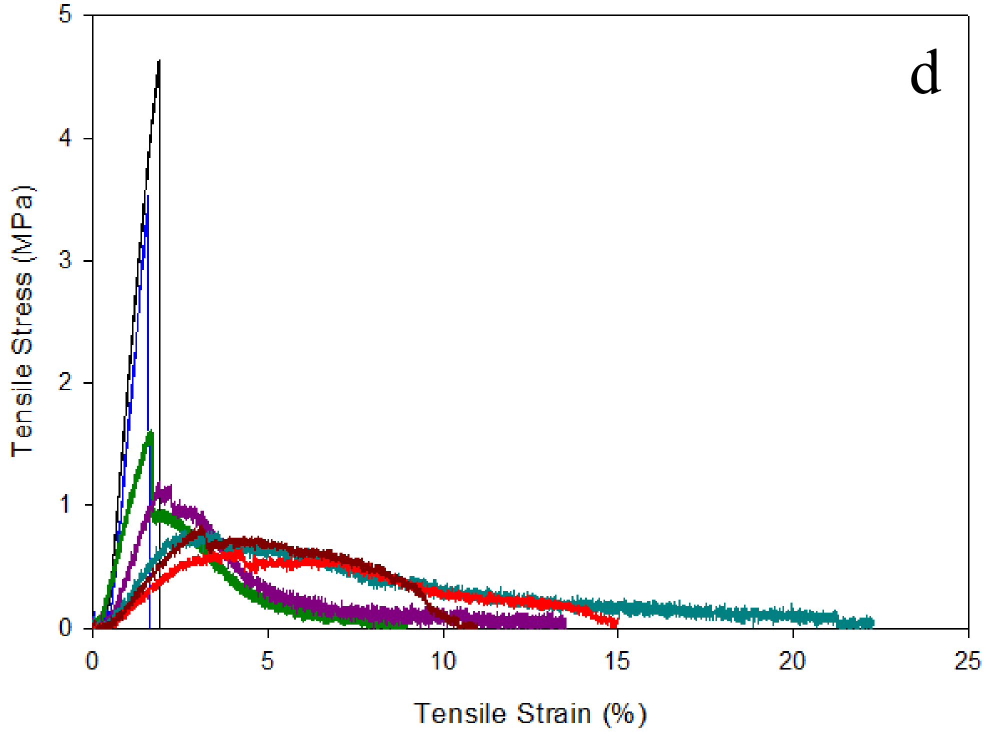
d
Tensile Stress (MPa)
Tensile Strain (%)
0
1
2
3
4
5
0
5
10
15
20
25

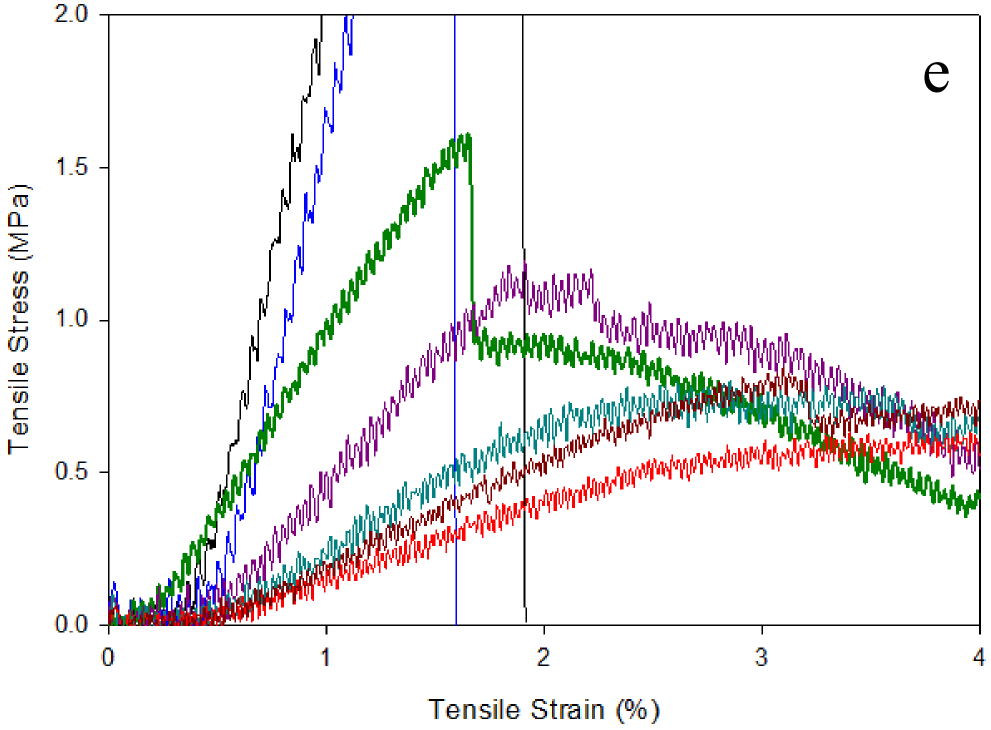
e
Tensile Stress (MPa)
2.0
1.5
1.0
0.5
0.0
0
1
2
3
4
Tensile Strain (%)

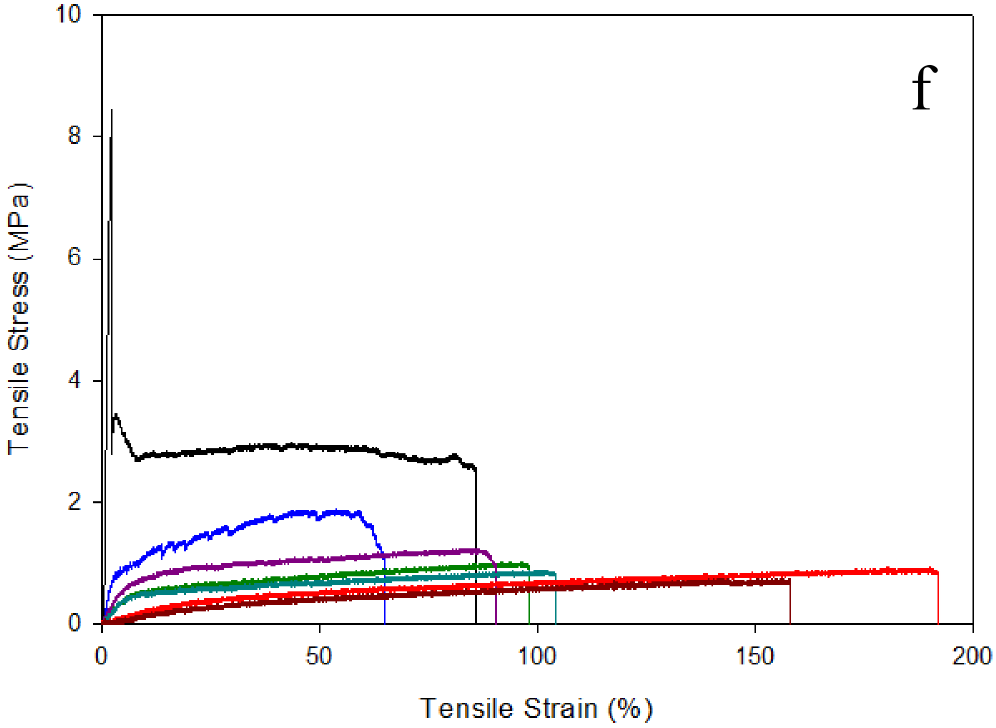
f
Tensile Stress (MPa)
10
8
6
4
2
0
0
50
100
150
200
Tensile Strain (%)

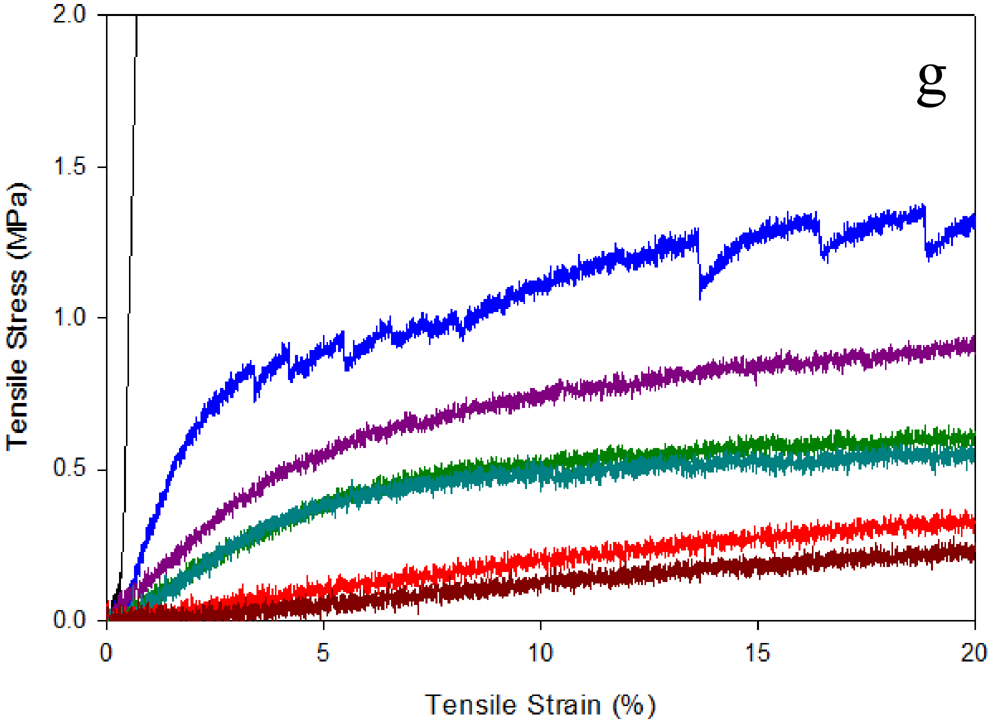

Figure 2-10: Representative stress-strain curves and magnified view of the elastic deformation for (a) poly(methyl methacrylate), (b) magnified poly(methyl methacrylate), (c) Pellethane, (d) dual electrospun, (e) magnified dual electrospun, (f) trilayer and (g) magnified view of trilayer . Each graph shows seven distinct fiber orientation angles (Δθ) of 0° (black), 15° (blue), 30° (green) 45°(purple), 60° (turquoise), 75° (red) and 90° (brown). All sample curves are an average of n = 5.

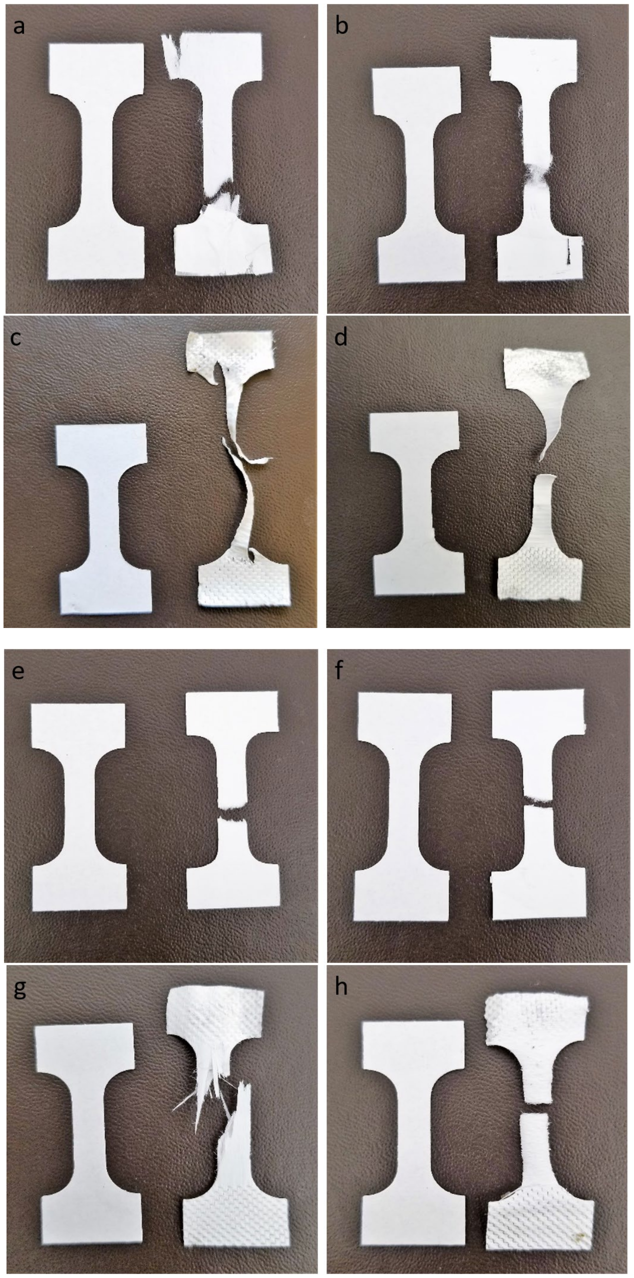

Figure 2-11: Representative post tensile tested dog bones (right) with pre tensile tested dog bones (left) for (a) poly(methyl methacrylate) 0°, (b) poly(methyl methacrylate) 90°, (c) Pellethane 0°, (d) Pellethane 90°, (e) dual spun 0°, (f) dual spun 90°, (g) trilayer 0° and (h) trilayer 90°.

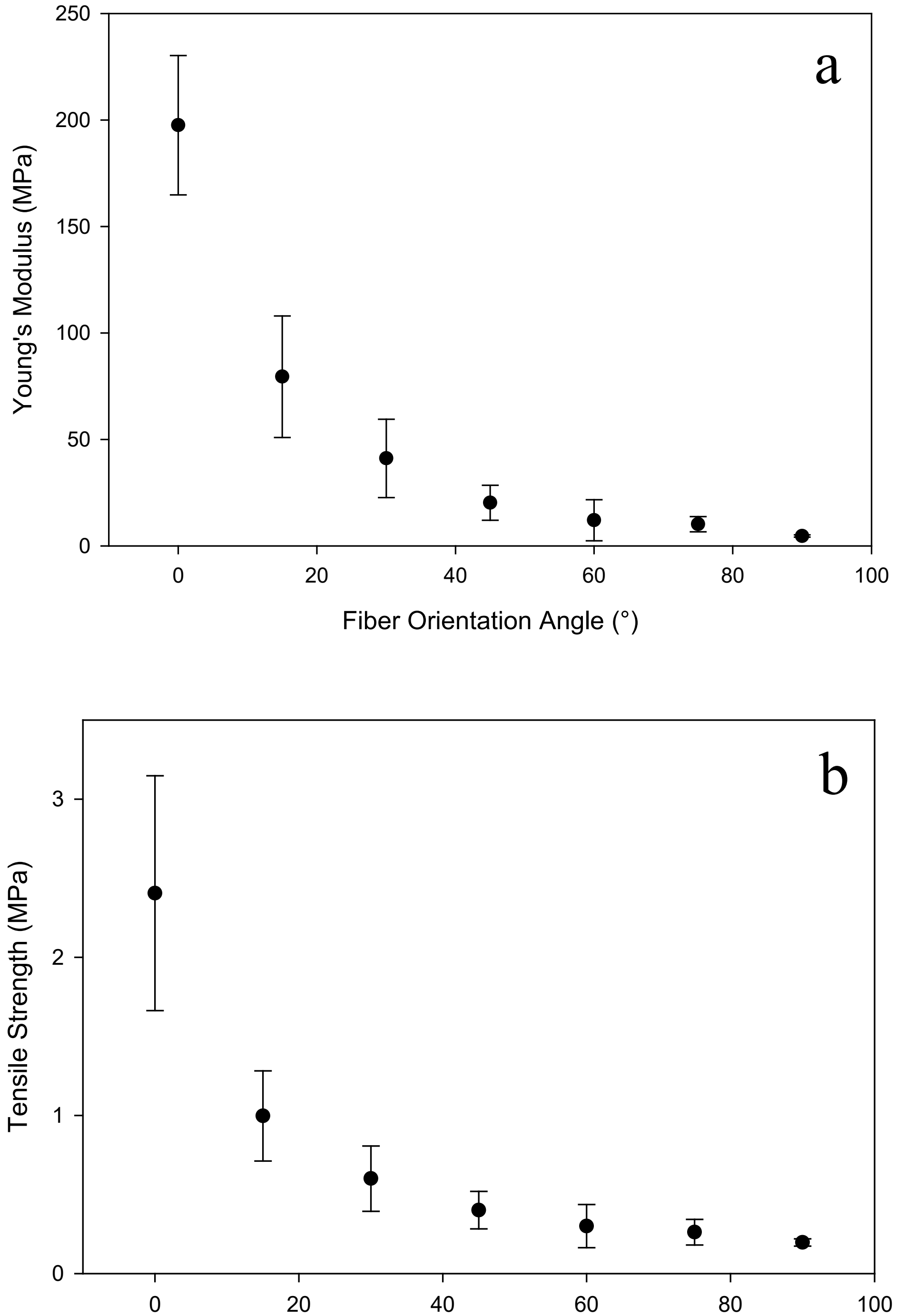
a
Young's Modulus (MPa)
250
200
150
100
50
0
0
20
40
60
80
100
Fiber Orientation Angle (°)
b
Tensile Strength (MPa)
3
2
1
0
0
20
40
60
80
100
Fiber Orientation Angle (°)

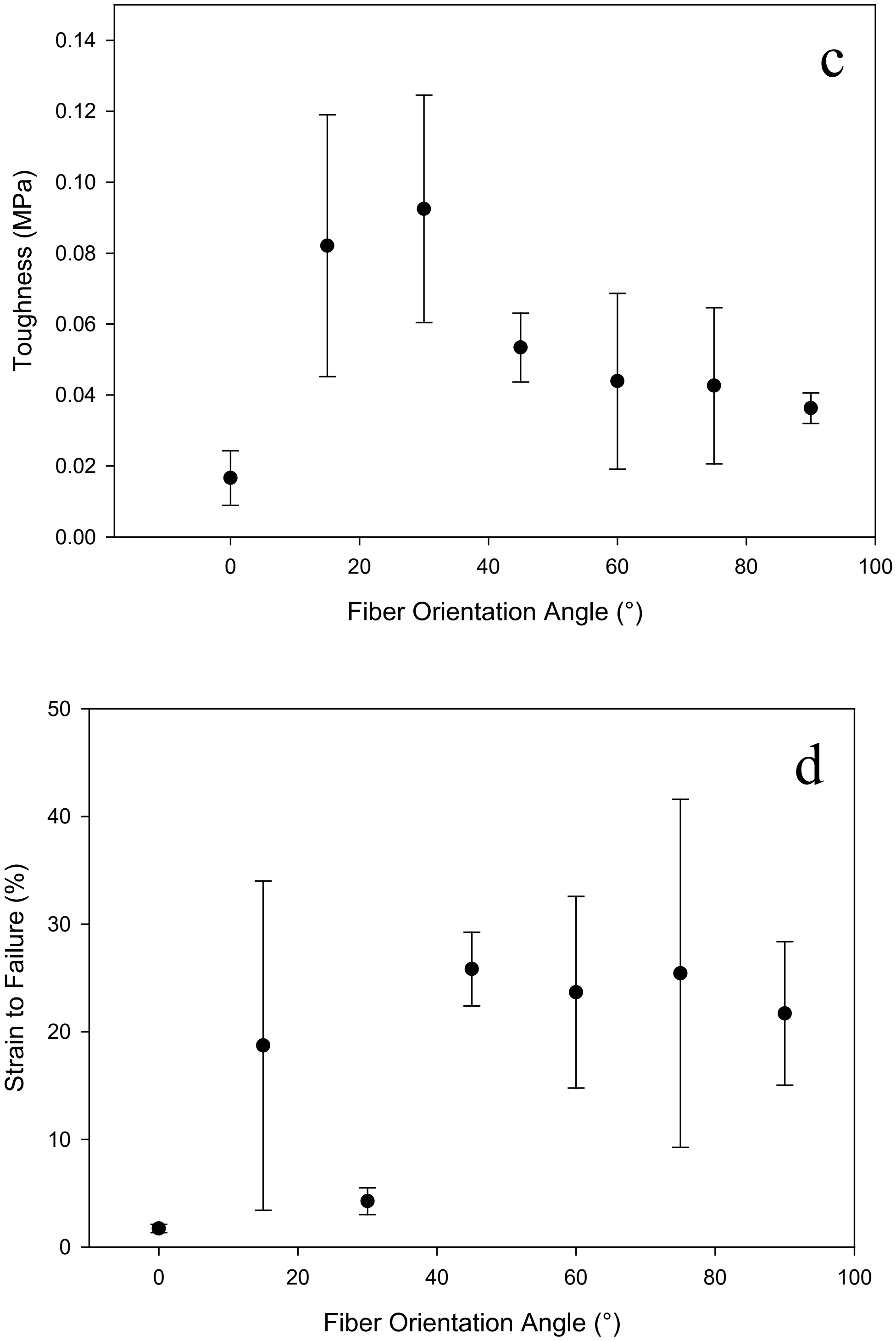

Figure 2-12: Resulting mechanical properties of electrospun poly(methyl methacrylate) with 10wt. % sol. concentration from tensile testing as a function of the fiber orientation angle. (a) Young's modulus, (b) tensile strength, (c) toughness and (d) strain-to-failure. All data points are an average of n = 5.

Table 2-3: Average Young’s modulus, toughness, tensile strength and strain to failure for all fiber orientation angles (Δθ) interpreted from the stress strain curves of electrospun poly(methyl methacrylate) with 10wt. % sol. concentration.

Material Property	**Fiber Orientation Angle [°]**						
	0	*15*	*30*	*45*	*60*	*75*	*90*
Young's Modulus [MPa]	197.62 ± 32.73	79.47 ± 28.56	41.09 ± 18.39	20.26 ± 8.24	12.04 ± 9.65	10.16 ± 3.56	4.63 ± 0.55
Toughness [MPa]	0.02 ± 0.007	0.08 ± 0.037	0.09 ± 0.032	0.05 ± 0.009	0.04 ± 0.025	0.04 ± 0.022	0.04 ± 0.004
Tensile Strength [MPa]	2.41 ± 0.74	0.96 ± 0.26	0.60 ± 0.21	0.40 ± 0.12	0.29 ± 0.14	0.26 ± 0.08	0.19 ± 0.02
Strain to Failure [%]	1.73 ± 0.34	18.72 ± 15.29	4.26 ± 1.24	25.83 ± 3.42	23.69 ± 8.91	25.44 ± 16.17	21.71 ± 6.68

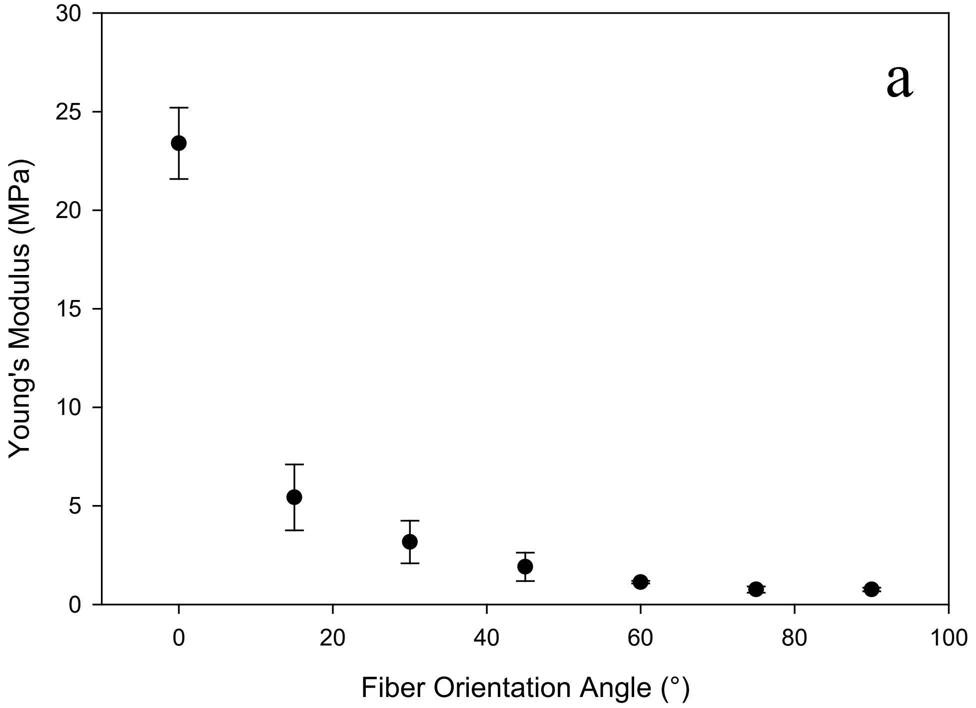
a
Young's Modulus (MPa)
30
25
20
15
10
5
0
0
20
40
60
80
100
Fiber Orientation Angle (°)

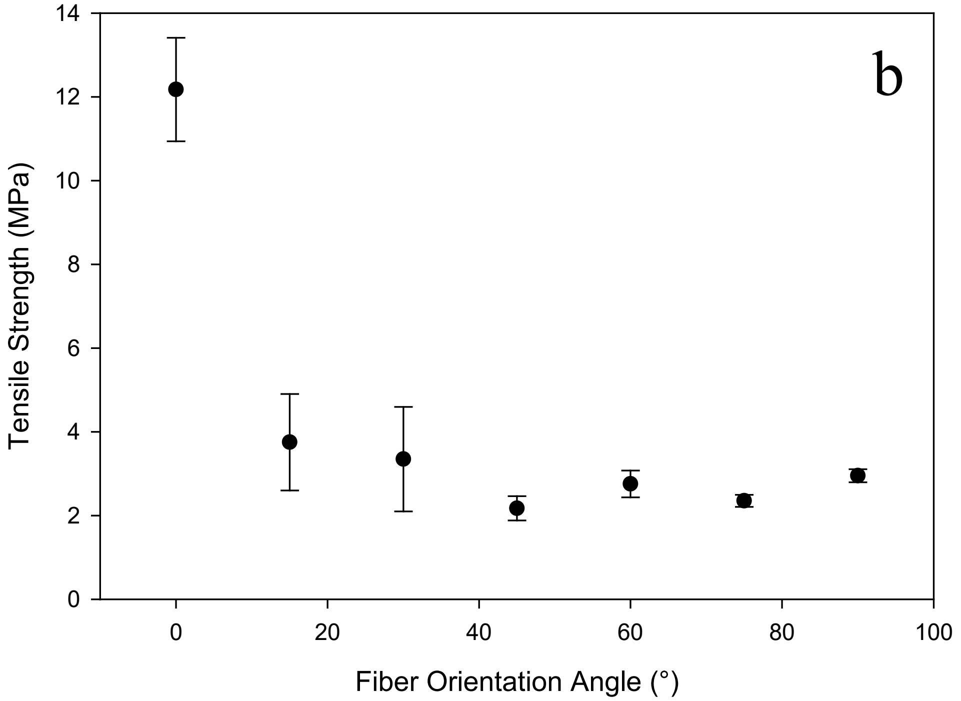
b
Tensile Strength (MPa)
14
12
10
8
6
4
2
0
0
20
40
60
80
100
Fiber Orientation Angle (°)

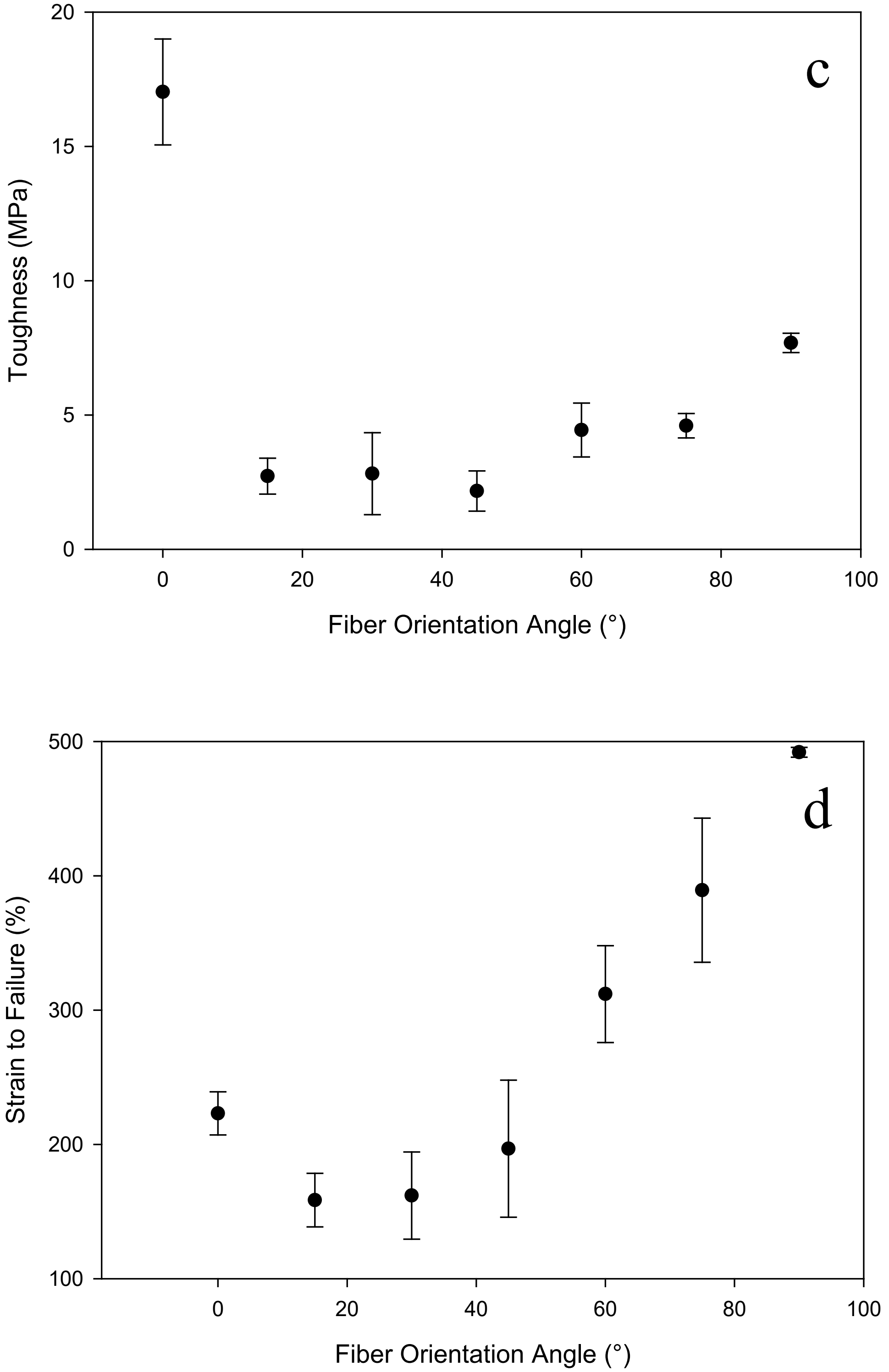

Figure 2-13: Resulting mechanical properties of electrospun Pellethane from tensile testing as a function of the fiber orientation angle. (a) Young's modulus, (b) tensile strength, (c) toughness and (d) strain-to-failure. All data points are an average of n = 5.

Table 2-4: Average Young's modulus, toughness, tensile strength and strain to failure for all fiber orientation angles (Δθ) interpreted from the stress strain curves of electrospun Pellethane.

Material Property	**Fiber Orientation Angle [°]**						
	0	*15*	*30*	*45*	*60*	*75*	*90*
Young's Modulus [MPa]	23.40 ± 1.81	5.43 ± 1.67	3.17 ± 1.08	1.91 ± 0.72	1.13 ± 0.06	0.75 ± 0.16	0.76 ± 0.09
Toughness [MPa]	17.03 ± 1.97	2.72 ± 0.67	2.81 ± 1.53	2.17 ± 0.75	4.44 ± 1.00	4.59 ± 0.45	7.69 ± 0.36
Tensile Strength [MPa]	12.18 ± 1.24	3.75 ± 1.15	3.35 ± 1.25	2.17 ± 0.29	2.75 ± 0.32	2.35 ± 0.14	2.95 ± 0.16
Strain to Failure [%]	223.07 ± 16.04	158.51 ± 19.93	161.88 ± 32.45	196.78 ± 51.03	312.03 ± 36.07	389.35 ± 53.65	492.07 ± 3.69

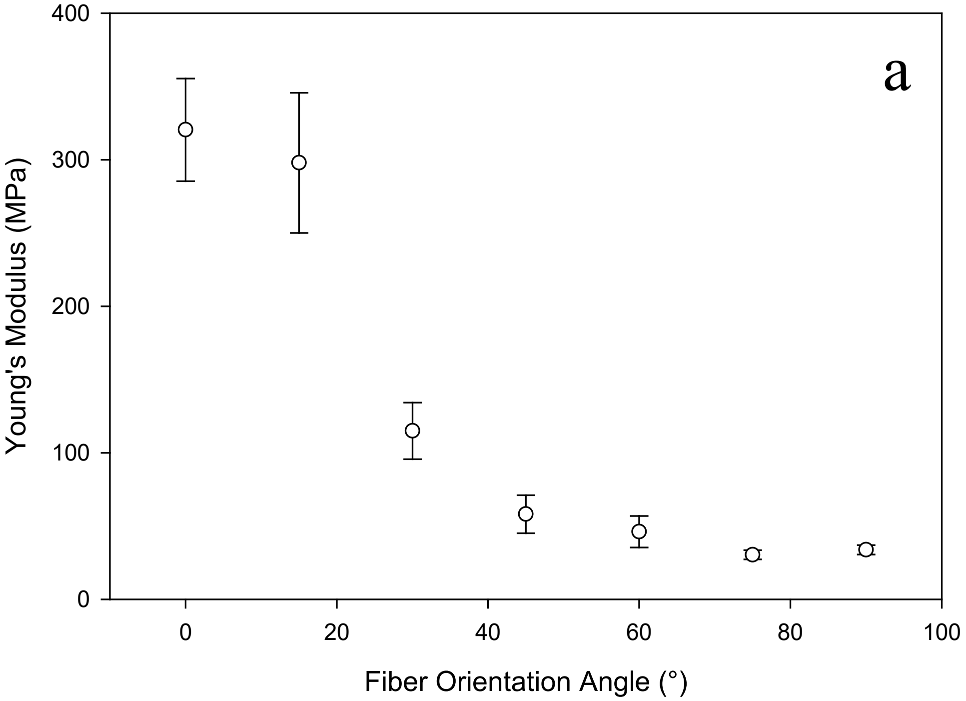
a
Young's Modulus (MPa)
0
100
200
300
400
0
20
40
60
80
100
Fiber Orientation Angle (°)

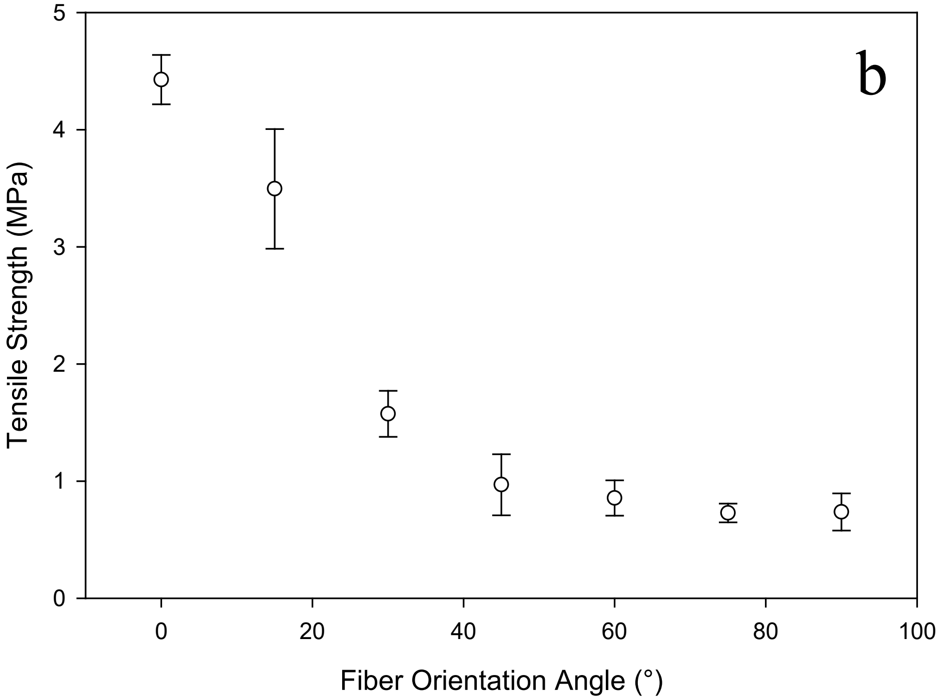
b
Tensile Strength (MPa)
0
1
2
3
4
5
0
20
40
60
80
100
Fiber Orientation Angle (°)

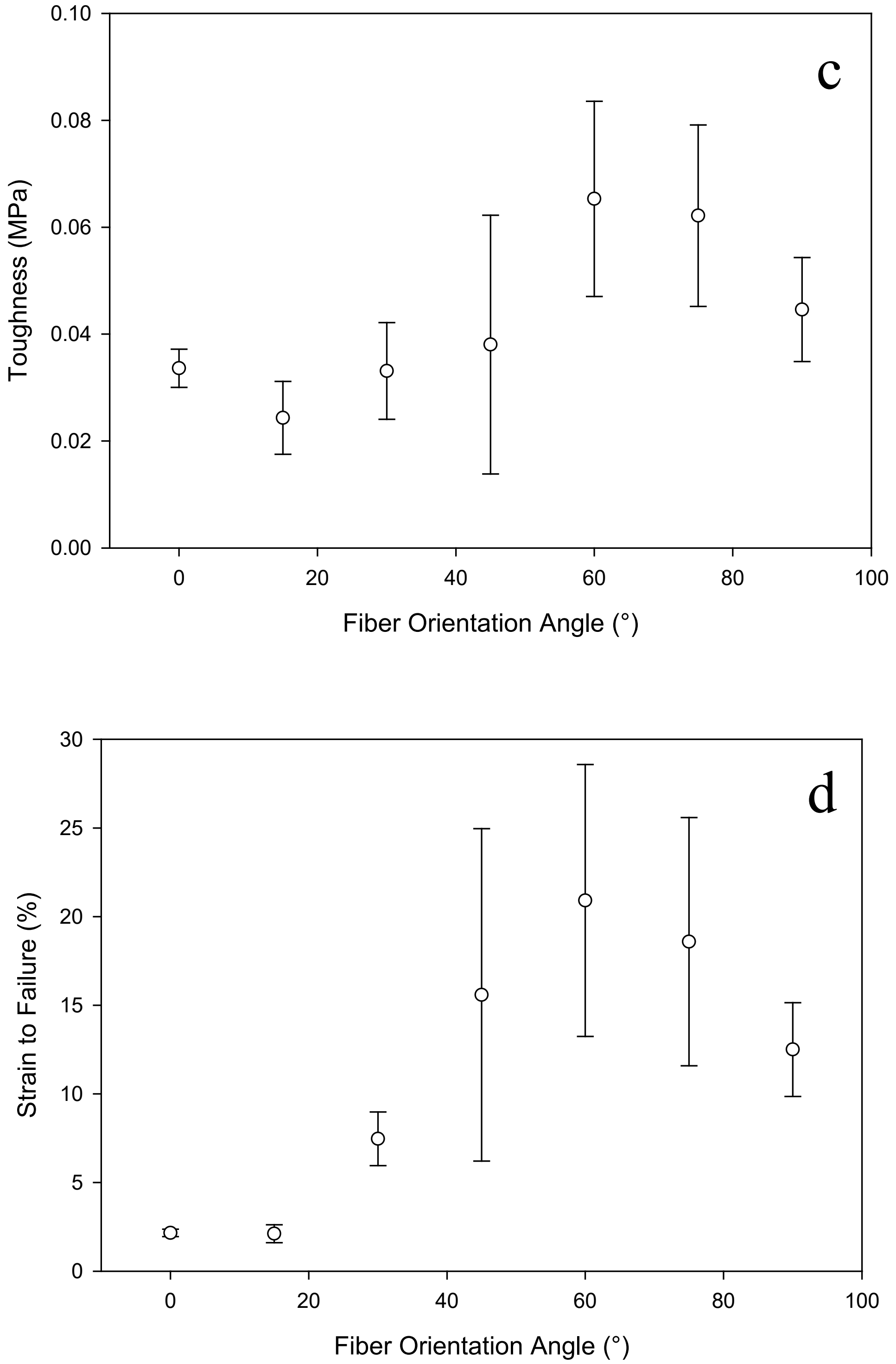

Figure 2-14: Resulting mechanical properties of dual electrospun poly(methyl methacrylate) with Pellethane from tensile testing as a function of the fiber orientation angle. (a) Young's modulus, (b) tensile strength, (c) toughness and (d) strain-to-failure. All data points are an average of n = 5.

Table 2-5: Average Young's modulus, toughness, tensile strength and strain to failure for all fiber orientation angles (Δθ) interpreted from the stress strain curves of dual electrospun poly(methyl methacrylate) with Pellethane.

Material Property	**Fiber Orientation Angle [°]**						
	0	*15*	*30*	*45*	*60*	*75*	*90*
Young's Modulus [MPa]	320.46 ± 35.00	297.95 ± 47.85	114.89 ± 19.34	58.08 ± 12.96	46.13 ± 10.78	30.40 ± 3.15	33.77 ± 3.25
Toughness [MPa]	0.033 ± 0.004	0.024 ± 0.007	0.033 ± 0.009	0.049 ± 0.013	0.065 ± 0.018	0.062 ± 0.017	0.044 ± 0.009
Tensile Strength [MPa]	4.43 ± 0.21	3.49 ± 0.51	1.57 ± 0.19	1.09 ± 0.17	0.85 ± 0.15	0.73 ± 0.08	0.74 ± 0.16
Strain to Failure [%]	2.16 ± 0.21	2.11 ± 0.51	7.46 ± 1.51	19.63 ± 5.84	20.91 ± 7.66	18.57 ± 7.00	12.50 ± 2.65

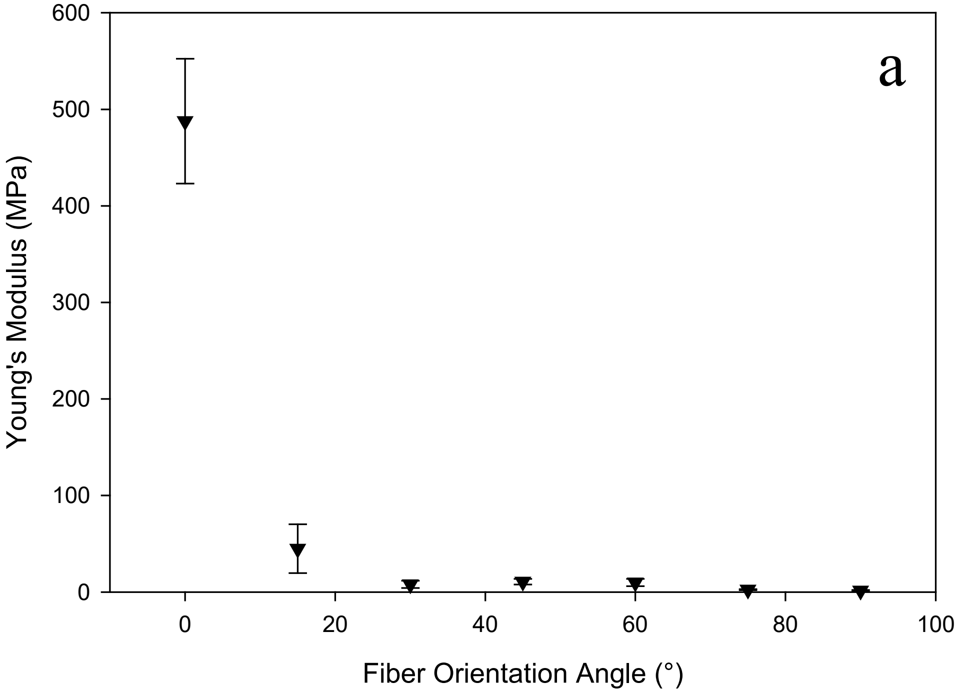
a
Young's Modulus (MPa)
600
500
400
300
200
100
0
0
20
40
60
80
100
Fiber Orientation Angle (°)

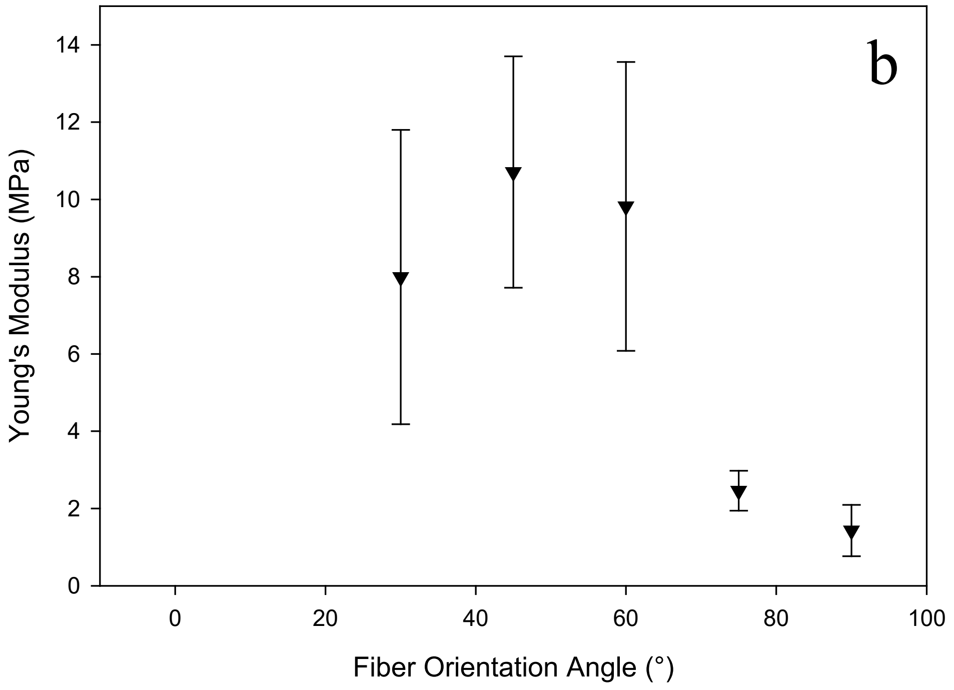
b
Young's Modulus (MPa)
14
12
10
8
6
4
2
0
0
20
40
60
80
100
Fiber Orientation Angle (°)

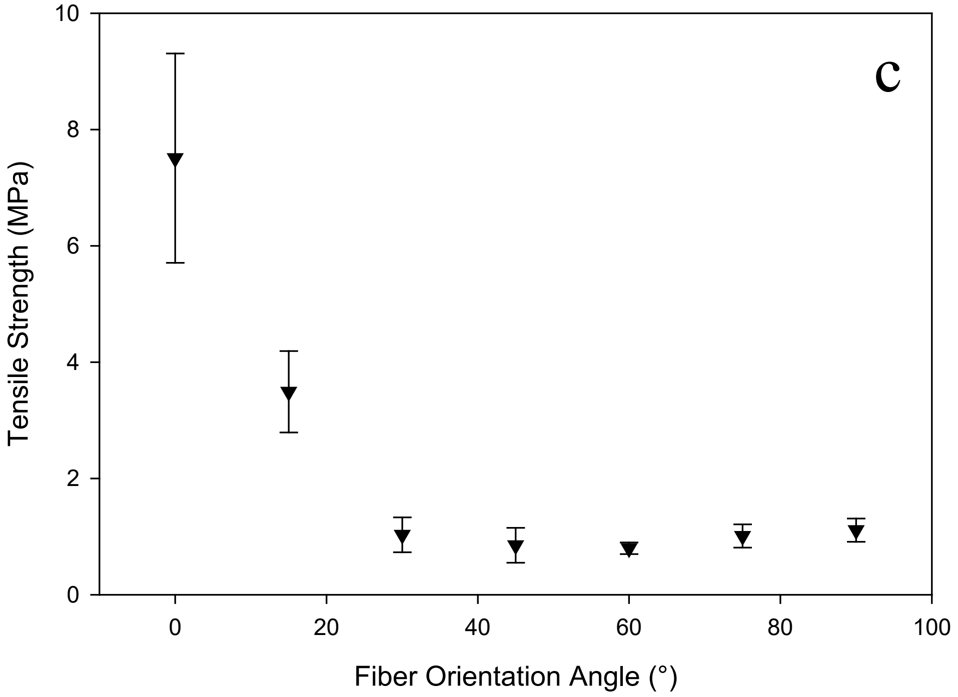
c
Tensile Strength (MPa)
Fiber Orientation Angle (°)
0
2
4
6
8
10
0
20
40
60
80
100

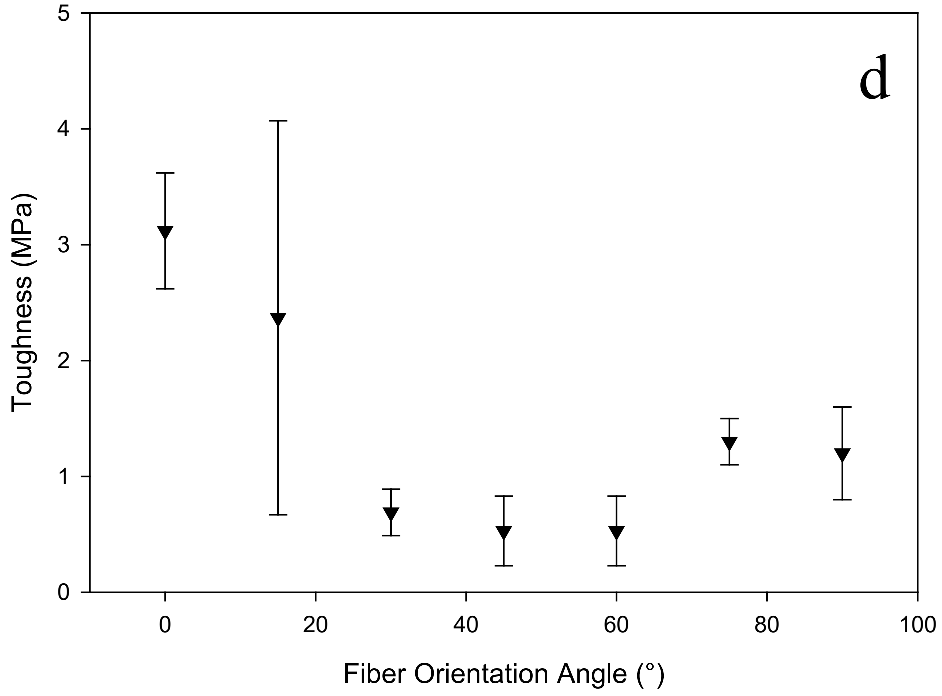
d
Toughness (MPa)
Fiber Orientation Angle (°)
0
1
2
3
4
5
0
20
40
60
80
100

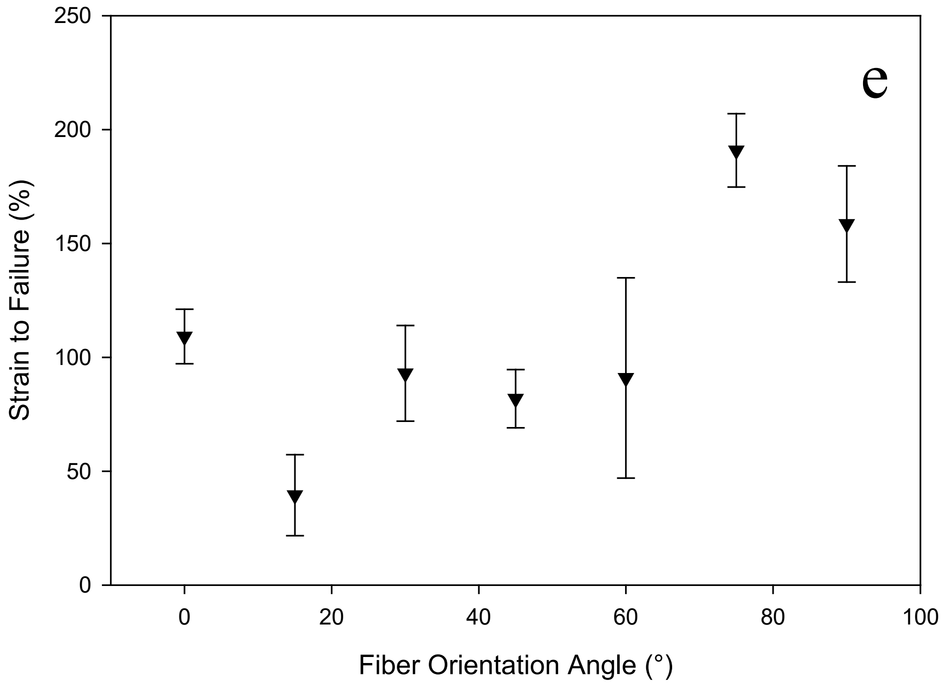

Figure 2-15: Resulting mechanical properties of electrospun trilayer of poly(methyl methacrylate) with Pellethane from tensile testing as a function of the fiber orientation angle. (a) Young's modulus, (b) tensile strength, (c) toughness and (d) strain-to-failure. All data points are an average of n = 5.

Table 2-6: Average Young's modulus, toughness, tensile strength and strain to failure for all fiber orientation angles (Δθ) interpreted from the stress strain curves of the electrospun trilayer of poly(methyl methacrylate) with Pellethane.

Material Property	**Fiber Orientation Angle [°]**						
	0	*15*	*30*	*45*	*60*	*75*	*90*
Young's Modulus [MPa]	487.80 ± 64.7	44.86 ± 25.3	7.99 ± 3.8	10.71 ± 2.9	9.81 ± 3.7	2.46 ± 0.5	1.43 ± 0.7
Toughness [MPa]	3.12 ± 0.5	2.37 ± 1.7	0.69 ± 0.2	0.53 ± 0.3	0.53 ± 0.3	1.3 ± 0.2	1.20 ± 0.4
Tensile Strength [MPa]	7.51 ± 1.8	3.49 ± 0.7	1.03 ± 0.3	0.85 ± 0.3	0.80 ± 0.1	1.01 ± 0.2	1.11 ± 0.2
Strain to Failure [%]	109.17 ± 12.0	39.45 ± 17.8	93.0 ± 21.0	81.8 ± 12.8	90.98 ± 44.0	190.92 ± 16.1	158.64 ± 25.5

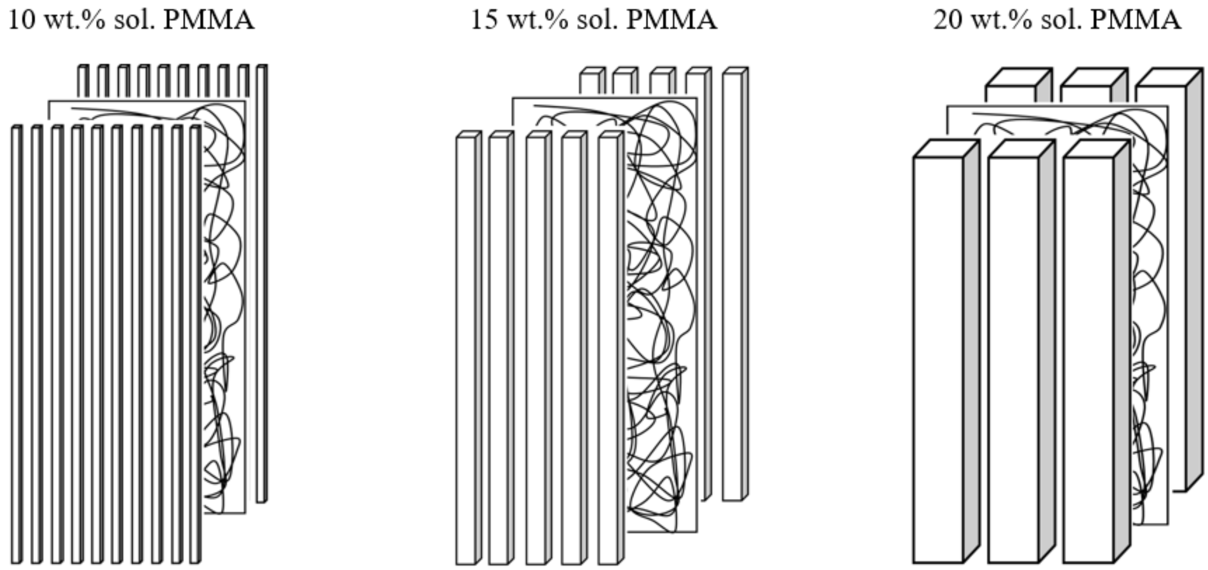

Scheme 2-7: A depiction of anisotropic electrospun trilayer materials fabricated and tested. All three trilayer fiber mats are constructed with the same amount of as well as thickness of the outer poly(methyl methacrylate) and inner Pellethane layers. The poly(methyl methacrylate) solution concentration was systematically increased, which theoretically increases the fiber diameter.

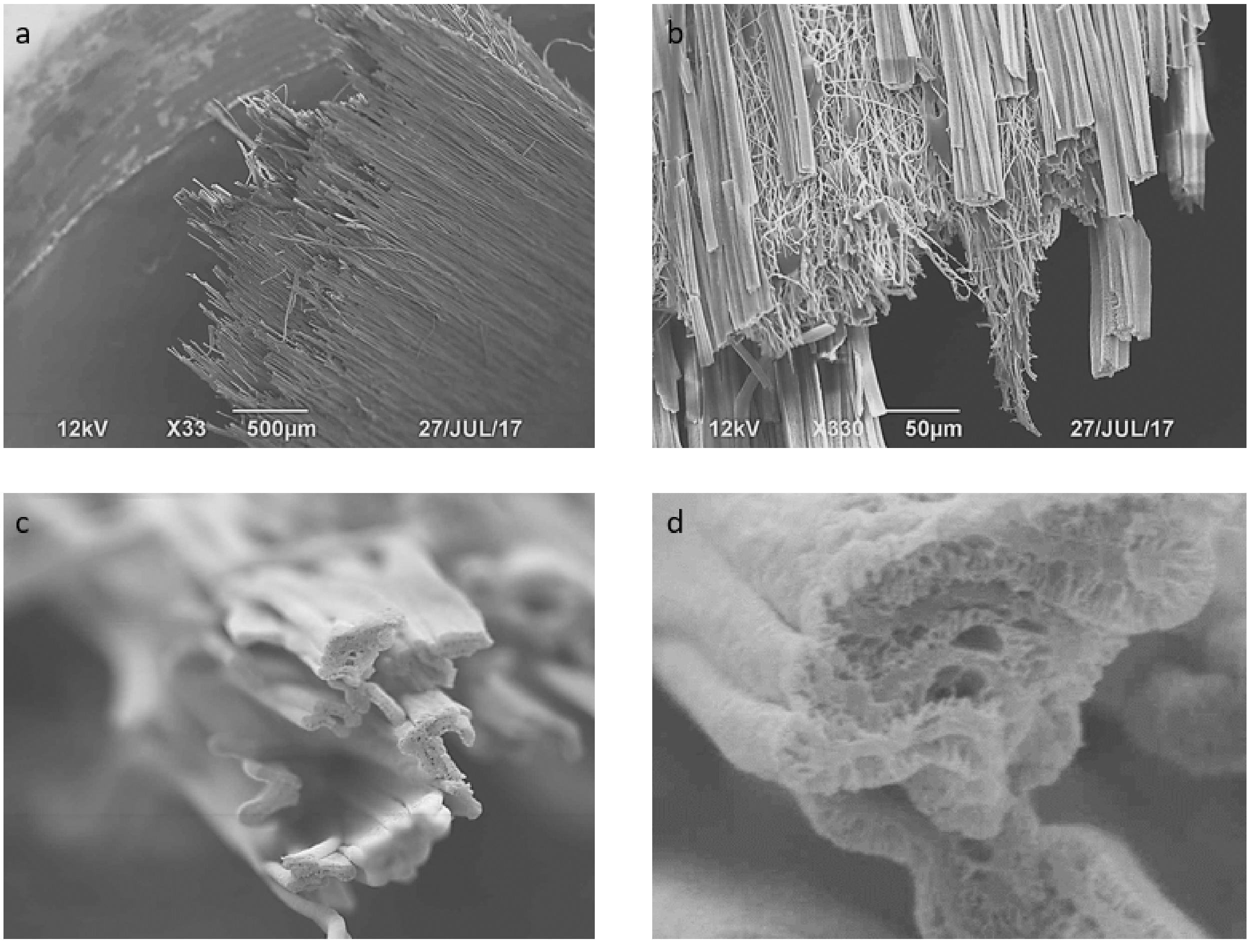

Figure 2-16: SEM micrographs of electrospun trilayer of anisotropic poly(methyl methacrylate) 10wt. % sol. concentration and Pellethane fibers. The large fibers are the poly(methyl methacrylate) fibers. Images (c) and (d) show a complex fiber morphology of the poly(methyl methacrylate).

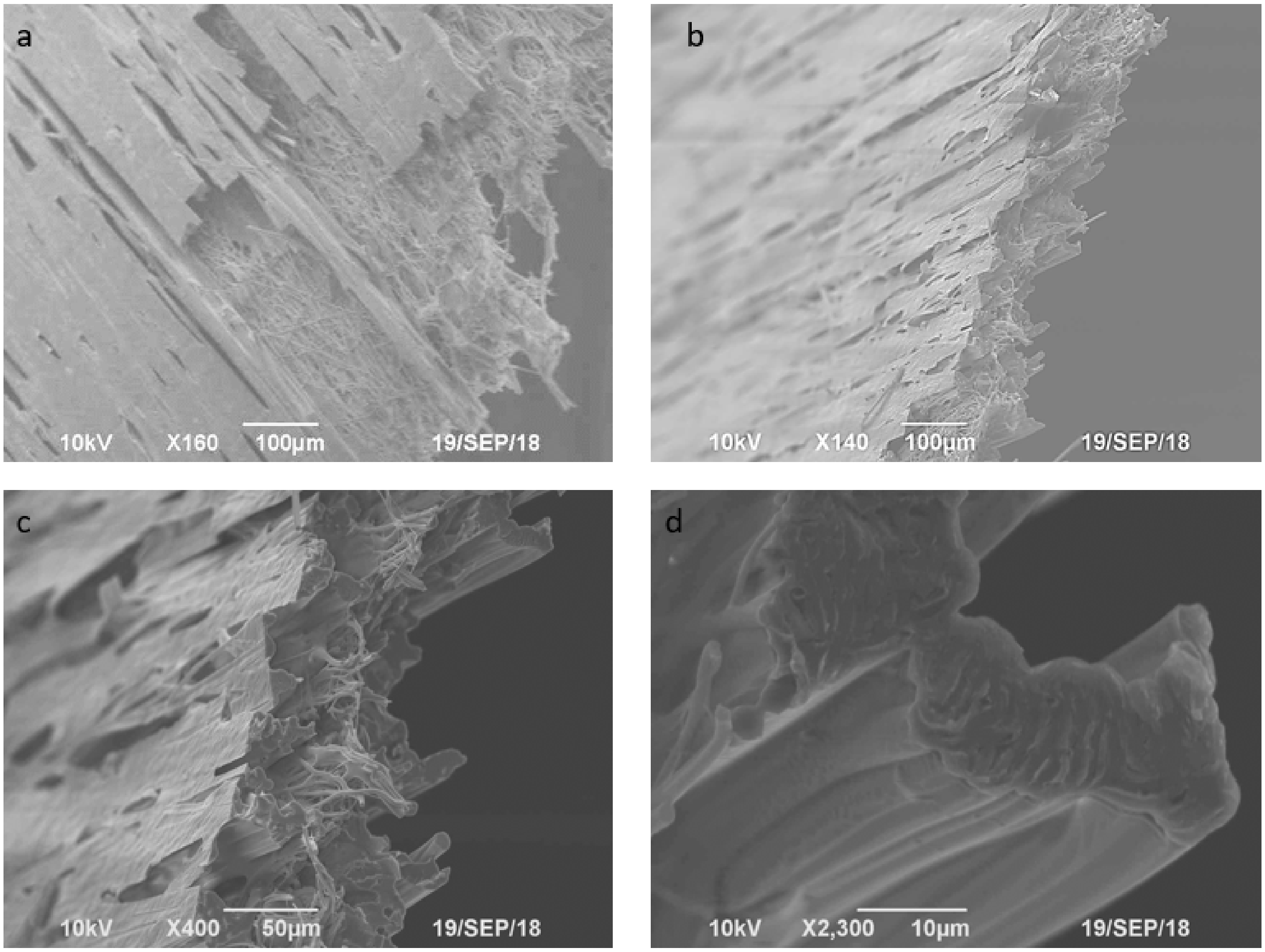

Figure 2-17: SEM micrographs of electrospun trilayer of anisotropic poly(methyl methacrylate) 15wt. % sol. concentration and Pellethane fibers. The large fibers are the poly(methyl methacrylate) fibers. Image (d) shows a solid fiber morphology of the poly(methyl methacrylate).

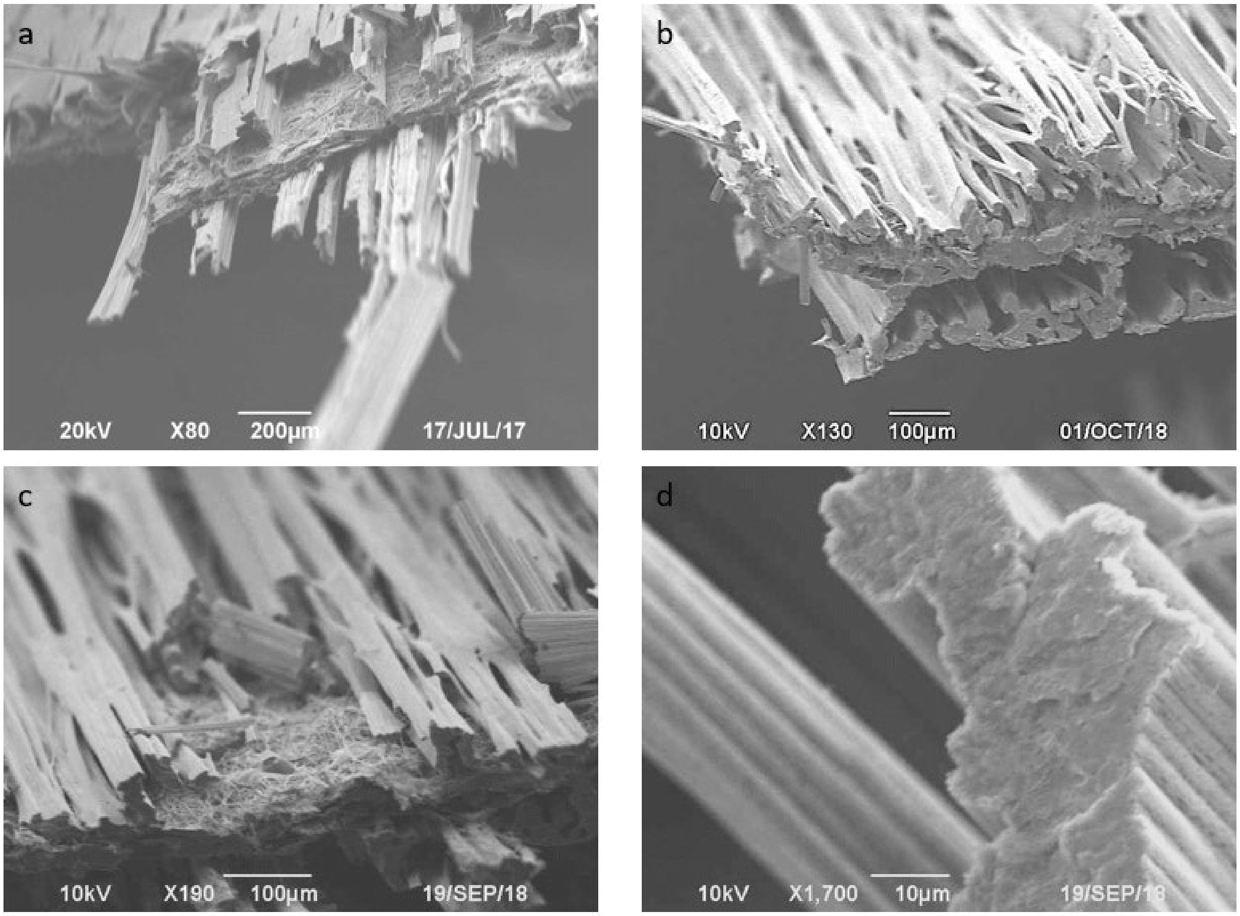

Figure 2-18: SEM micrographs of electrospun trilayer of anisotropic poly(methyl methacrylate) 20wt. % sol. concentration and Pellethane fibers. The large fibers are the poly(methyl methacrylate) fibers. Image (d) shows a solid fiber morphology of the poly(methyl methacrylate).

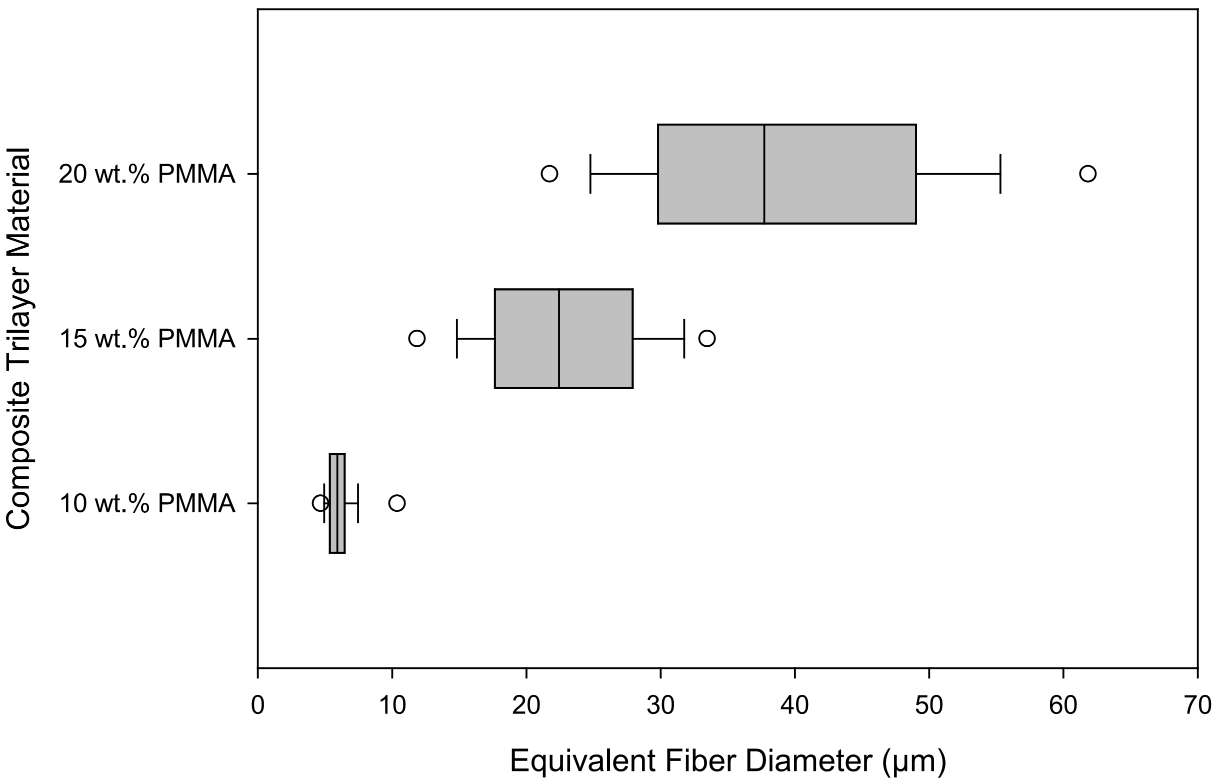

Figure 2-19: Box and whisker plot of the equivalent fiber diameter as measured using scanning electron microscopy and the distribution of poly(methyl methacrylate) fiber size difference as a function of the solution wt. %.

Table 2-7: Average fiber diameter of the poly(methyl methacrylate) fibers on the trilayer composites as a function of poly(methyl methacrylate) sol. concentration. Unpaired t-test analysis shows that there is statistical difference between the means of the groups compared, with h = 1.

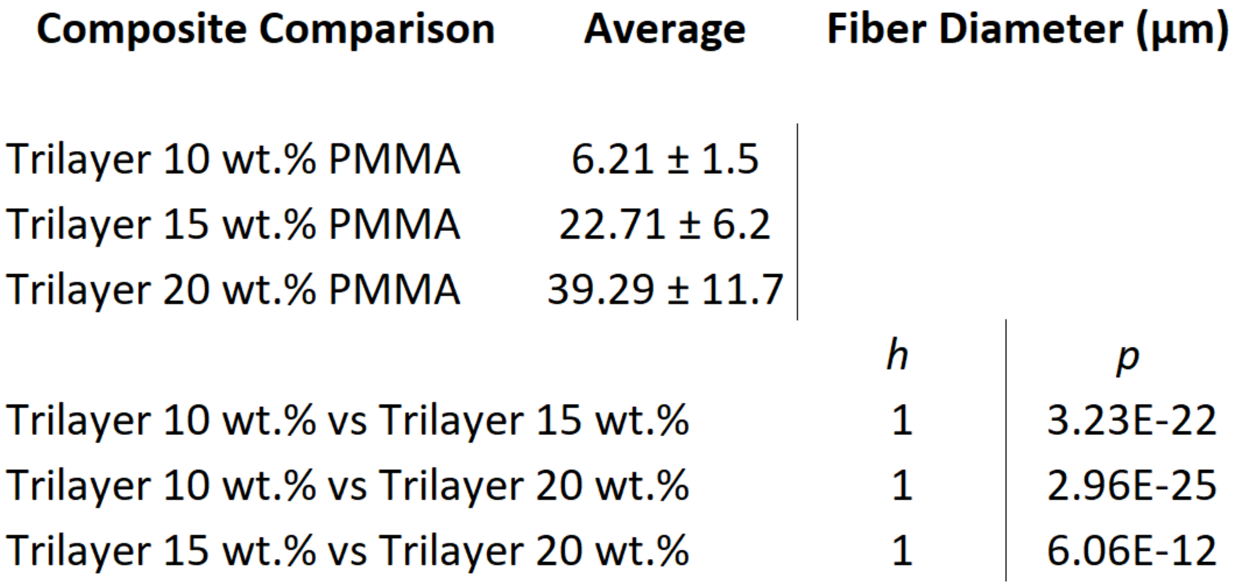

Composite Comparison	Average Fiber Diameter (μm)		
Trilayer 10 wt.% PMMA	6.21 ± 1.5		
Trilayer 15 wt.% PMMA	22.71 ± 6.2		
Trilayer 20 wt.% PMMA	39.29 ± 11.7		
		h	*p*
Trilayer 10 wt.% vs Trilayer 15 wt.%		1	3.23E-22
Trilayer 10 wt.% vs Trilayer 20 wt.%		1	2.96E-25
Trilayer 15 wt.% vs Trilayer 20 wt.%		1	6.06E-12

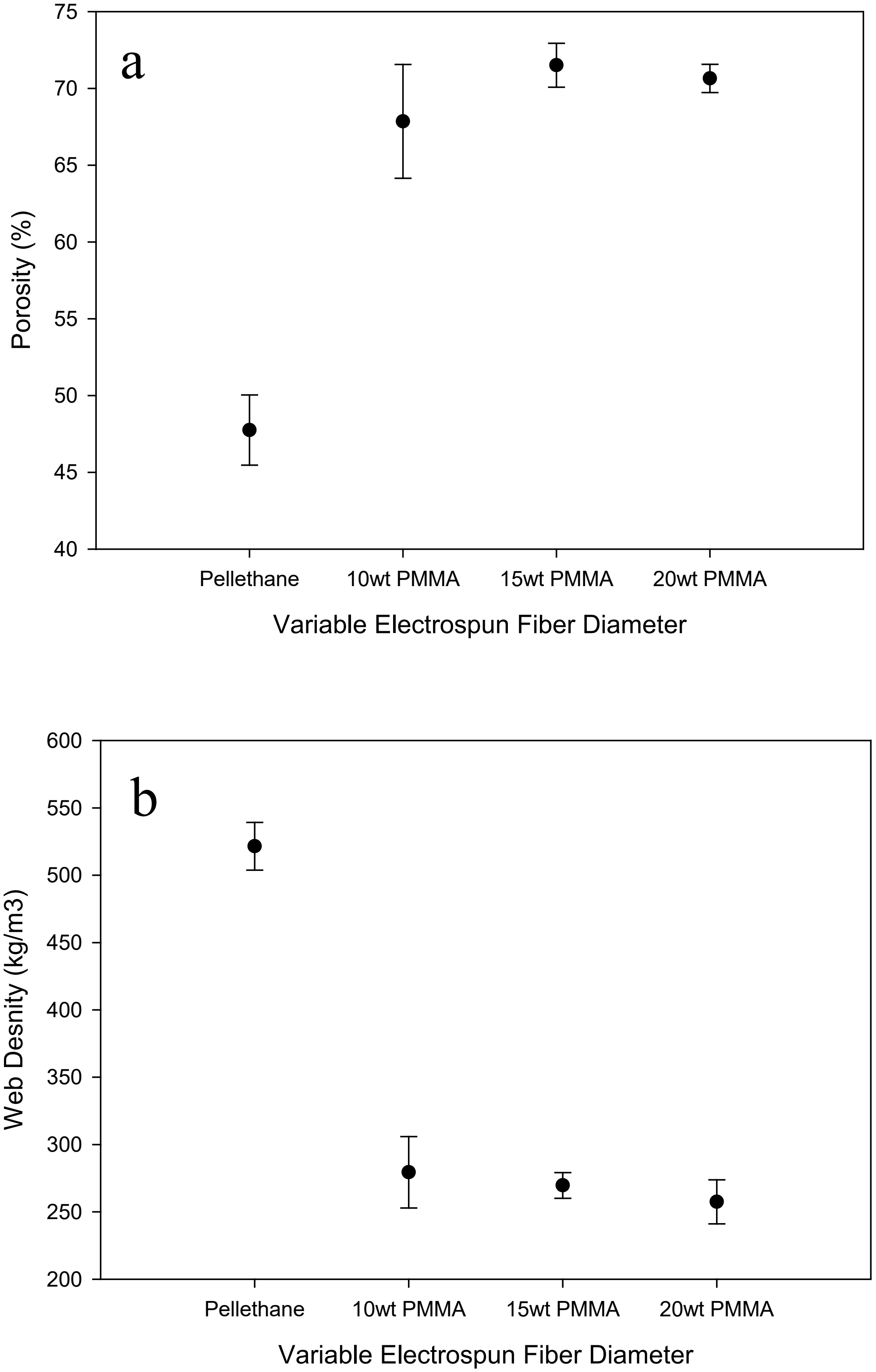

Figure 2-20: Plot of porosity (a) and web density (b) as a function of pure electrospun fiber.

Table 2-8: Unpaired t-test analysis comparing the solution densities of poly(methyl methacrylate) to each other as well as comparing each to pure electrospun Pellethane.

Pure Material Comparison	**Porosity (%)**		**Web Density (kg/m^3)**	
	h	*p*	*h*	*p*
10 wt.% PMMA vs 15 wt.% PMMA	0	0.3400	0	0.6653
10 wt.% PMMA vs 20 wt.% PMMA	0	0.5405	0	0.3858
15 wt.% PMMA vs 20 wt.% PMMA	0	0.6455	0	0.1390
Pellethane vs 10 wt. % PMMA	1	0.0086	1	0.0110
Pellethane vs 15 wt. % PMMA	1	0.0071	1	0.0009
Pellethane vs 15 wt.% PMMA	1	0.0225	1	0.0020

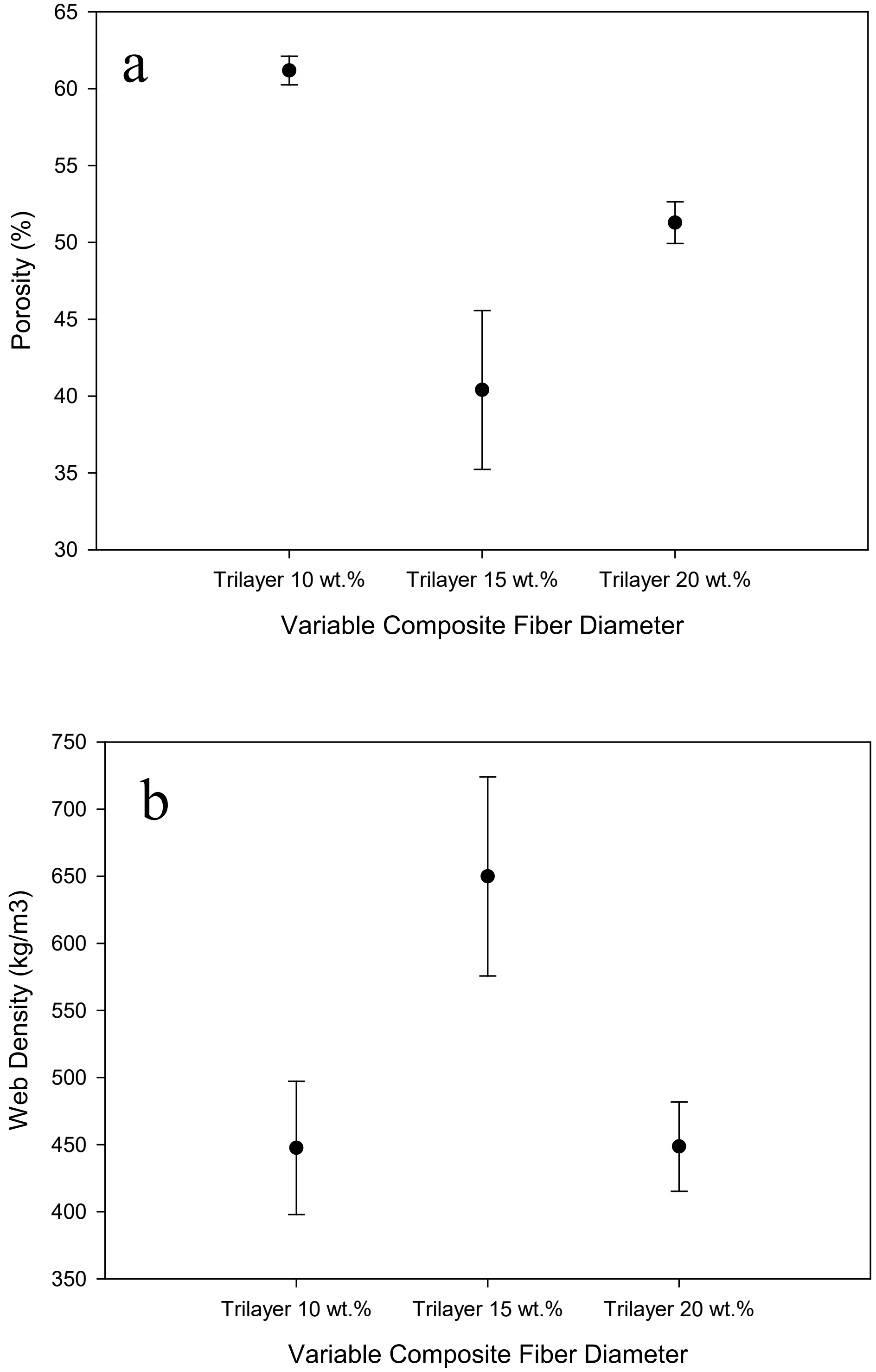

Figure 2-21: Plot of porosity (a) and web density (b) as a function of electrospun trilayers with varying poly(methyl methacrylate) sol. concentration.

Table 2-9: Unpaired t-test analysis comparing porosity and web density of the trilayer composites with varying solution densities of poly(methyl methacrylate) to each other. Statistically significant difference h = 1.

Composite Comparison	**Porosity (%)**		**Web Density (kg/m^3)**	
	h	*p*	*h*	*p*
Trilayer 10 wt.% vs Trilayer 15 wt.%	1	0.0271	0	0.0985
Trilayer 10 wt.% vs Trilayer 20 wt.%	1	0.0007	0	0.9840
Trilayer 15 wt.% vs Trilayer 20 wt.%	0	0.1007	1	0.0443

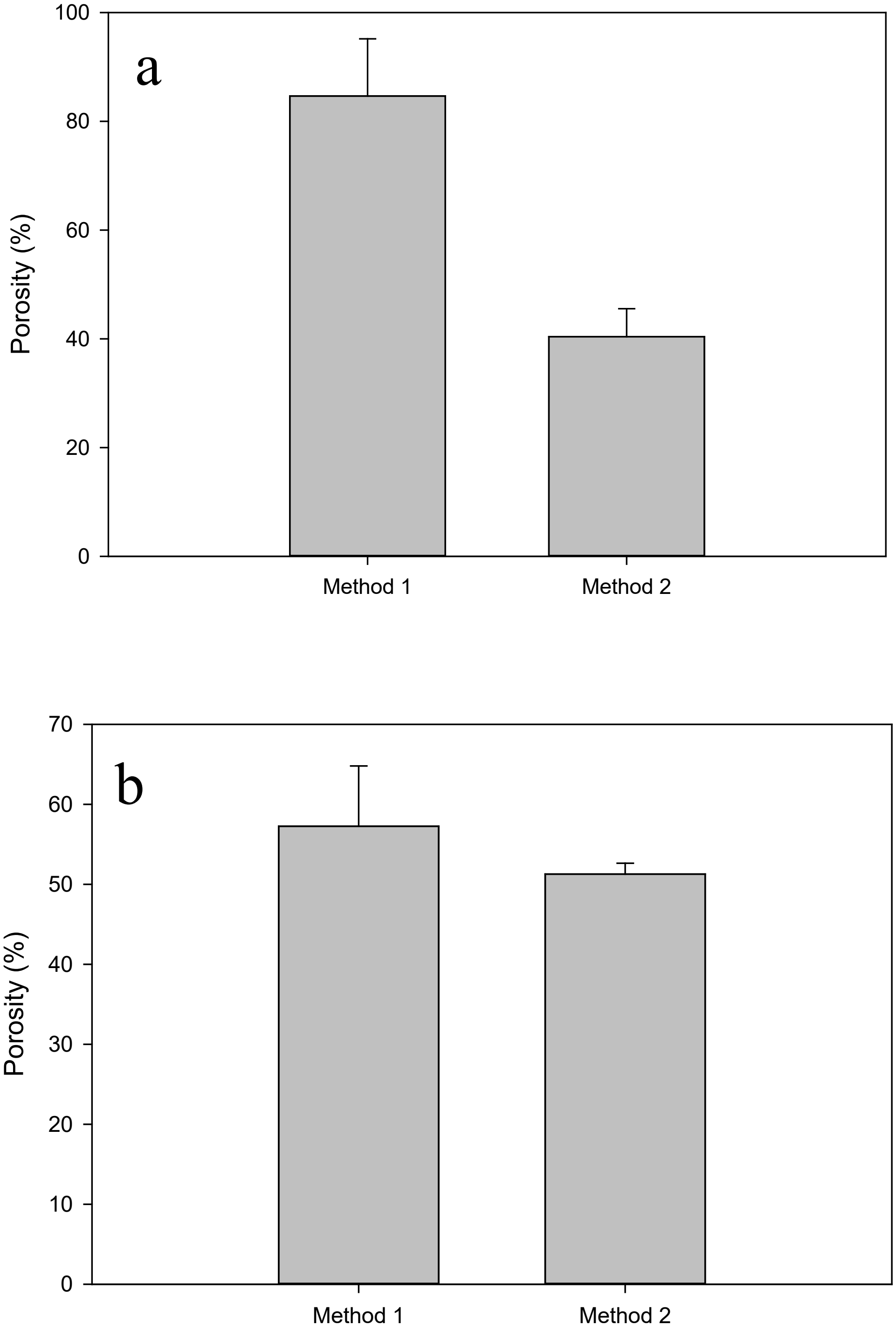

Figure 2-22: Bar charts of the measured apparent porosity (method 1) and porosity (method 2) for (a) trilayer of 15wt. % solution concentration of poly(methyl methacrylate) and (b) trilayer of 20wt. % solution concentration of poly (methyl methacrylate Pellethane.

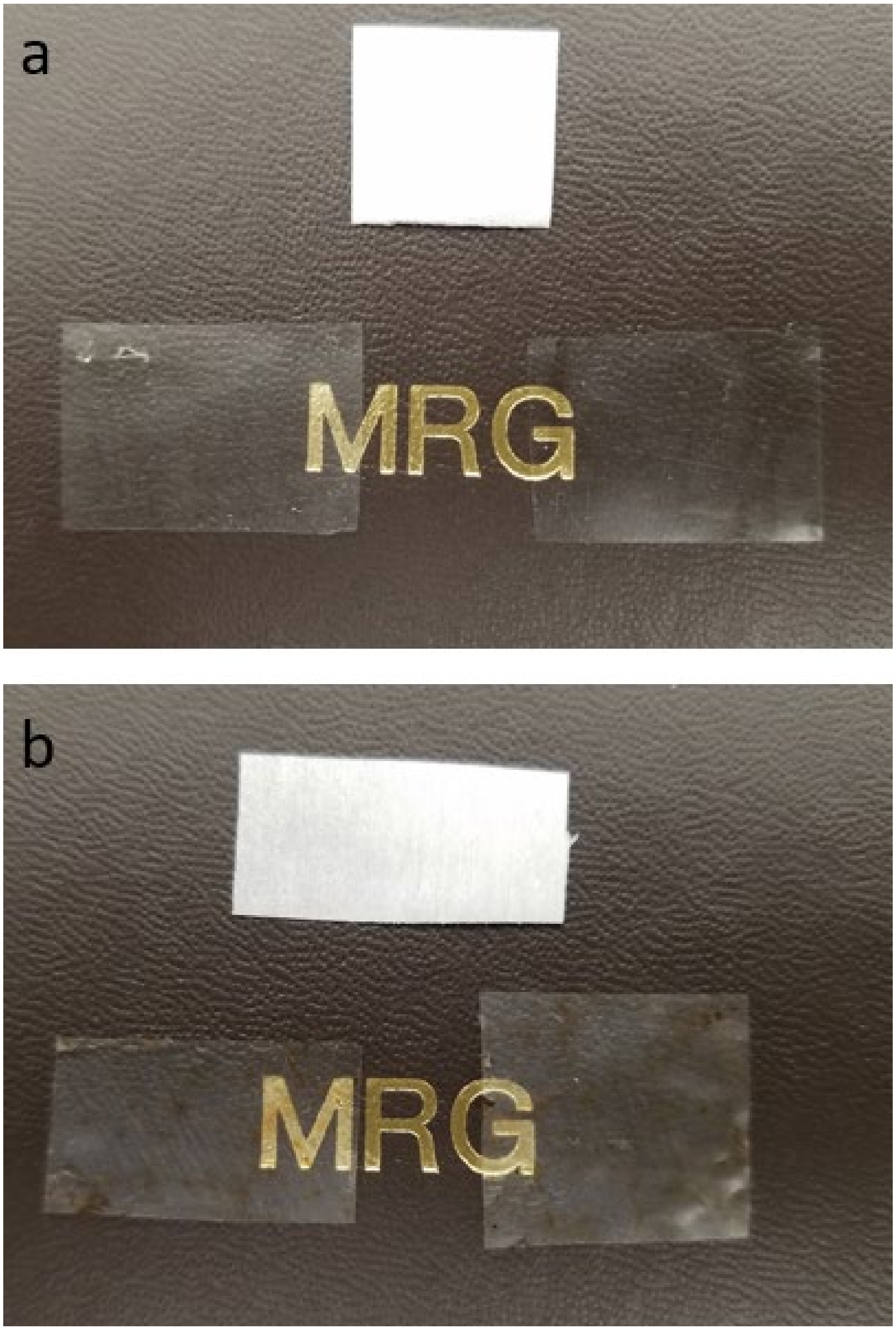

Figure 2-23: Representative images showing the change in physical appearance between the as spun fiber sheet (top) and the melted film (bottom) for (a) trilayer of 15wt. % solution concentration of poly(methyl methacrylate) and (b) trilayer of 20wt. % solution concentration of poly (methyl methacrylate Pellethane.

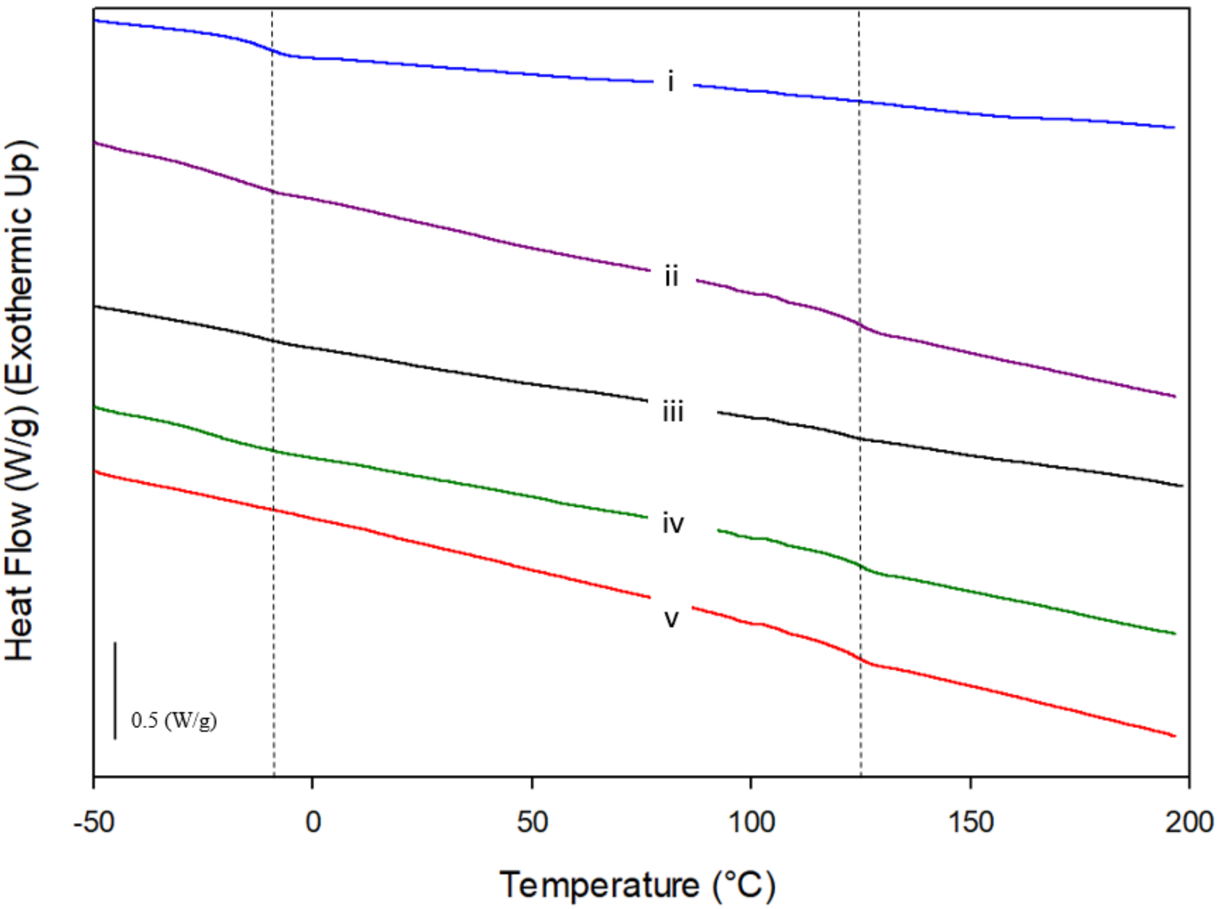

Figure 2-24: DSC of the second heat for electrospun (i) Pellethane, (ii) 10 wt. % solution concentration trilayer, (iii) 15 wt. % solution concentration trilayer, (iv) 20 wt. % solution concentration trilayer and (v) electrospun poly(methyl methacrylate). The measured glass transition temperatures (T_g) for Pellethane is -10 °C and 125°C for poly(methyl methacrylate). Pellethane is a thermoplastic elastomer and has a small melt peak around 155 °C.

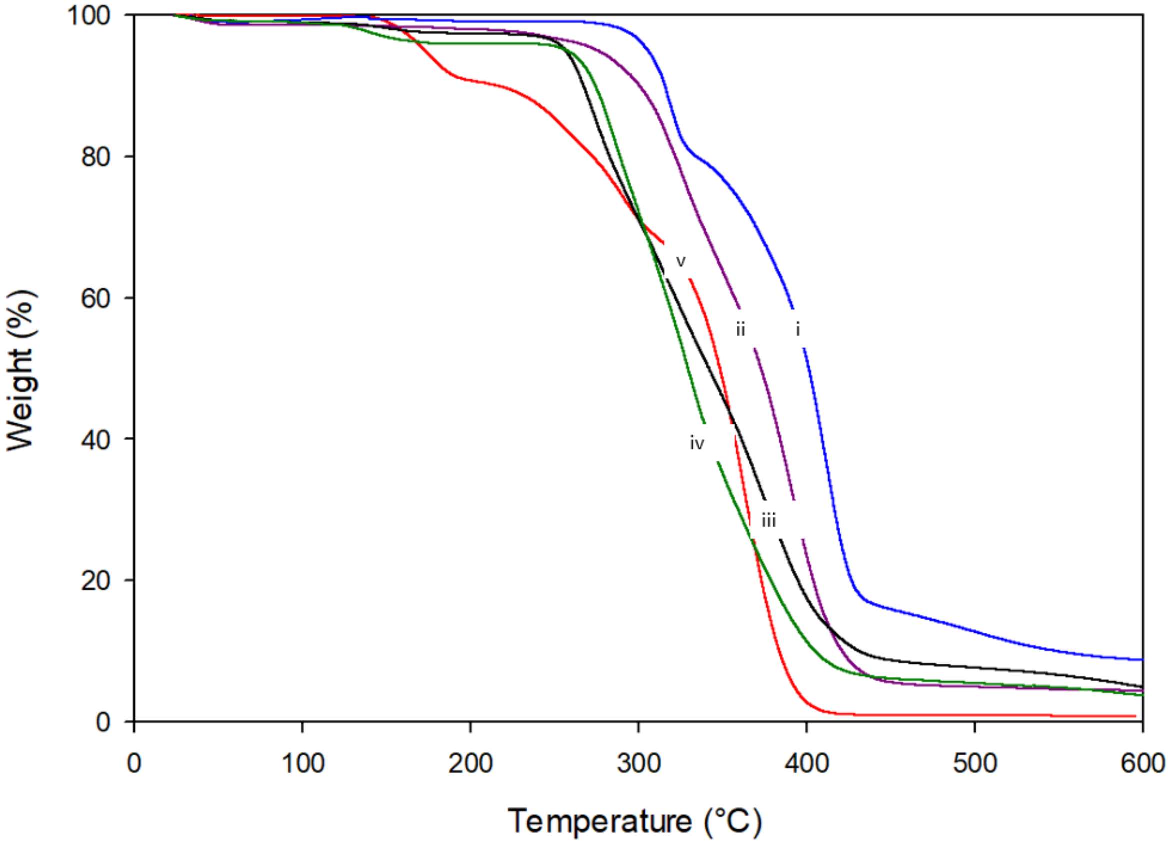

Figure 2-25: TGA of mass loss as a function of temperature for the (i) Pellethane, (ii) 10 wt. % solution concentration trilayer, (iii) 15 wt. % solution concentration trilayer, (iv) 20 wt. % solution concentration trilayer and (v) electrospun poly(methyl methacrylate).

Table 2-10: Char yield of trilayer composites in relation to the amount of and sol. concentration of poly(methyl methacrylate) and Pellethane present based on TGA and DSC analysis.

Sample Name	PMMA Amount (%)	Pellethane Amount (%)	Char Yield (%)
PMMA	100	0	0.72
10 wt.% Trilayer	27.01	72.99	4.18
15 wt.% Trilayer	31.22	68.78	4.85
20 wt.% Trilayer	29.31	70.69	3.65
Pellethane	0	100	8.13

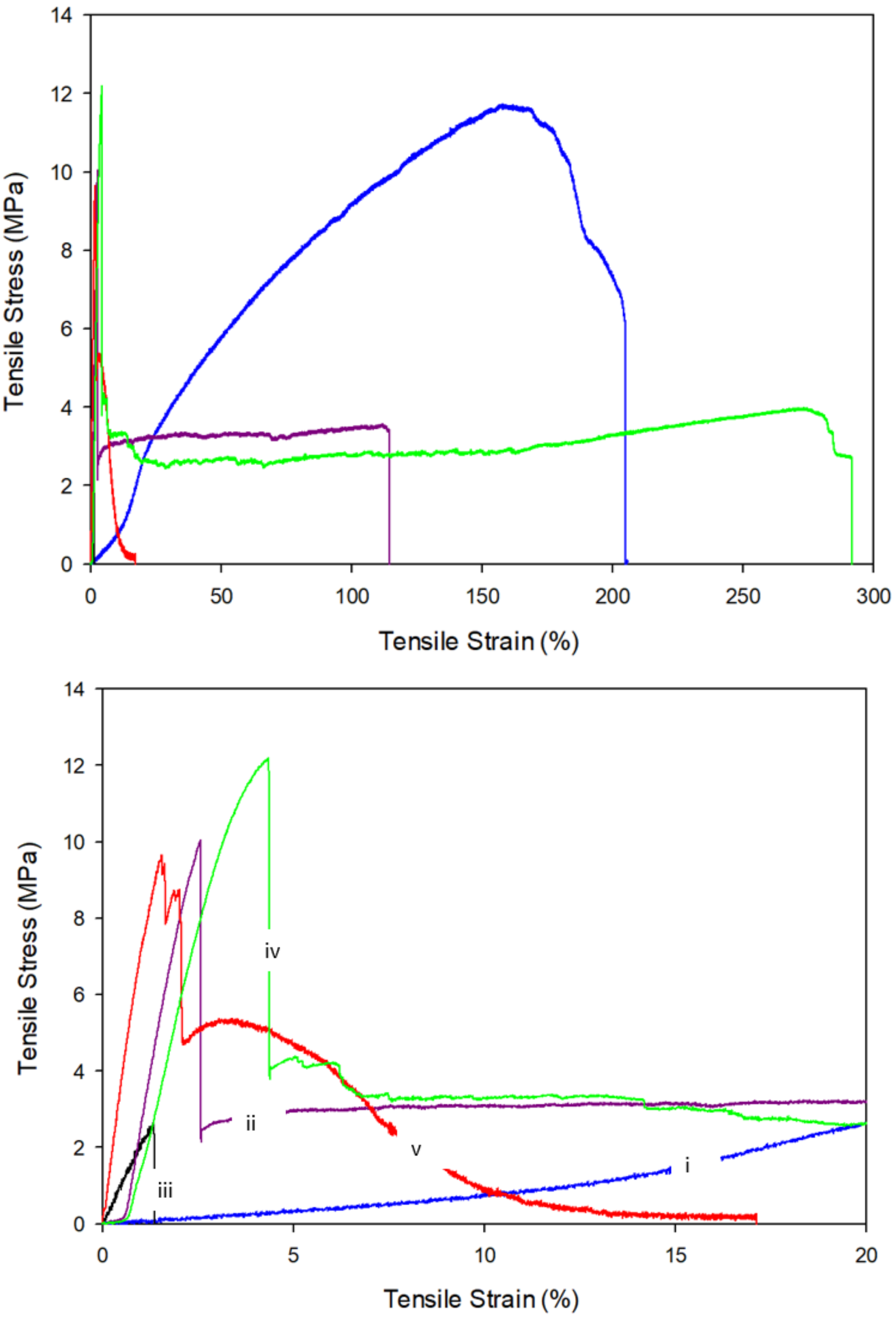

Figure 2-26: Representative stress strain curves (top) and magnified view of the elastic deformation (bottom) for (i) Pellethane, (ii) 10 wt. % solution concentration trilayer, (iii) 15 wt. % solution concentration trilayer, (iv) 20 wt. % solution concentration trilayer and (v) electrospun poly(methyl methacrylate). All samples are θ = 0° with n of 5.

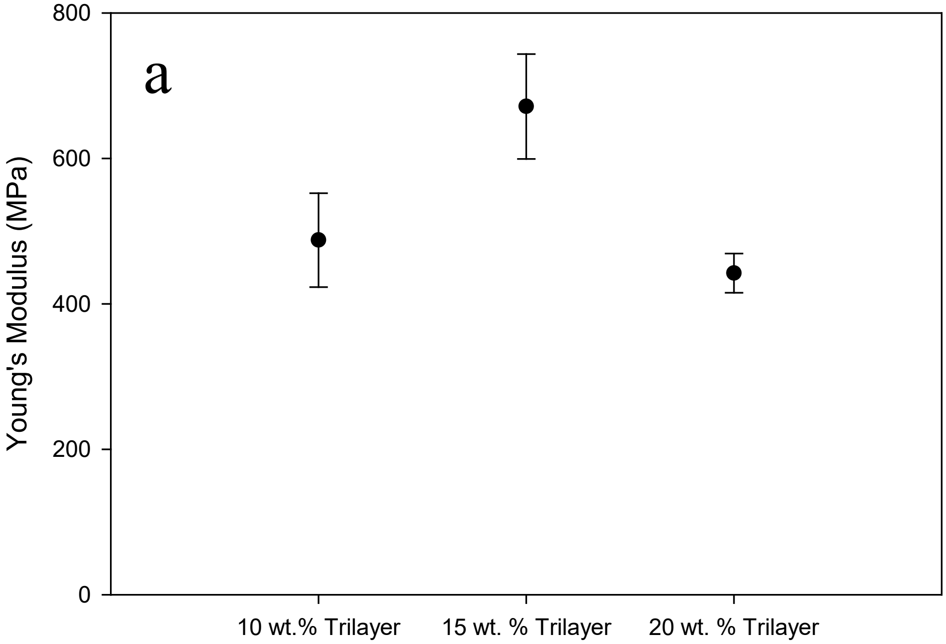
a
Young's Modulus (MPa)
0
200
400
600
800
10 wt.% Trilayer
15 wt. % Trilayer
20 wt. % Trilayer

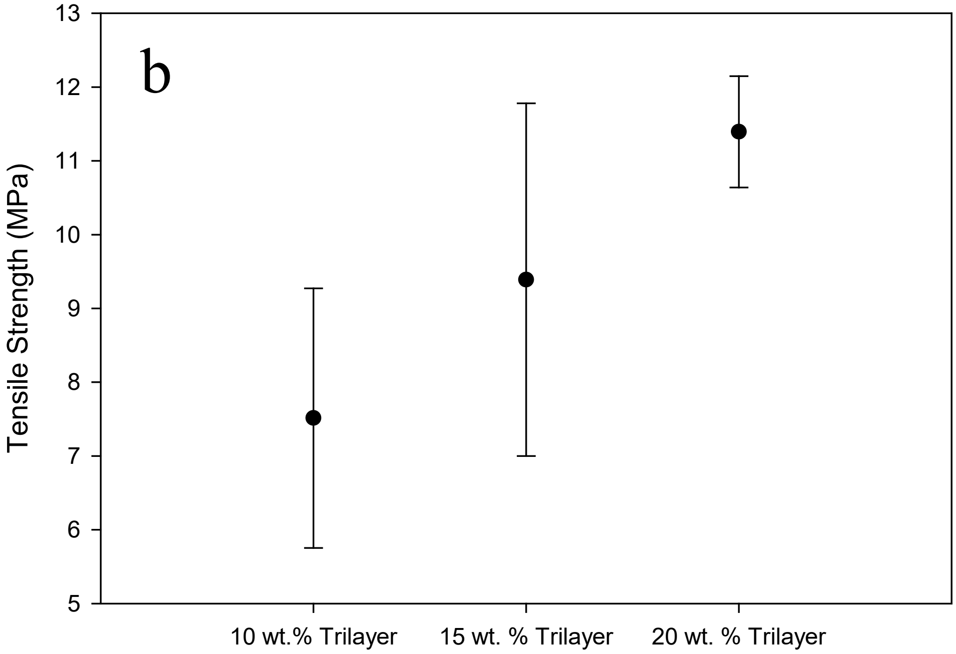
b
Tensile Strength (MPa)
5
6
7
8
9
10
11
12
13
10 wt.% Trilayer
15 wt. % Trilayer
20 wt. % Trilayer

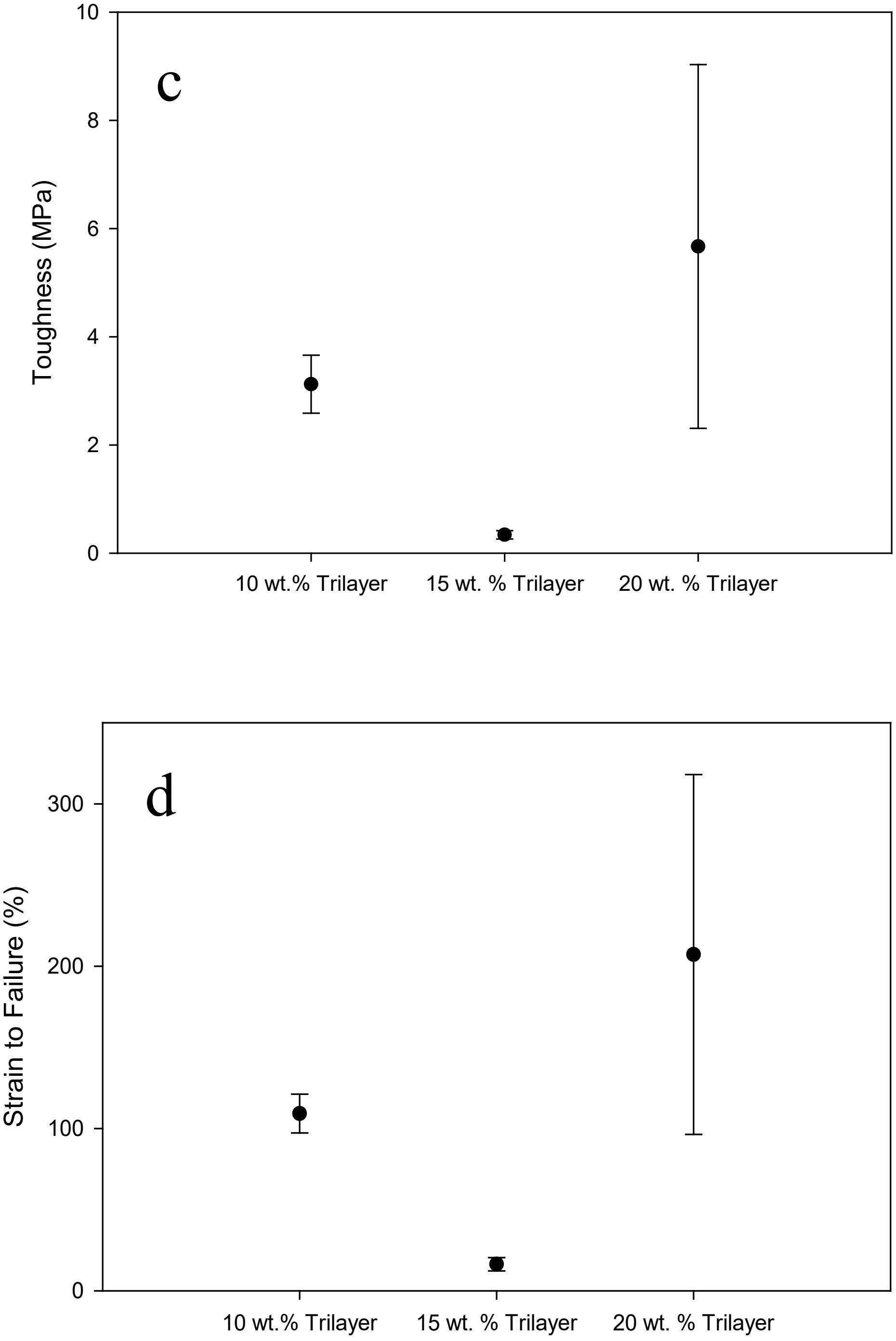

Figure 2-27: Summation of mechanical properties of the trilayer samples obtained through interpretation of the stress-strain curves for all samples with the fiber orientation angle θ = 0°. (a) Young's modulus, (b) tensile strength, (c) toughness, (d) magnified view of toughness, (e) strain-to-failure and (f) magnified view of strain-to-failure. All data points are an average of n = 5.

Table 2-11: Unpaired t-test analysis comparing mechanical properties obtained through tensile testing of the trilayer composites with varying solution densities of poly(methyl methacrylate) to each other for θ = 0°. Statistically significant difference h = 1.

	Trilayer 10wt.% vs Trilayer 20wt.%	
	h	*p*
Young's Modulus (MPa)	0	0.5579
Tensile Strength (MPa)	1	0.0081
Toughness (MPa)	0	0.2323
Strain to Failure (%)	0	0.1924

Composite Comparison	**Tensile Strength (MPa)**	
	h	*p*
Trilayer 10wt.% vs Trilayer 15wt.%	0	0.148
Trilayer 15wt.% vs Trilayer 20wt.%	0	0.1226

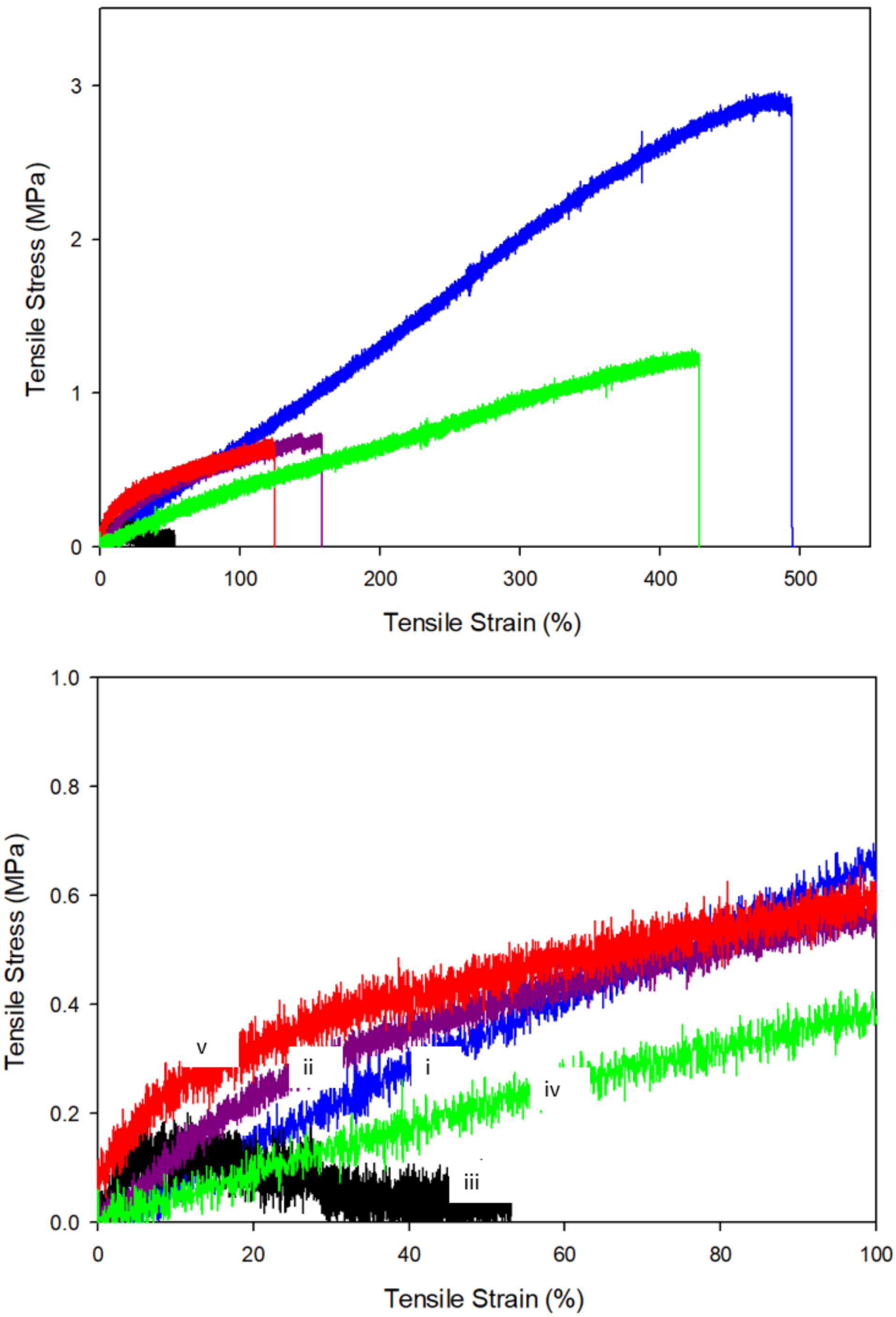

Figure 2-28: Representative stress strain curves (top) and magnified view of the elastic deformation (bottom) for (i) Pellethane, (ii) 10 wt. % solution concentration trilayer, (iii) 15 wt. % solution concentration trilayer, (iv) 20 wt. % solution concentration trilayer and (v) electrospun poly(methyl methacrylate). Noise of the samples in the magnified view is due to the sensitivity limitation of the Instron force gauge. All samples are θ = 90° with n of 5.

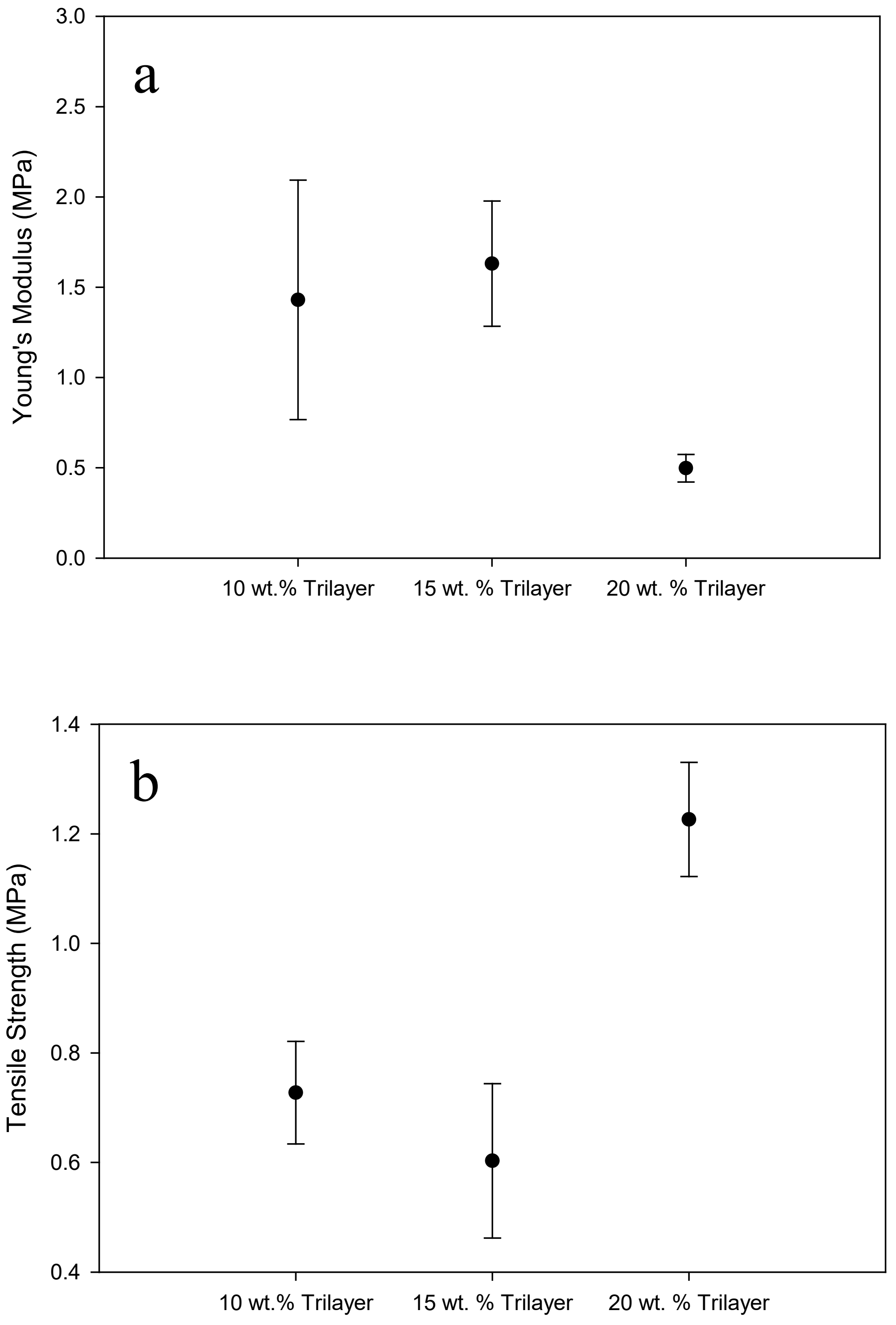
a
Young's Modulus (MPa)
3.0
2.5
2.0
1.5
1.0
0.5
0.0
10 wt.% Trilayer
15 wt. % Trilayer
20 wt. % Trilayer
b
Tensile Strength (MPa)
1.4
1.2
1.0
0.8
0.6
0.4
10 wt.% Trilayer
15 wt. % Trilayer
20 wt. % Trilayer

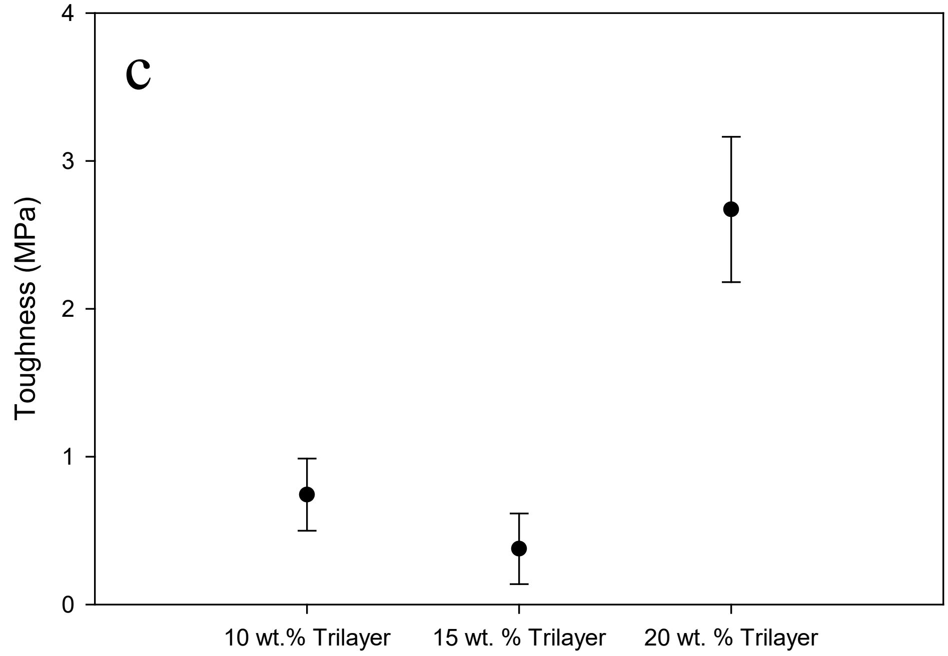

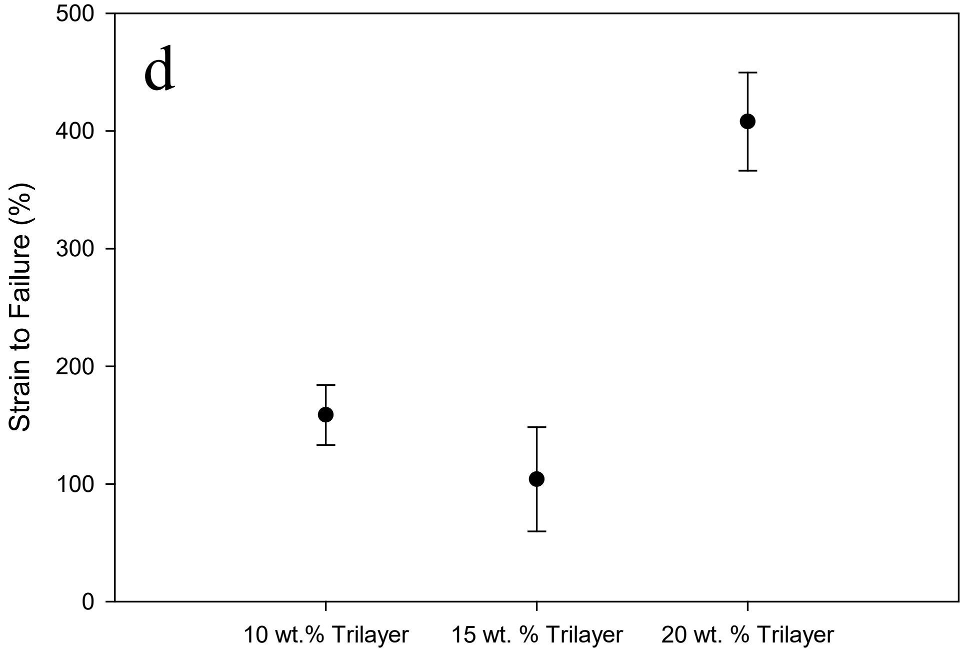

Figure 2-29: Summation of mechanical properties of the trilayer samples obtained through interpretation of the stress-strain curves for all samples with the fiber orientation angle θ = 90°. (a) Young's modulus, (b) tensile strength, (c) toughness, (d) magnified view of toughness, (e) strain-to-failure and (f) magnified view of strain-to-failure. All data points are an average of n = 5.

Table 2-12: Unpaired t-test analysis comparing mechanical properties obtained through tensile testing of the trilayer composites with varying solution densities of poly(methyl methacrylate) to each other for θ = 90°. Statistically significant difference h = 1.

	Trilayer 10wt.% vs Trilayer 15wt.%	
	h	*p*
Young's Modulus (MPa)	0	0.6445
Tensile Strength (MPa)	0	0.1728
Toughness (MPa)	1	0.0440
Strain to Failure (%)	0	0.0704

Table 2-13: Anisotropy of the electrospun fiber samples quantified as a function of Young's modulus in a ratio of the 0° / 90° fiber orientation angles obtained through interpreting the stress-strain curves.

Sample	Fiber Orientation Angle [°]	Young's Modulus [MPa]	Anisotropy
Pellethane	0	23.40	30.8
	90	0.76	
10 wt.% PMMA	0	197.62	42.7
	90	4.63	
15 wt.% PMMA	0	-	NA
	90	-	
20 wt.% PMMA	0	-	NA
	90	-	
Trilayer 10 wt.%	0	487.80	341.1
	90	1.43	
Trilayer 15 wt.%	0	671.54	412.0
	90	1.63	
Trilayer 20 wt.%	0	442.38	902.8
	90	0.49	

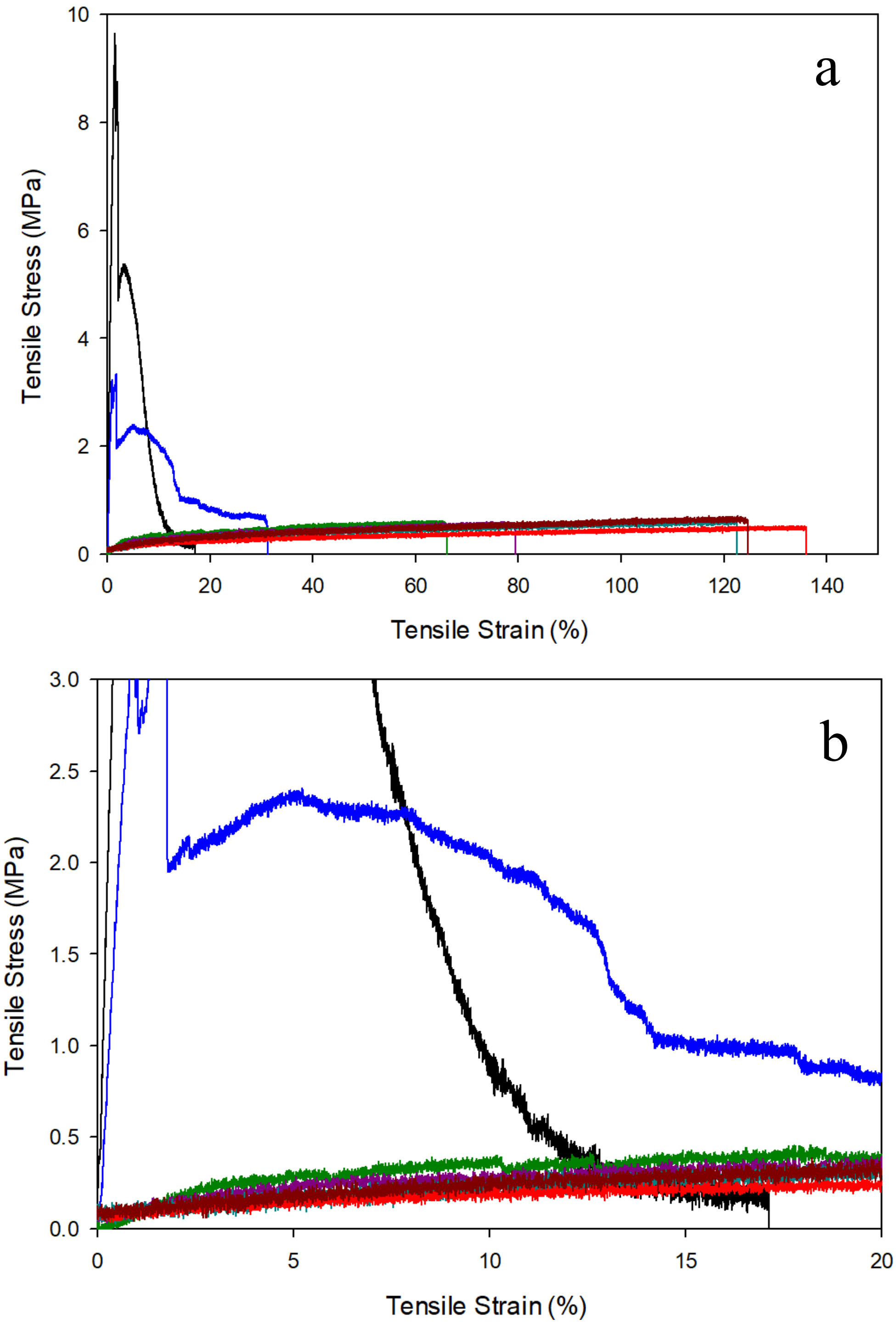
a
Tensile Stress (MPa)
0
2
4
6
8
10
Tensile Strain (%)
0
20
40
60
80
100
120
140
b
Tensile Stress (MPa)
0.0
0.5
1.0
1.5
2.0
2.5
3.0
Tensile Strain (%)
0
5
10
15
20

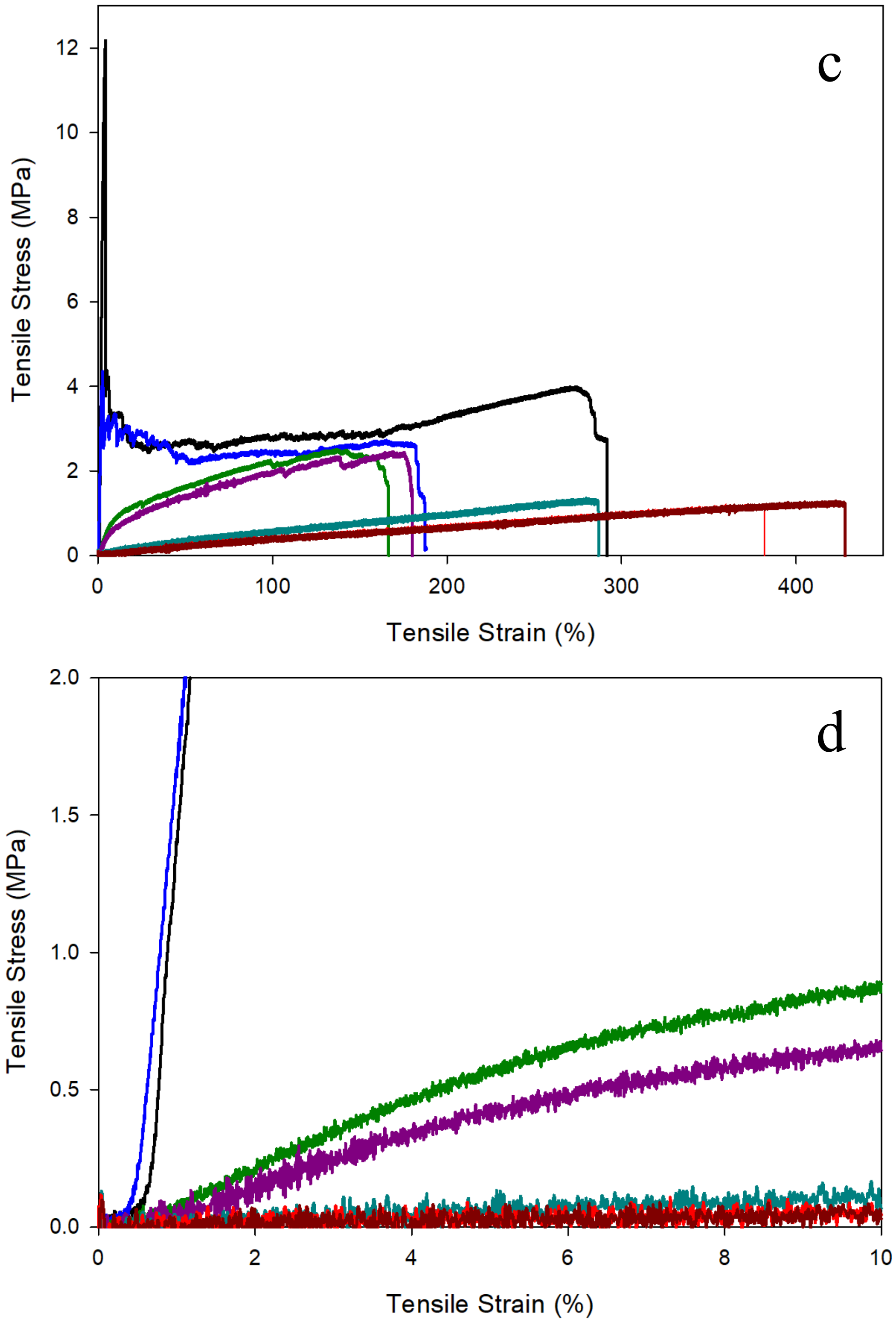

Figure 2-30: Representative stress-strain curves for (a) trilayer with 15wt. % solution concentration of poly(methyl methacrylate), (b) magnified view of trilayer with 15wt. % solution concentration of poly(methyl methacrylate), (c) trilayer with 20wt. % solution concentration of poly(methyl methacrylate) and (d) magnified view of trilayer with 20wt. % solution concentration of poly(methyl methacrylate).. Each graph shows seven distinct fiber orientation angles (Δθ) of 0° (black), 15° (blue), 30° (green) 45°(purple), 60° (turquoise), 75° (red) and 90° (brown). All sample curves are an average of n = 5.

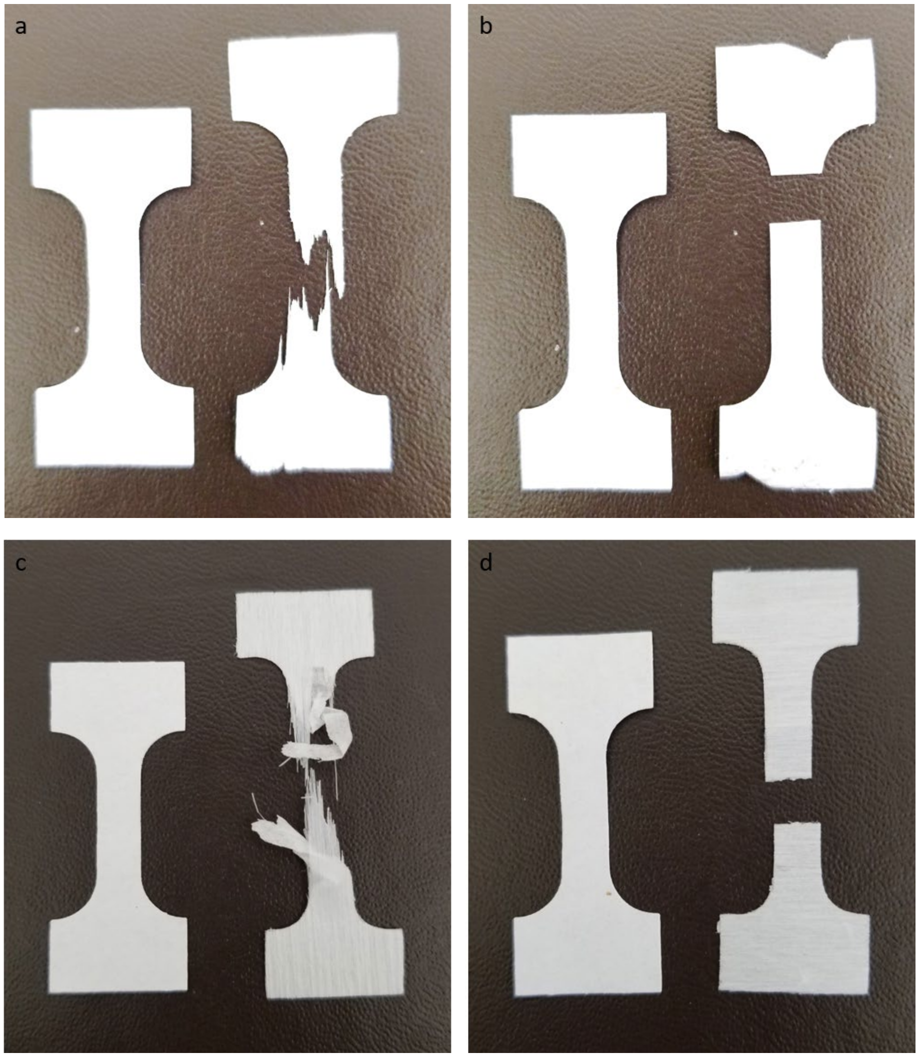

Figure 2-31: Representative post tensile tested dog bones (right) with pre tensile tested dog bones (left) for (a) trilayer with 15wt. % solution concentration of poly(methyl methacrylate) 0°, (b) trilayer with 15wt. % solution concentration of poly(methyl methacrylate) 90°, (c) trilayer with 20wt. % solution concentration of poly(methyl methacrylate) 0°, (d) trilayer with 20wt. % solution concentration of poly(methyl methacrylate) 90°.

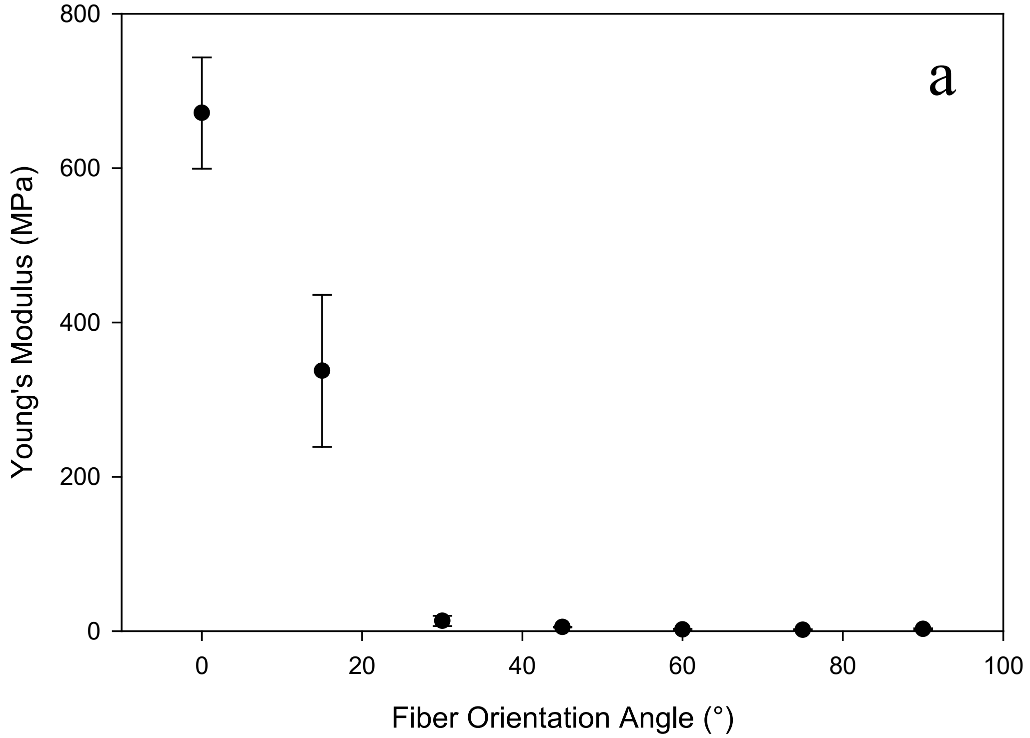
a
Young's Modulus (MPa)
0
200
400
600
800
Fiber Orientation Angle (°)
0
20
40
60
80
100

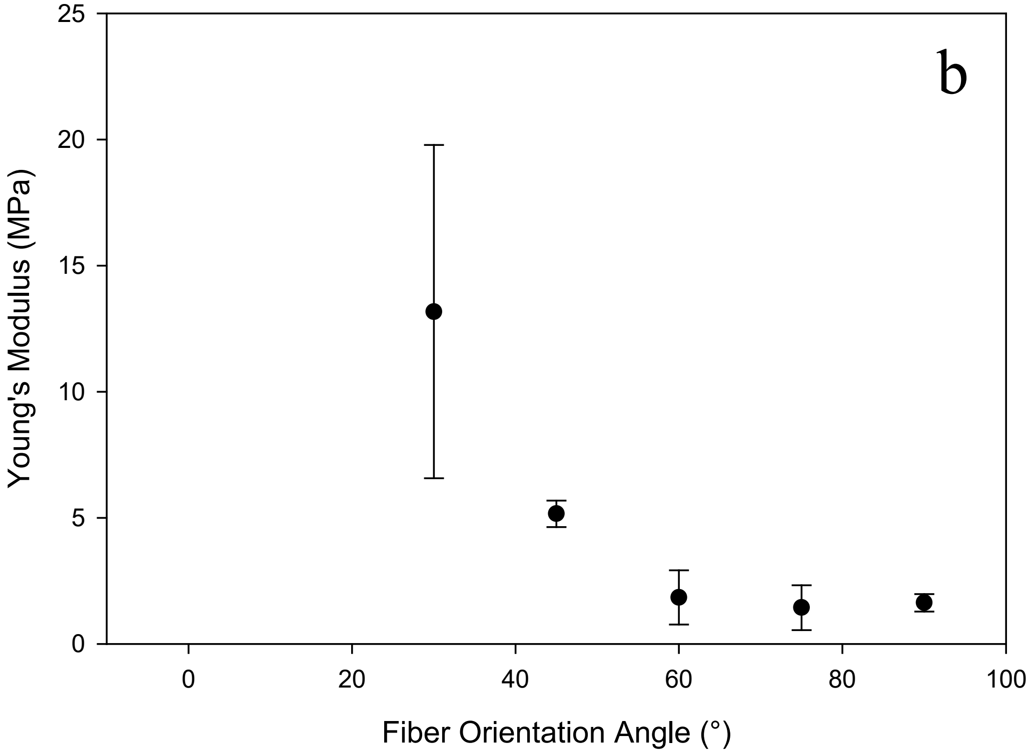
b
Young's Modulus (MPa)
0
5
10
15
20
25
Fiber Orientation Angle (°)
0
20
40
60
80
100

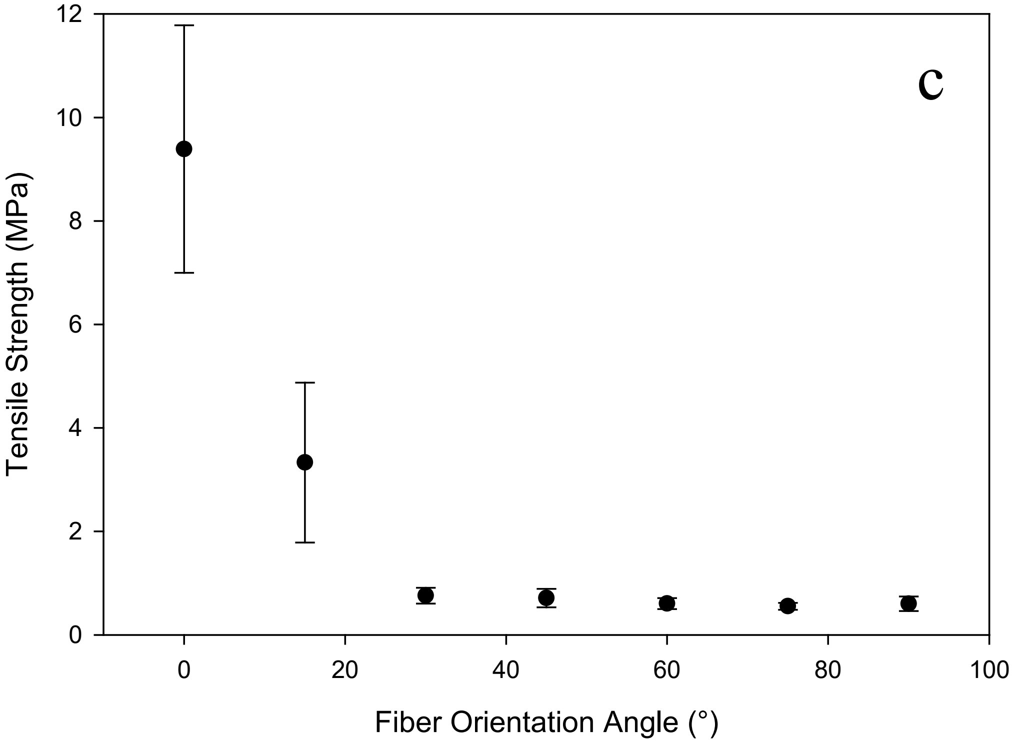
c
Tensile Strength (MPa)
0
2
4
6
8
10
12
0
20
40
60
80
100
Fiber Orientation Angle (°)

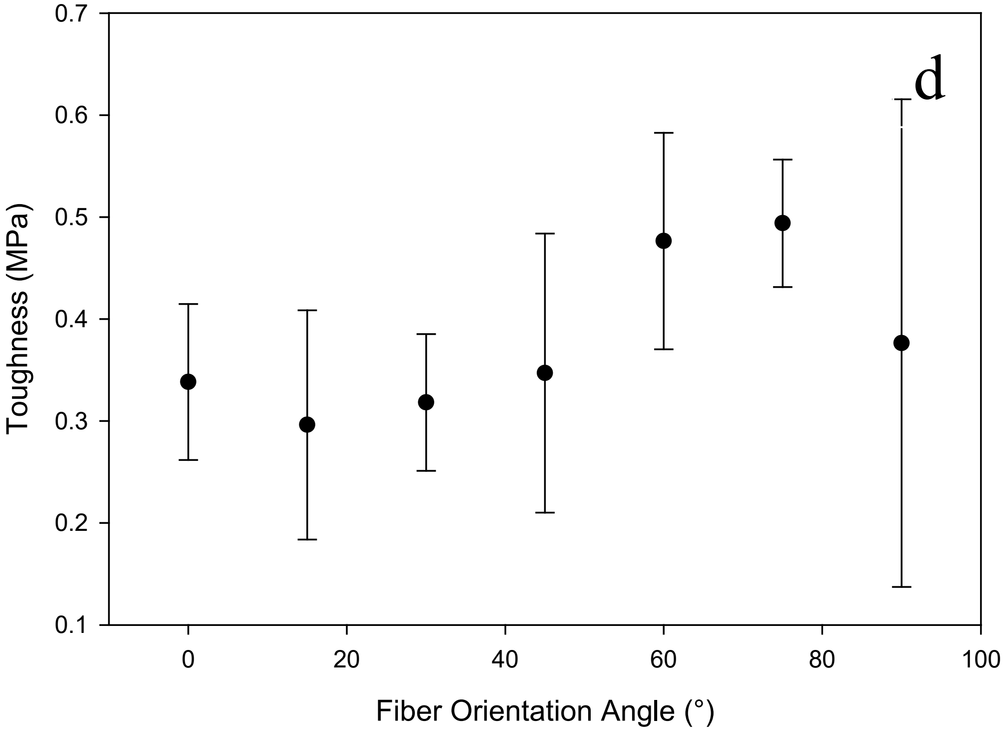
d
Toughness (MPa)
0.1
0.2
0.3
0.4
0.5
0.6
0.7
0
20
40
60
80
100
Fiber Orientation Angle (°)

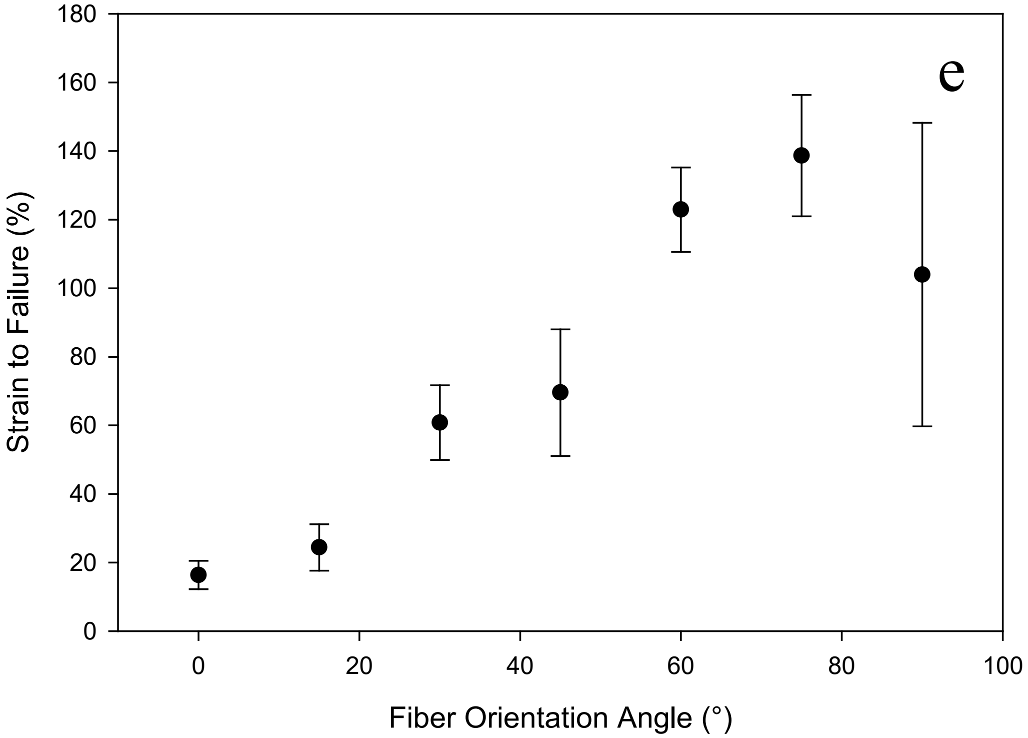

Figure 2-32: Resulting mechanical properties of electrospun trilayer of 15wt. % solution concentration of poly(methyl methacrylate) from tensile testing as a function of the fiber orientation angle. (a) Young's modulus, (b) magnified view of Young's modulus, (c) tensile strength, (d) toughness and (e) strain-to-failure. All data points are an average of n = 5.

Table 2-14: Average Young's modulus, toughness, tensile strength and strain to failure for all fiber orientation angles (Δθ) interpreted from the stress strain curves of the electrospun trilayer of 15wt. % solution concentration of poly(methyl methacrylate).

Material Property	**Fiber Orientation Angle [°]**						
	0	*15*	*30*	*45*	*60*	*75*	*90*
Young's Modulus [MPa]	671.54 ± 72.1	337.27 ± 98.6	13.18 ± 6.6	5.15 ± 0.5	1.84 ± 1.1	1.44 ± 0.9	1.63 ± 0.3
Toughness [MPa]	0.34 ± 0.08	0.29 ± 0.1	0.32 ± 0.07	0.35 ± 0.1	0.47 ± 0.1	0.49 ± 0.06	0.38 ± 0.2
Tensile Strength [MPa]	9.39 ± 2.4	3.33 ± 1.5	0.76 ± 0.2	0.71 ± 0.2	0.61 ± 0.1	0.55 ± 0.07	0.60 ± 0.1
Strain to Failure [%]	16.35 ± 4.1	24.38 ± 6.7	60.77 ± 10.9	69.55 ± 18.5	122.91 ± 12.3	138.68 ± 17.7	103.95 ± 44.3

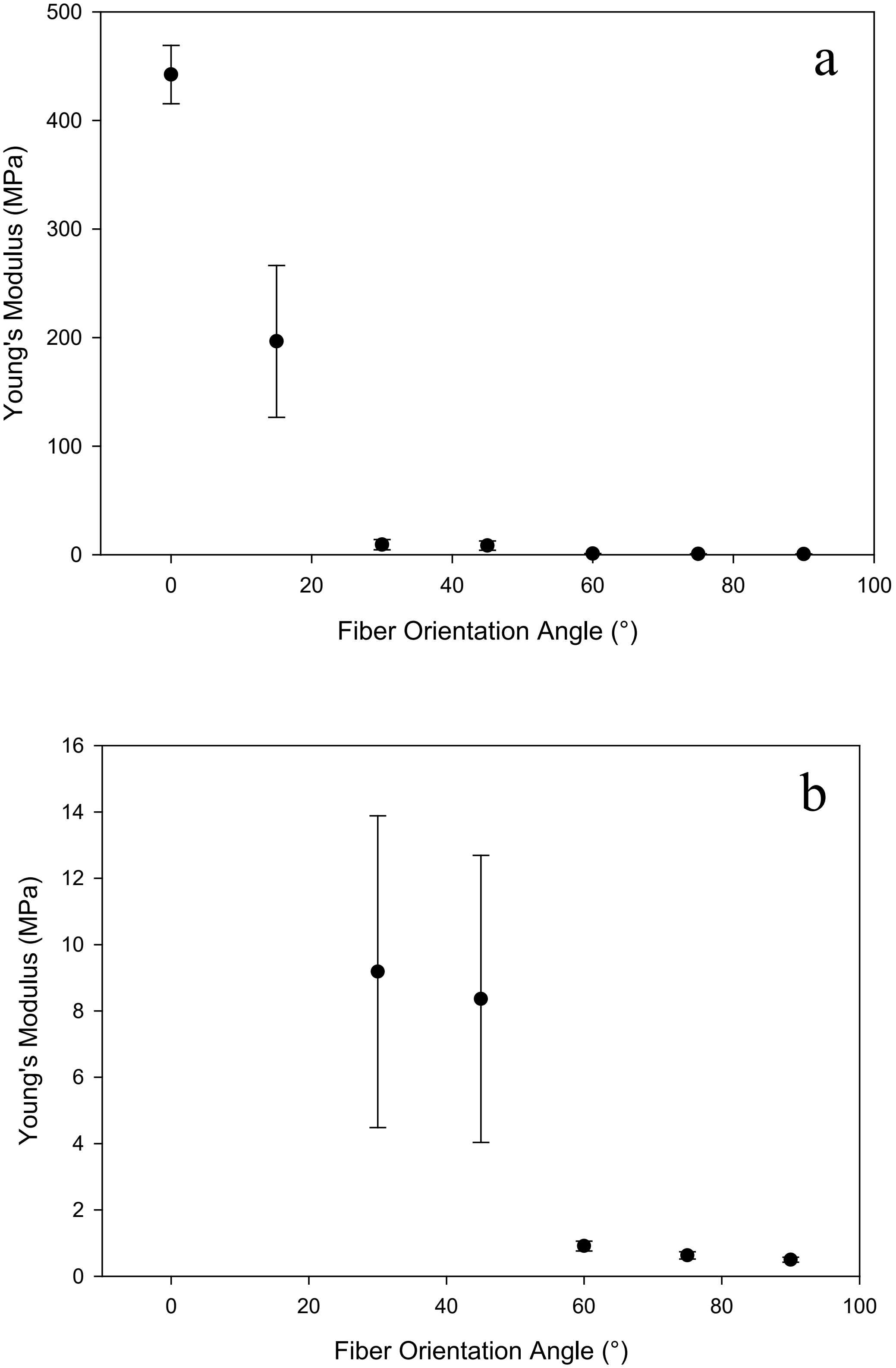
a
Young's Modulus (MPa)
500
400
300
200
100
0
0
20
40
60
80
100
Fiber Orientation Angle (°)
b
Young's Modulus (MPa)
16
14
12
10
8
6
4
2
0
0
20
40
60
80
100
Fiber Orientation Angle (°)

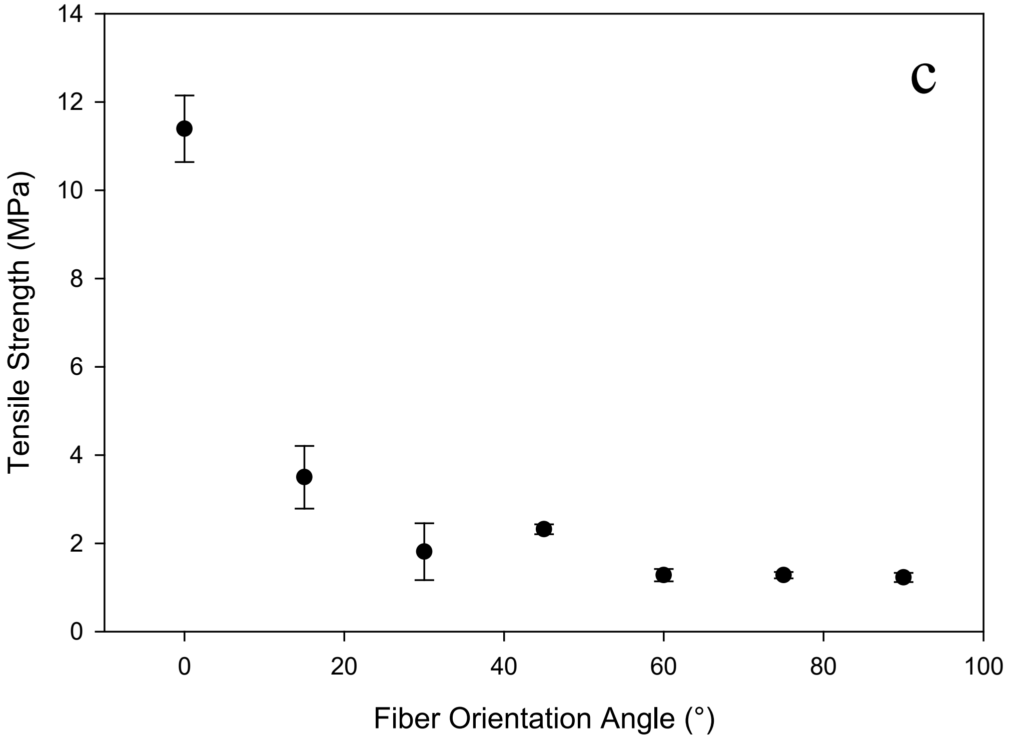
c
Tensile Strength (MPa)
0
2
4
6
8
10
12
14
Fiber Orientation Angle (°)
0
20
40
60
80
100

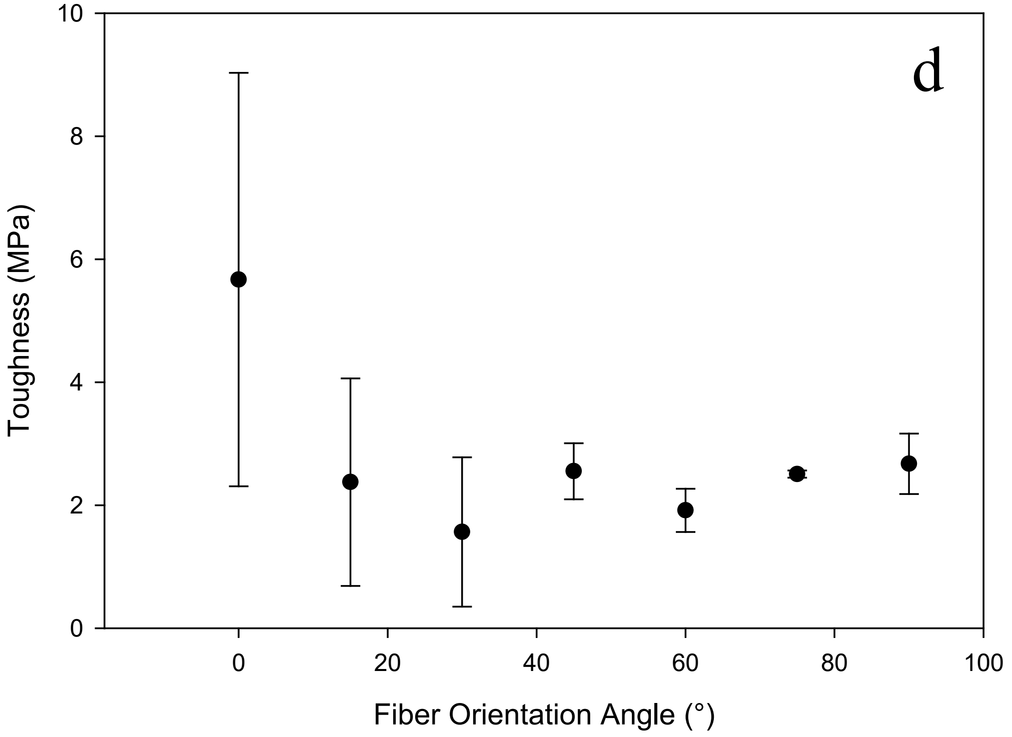
d
Toughness (MPa)
0
2
4
6
8
10
Fiber Orientation Angle (°)
0
20
40
60
80
100

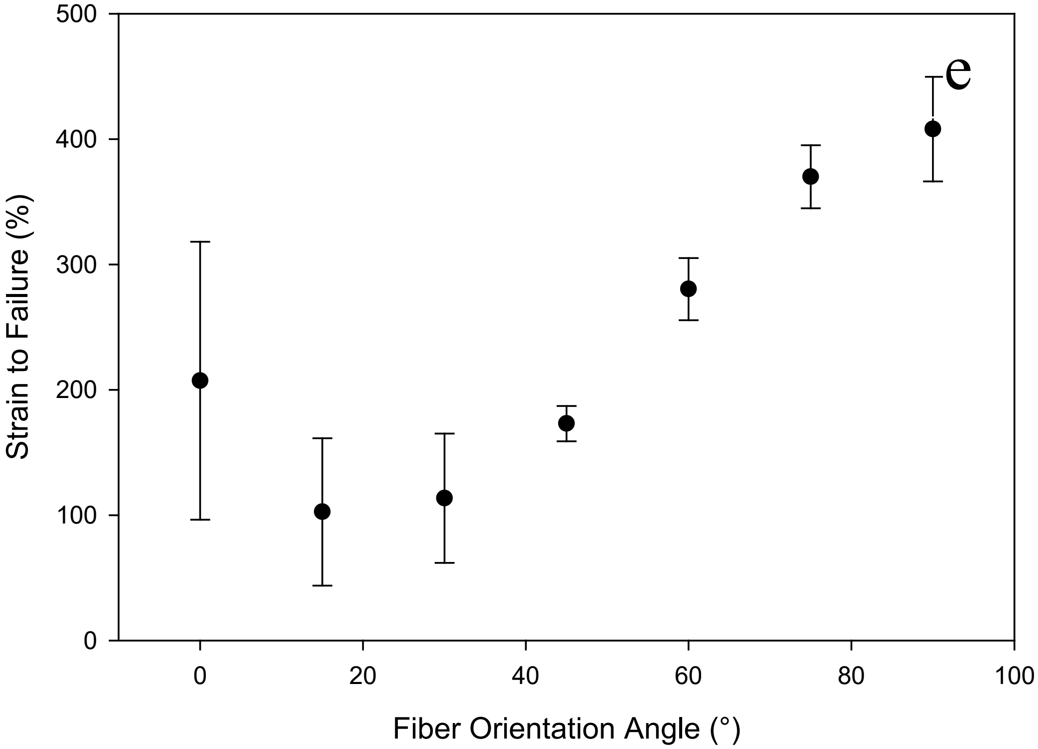

Figure 2-33: Resulting mechanical properties of electrospun trilayer of 20wt. % solution concentration of poly(methyl methacrylate) from tensile testing as a function of the fiber orientation angle. (a) Young's modulus, (b) magnified view of Young's modulus, (c) tensile strength, (d) toughness and (e) strain-to-failure. All data points are an average of n = 5.

Table 2-15: Average Young's modulus, toughness, tensile strength and strain to failure for all fiber orientation angles (Δθ) interpreted from the stress strain curves of the electrospun trilayer of 20wt. % solution concentration of poly(methyl methacrylate).

Material Property	**Fiber Orientation Angle [°]**						
	0	*15*	*30*	*45*	*60*	*75*	*90*
Young's Modulus [MPa]	442.38 ± 26.9	196.44 ± 70.0	9.19 ± 4.7	8.36 ± 4.3	0.91 ± 0.1	0.63 ± 0.1	0.49 ± 0.1
Toughness [MPa]	5.67 ± 3.4	2.37 ± 1.7	1.56 ± 1.2	2.55 ± 0.5	1.91 ± 0.3	2.50 ± 0.05	2.68 ± 0.5
Tensile Strength [MPa]	11.39 ± 0.8	3.50 ± 0.7	1.81 ± 0.6	2.32 ± 0.1	1.28 ± 0.4	1.28 ± 0.1	1.22 ± 0.1
Strain to Failure [%]	207.25 ± 110.9	102.58 ± 58.76	113.47 ± 51.6	173.04 ± 14.1	280.49 ± 24.8	370.10 ± 25.2	408.03 ± 41.7

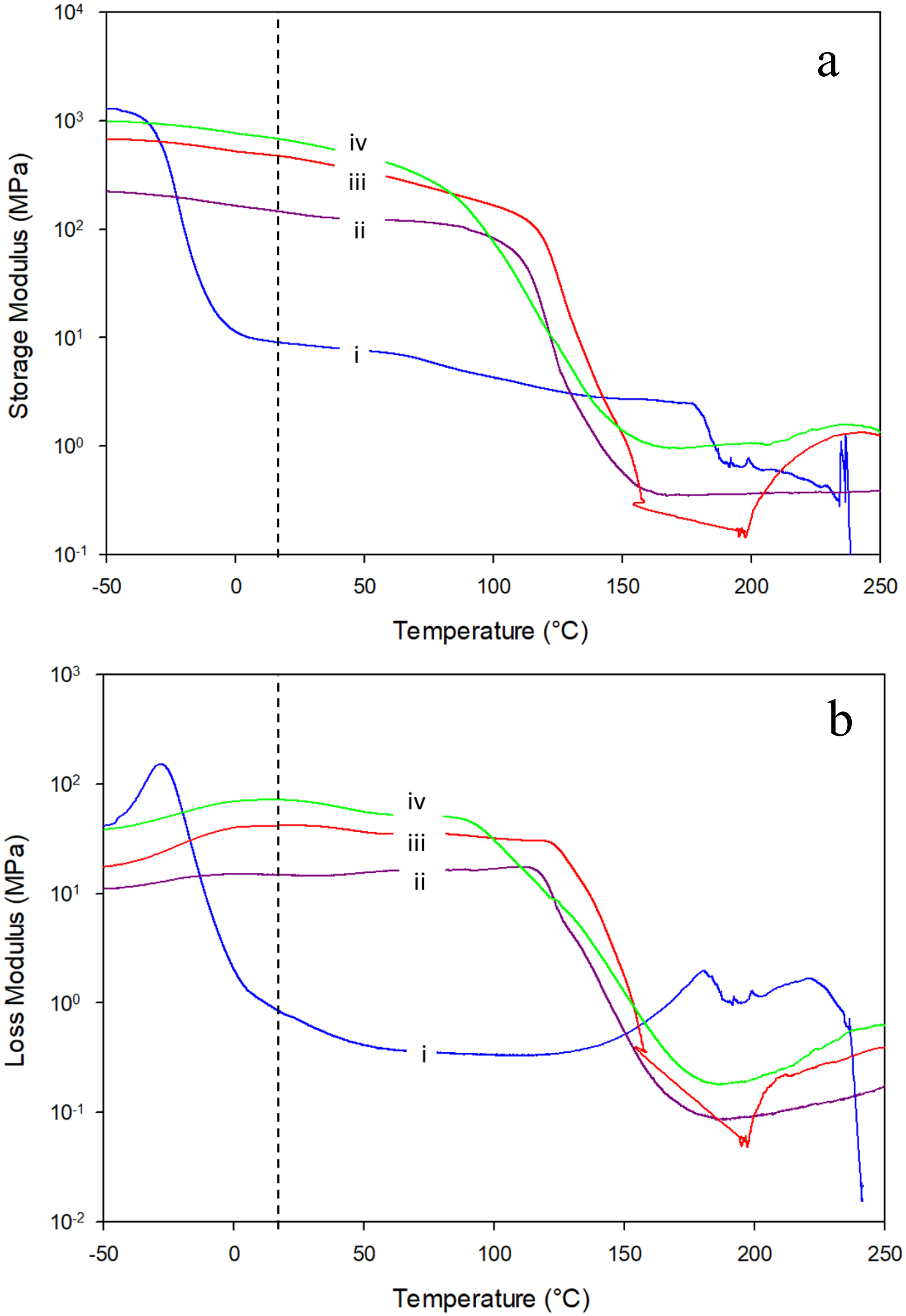
a
10^4
10^3
10^2
10^1
10^0
10^-1
Storage Modulus (MPa)
iv
iii
ii
i
-50
0
50
100
150
200
250
Temperature (°C)
b
10^3
10^2
10^1
10^0
10^-1
10^-2
Loss Modulus (MPa)
iv
iii
ii
i
-50
0
50
100
150
200
250
Temperature (°C)

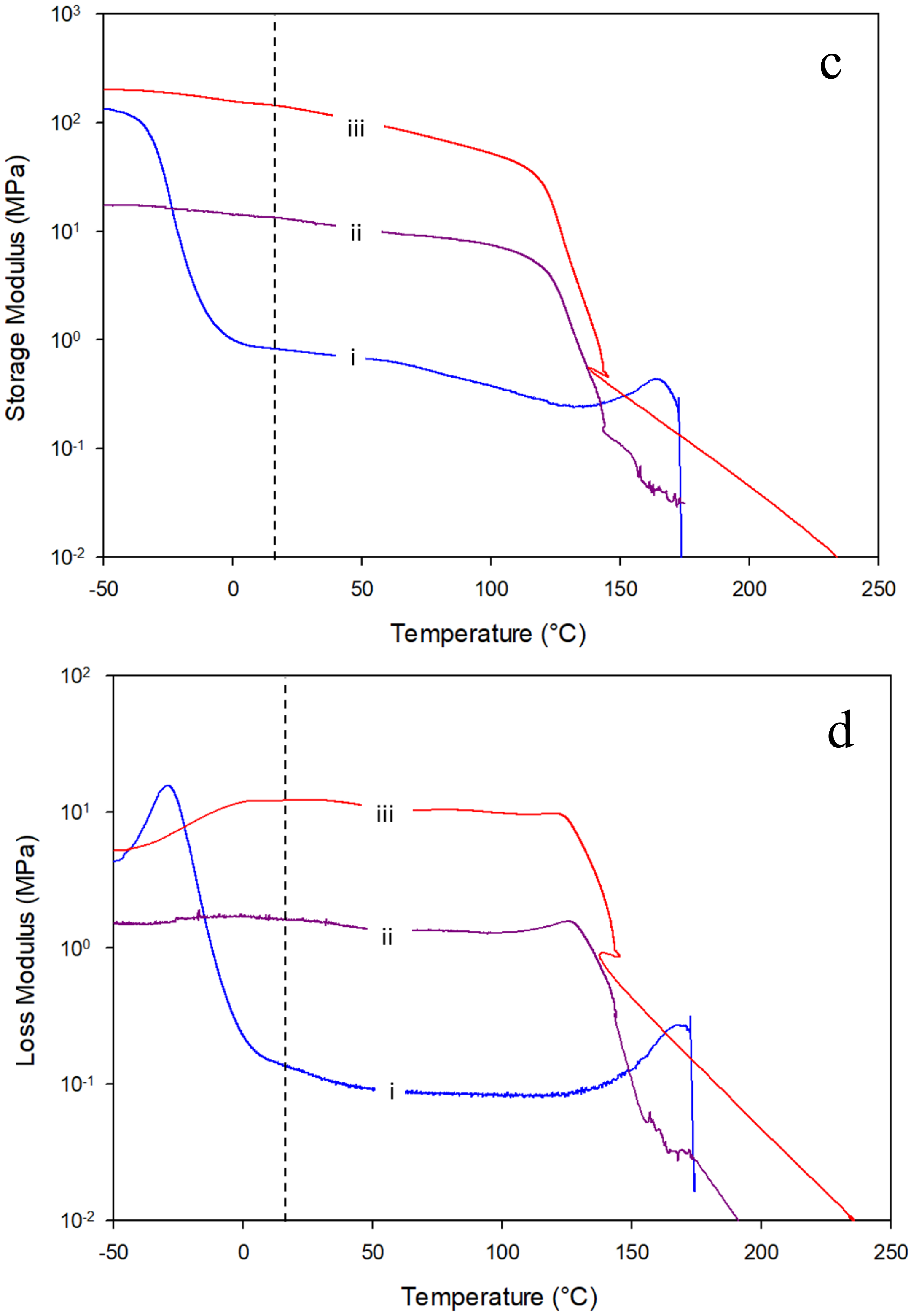

Figure 2-34: Dynamic mechanical analysis of (a) storage and (b) loss modulus for θ = 0° and (c) storage and (d) loss modulus for θ = 90° of electrospun (i) Pellethane, (ii) 10wt. % sol. concentration poly(methyl methacrylate), (iii) 15wt. % sol. concentration poly(methyl methacrylate) and (iv) 20wt. % sol. concentration poly(methyl methacrylate).

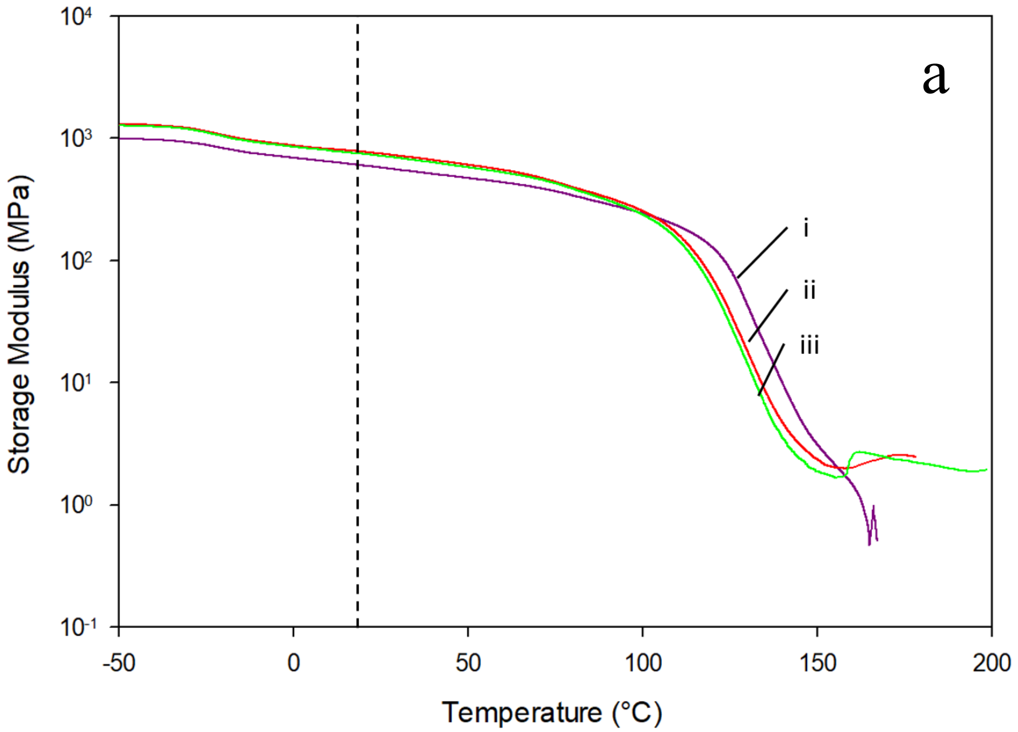
a
Storage Modulus (MPa)
10^{4}
10^{3}
10^{2}
10^{1}
10^{0}
10^{-1}
-50
0
50
100
150
200
Temperature (°C)
i
ii
iii

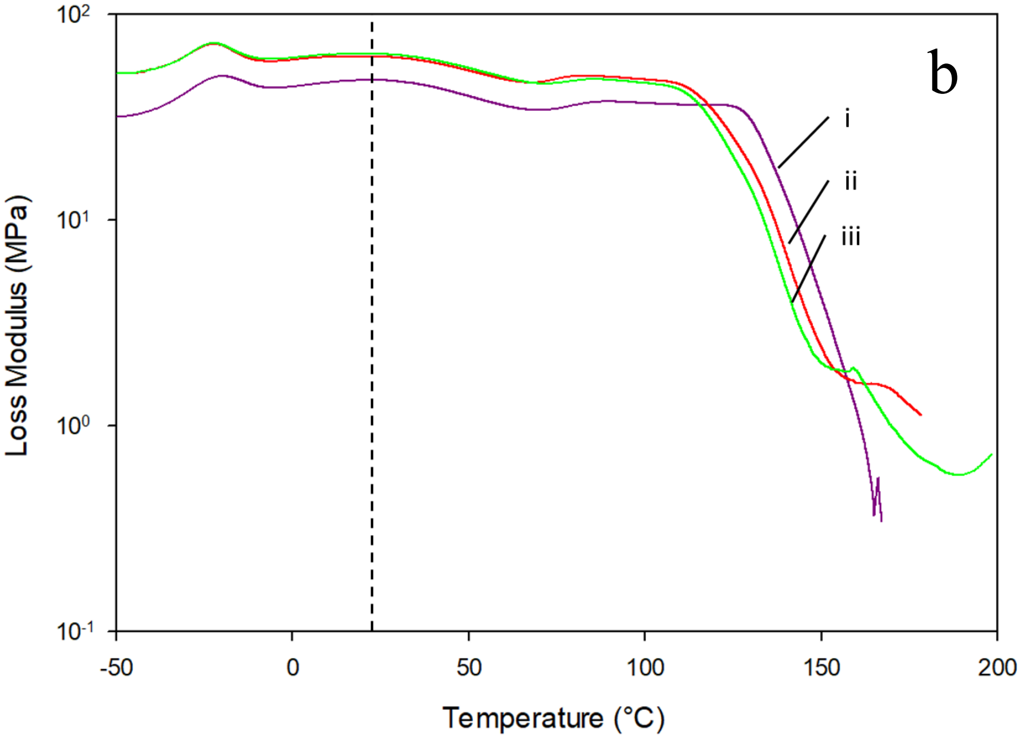
b
Loss Modulus (MPa)
10^{2}
10^{1}
10^{0}
10^{-1}
-50
0
50
100
150
200
Temperature (°C)
i
ii
iii

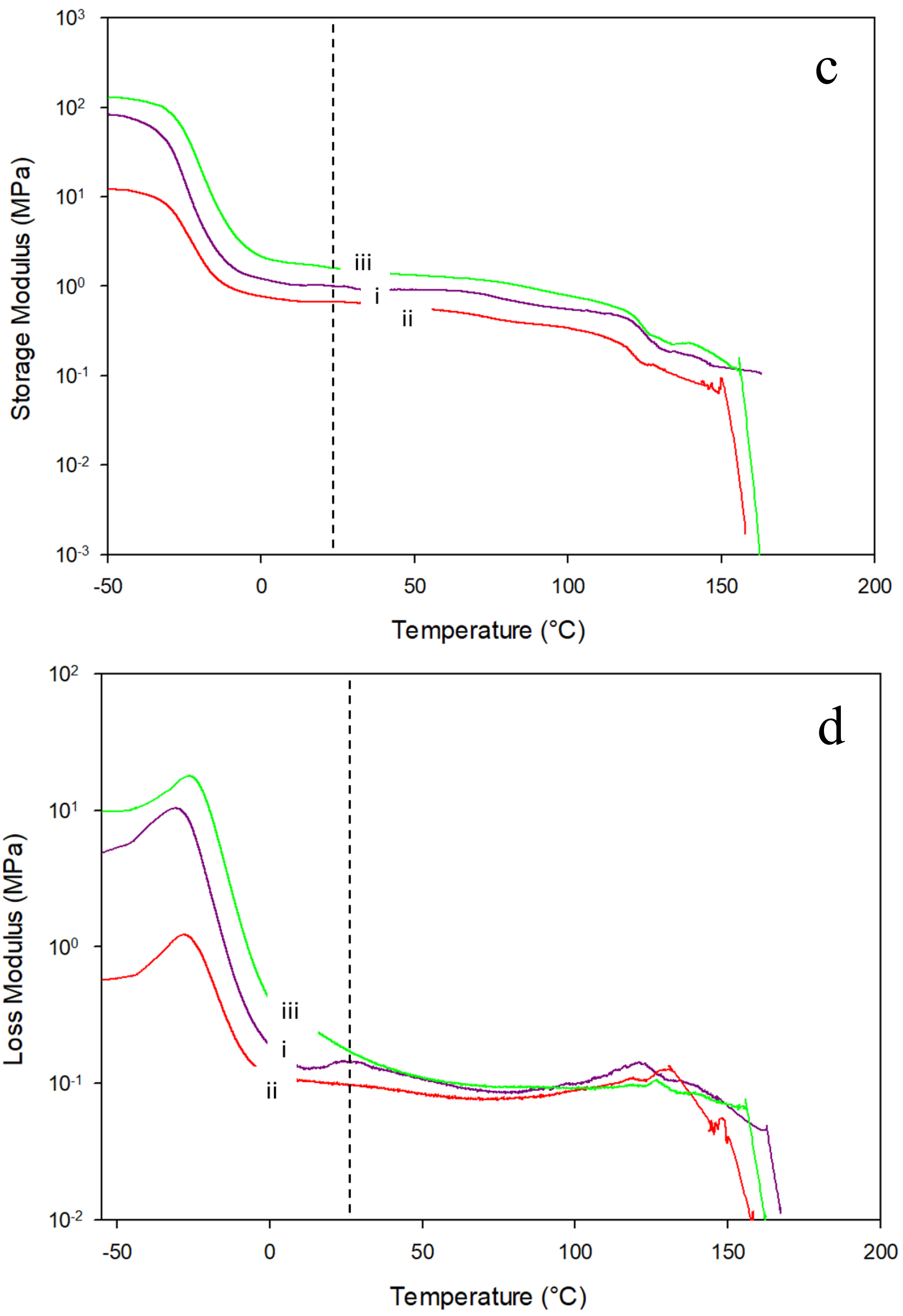

Figure 2-35: Dynamic mechanical analysis of (a) storage and (b) loss modulus for θ = 0° and (c) storage and (d) loss modulus for θ = 90° of electrospun (i) trilayer with 10wt. % sol. concentration poly(methyl methacrylate), (ii) trilayer with 15wt. % sol. concentration poly(methyl methacrylate) and (iii) trilayer with 20wt. % sol. concentration poly(methyl methacrylate).

Table 2-16: Anisotropy of the electrospun fiber samples quantified as a function of storage modulus in a ratio of the 0° / 90° fiber orientation angles obtained through interpreting the stress-strain curves.

Sample	Fiber Orientation Angle [°]	$E'_{20\,°C}$ (MPa)	Anisotropy
Pellethane	0	8.78	10.9
	90	0.81	
10 wt.% PMMA	0	141.72	10.9
	90	13.04	
15 wt.% PMMA	0	461.75	3.3
	90	139.85	
20 wt.% PMMA	0	659.50	NA
	90	-	
Trilayer 10 wt.%	0	597.84	582.1
	90	1.03	
Trilayer 15 wt.%	0	775.20	1157.0
	90	0.67	
Trilayer 20 wt.%	0	714.10	4200.6
	90	0.17	

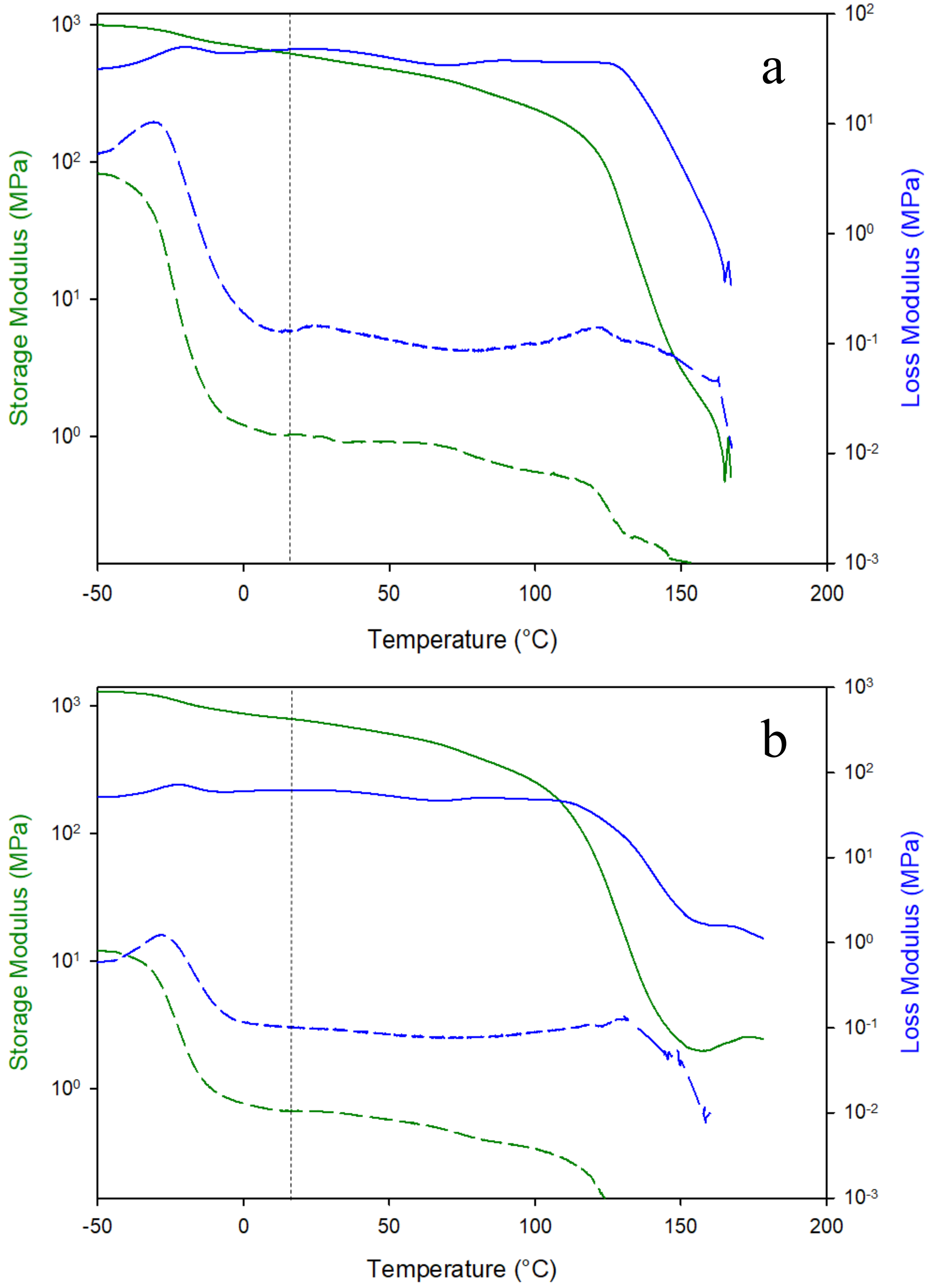
a
Storage Modulus (MPa)
Loss Modulus (MPa)
10^3
10^2
10^1
10^0
10^2
10^1
10^0
10^{-1}
10^{-2}
10^{-3}
-50
0
50
100
150
200
Temperature (°C)
b
Storage Modulus (MPa)
Loss Modulus (MPa)
10^3
10^2
10^1
10^0
10^3
10^2
10^1
10^0
10^{-1}
10^{-2}
10^{-3}
-50
0
50
100
150
200
Temperature (°C)

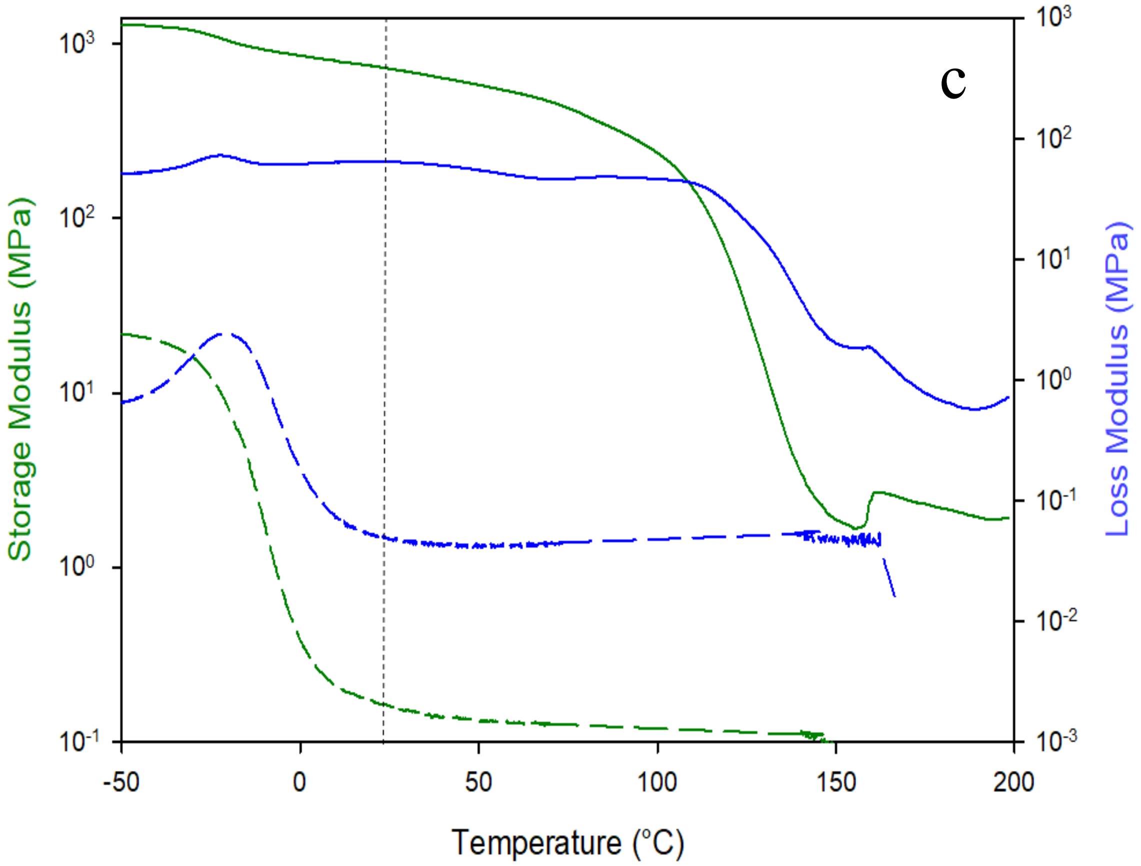

Figure 2-36: Dynamic mechanical analysis of 0° fiber orientation (solid) and 90° fiber orientation (dashed) for (a) electrospun trilayer of 10wt. % solution concentration of poly(methyl methacrylate), (b) electrospun trilayer of 15wt. % solution concentration of poly(methyl methacrylate) and (c) electrospun trilayer of 20wt. % solution concentration of poly(methyl methacrylate).

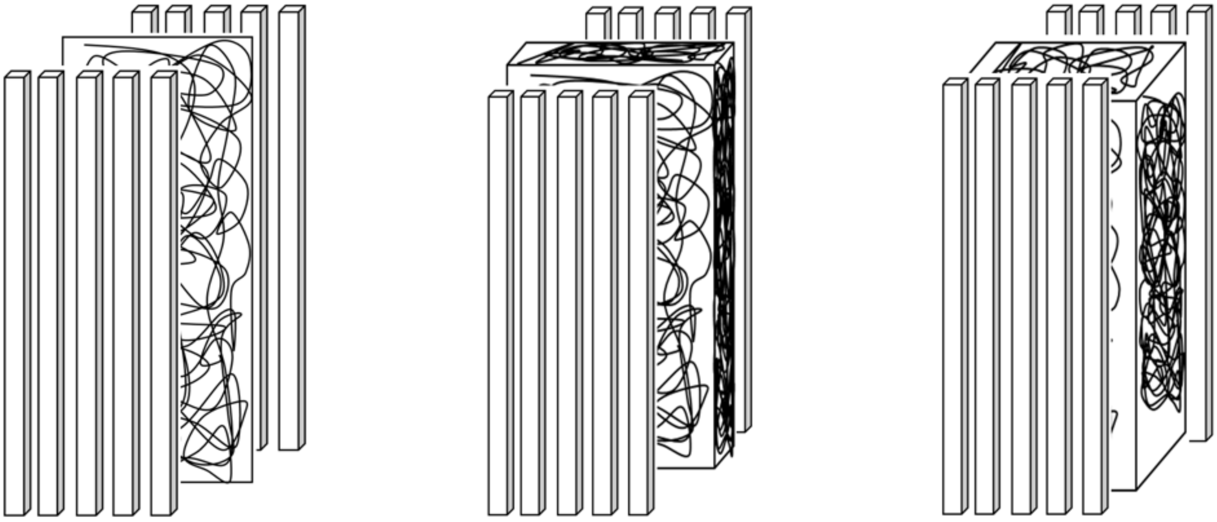

Thin-pellethane layer Medium-pellethane layer Thick-pellethane layer

Scheme 2-8: A depiction of anisotropic electrospun trilayer materials fabricated and tested. All three trilayer fiber mats are constructed with the same polymer solution concentration of as well as thickness of the outer poly(methyl methacrylate) layers. The Pellethane layer thickness was systematically increased.

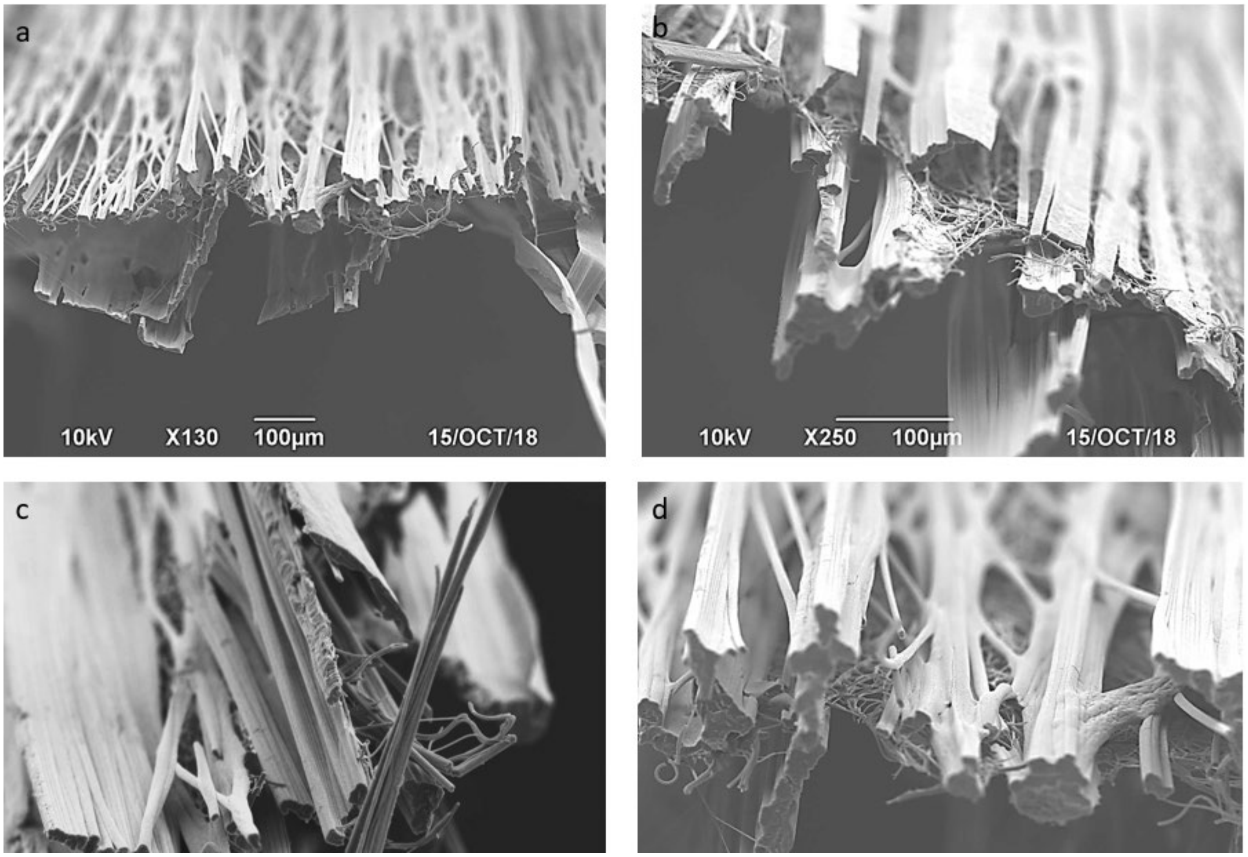

Figure 2-37: SEM micrographs of electrospun trilayer of anisotropic poly(methyl methacrylate) 20wt. % sol. concentration and $9.8x10^{-3}$ g/cm^2 of Pellethane fibers.

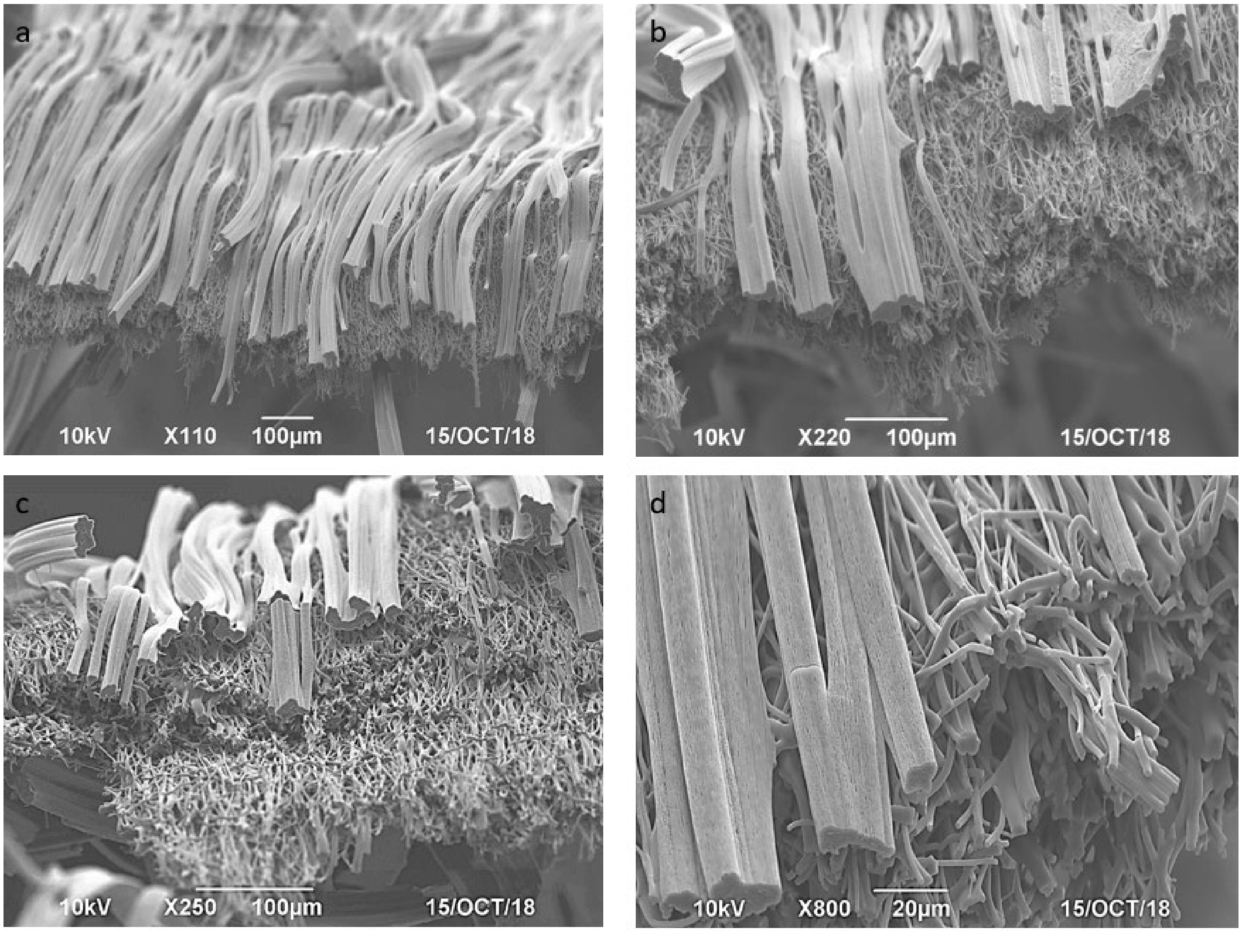

Figure 2-38: SEM micrographs of electrospun trilayer of anisotropic poly(methyl methacrylate) 20wt. % sol. concentration and 3.9x10^{-2} g/cm^{2} of Pellethane fibers.

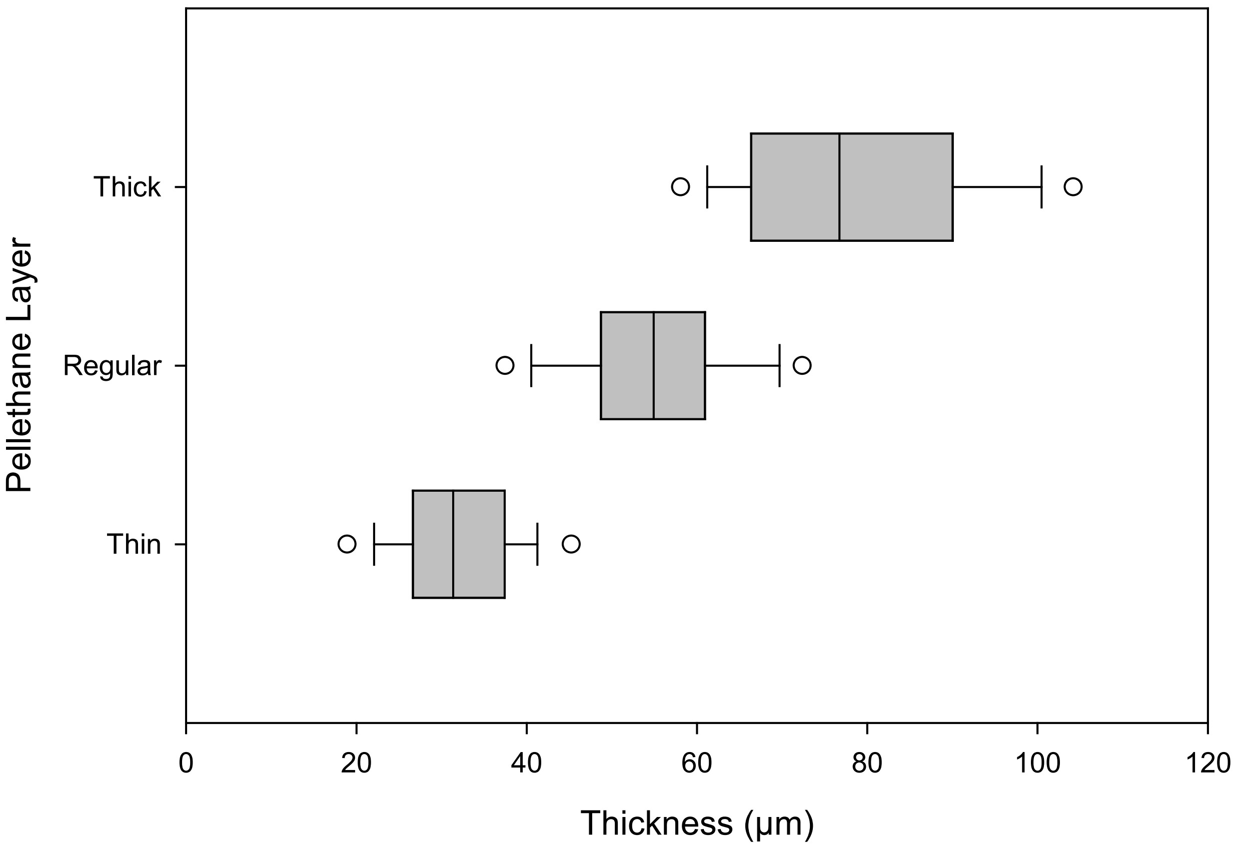

Figure 2-39: Box and whisker plot of the thickness of the Pellethane layer as measured using scanning electron microscopy.

Table 2-17: Average thickness as measured using SEM of the middle Pellethane layer thickness and the thickness of the poly(methyl methacrylate) layer for each composite.

	Variable Pellethane Trilayer		
	Thin	***Medium***	***Thick***
Total Thickness (µm):	250.96 ± 31.9	275.23 ± 30.6	304.16 ± 50.16
Pellethane Thickness (µm):	32.07 ± 7.8	54.9 ± 10.2	78.3 ± 14.96
PMMA Thickness (µm):	218.53	220.31	225.83

Table 2-18: Unpaired t-test comparing the thickness of Pellethane of each composite with each other, showing there is a statistical difference between the total thickness of each composite and the middle Pellethane layer. Statistical difference h = 1.

Composite Comparison	Pellethane Layer Thickness (µm)	
	h	*p*
Thin vs Medium	1	7.54E-16
Thin vs Thick	1	1.58E-27
Medium vs Thick	1	1.77E-11

Composite Comparison	Total Composite Thickness (µm)	
	h	*p*
Thin vs Medium	1	1.38E-04
Thin vs Thick	1	1.75E-05
Medium vs Thick	1	2.72E-04

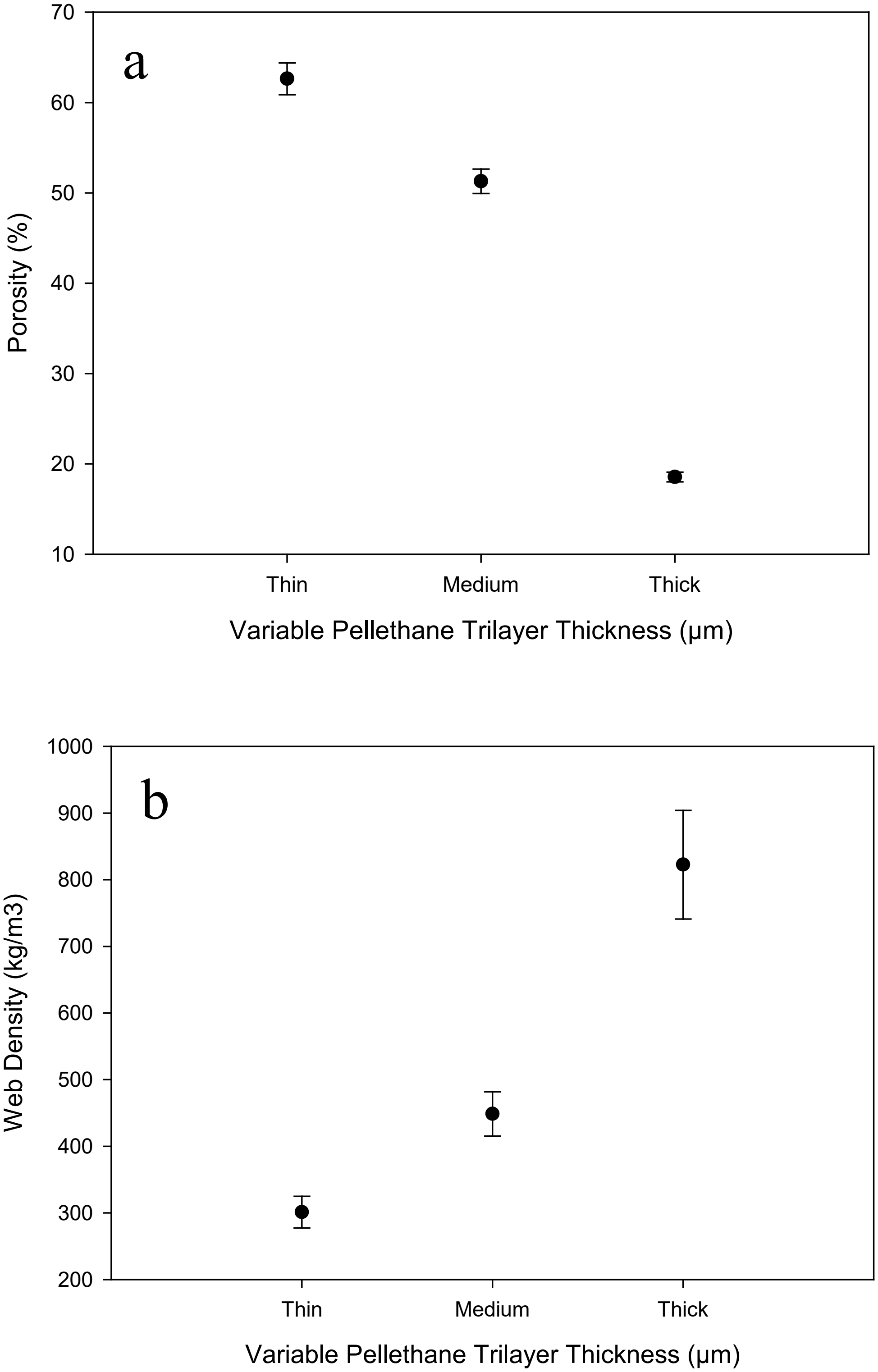

Figure 2-40: Plot of porosity (a) and web density (b) as a function of Pellethane thickness within each trilayer composite.

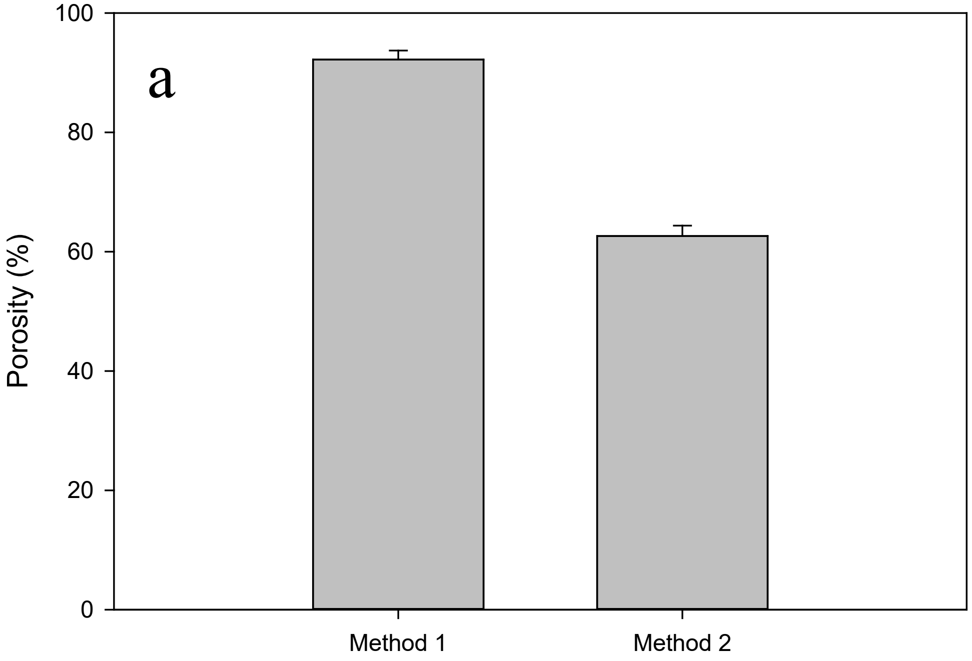

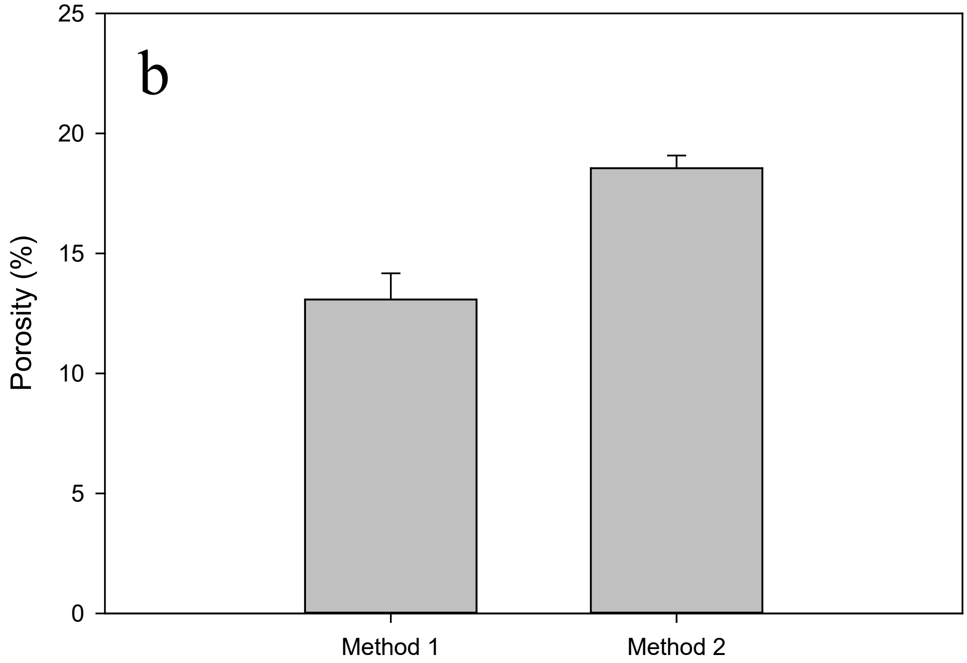

Figure 2-41: Bar charts of the measured apparent porosity (method 1) and porosity (method 2) for (a) trilayer with 9.8x10^{-3} g/cm^2 of Pellethane and (b) trilayer with 3.9x10^{-2} g/cm^2 of Pellethane.

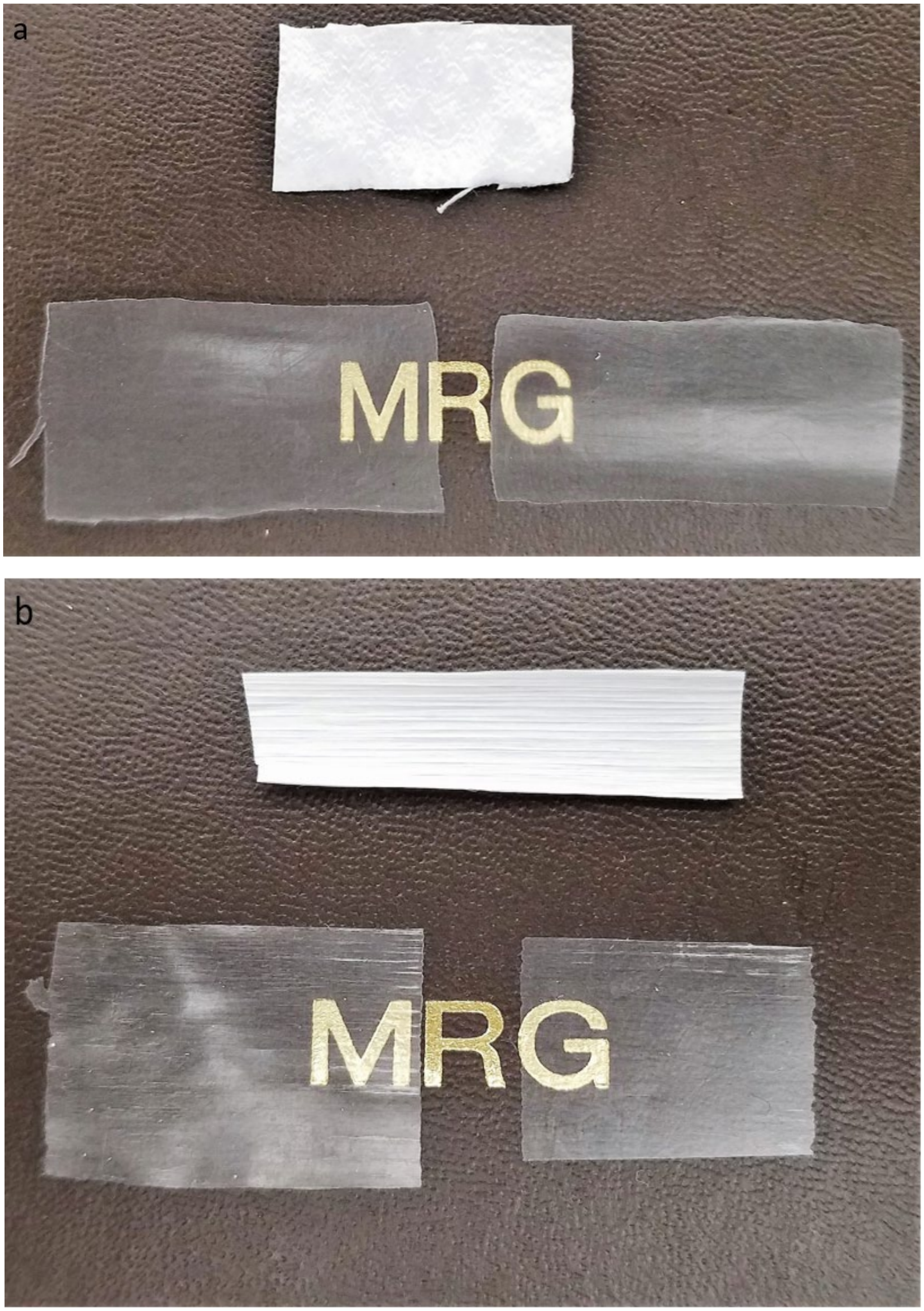

Figure 2-42: Representative images showing the change in physical appearance between the as spun fiber sheet (top) and the melted film (bottom) for (a) trilayer with $9.8\text{x}10^{-3}$ g/cm^2 of Pellethane and (b) trilayer with with $3.9\text{x}10^{-2}$ g/cm^2 of Pellethane.

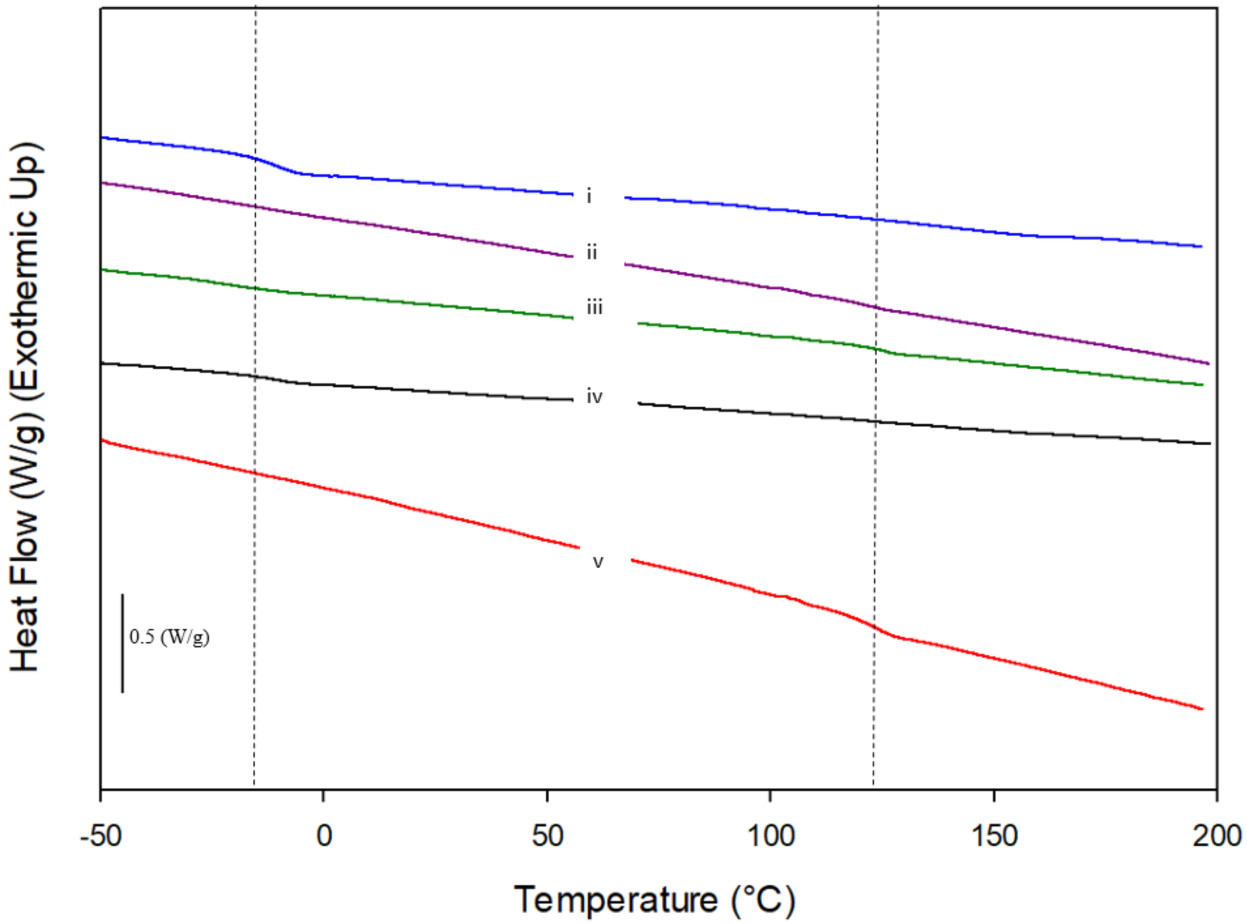

Figure 2-43: DSC of the second heat for electrospun (i) Pellethane, (ii) 9.8×10^{-3} g/cm^2 of Pellethane in the trilayer, (iii) 1.9×10^{-2} g/cm^2 of Pellethane in the trilayer, (iv) 3.9×10^{-2} g/cm^2 of Pellethane in the trilayer and (v) electrospun poly(methyl methacrylate). The measured glass transition temperatures (T_g) for Pellethane is -10 °C and 125°C for poly(methyl methacrylate). Pellethane is a thermoplastic elastomer and has a small melt peak around 155 °C.

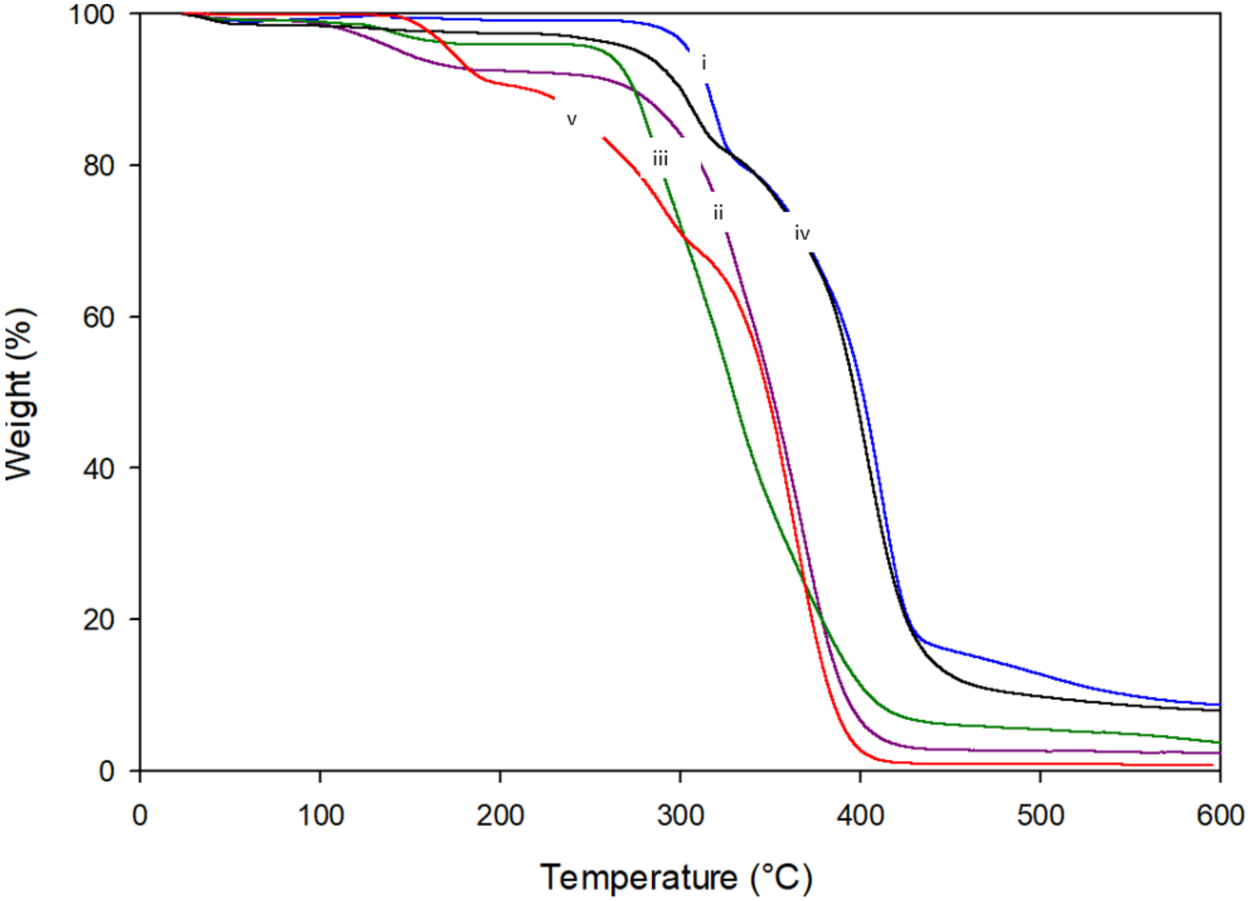

Figure 2-44: TGA of mass loss as a function of temperature for the (i) Pellethane, (ii) 9.8×10^{-3} g/cm^2 of Pellethane in the trilayer, (iii) 1.9×10^{-2} g/cm^2 of Pellethane in the trilayer, (iv) 3.9×10^{-2} g/cm^2 of Pellethane in the trilayer and (v) electrospun poly(methyl methacrylate).

Table 2-19: Char yield of trilayer composites in relation to the amount of Pellethane present based on TGA and DSC analysis. The thin, medium and thick layer of Pellethane trilayers have 9.8×10^{-3} g/cm^2, 1.9×10^{-2} g/cm^2 and 3.9×10^{-2} g/cm^2 of Pellethane respectively.

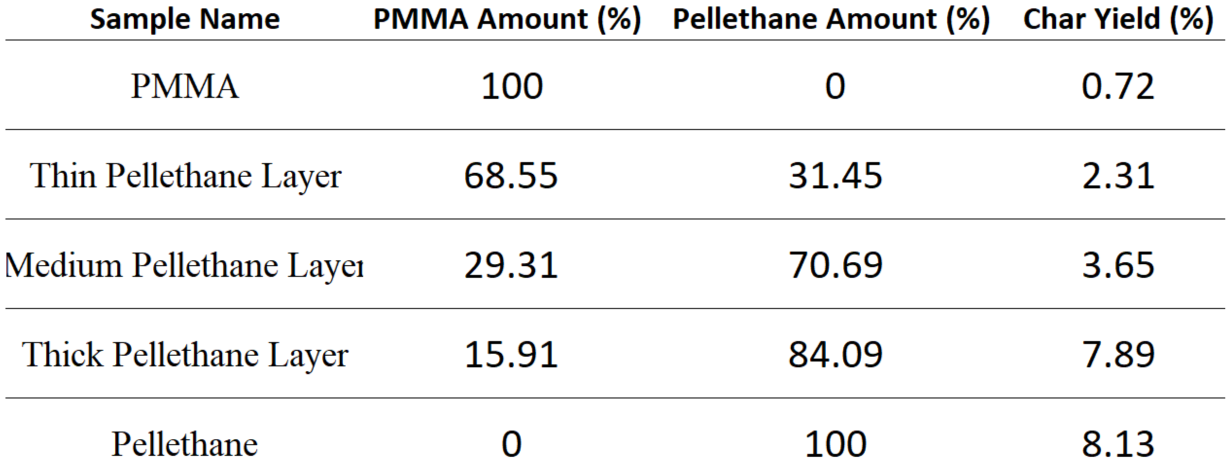

Sample Name	PMMA Amount (%)	Pellethane Amount (%)	Char Yield (%)
PMMA	100	0	0.72
Thin Pellethane Layer	68.55	31.45	2.31
Medium Pellethane Layer	29.31	70.69	3.65
Thick Pellethane Layer	15.91	84.09	7.89
Pellethane	0	100	8.13

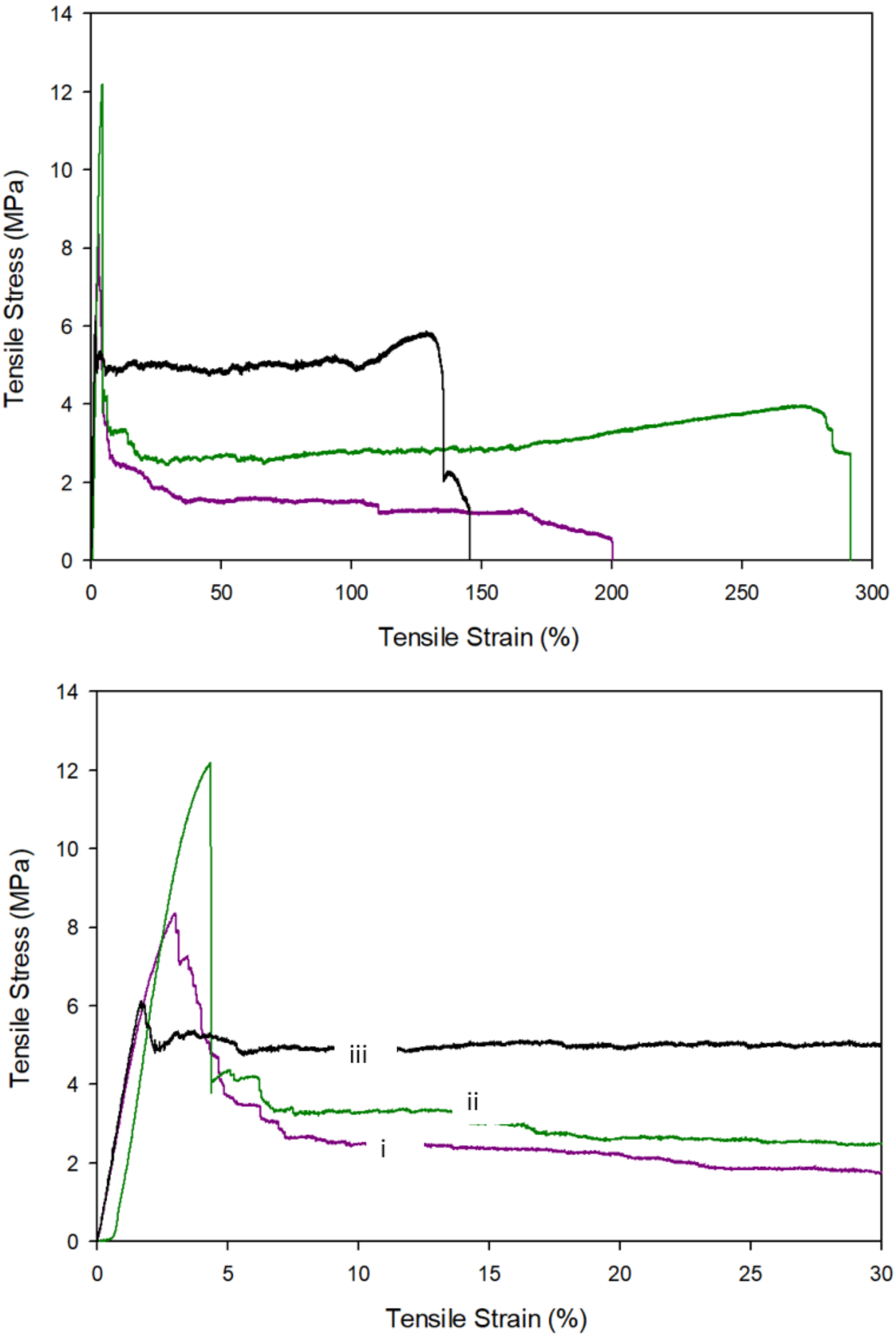

Figure 2-45: Representative stress strain curves (top) and magnified view of the elastic deformation (bottom) for (i) $9.8x10^{-3}$ g/cm^2 of Pellethane in the trilayer, (ii) $1.9x10^{-2}$ g/cm^2 of Pellethane in the trilayer, (iii) $3.9x10^{-2}$ g/cm^2 of Pellethane in the trilayer. All samples are $\theta = 0°$ with n of 5.

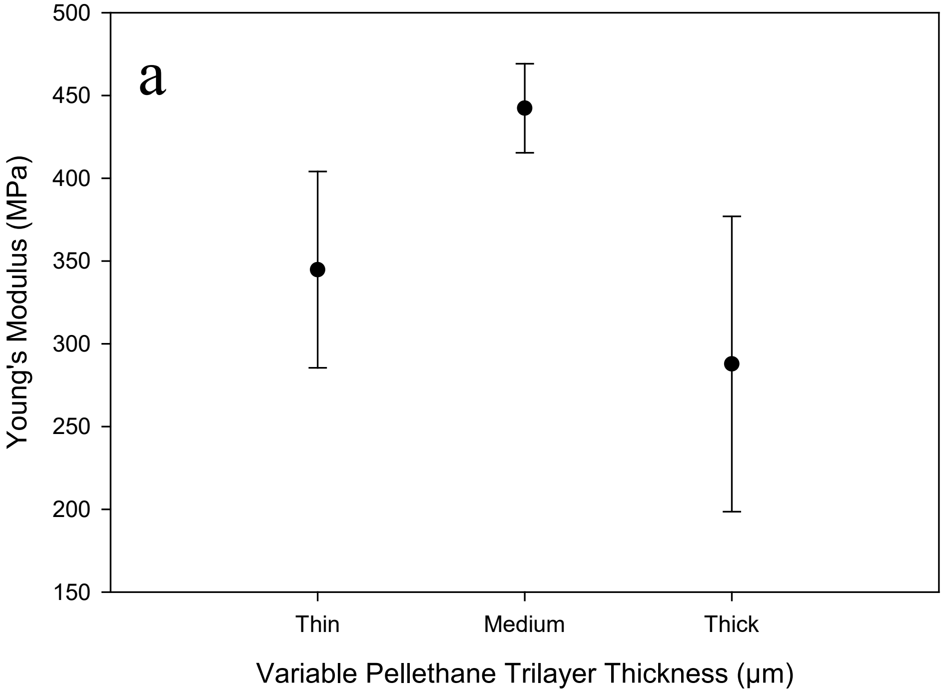
a
Young's Modulus (MPa)
500
450
400
350
300
250
200
150
Thin
Medium
Thick
Variable Pellethane Trilayer Thickness (μm)

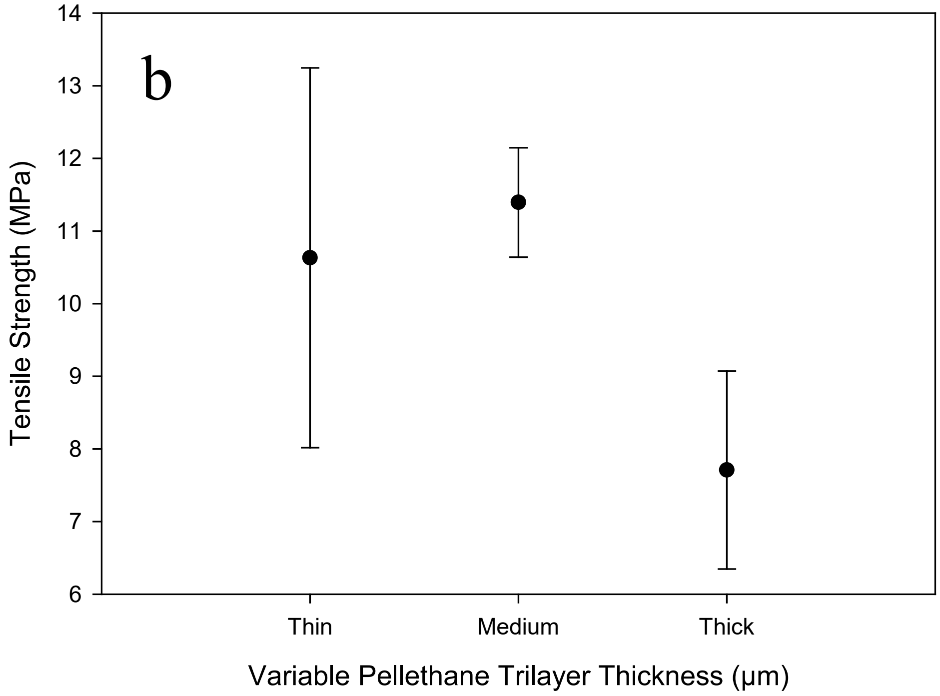
b
Tensile Strength (MPa)
14
13
12
11
10
9
8
7
6
Thin
Medium
Thick
Variable Pellethane Trilayer Thickness (μm)

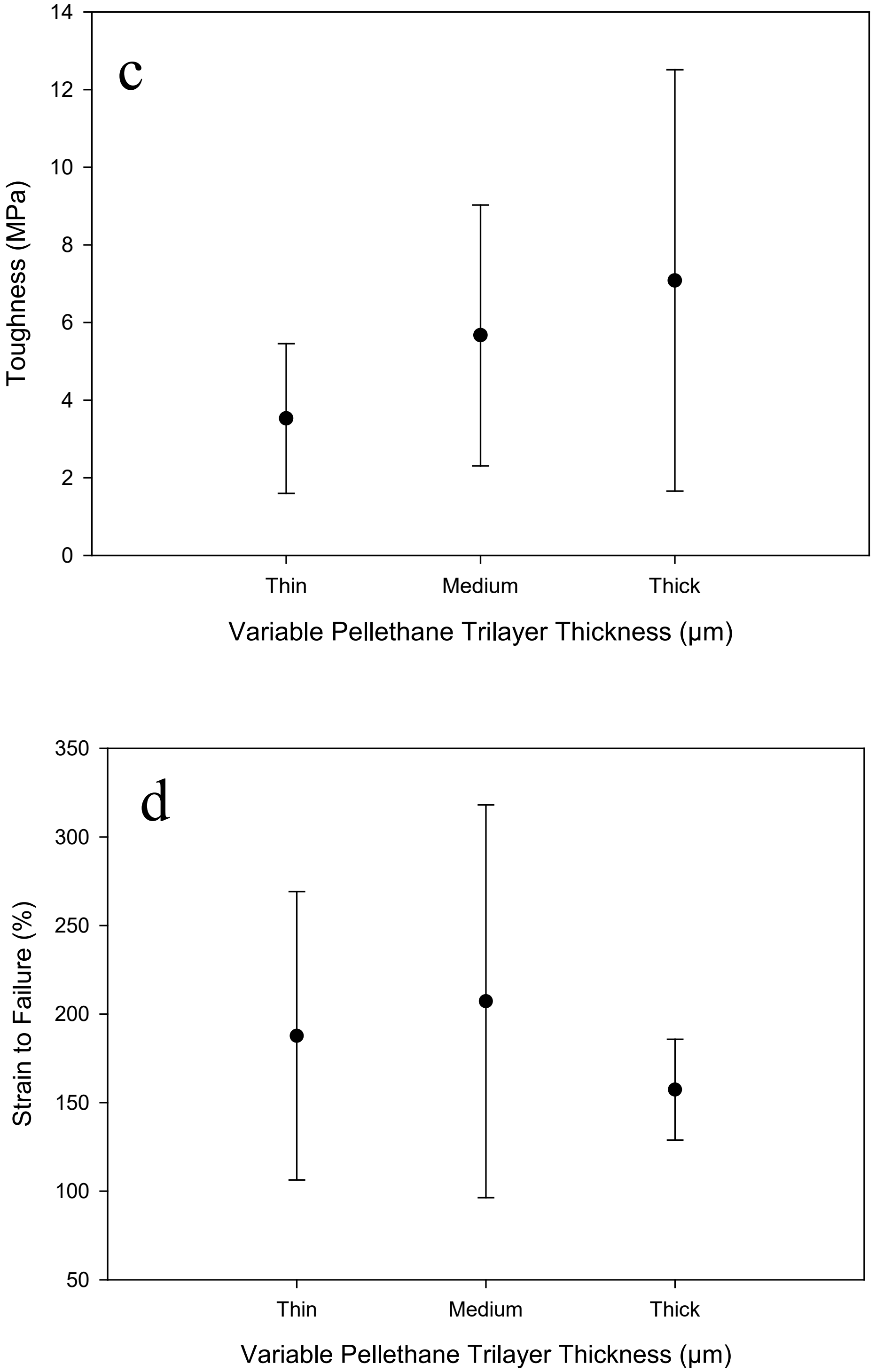

Figure 2-46: Summation of mechanical properties of the trilayer samples with variable Pellethane thickness obtained through interpretation of the stress-strain curves for all samples with the fiber orientation angle θ = 0°. (a) Young's modulus, (b) tensile strength, (c) toughness and (d) strain-to-failure. All data points are an average of n = 5.

Table 2-20: Unpaired t-test comparing the mechanical properties of the variable thickness Pellethane trilayers with each other, showing there is no statistical difference between them θ = 0°. Statistical difference h = 1.

	Young's Modulus (MPa)	
	h	*p*
Thin vs Medium	0	0.0756
Thin vs Thick	0	0.2510
Medium vs Thick	0	0.1498

	Tenisle Strength (MPa)	
	h	*p*
Thin vs Medium	0	0.6604
Thin vs Thick	0	0.0975
Medium vs Thick	0	0.1084

	Toughness (MPa)	
	h	*p*
Thin vs Medium	0	0.2573
Thin vs Thick	0	0.5238
Medium vs Thick	0	0.9823

	Strain to Failure (%)	
	h	*p*
Thin vs Medium	0	0.7659
Thin vs Thick	0	0.7570
Medium vs Thick	0	0.1484

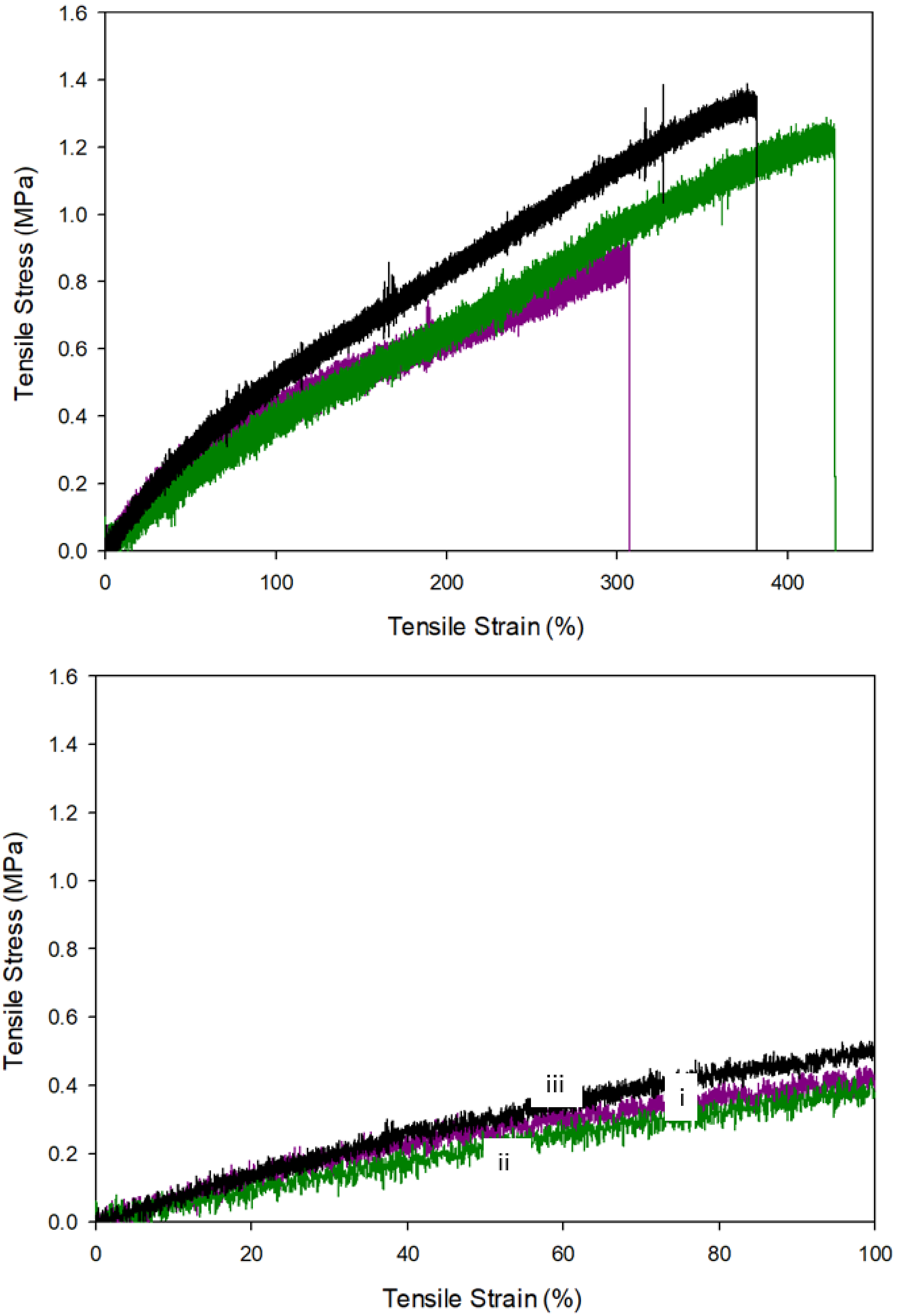

Figure 2-47: Representative stress strain curves (top) and magnified view of the elastic deformation (bottom) for (i) 9.8x10^{-3} g/cm^2 of Pellethane in the trilayer, (ii) 1.9x10^{-2} g/cm^2 of Pellethane in the trilayer, (iii) 3.9x10^{-2} g/cm^2 of Pellethane in the trilayer. Noise of the samples in the magnified view is due to the sensitivity limitation of the Instron force gauge. All samples are θ = 90° with n of 5.

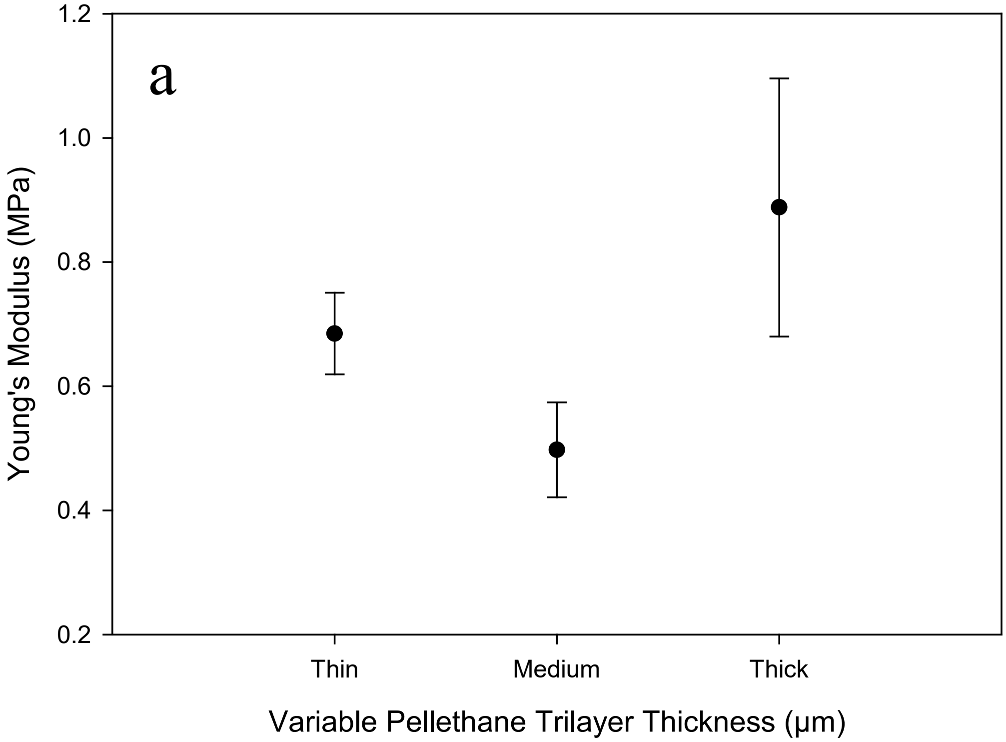
a
Young's Modulus (MPa)
1.2
1.0
0.8
0.6
0.4
0.2
Thin
Medium
Thick
Variable Pellethane Trilayer Thickness (µm)

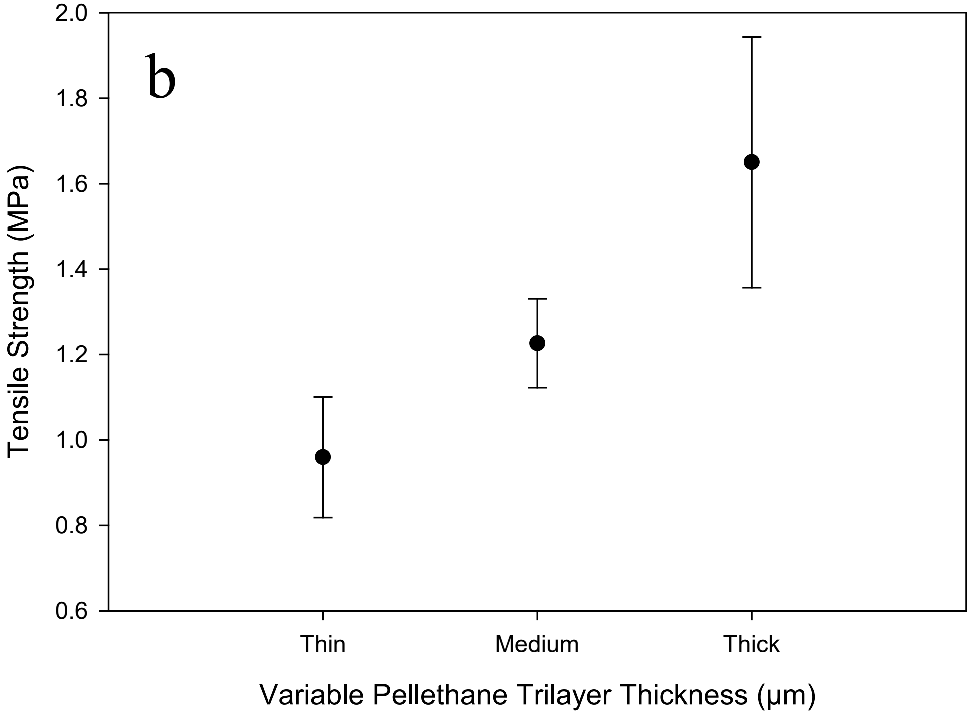
b
Tensile Strength (MPa)
2.0
1.8
1.6
1.4
1.2
1.0
0.8
0.6
Thin
Medium
Thick
Variable Pellethane Trilayer Thickness (µm)

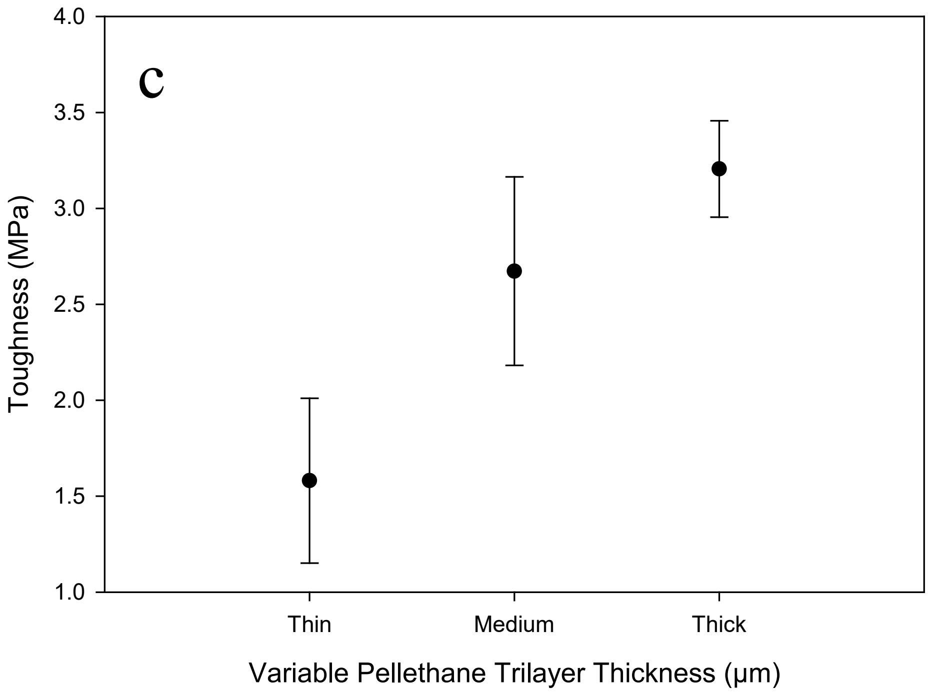

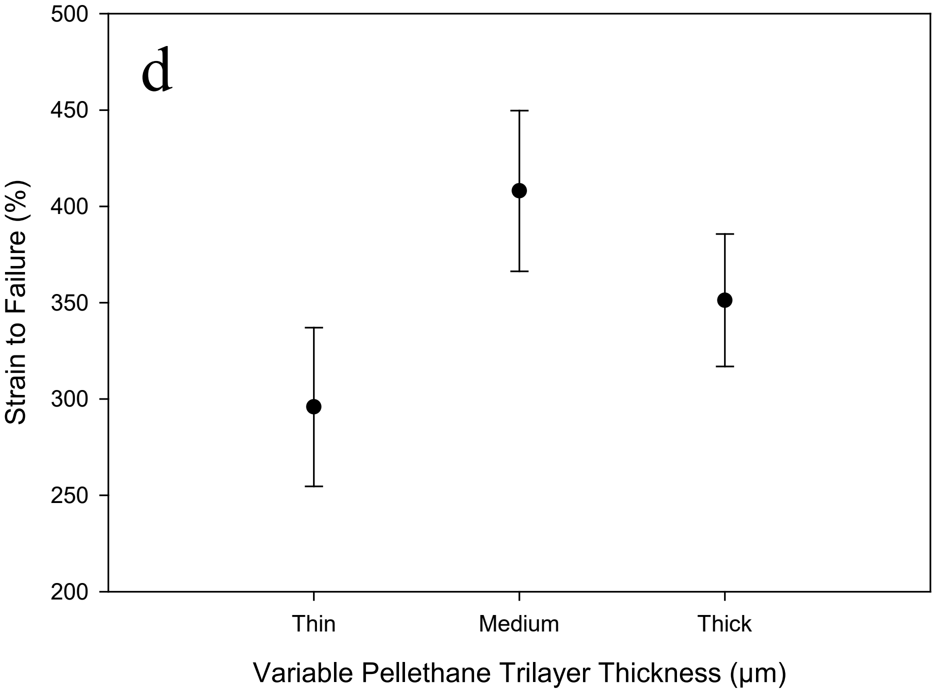

Figure 2-48: Summation of mechanical properties of the trilayer samples with variable Pellethane thickness obtained through interpretation of the stress-strain curves for all samples with the fiber orientation angle θ = 90°. (a) Young's modulus, (b) tensile strength, (c) toughness and (d) strain-to-failure. All data points are an average of n = 5.

Table 2-21: Unpaired t-test comparing the mechanical properties of the variable thickness Pellethane trilayers with each other, showing statistical difference between them θ = 90°. Statistical difference h = 1.

	Young's Modulus (MPa)	
	h	*p*
Thin vs Medium	1	0.0094
Thin vs Thick	0	0.2670
Medium vs Thick	0	0.1220

	Tenisle Strength (MPa)	
	h	*p*
Thin vs Medium	0	0.0965
Thin vs Thick	0	0.0876
Medium vs Thick	0	0.0823

	Toughness (MPa)	
	h	*p*
Thin vs Medium	0	0.1038
Thin vs Thick	1	0.0432
Medium vs Thick	0	0.0950

	Strain to Failure (%)	
	h	*p*
Thin vs Medium	0	0.1050
Thin vs Thick	0	0.0559
Medium vs Thick	0	0.3101

Table 2-22: Anisotropy of the electrospun fiber samples quantified as a function of Young's modulus in a ratio of the 0° / 90° fiber orientation angles obtained through interpreting the stress-strain curves.

Sample	Fiber Orientation Angle [°]	Youngs Modulus [MPa]	Anisotropy
Thin	0	345	507.4
	90	0.68	
Medium	0	442.38	902.8
	90	0.49	
Thick	0	288	323.6
	90	0.89	

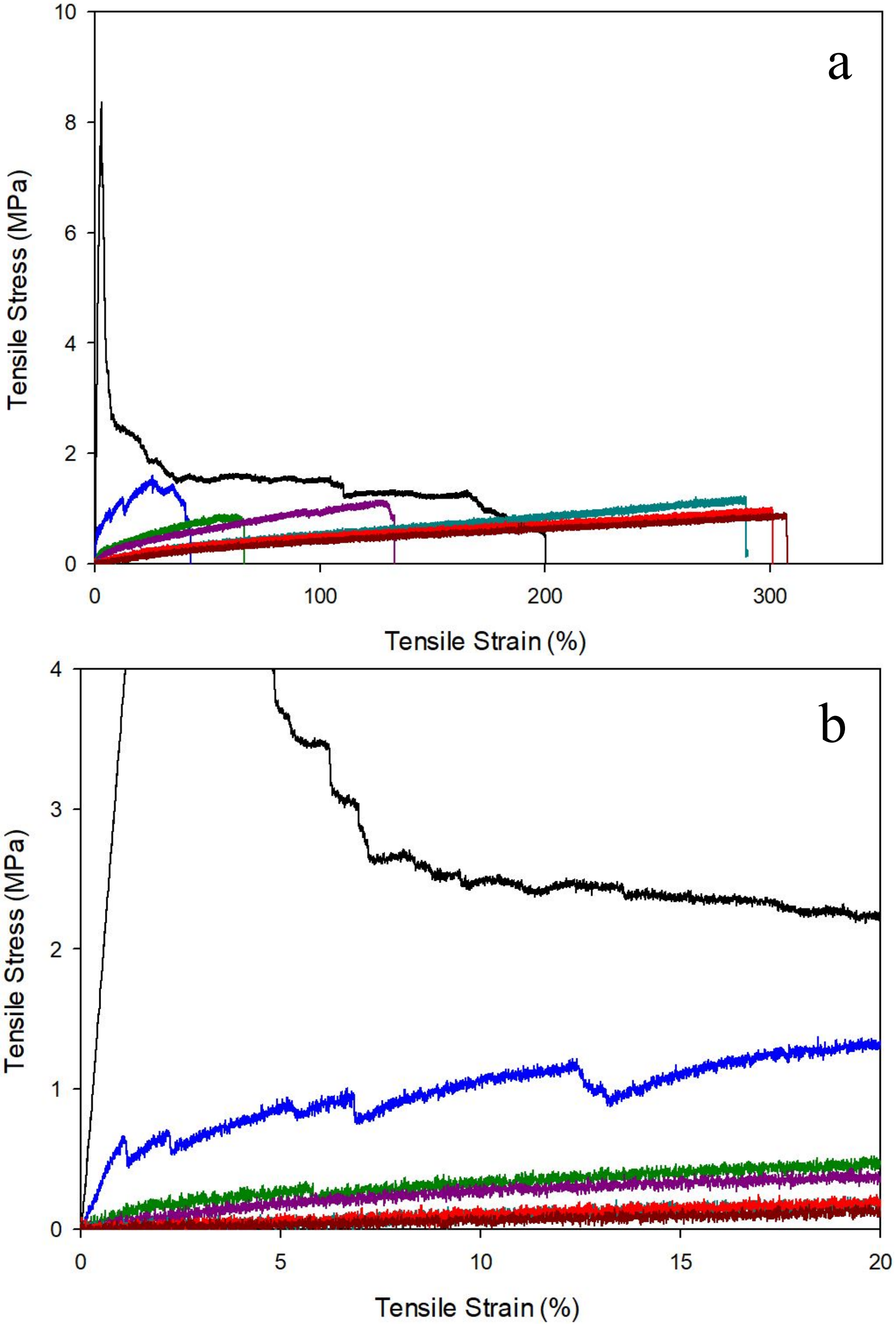
a
Tensile Stress (MPa)
10
8
6
4
2
0
Tensile Strain (%)
0
100
200
300
b
Tensile Stress (MPa)
4
3
2
1
0
Tensile Strain (%)
0
5
10
15
20

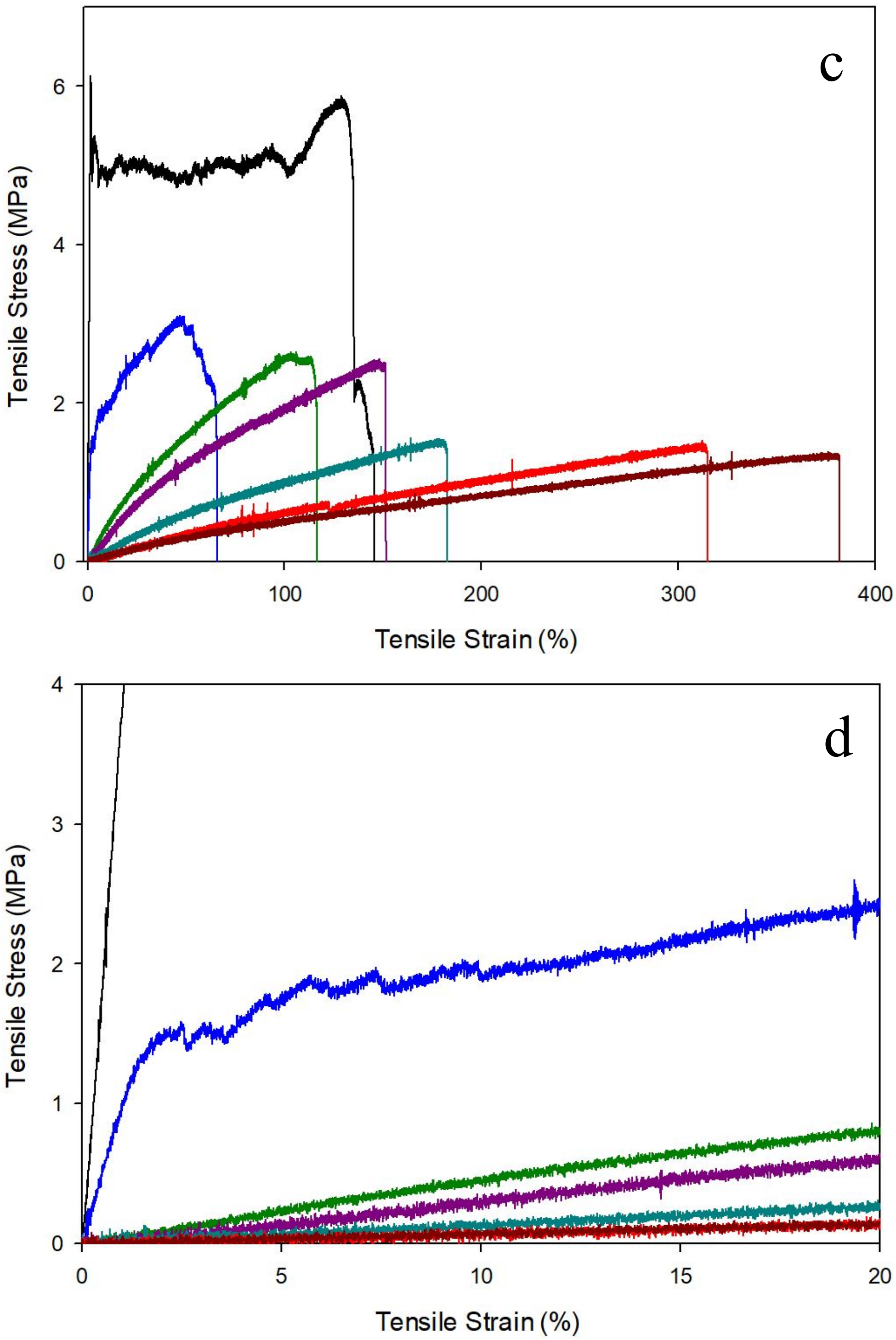

Figure 2-49: Representative stress-strain curves for (a) trilayer with 9.8x10^{-3} g/cm^2 of Pellethane (b) magnified view of trilayer with 9.8x10^{-3} g/cm^2 of Pellethane (c) trilayer with 3.9x10^{-2} g/cm^2 of Pellethane and (d) magnified view of trilayer with 3.9x10^{-2} g/cm^2 of Pellethane. Each graph shows seven distinct fiber orientation angles (Δθ) of 0° (black), 15° (blue), 30° (green) 45°(purple), 60° (turquoise), 75° (red) and 90° (brown). All sample curves are an average of n = 5.

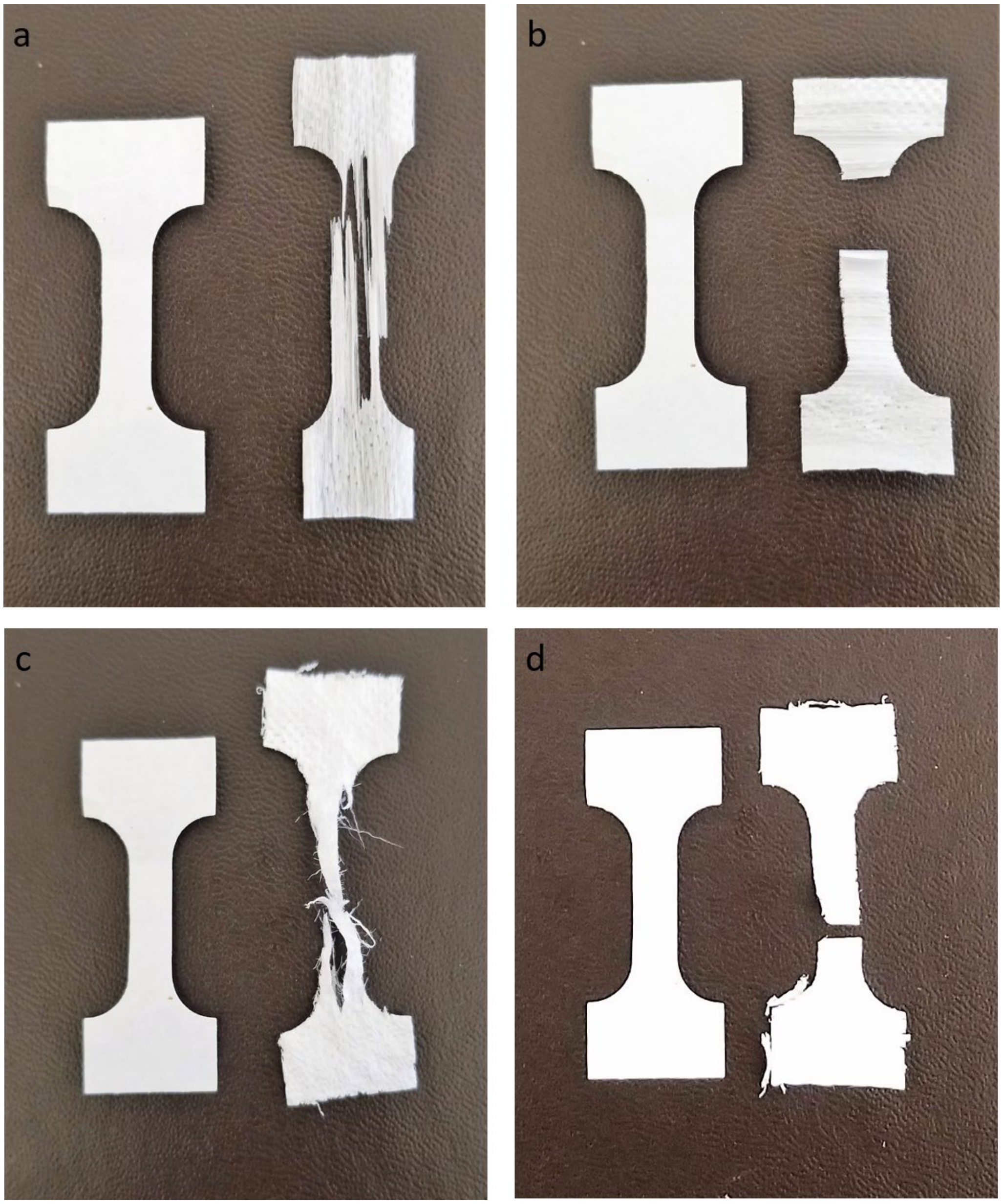

Figure 2-50: Representative post tensile tested dog bones (right) with pre tensile tested dog bones (left) for (a) trilayer with $9.8\text{x}10^{-3}$ g/cm^2 of Pellethane 0°, (b) trilayer with $9.8\text{x}10^{-3}$ g/cm^2 of Pellethane 90°, (c) trilayer with $3.9\text{x}10^{-2}$ g/cm^2 of Pellethane 0°and (d) trilayer with $3.9\text{x}10^{-2}$ g/cm^2 of Pellethane 90°.

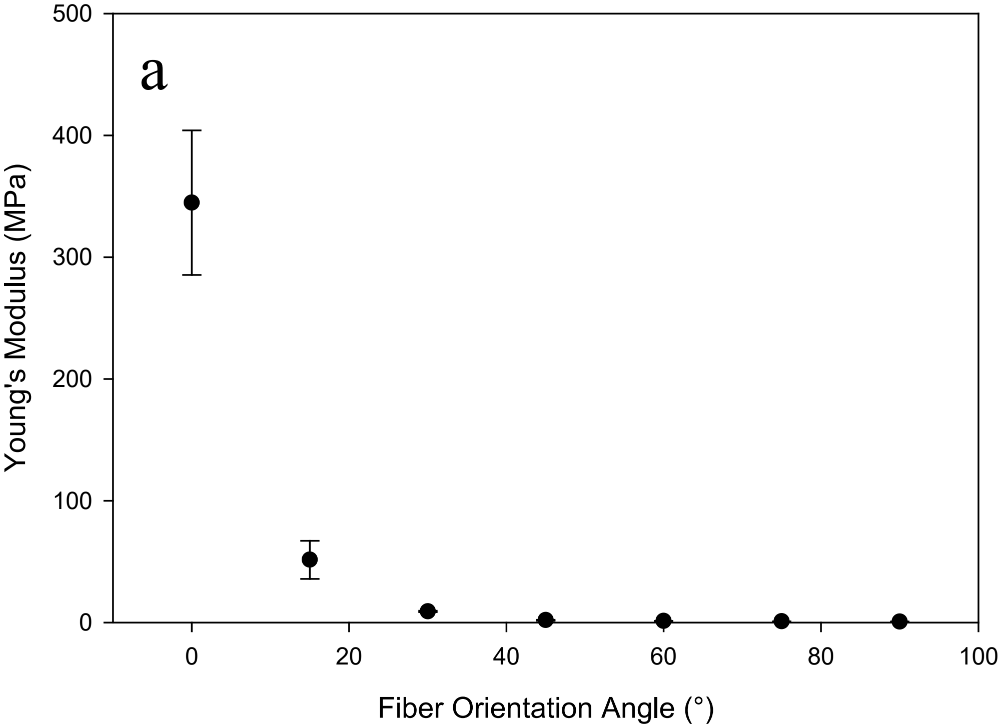
a
Young's Modulus (MPa)
500
400
300
200
100
0
0
20
40
60
80
100
Fiber Orientation Angle (°)

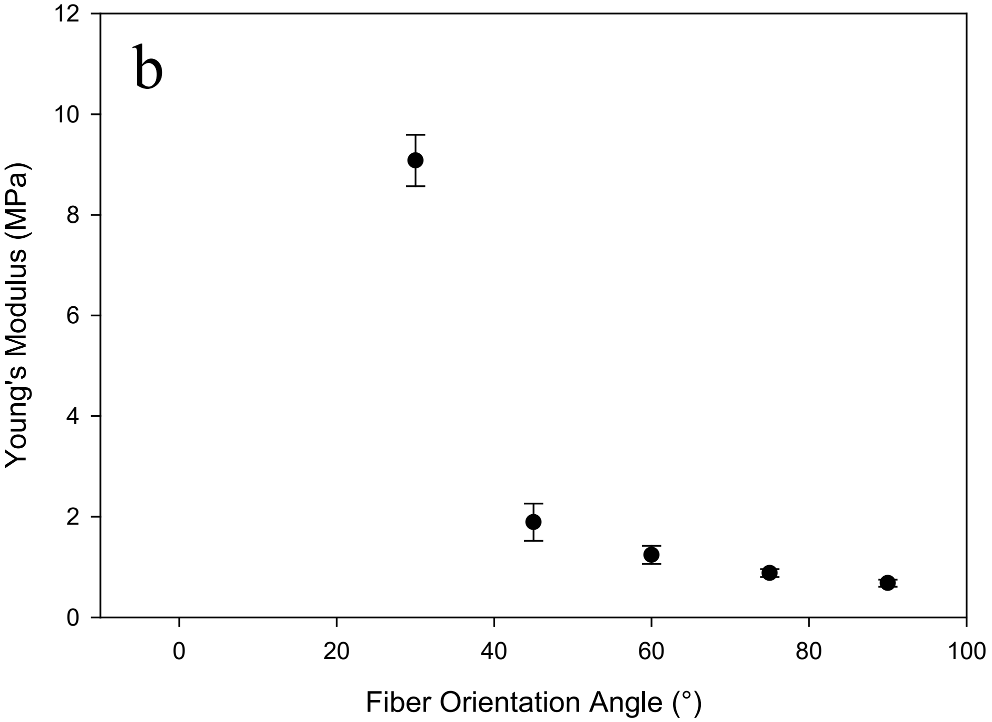
b
Young's Modulus (MPa)
12
10
8
6
4
2
0
0
20
40
60
80
100
Fiber Orientation Angle (°)

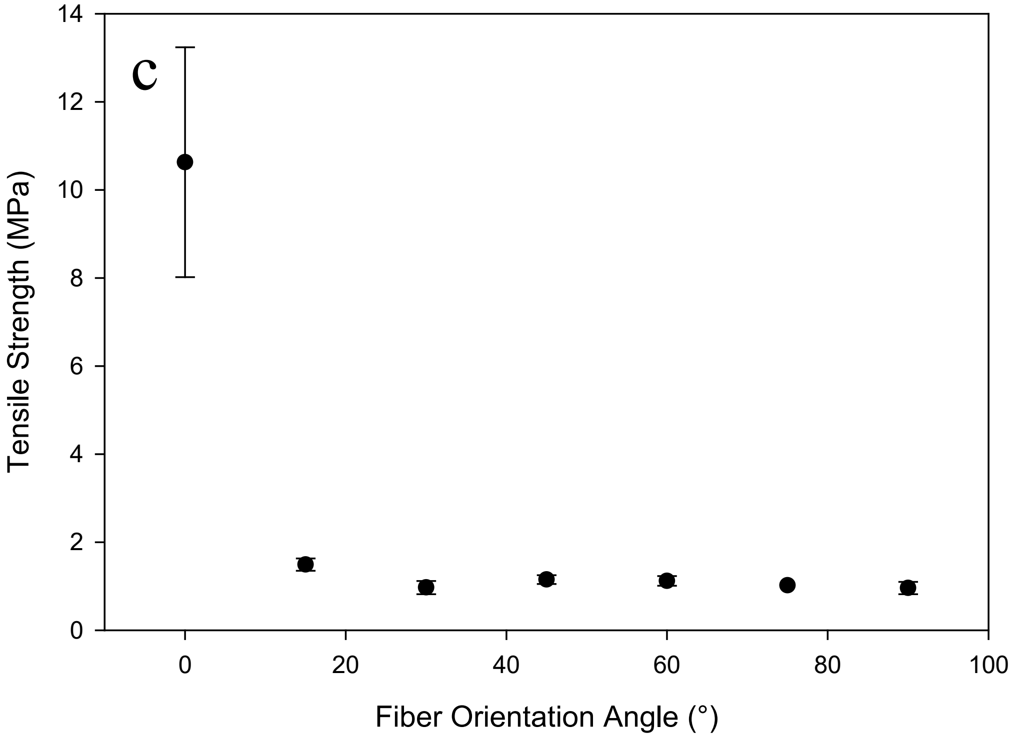
c
Tensile Strength (MPa)
0
2
4
6
8
10
12
14
0
20
40
60
80
100
Fiber Orientation Angle (°)

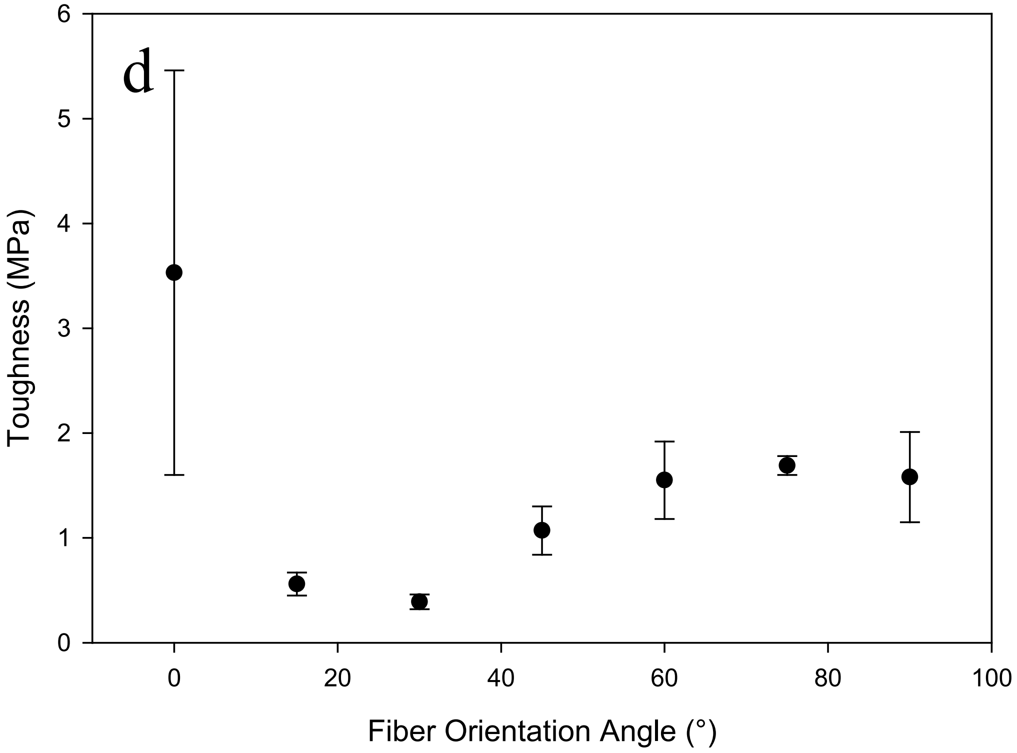
d
Toughness (MPa)
0
1
2
3
4
5
6
0
20
40
60
80
100
Fiber Orientation Angle (°)

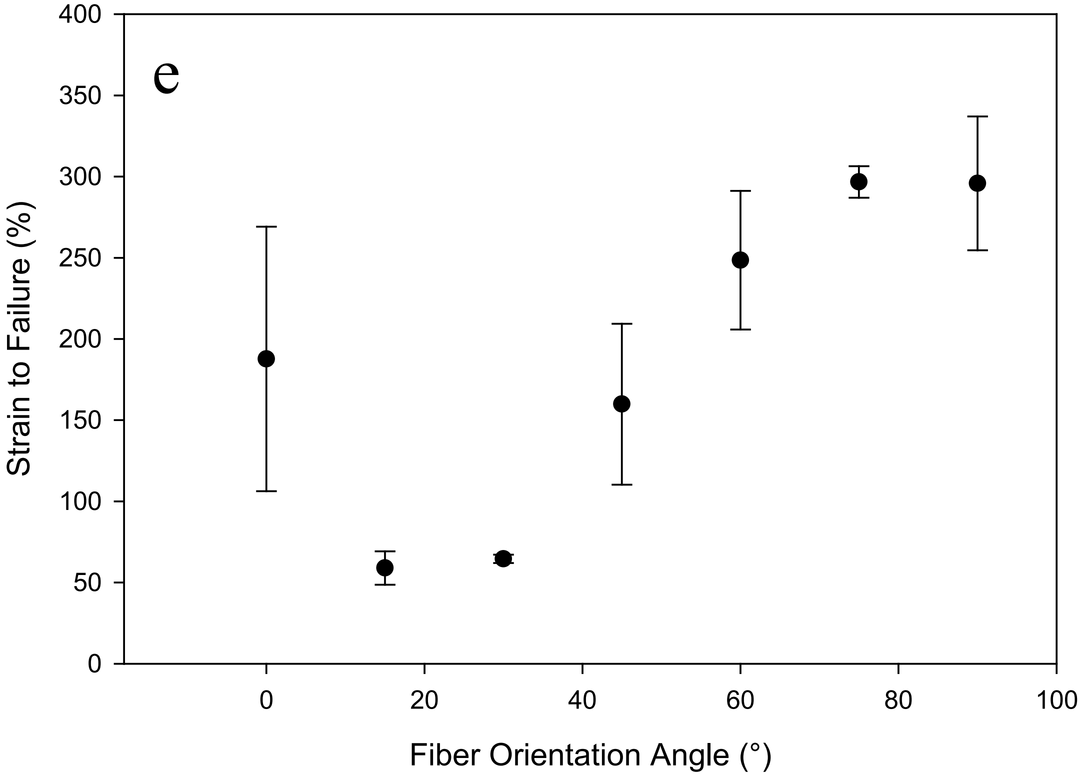

Figure 2-51: Resulting mechanical properties of electrospun trilayer with 9.8x10^{-3} g/cm^{2} of Pellethane from tensile testing as a function of the fiber orientation angle. (a) Young's modulus, (b) magnified view of Young's modulus, (c) tensile strength, (d) toughness and (e) strain-to-failure. All data points are an average of n = 5.

Table 2-24: Average Young’s modulus, toughness, tensile strength and strain to failure for all fiber orientation angles (Δθ) interpreted from the stress strain curves of the electrospun trilayer with 9.8x10^{-3} g/cm^2 of Pellethane.

Material Property	**Fiber Orientation Angle [°]**						
	0	*15*	*30*	*45*	*60*	*75*	*90*
Young's Modulus [MPa]	344.79 ± 59.4	51.43 ± 15.6	9.08 ± 0.5	1.89 ± 0.4	1.24 ± 0.2	0.88 ± 0.1	0.68 ± 0.1
Toughness [MPa]	3.52 ± 1.9	0.56 ± 0.1	0.39 ± 0.1	1.07 ± 0.2	1.55 ± 0.4	1.69 ± 0.1	1.58 ± 0.4
Tensile Strength [MPa]	10.63 ± 2.6	1.49 ± 0.1	0.97 ± 0.1	1.14 ± 0.1	1.12 ± 0.1	1.02 ± 0.0	0.96 ± 0.1
Strain to Failure [%]	187.74 ± 81.5	58.92 ± 10.3	64.56 ± 2.58	159.85 ± 49.6	248.55 ± 42.7	296.78 ± 9.7	295.86 ± 41.2

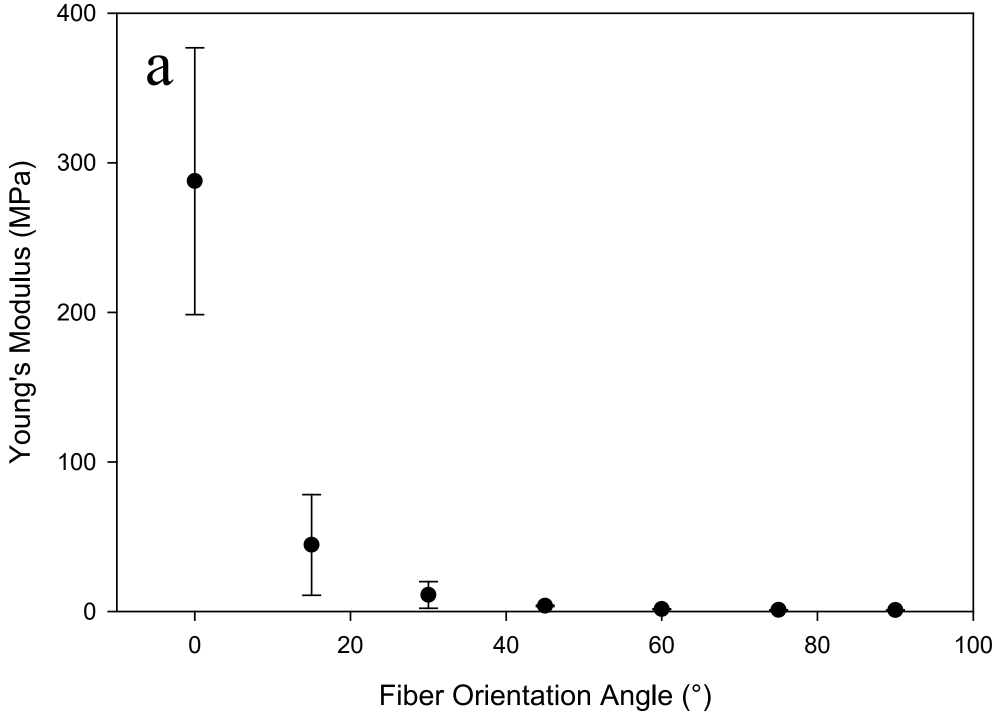
a
Young's Modulus (MPa)
400
300
200
100
0
0
20
40
60
80
100
Fiber Orientation Angle (°)

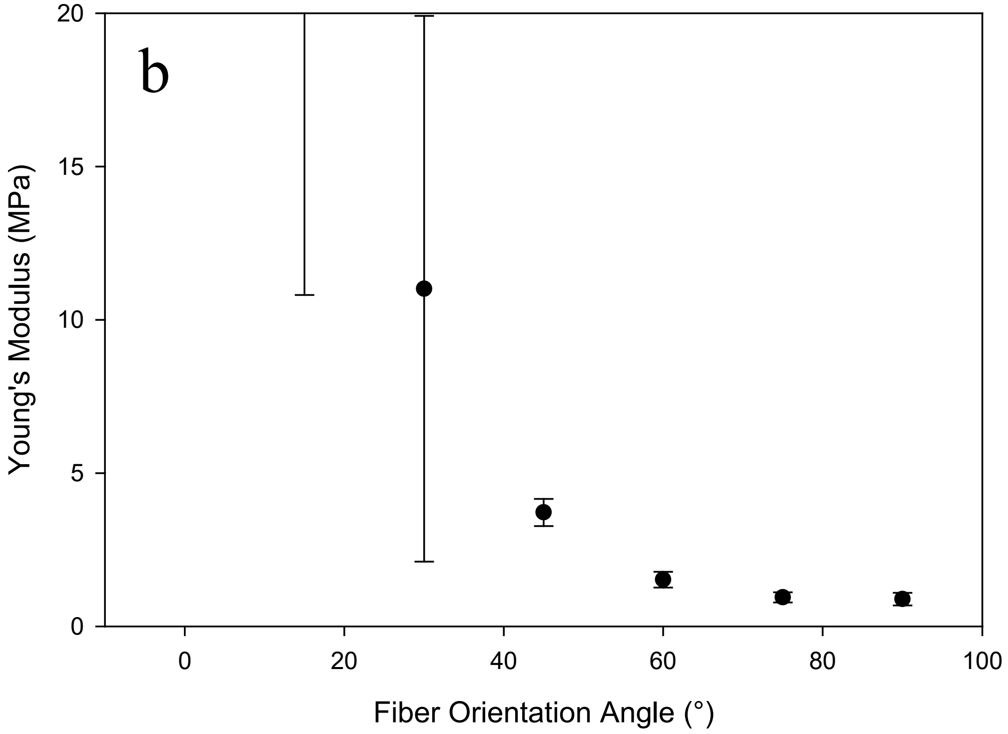
b
Young's Modulus (MPa)
20
15
10
5
0
0
20
40
60
80
100
Fiber Orientation Angle (°)

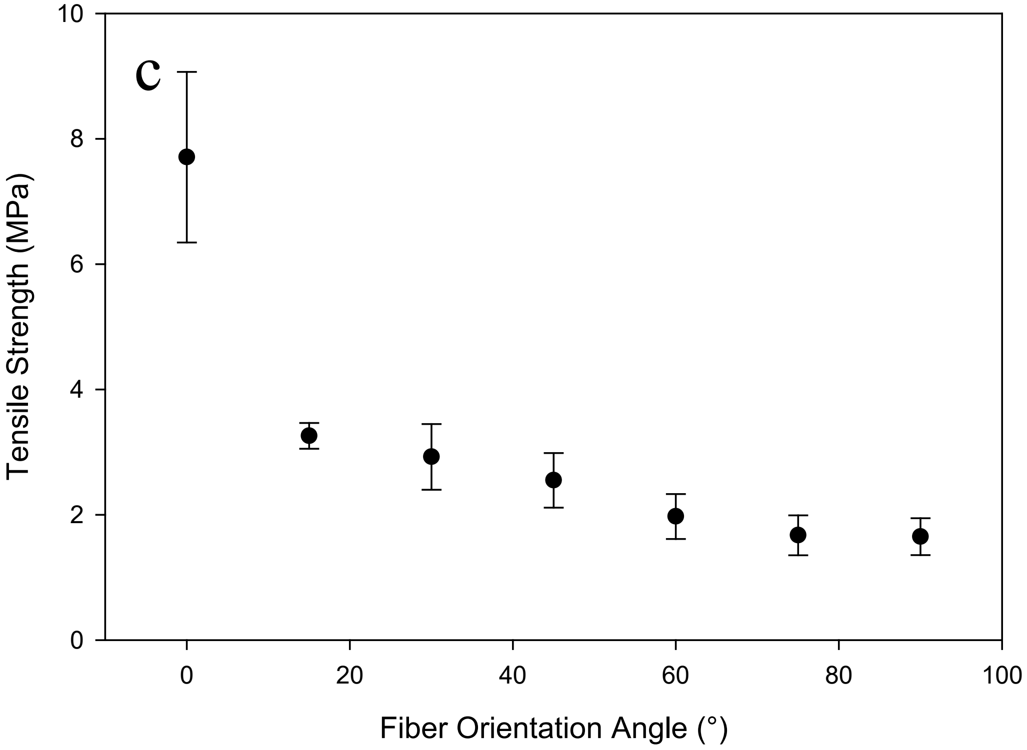
c
Tensile Strength (MPa)
0
2
4
6
8
10
Fiber Orientation Angle (°)
0
20
40
60
80
100

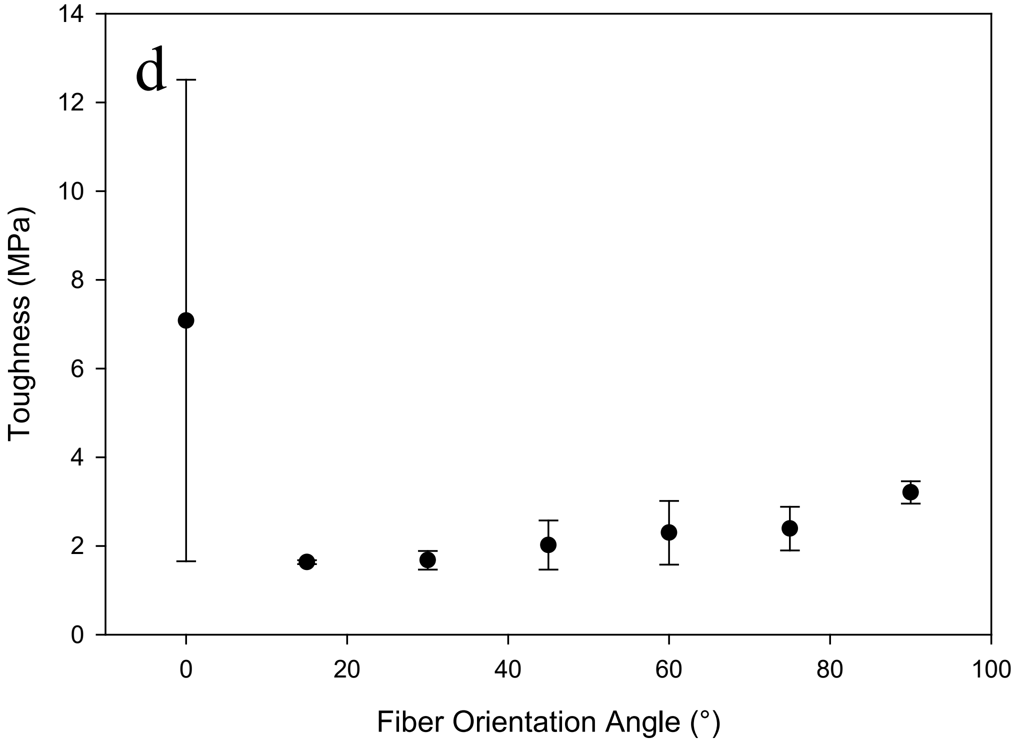
d
Toughness (MPa)
0
2
4
6
8
10
12
14
Fiber Orientation Angle (°)
0
20
40
60
80
100

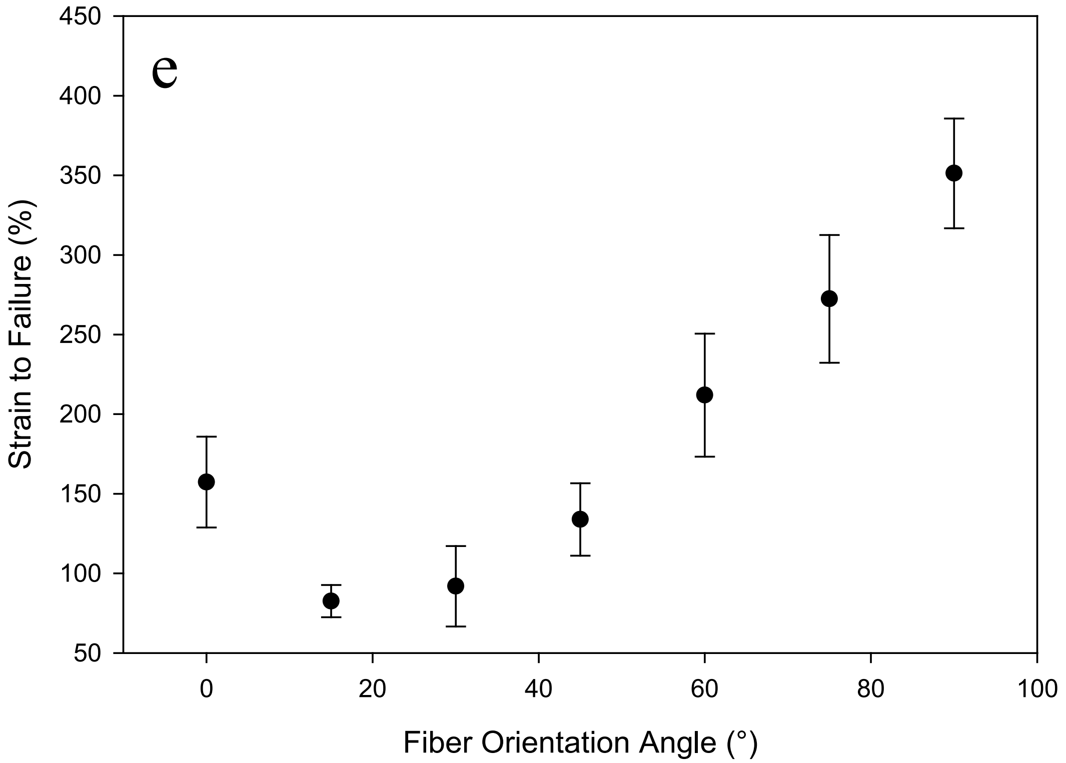

Figure 2-52: Resulting mechanical properties of electrospun trilayer with 3.9×10^{-2} g/cm^2 of Pellethane from tensile testing as a function of the fiber orientation angle. (a) Young's modulus, (b) magnified view of Young's modulus, (c) tensile strength, (d) toughness and (e) strain-to-failure. All data points are an average of n = 5.

Table 2-25: Average Young's modulus, toughness, tensile strength and strain to failure for all fiber orientation angles (Δθ) interpreted from the stress strain curves of the electrospun trilayer with 3.9×10^{-2} g/cm^2 of Pellethane.

Material Property	**Fiber Orientation Angle [°]**						
	0	*15*	*30*	*45*	*60*	*75*	*90*
Young's Modulus [MPa]	287.77 ± 89.3	44.46 ± 33.6	11.01 ± 8.9	3.71 ± 0.4	1.52 ± 0.3	0.94 ± 0.2	0.89 ± 0.2
Toughness [MPa]	7.08 ± 5.4	1.63 ± 0.05	1.68 ± 0.2	2.02 ± 0.5	2.29 ± 0.7	2.39 ± 0.5	3.21 ± 0.3
Tensile Strength [MPa]	7.71 ± 1.4	3.26 ± 0.2	2.92 ± 0.5	2.55 ± 0.4	1.97 ± 0.4	1.67 ± 0.3	1.65 ± 0.3
Strain to Failure [%]	157.28 ± 28.5	82.56 ± 10.1	91.90 ± 25.3	133.79 ± 22.7	211.93 ± 38.7	272.43 ± 40.1	351.28 ± 34.4

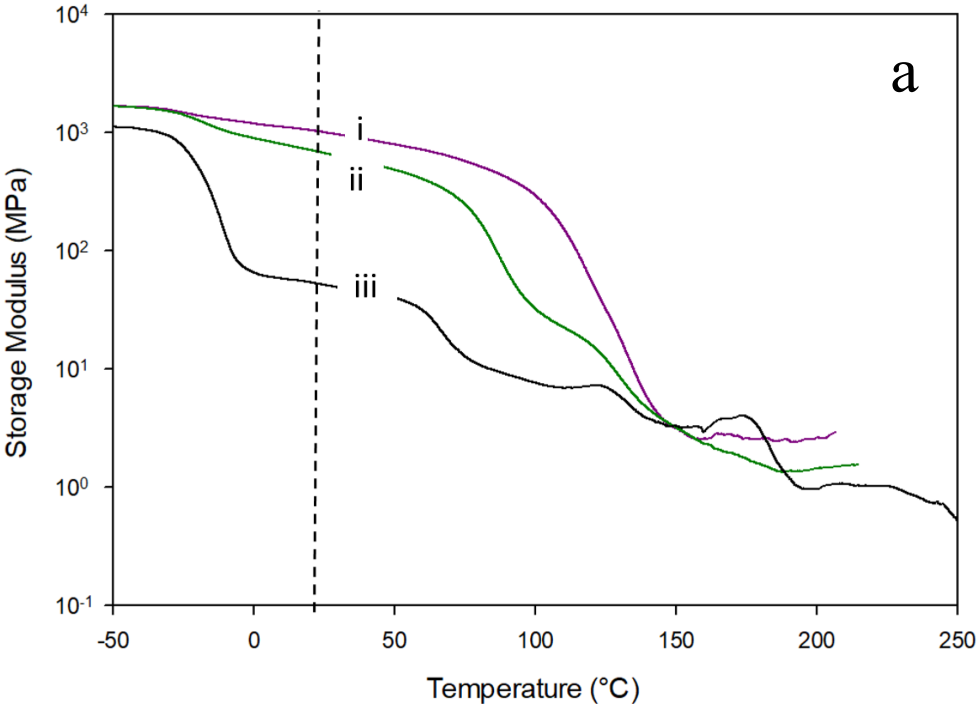
a
Storage Modulus (MPa)
10^4
10^3
10^2
10^1
10^0
10^{-1}
i
ii
iii
-50
0
50
100
150
200
250
Temperature (°C)

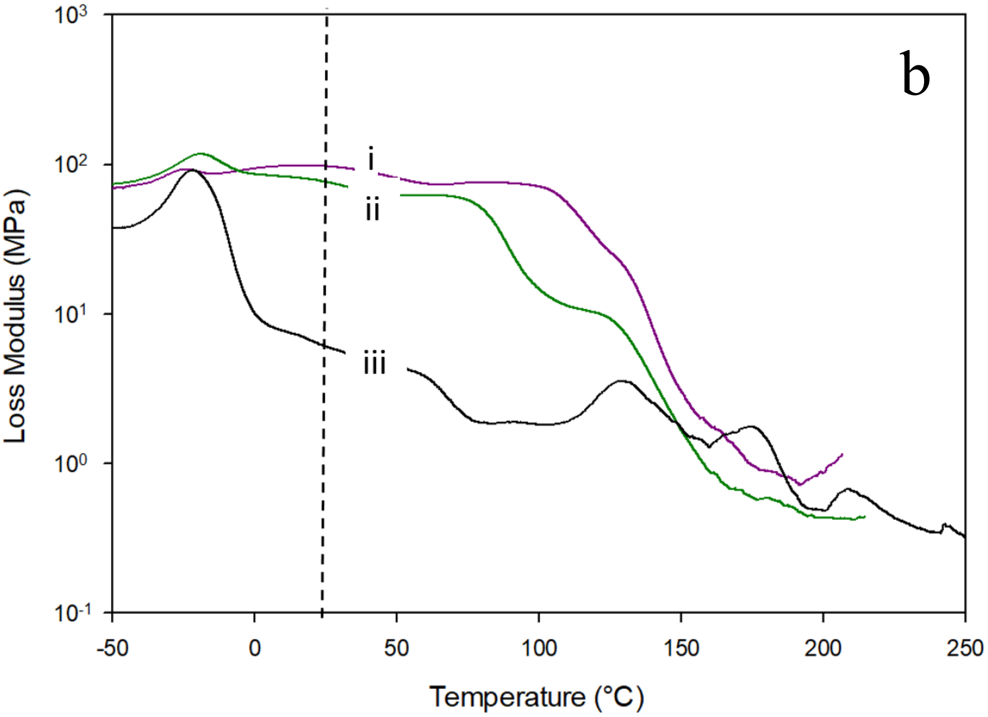
b
Loss Modulus (MPa)
10^3
10^2
10^1
10^0
10^{-1}
i
ii
iii
-50
0
50
100
150
200
250
Temperature (°C)

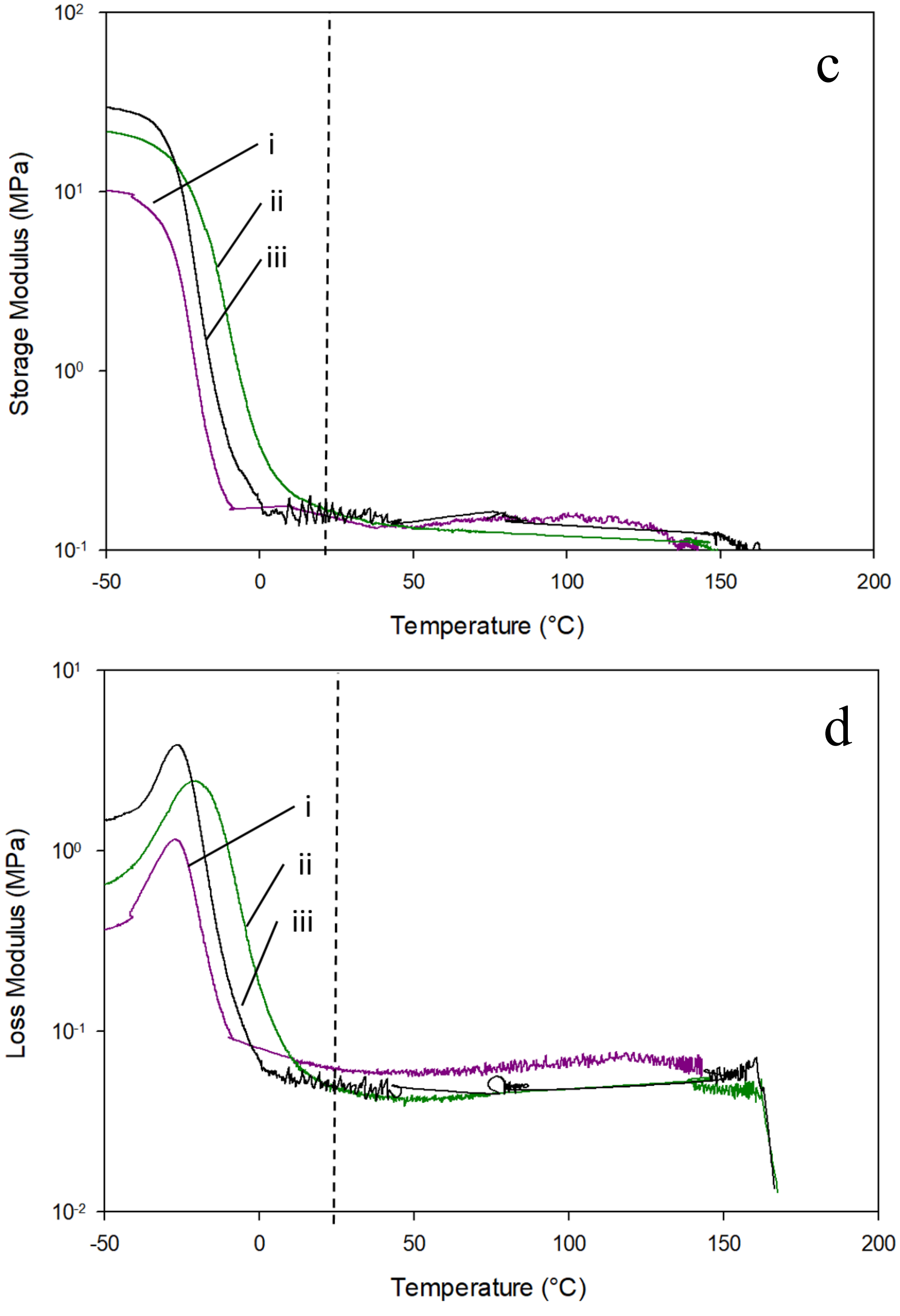

Figure 2-53: Dynamic mechanical analysis of (a) storage and (b) loss modulus for θ = 0° and (c) storage and (d) loss modulus for θ = 90° of electrospun (i) trilayer with $9.8\text{x}10^{-3}$ g/cm^2 of Pellethane (ii) trilayer with $1.9\text{x}10^{-2}$ g/cm^2 of Pellethane and (iii) trilayer with $3.9\text{x}10^{-2}$ g/cm^2 of Pellethane.

Table 2- 26: Anisotropy of the electrospun fiber samples quantified as a function of storage modulus in a ratio of the 0° / 90° fiber orientation angles obtained through interpreting the stress-strain curves.

Sample	Fiber Orientation Angle [°]	$E'_{20\,^{\circ}C}$ (MPa)	Anisotropy
Thin	0	1051.6	7010.7
	90	0.15	
Medium	0	714.1	4200.6
	90	0.17	
Thick	0	54.3	339.4
	90	0.16	

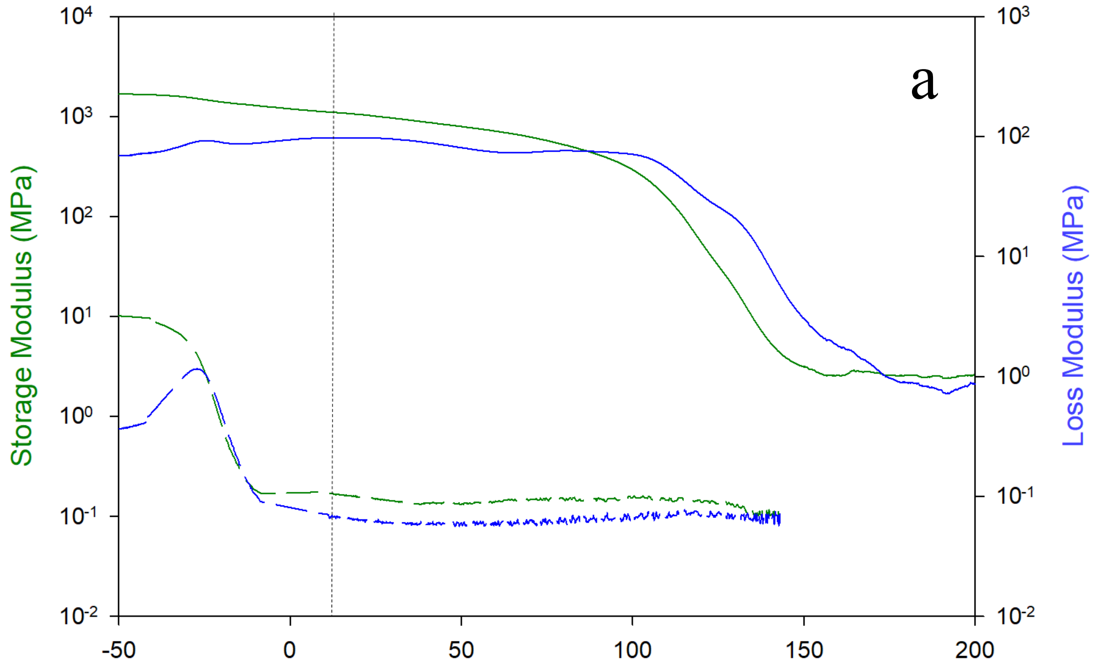

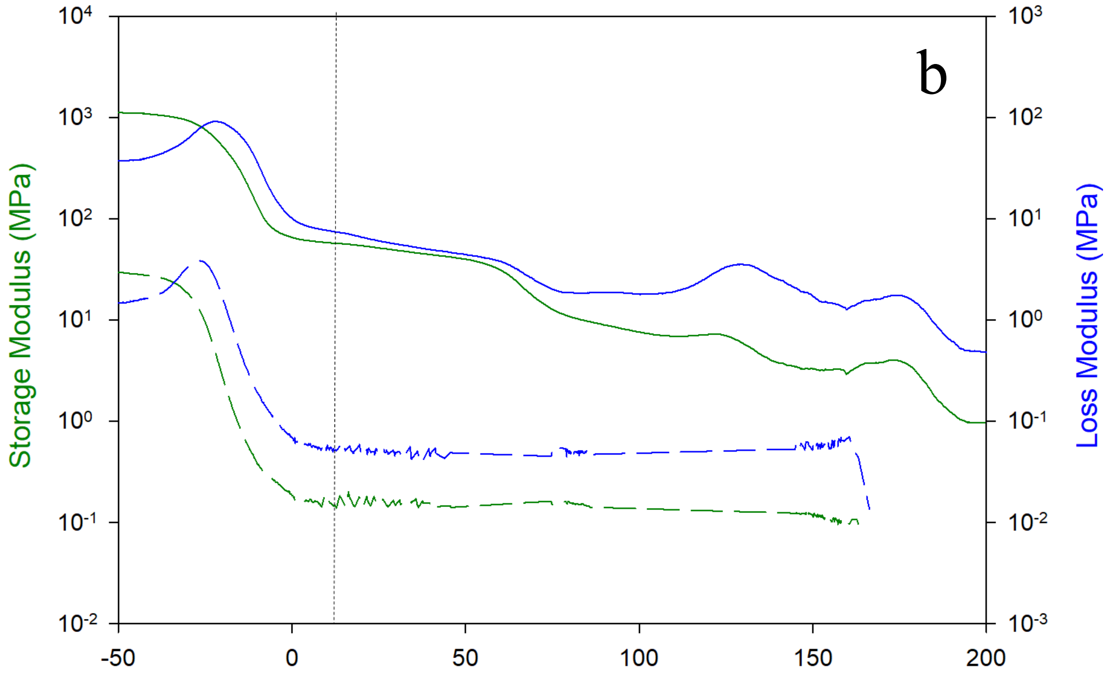

Figure 2- 54: Dynamic mechanical analysis of 0° fiber orientation (solid) and 90° fiber orientation (dashed) for (a) electrospun trilayer with 9.8×10^{-3} g/cm^2 of Pellethane and (b) electrospun trilayer with 3.9×10^{-2} g/cm^2 of Pellethane.

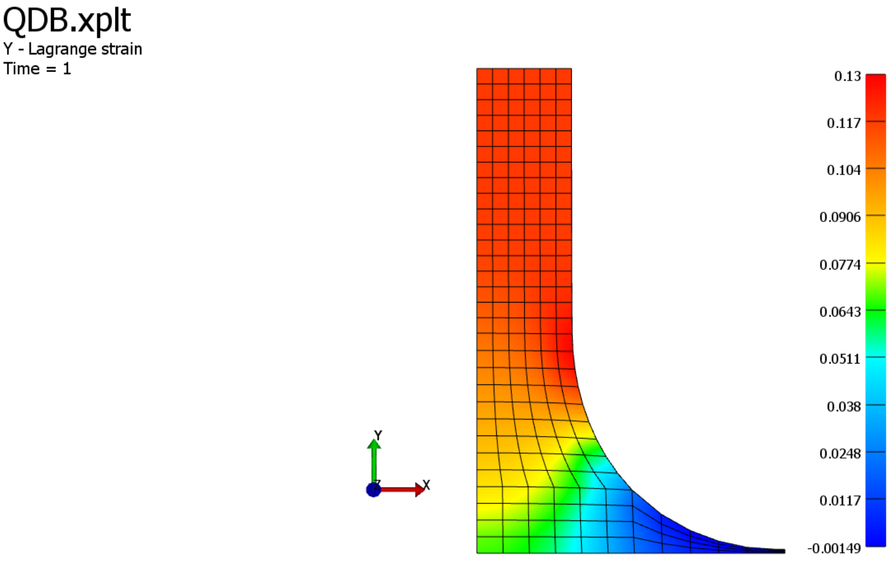

Poisson's Ratio	Strain Multiplier
0.35	1.119
0.4	1.125
0.45	1.131
0.499	1.136

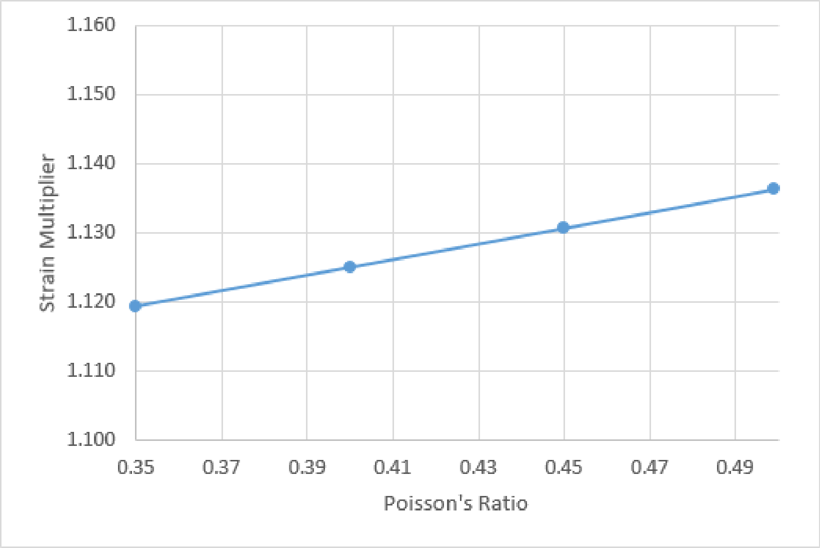

Figure 2-55: Finite element analysis performed by Dr. Benjamin Wheatley[2] to calculate the correction factor for incorrect ASTM dog bones used. The strain multiplier is correlated with Poisson's ratio.

---

[2] . Collaboration with Dr. Benjamin Wheatley (Bucknell University, Mechanical Engineering) 2018

Chapter 3. Design, Processing, and Characterization of a Thermally Triggered Shape Memory Optical Shutter

3.1 Synopsis

This chapter aims to design, fabricate, and characterize a new polymeric composite system that has a shape memory induced change in optical translucency using a thermal trigger. Previous attempts show that the optical translucency of a rubber polymer impregnated with nanoparticles can be reversibly altered through physical deformation. Using this as a proof-of-concept, the current research will use cross-linked poly(*tert*-butyl acrylate) as the thermally triggered shape memory polymer, incorporating silica nanoparticles to achieve a similar effect. In this chapter the optimal method for achieving the shape memory induced optical change, as well as functionally grading the material glass transition temperature, will be investigated.

3.2 Introduction

Developing materials that are thermally responsive is of interest to the packaging industry. How the product is packaged has a profound effect on the efficacy, stability, and even how the consumer views the product.

For instance, packaging[1] of pharmaceuticals is a serious consideration that has highly specific design constraints dictated by the customer. It is prudent to think about the packaging of drugs as a value added product. How the drugs are stored and how they are shipped are often times crucial to the efficacy to the consumer[2]. This concept has already been adopted to prevent a discoloring of the package from chemical interactions between drug and package[2]. Regardless of the general harmlessness of the discoloring to the package, customers will have a negative view of the drug and will be less likely to buy and even use it.

One method developed to address this issue is using thermochromic dyes integrated into polymers to change color and or transparency based on exposure to heat. As demonstrated by

Kanakkanatt[3], the integration of various environmentally sensitive dyes like thermochromic, photochromic, chemichromic, and piezochromic into polymer dispersions is an effective method for color sensing. These dispersions can then be used as coatings for common clear packaging material to enhance the detection of various environmental changes. This technology is desired for the application for transparent containers. Individually such dyes can provide a visually detectable change so that it is apparent to the human eye. Thermochromic dyes can be applied to make visually detectable temperature sensors as demonstrated by Huffer et al[4]. This can be achieved through applying the dye underneath a calibrated scale, to be used near the temperature sensitive area. This dye can be used in application to bar codes labels, which has been shown by Cameron[5]. The previous designs all attempt to address the problem of determining if a container has been exposed to an unsafe temperature.

Transitioning the idea of color change from temperature triggered into mechanically triggered via mechanochromic materials[6], which are materials that will change their color or transparency when pulled or stretched. Research done by Ge et al[7] showed the integration of a Polydimethylsiloxane (PDMS) elastomer matrix with silica nanoparticles. Their work showed that through the mechanical stretching of their composite they were able to achieve local opacity in an otherwise fully transparent material. Once the strain was released, the material would regain its regular transparency. The proposed mechanism of action is local debonding of the elastomer from the incorporated nanoparticles. This deformation causes the matrix to pull away from the particles, which creates void spaces around the particles where light will scatter. Once the strain is released the matrix will re-bond to the particles, removing the void area and minimizing the light scattering.

The present work seeks to develop a new optical shutter with functional grading in the local trigger temperature. Here, functional grading is a variation in composition or structure spatially in one or more directions of a material, resulting in changes in the corresponding material properties. As shown by DiOrio et al[8]. they were able to demonstrate functional grading of glass transition temperature in a curing polymer, namely NOA63. This was accomplished through curing the shape memory polymer[9–11] on a temperature stage where one side was cooled and the opposite side was heated. The altering of the curing kinetics of the polymer in segments causes the resulting polymer to have a different glass transition temperature along the length.

The present research focuses on the development of a transparency-changing thermochromic polymer[12] using the shape memory effect. *Tert*-butyl acrylate monomers[13] will be polymerized when mixed with a photo-initiator and cross linking agent through UV and heat exposure. Functional grading of this material will also be achieved by curing on a temperature stage as shown by DiOrio et al. The material, upon heating and deformation will become optically opaque[14]. Upon the exposure to heat the material will recover to its originally optical clear state. Through functional grading, the recovery will occur in a spatially graded manner, from one sample end to the other, as the temperature is increased.

3.3 Experimental

3.3.1 Materials

Tert-butyl acrylate monomer (TBA), azobisisobutyronitrile (AIBN), triethylene glycol dimethacrylate (TEGDMA) and silica nanoparticles (200 nm) (CAS # 7631-86-9) were all purchased from Sigma- Aldrich. The tert-butyl acrylate was filtered through a column drop wise to remove the monomethyl ether hydroquinone, which is an inhibitor. All other materials were used as received.

3.3.2 Mold Fabrication

A mold was created using two standard sized glass slides (75 mm x 25 mm x 1 mm), a Teflon spacer (0.381 mm thick) and binder clips. Commercially available Rain-x was applied to the glass slides to prevent adhesion of the polymer to the glass. A Teflon spacer was sandwiched between the two glass slides. Binder clips were placed around the perimeter of the mold, which sealed the mold together to prevent the *tert*-butyl acrylate solution from leaking out.

3.3.3 Polymerization

Tert-butyl acrylate monomer was mixed with 5 wt.% triethylene glycol dimethacrylate, 0.3 wt.% of azobisisobutyronitrile and 3 wt.% of silica nanoparticles. This solution was sealed in a vial and sonicated for 20 mins to create a uniform suspension of silica nanoparticles as shown in **Scheme 3-1**. The solution was injection into a mold, made as per section 3.3.2, and allowed to cure under UV light (400nm) for 45 min, which caused the monomer to undergo radical polymerization **Scheme 3-2**.

3.3.4 Temperature Stage

Custom temperature stage was fabricated that follows a technical guide published by NIST[8]. A temperature gradient is created by heating one end (via a heating element) and cooling the other end (via a cooling unit). The heating unit is a cartridge heater (300W McMaster-Carr) and temperature controller (ETR-9090 from OGDEN) with a type T thermocouple. The cooling unit circulates room temperature water at a constant flow rate using a submersion pump (model 1C-MD-1, March MFG., Inc.).

3.3.5 Functional Grading

All samples were partially cured under UV light for 10 min. This was used to increase the viscosity of the solution enough to remove the molds binder clips, which allows it to be free standing, and then placed directly onto the temperature stage. The heating element was set to 143 °C, and cooling unit using 32 °C water was allowed to circulate. Temperature stage was equilibrated for 1h. The partially cured sample was placed onto stage with a singular glass slide underneath it. Samples were allowed to cure on temperature stage for a continuous 16 h.

3.3.6 Shape Memory Characterization

Dynamic mechanical analysis (DMA) was used on samples of poly(*tert*-butyl acrylate) for shape memory characterization using a custom program for the TA Instruments Q800 dynamic mechanical analyzer. Each sample was first heated to 90 °C, an oscillatory stress of 1Hz with a displacement amount of 30 % was then applied. The samples were then quenched to 0 °C, a release of the applied stress, followed by the samples being heated to 90 °C. All heating and cooling rates were done at 2 °C/min.

3.3.7 Optical Spectroscopy

Each sample opacity was determined through directly measuring the transmittance, which was done using an Ocean Optics S200 fiber optic spectrometer which is integrated onto an optical microscope. All samples were tested in the initial optically clear state to establish a clear base line $I_0(\lambda)$. The sample were tested again once stretched and optically opaque to quantify the sample translucency $I(\lambda)$. All raw data's are collected and translucency is calculated using the **Eq. 3-1** below

$$\text{Translucency (\%)} = \frac{I(\lambda) - I_{dark}(\lambda)}{I_0(\lambda) - I_{dark}(\lambda)} * 100 \tag{3-1}$$

The spectra sample curve $I(\lambda)$, dark reference $I_{dark}(\lambda)$, and light reference $I_0(\lambda)$ correspond to the integration of the graph of intensity (y-axis) vs wavelength (x-axis) for the intensity of light transmittance for the sample, with complete opacity and with complete transparency respectively.

3.4 Results

3.4.1 Poly(*tert*-butyl acrylate)

3.4.1.1 Synthesis

The poly(*tert*-butyl acrylate) polymer was successfully synthesized using the process roughly shown in **Scheme 3-1**, excluding the silica nanoparticles. The low viscosity fluid containing *tert*-butyl acrylate monomer, azobisisobutyronitrile photoinitiator, and triethylene glycol dimethacrylate crosslinking agent were polymerized together following **Scheme 3-2**. When completely polymerized the resulting material is rigid and optically clear at room temperature.

3.4.1.2 Thermal Analysis

Thermogravimetric analysis was used to determine the thermal stability of the polymer and understand its thermally induced degradation as seen in **Figure 3-1**. The non-monotonic response in its thermal decay shows the *tert*-butyl acrylate groups being removed abruptly, followed by the slower backbone degradation.

Dynamic scanning calorimetry (DSC) was used to determine the glass transition of pure poly(*tert*-butyl acrylate) shown in **Figure 3-2**. The poly(*tert*-butyl acrylate) polymer has a glass transition temperature of 45 °C. This was used as a guidance for determining an appropriate upper limit for shape memory characterization. The heating phase of shape memory testing should be done above the polymers glass transition temperature.

3.4.1.3 Shape Memory Characterization

Quantifying the shape memory ability of poly(*tert*-butyl acrylate) was done using the method described in section 3.3.6 and shown in **Figure 3-3**. The polymers ability to fix a temporary second shape, seen in section (iii) of the graph, was quantified using **Eq.1-1**. The poly(*tert*-butyl acrylate) has a 99% fixing ratio. The ability of the polymer to recover, seen in section (iv) of the graph was quantified using **Eq.1-2**. The poly(*tert*-butyl acrylate) has a 99% recovery ratio.

3.4.2 Combinations of poly(*tert*-butyl acrylate)

Several variations of silica nanoparticles and electrospun fibers were integrated with poly(*tert*-butyl acrylate) for the purpose of determining which variation has the highest initial optical clarity, the lowest stretched optical clarity, and highest recovery clarity. A modified shape memory method was applied to these materials as shown in **Scheme 3-3** using the manual stretcher shown in **Figure 3-4**. For visual identification of the optical change in the material the shape memory method was applied manually, and not via the DMA.

The different samples made are shown in **Figure 3-5**. The left column in **Figure 3-5** shows the as cured state of the composites and all but one of the samples begins translucent. The refractory index between the electrospun poly(ε-caprolactone) fibers and poly(tert-butyl acrylate) are different, which negatively affects the materials optical clarity. Each sample was heated then manually stretch 40% and cooled while in the deformed state as shown in the middle column in **Figure 3-5**. The optical change from translucent to opaque for the samples with 3 wt.% and 5 wt.% silica nanoparticles is immediately apparent. Upon recovery of the samples as seen in the right column in **Figure 3-5**. all of them return to optically translucent.

The best performing composites, in terms of a change in optical clarity upon deformation, are the composites with 3 wt.% and 5 wt.% silica nanoparticles incorporated.

3.4.2.1 Optical Spectroscopy Analysis

Quantifying the optical translucency of all the composites made was done according to section 3.3.7 as shown in **Figure 3-6**. The data collected from this method is summarized in graphical form in **Figure 3-7** and tabular form in **Table 3-1**. The composites that had the biggest change of their optical clarity from the "as cured" state to the "recovered" state was the composites with 3 wt.% and 5 wt.% silica nanoparticles incorporated. Although both composites performed comparably the composite using 3 wt.% silica nanoparticles was used for all subsequent experiments. The reason for this was that the 3 wt. % silica nanoparticle sample used less silica nanoparticles, and thus it was less expensive to fabricate.

3.4.2.2 Image analysis

The theorized mechanism for the translucency change that occurs, in the composite with 3 wt.% silica nanoparticles incorporated, during specifically the stretching phase is depicted in **Scheme 3-4**. This mechanism is similar to that proposed by Ge et.al[7] which states that the matrix material is able to partially detach from the dispersed particles. This in turn creates void spaces by which light can scatter. This mechanistic evidence is shown in **Figure 3-8** where an SEM image of void spaces created in the matrix around the silica particles, for a stretched sample of poly(*tert*-butyl acrylate) with 3 wt.% silica nanoparticles dispersed, can be seen.

3.4.3 Poly(*tert*-butyl acrylate) incorporated with 3 wt.% Silica Nanoparticle

3.4.3.1 Cycling Strain Analysis Maximum Strain Analysis

The best preforming sample, poly(*tert*-butyl acrylate) with 3 wt. % silica nanoparticles was subjected to cyclical stretching, fixing and recovery cycles. This process was repeated for five cycles, with translucency data being collected for each step as seen in **Figure 3-9**. This graph shows that the fixed translucency remains low, and the recovered translucency remains high, which demonstrates there is no loss optical clarity in the sample over the cycling process.

3.4.3.2 Maximum Strain Analysis

Similarly to the cycling experiment, the poly(*tert*-butyl acrylate) with 3 wt. % silica nanoparticles was cycled similarly to section 3.4.3.1 with the difference being in the amount of strain applied in each cycle. This was to estimate the effect of strain for possible maximization of gain in optical opacity. As seen in **Figure 3-10** the translucency data beings to level off after 30 % strain. It was determined that 30% strain would be best for straining the samples. Increasing the strain doesn't increase the opacity, and it increased chance of tearing the sample.

3.4.4 Functional Grading of Poly(*tert*-butyl acrylate) incorporated with 3 wt.% Silica Nanoparticles

The poly(*tert*-butyl acrylate) polymer with 3 wt. % silica nanoparticles has a spatially graded glass transition temperature. The glass transition temperature was found to increase in response to thermal post curing at high temperatures. Generally this can be interpreted from the reaction kinetics. While the *tert*-butyl acrylate is being photocured the glass transition increases with the conversion until it reaches the ambient temperature. During this process, vitrification occurs which drastically limits the reaction rate due to polymer chain immobility and slow diffusion. When the ambient temperature is increased the polymer chains become mobile and continue with the polymerization reaction, until the material reaches the elevated ambient temperature or until the ultimate glass transition temperature is reached, whichever is the lowest. The complete conversion of monomers will cause the polymer to have the highest glass transition temperature possible, for that polymer. The result is a method to control the glass transition temperature by changing the ambient temperature as long as it is lower than the ultimate glass transition temperature. This process is most applicable for amorphous polymers like poly(*tert*-butyl acrylate).

A thermal gradient, for post curing was created using **Figure 3-11** and was confirmed using a thermal camera as shown in **Figure 3-12**. The polymer samples were partially cured under the UV light for 10 min and then placed directly onto the temperature gradient for 16 h. As seen in **Figure 3-13** temperature measurements were taken of the aluminum stage and glass slide, which confirm a thermally spaced gradient was achieved. The figure also shows the glass transition temperature of the sample, as measured by DSC, increases along the length of the polymer.

The sample was heated to 80 °C then stretched to make the sample fully opaque. The sample was then placed onto a Peltier plate for the AR-G2 TA rheometer for precise temperature control, and then slowly heated. As shown in **Figure 3-14** images taken of the sample at each temperature increment shows a slow partial recovery occurring from right to left. The far left of the sample (highest T_g) was kept clear for the purpose of tracking the length change. The releasing of trapped stresses causes a curling of the sample on the far right, which is indicative that it is recovery before the far left side. The temperature was incrementally heated until the entire sample has recovered at 51 °C. Translucency measurement were taken for each temperature increment along the length of the sample as seen in **Figure 3-15**. This shows that as the temperature is increased the translucency of the material increases from left to right as the lower T_g side(right) is recovering before the higher T_g side (left).

3.5 Conclusions

A unique thermally activated optical shutter using shape memory has been introduced. This has been achieved through integration of commercially available silica nanoparticle dispersed through a *poly*-*tert*-butyl acrylate polymer. Polymerized samples show high optical clarity, while stretched samples show high optical opacity. In a fixed opaque stretched state, using a thermal trigger, we can induce a relaxation of the sample to recover it to optically clear. Furthermore functional grading of this material was achieved via spatial control over the curing temperature. Demonstration of this showed the material will become optically clear in stages. This smart material could be adapted to work as a visually recognizable temperature sensor for high value products where temperature sensitivity is paramount.

3.6 References

1. Piringer, O. G. & Baner, A. L. *Plastic Packaging: Interactions with Food and Pharmaceuticals*. (John Wiley & Sons, 2008).

2. Farris, S., Schaich, K. M., Liu, L., Piergiovanni, L. & Yam, K. L. Development of polyion-complex hydrogels as an alternative approach for the production of bio-based polymers for food packaging applications: a review. *Trends Food Sci. Technol.* **20**, 316–332 (2009).

3. Kanakkanatt, S. V. Method of Using Multichromic Polymers in Packaging. US5501945A, March 26, 1996.

4. Huffer, S.; Rudick, A. Packaging with Incorporated Temperature Sensitive Label. US6544614B1, April 8, 2003.

5. Cameron, J. Thermochromic Bar Code. US6685094B2, February 3, 2004.

6. Pucci, A. & Ruggeri, G. Mechanochromic polymer blends. *J. Mater. Chem.* **21**, 8282–8291 (2011).

7. Ge, D. *et al.* A Robust Smart Window: Reversibly Switching from High Transparency to Angle-Independent Structural Color Display. *Adv. Mater.* **27**, 2489–2495 (2015).

8. DiOrio, A. M., Luo, X., Lee, K. M. & Mather, P. T. A functionally graded shape memory polymer. *Soft Matter* **7**, 68–74 (2011).

9. Liu, C., Qin, H. & Mather, P. T. Review of progress in shape-memory polymers. *J. Mater. Chem.* **17**, 1543–1558 (2007).

10. Rousseau, I. A. Challenges of shape memory polymers: A review of the progress toward overcoming SMP's limitations. *Polym. Eng. Amp Sci.* **48**, 2075–2089 (2008).

11. Meng, H. & Li, G. A review of stimuli-responsive shape memory polymer composites. *Polymer* **54**, 2199–2221 (2013).

12. Seeboth, A., Lötzsch, D., Ruhmann, R. & Muehling, O. Thermochromic Polymers—Function by Design. *Chem. Rev.* **114**, 3037–3068 (2014).

13. Page, Z. A. *et al.* A di-tert-butyl acrylate monomer for controlled radical photopolymerization. *J. Polym. Sci. Part Polym. Chem.* **55**, 801–807 (2017).

14. Goodman, M., Abe, A. & Fan, Y.-L. Optically active polymers. *J. Polym. Sci. Macromol. Rev.* **1**, 1–33 (1967).

3.8 Figures, Schemes and Tables

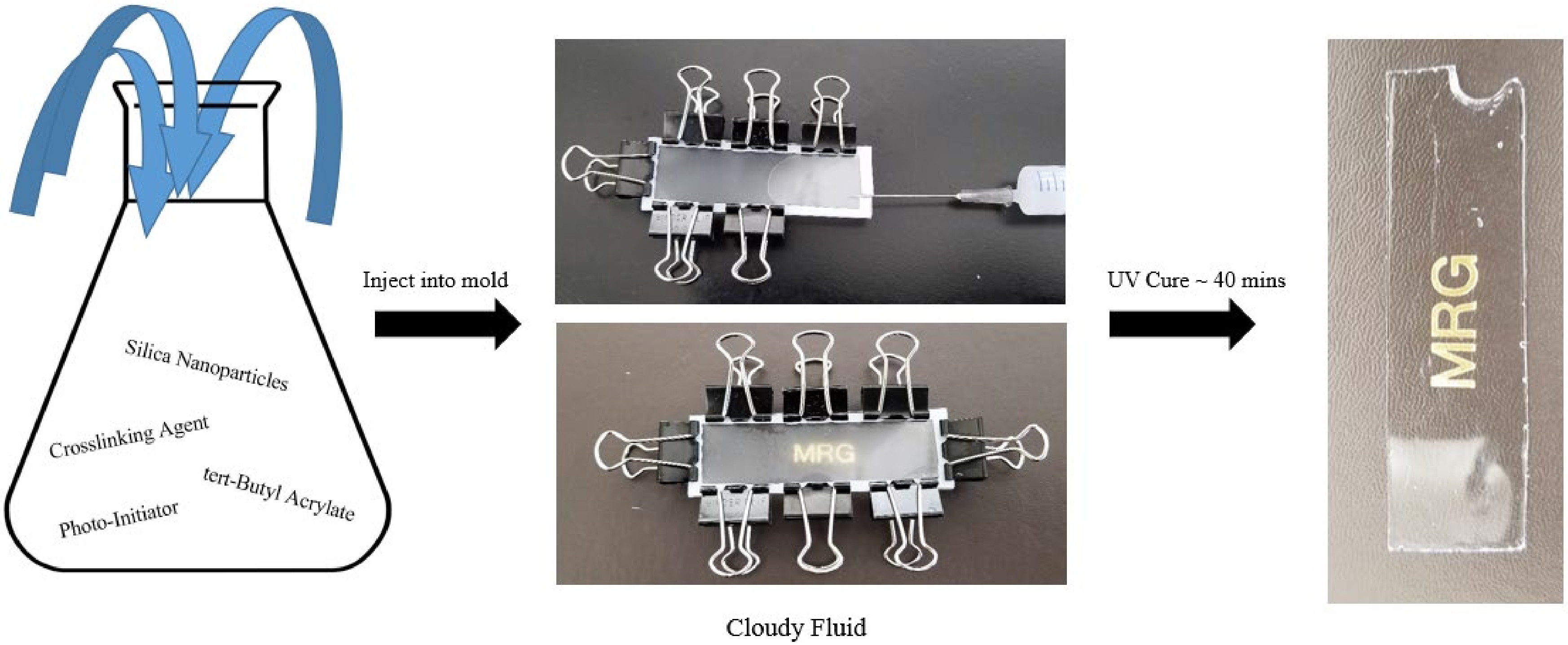

Scheme 3-1: General process for the fabrication of poly(tert-butyl acrylate) polymer film. Tert-butyl acrylate monomer, cross linking agent, photo initiator and the silica nanoparticles are mixed together in a reaction vessel. The solution is then injected into a mold, and then cured for 40 min under ultra violet lights. A final transparent rigid polymer is produced.

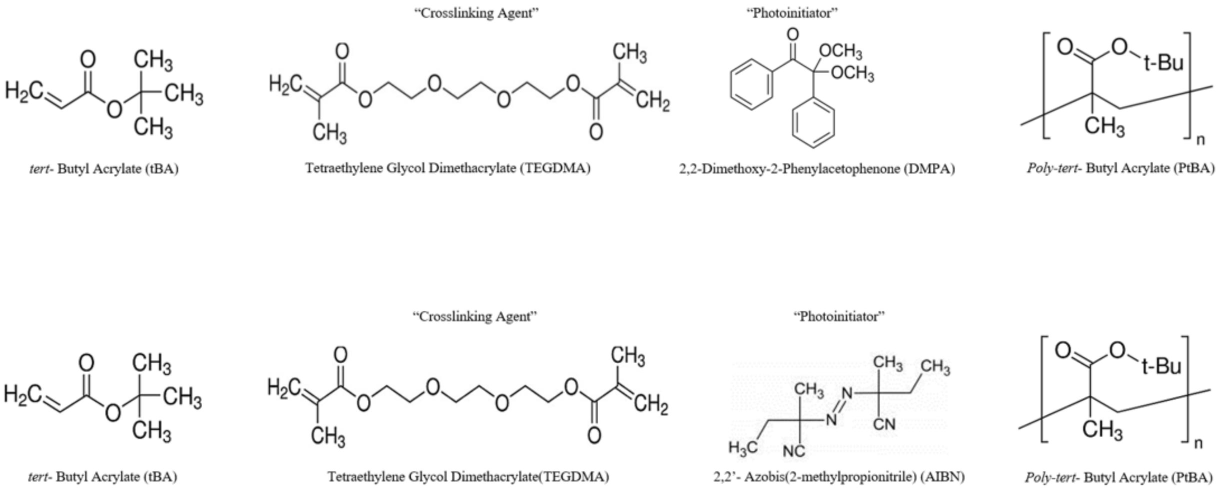

tert- Butyl Acrylate (tBA) Tetraethylene Glycol Dimethacrylate (TEGDMA) 2,2-Dimethoxy-2-Phenylacetophenone (DMPA) *Poly-tert-* Butyl Acrylate (PtBA)

tert- Butyl Acrylate (tBA) Tetraethylene Glycol Dimethacrylate(TEGDMA) 2,2'- Azobis(2-methylpropionitrile) (AIBN) *Poly-tert-* Butyl Acrylate (PtBA)

Scheme 3-2: Chemical structures of the various components responsible for the polymerization of tert-butyl acrylate monomer. Two separate photo initiators were used in the process, both DMPA and AIBN. AIBN is both a thermal and photo initiator, which was used for the functional grading.

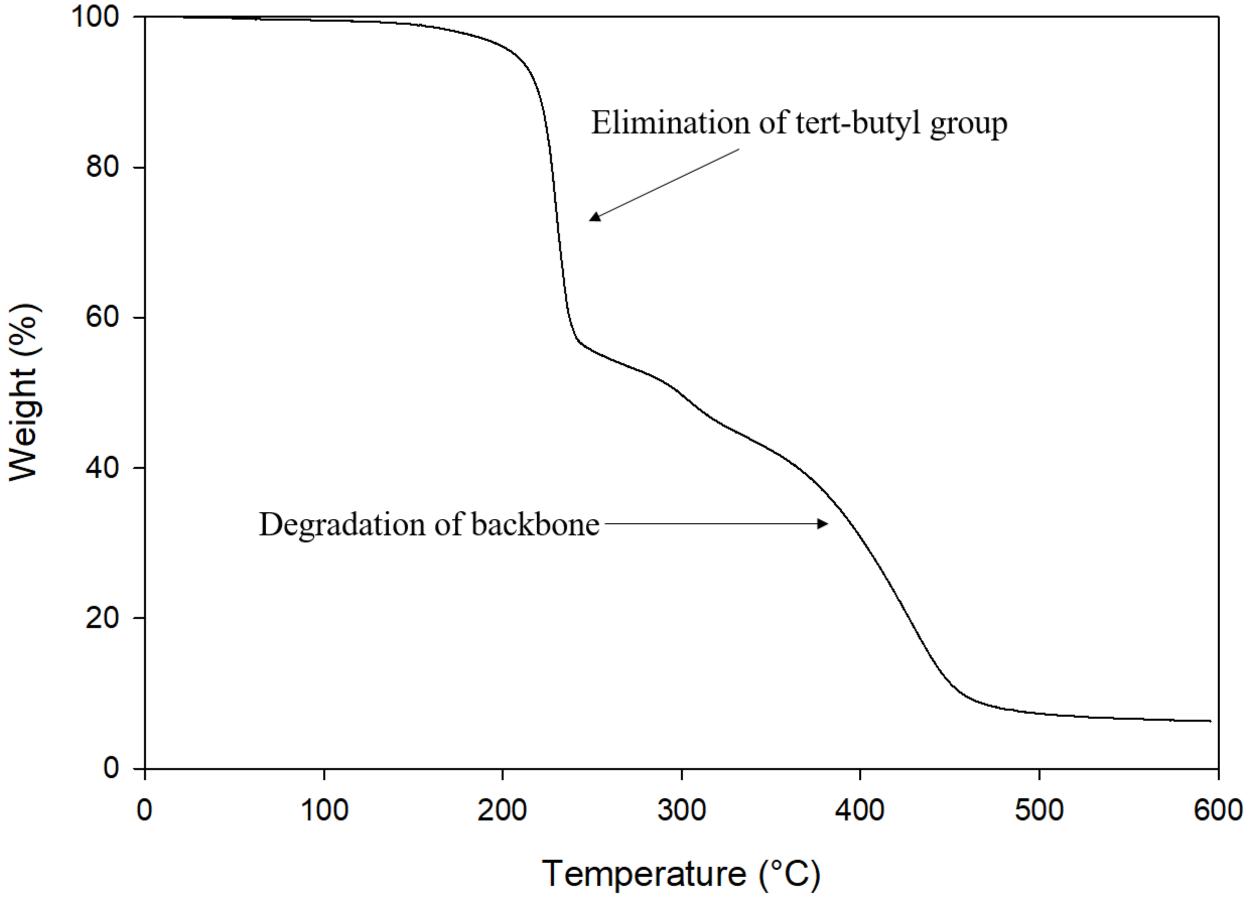

Figure 3-1: TGA mass loss curve as a function of temperature for poly(*tert*-butyl acrylate).

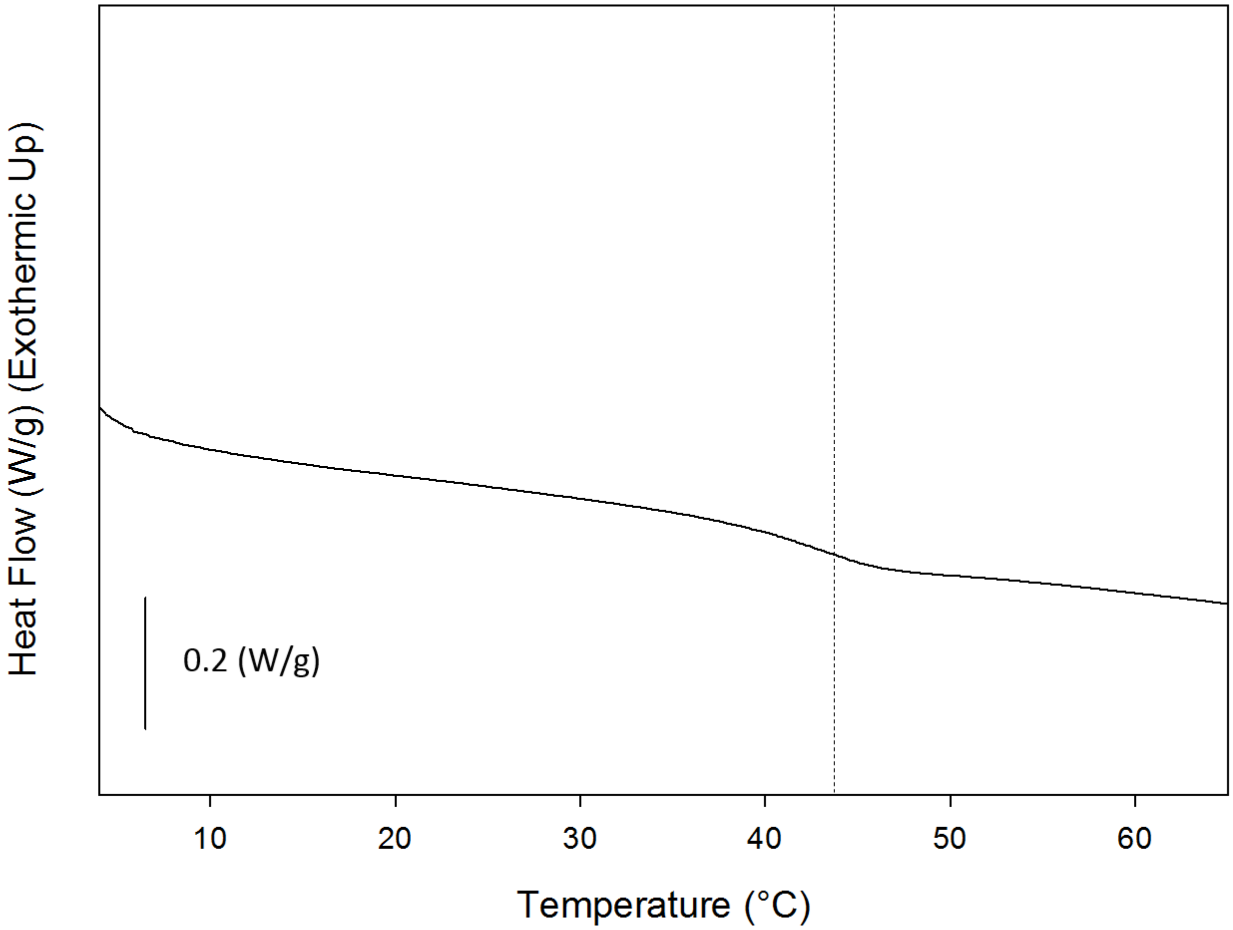

Figure 3-2: DSC of the second heating curve for poly(*tert*-butyl acrylate). The measured glass transition temperature (T_g) is 45 °C.

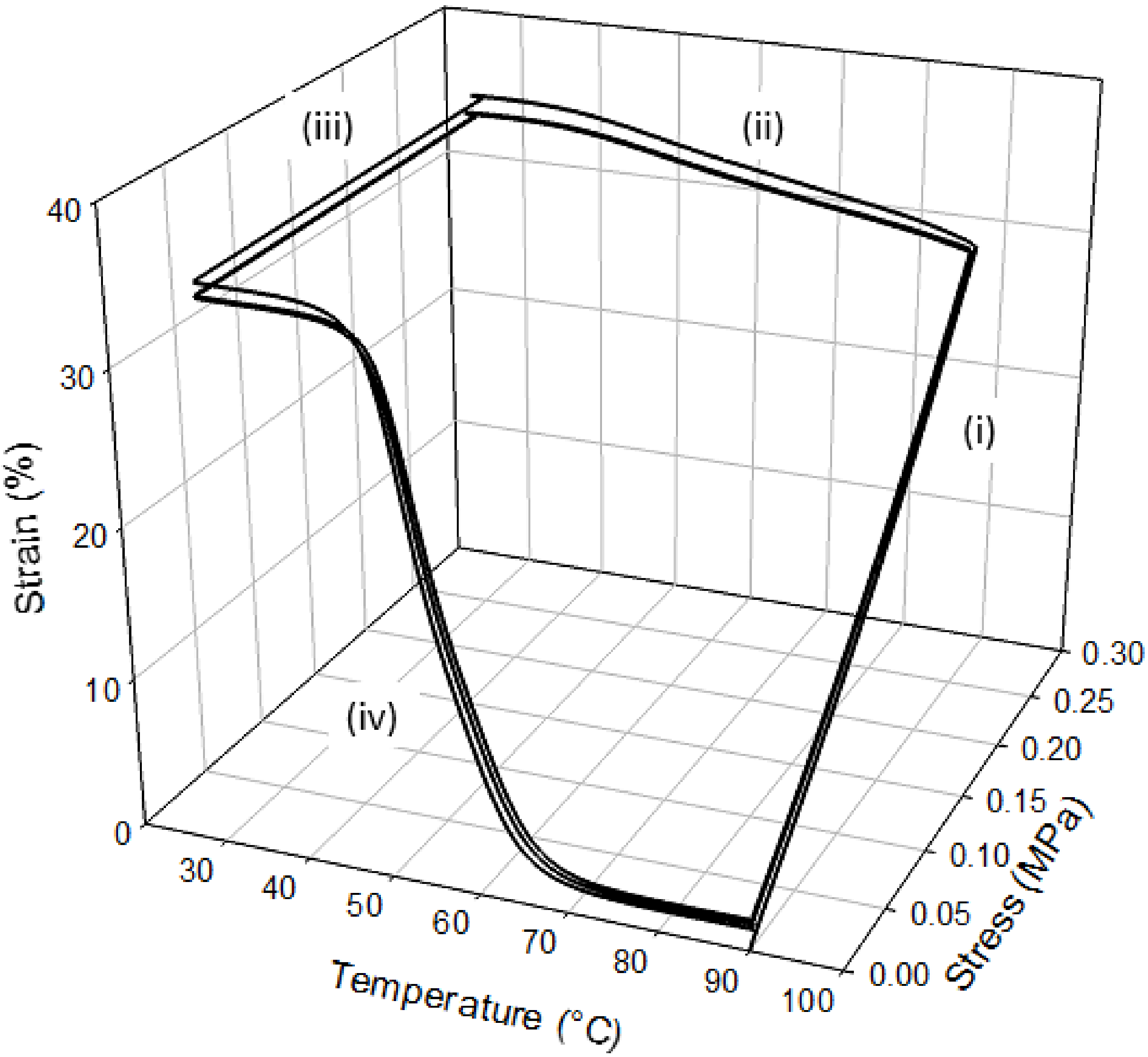

Figure 3-3: Conventional one way shape memory (1WSM) testing of poly(*tert*-butyl acrylate) showing four distinct steps. The 1WSM method involved equilibrating the temperature to 90.00 °C, isothermal for 5 min, then (i) ramped force at 0.0500 N/min to 0.25 N, isothermal for 2 min, (ii) ramped 2 °C/min to 0 °C, isothermal for 2 min, (iii) ramped force 0.2000 N/min to 0.0010 N, isothermal for 2 min and ramped 2 °C/min to 90.00 °C, isothermal for 2 min to complete cycle.

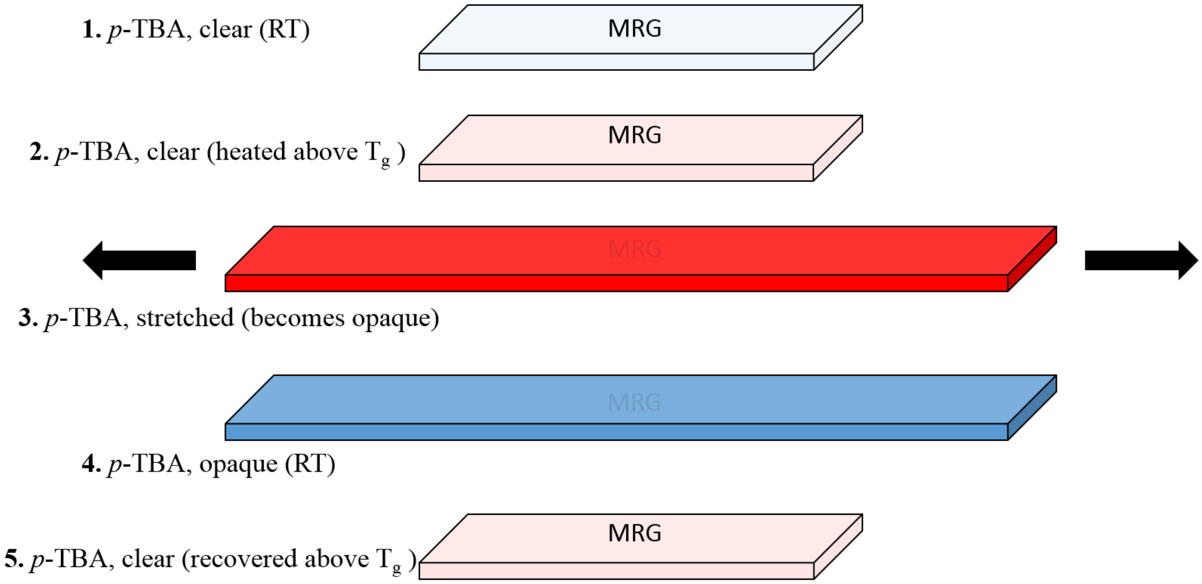

Scheme 3-3: Shape memory process used to measure translucency of all poly(*tert*-butyl acrylate) samples.

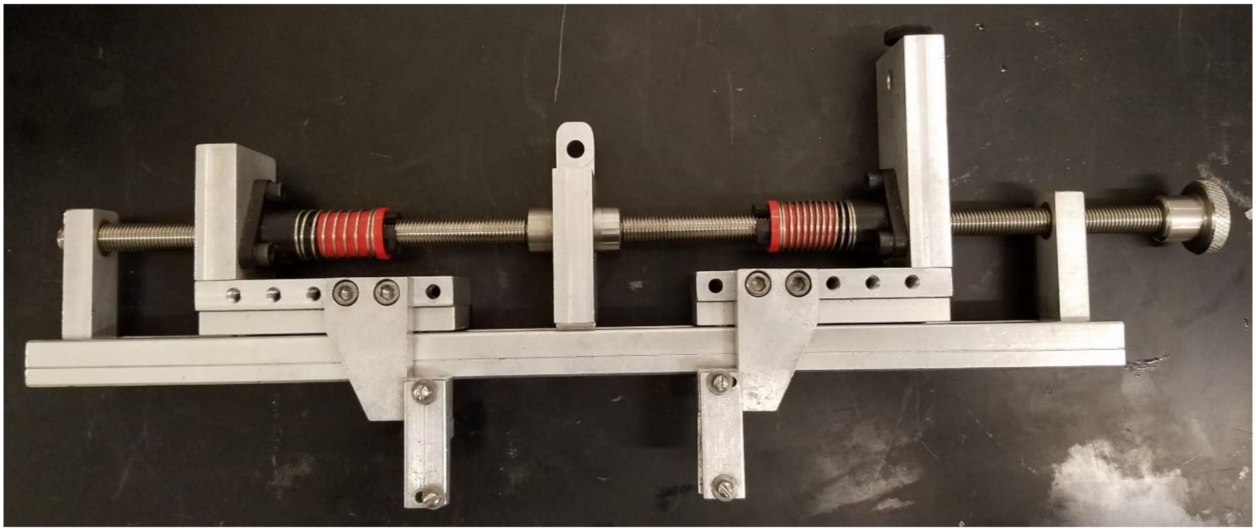

Figure 3-4: Manual stretcher custom made by the machine shop at Syracuse University.

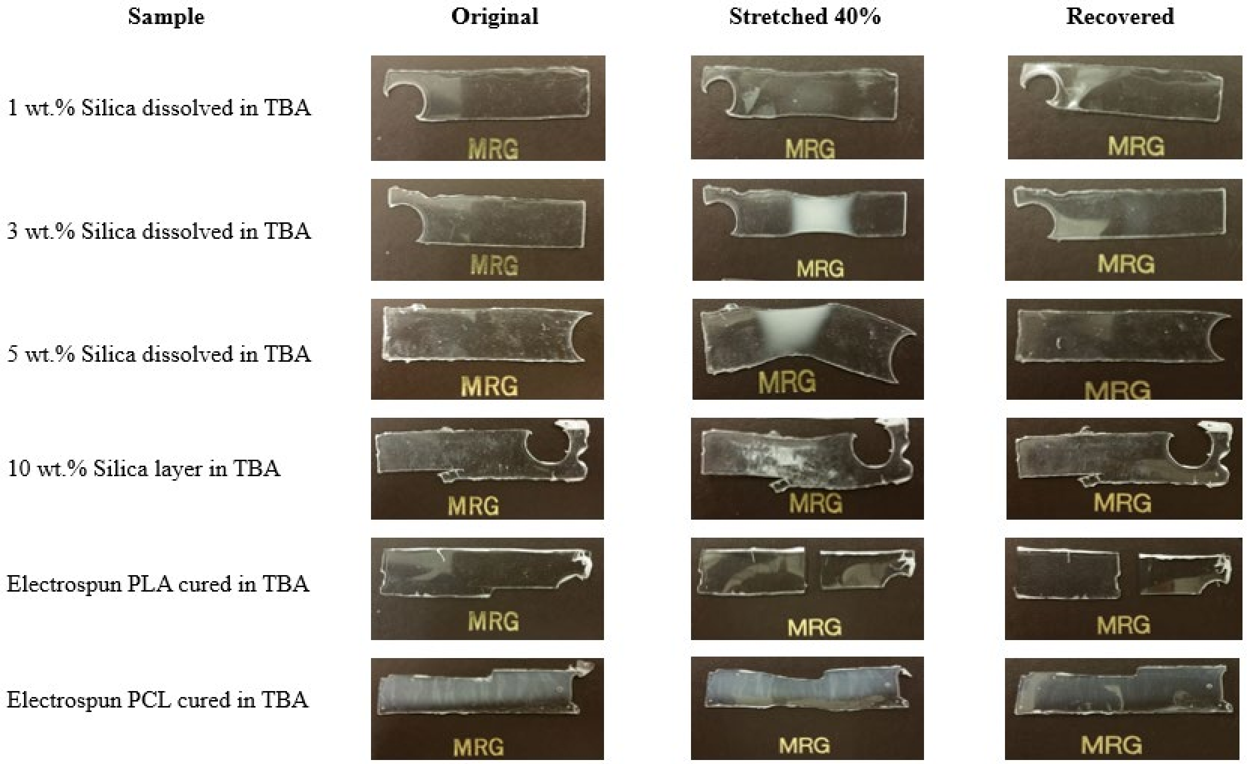

Figure 3-5: Series of images of showing the combinations used to achieve high stretched opacity. Each combination was cured (original), heated above the T_g, stretched and then cooled under constraint (stretched 40%) and finally heated above the T_g and allowed to recover (recovered).

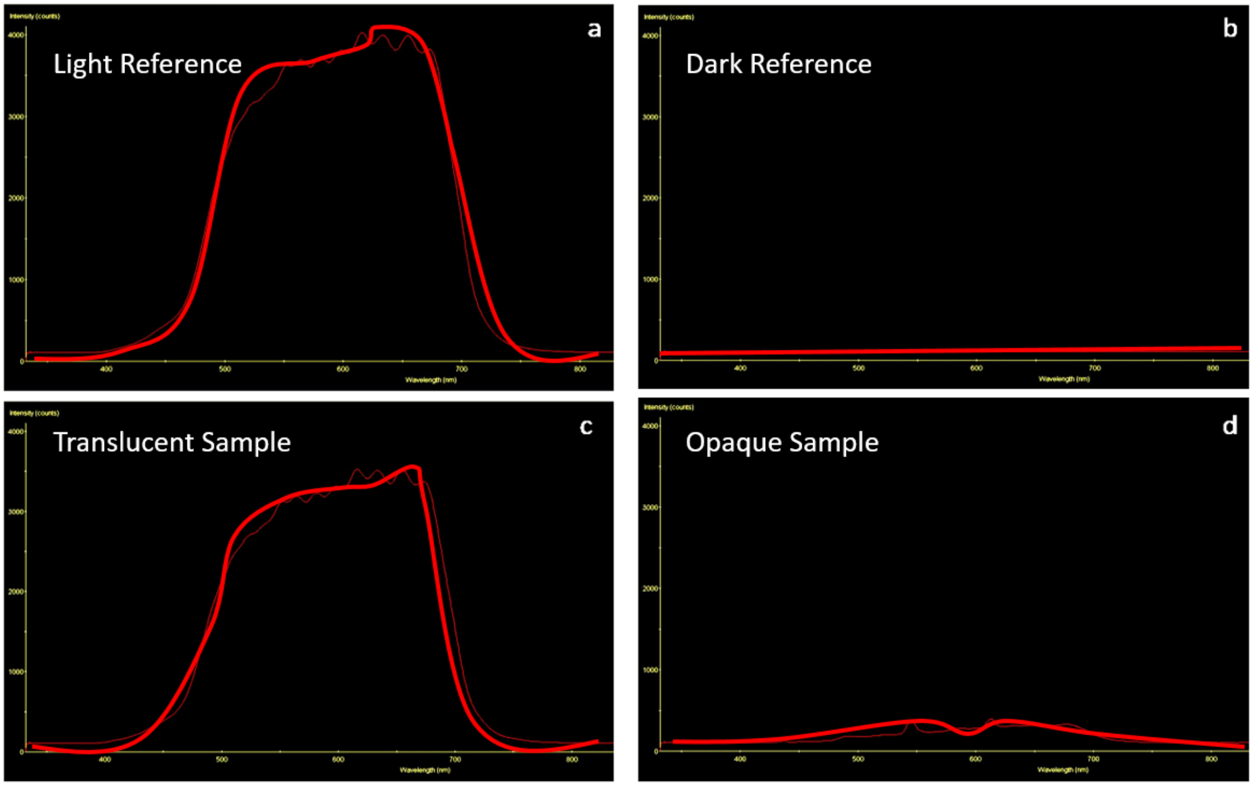

Figure 3-6: Sample graphs of intensity vs wavelength for the (a) light reference, (b) the dark reference, (c) the poly*(tert*-butyl acrylate) sample clear, (d) the poly(*tert*-butyl acrylate) sample opaque.

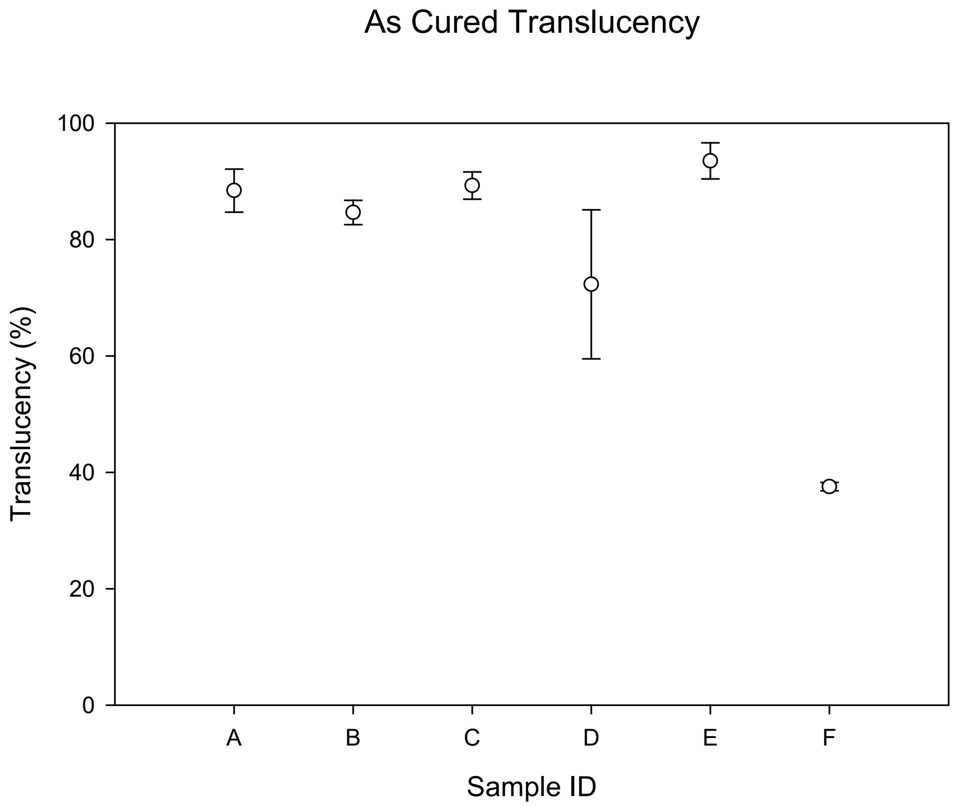

As Cured Translucency

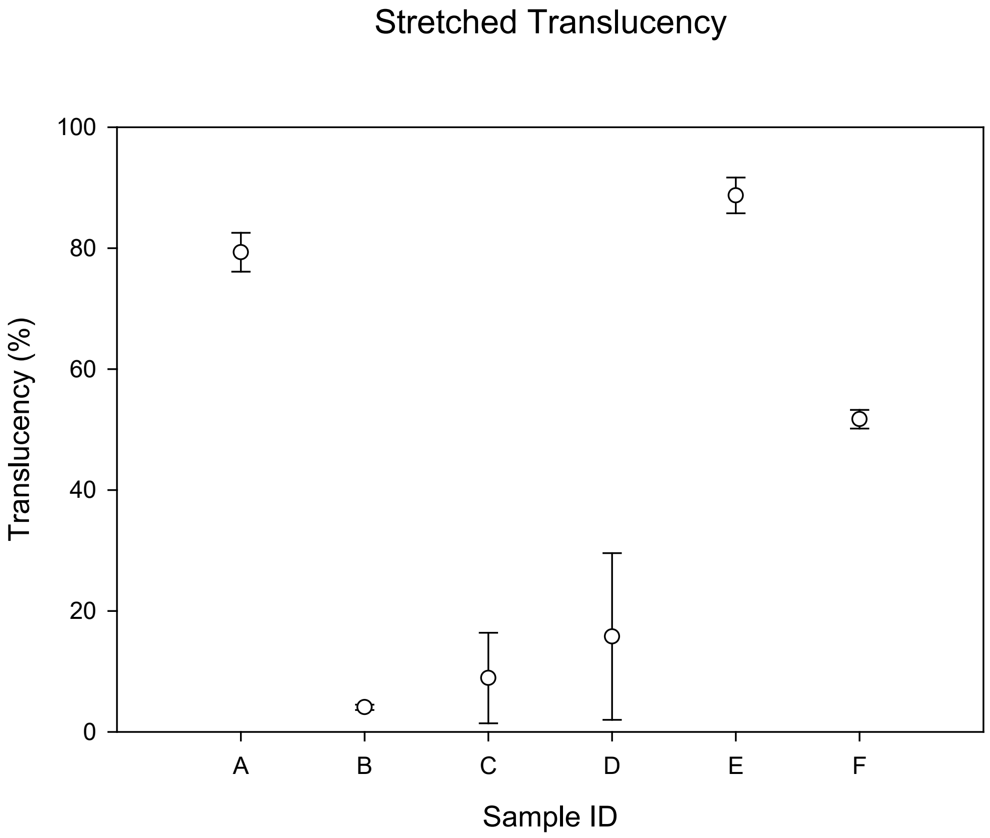

Stretched Translucency

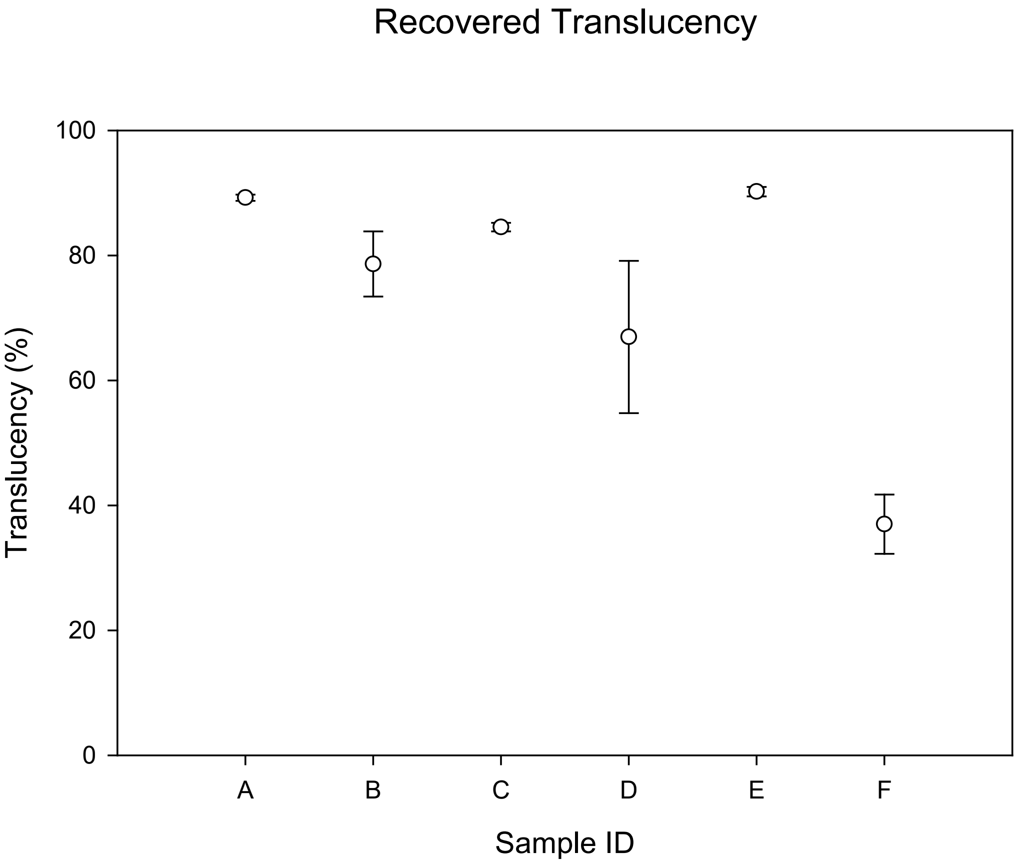

Figure 3-7: Translucency measured for each of the former combinations of poly(*tert*-butyl acrylate). The samples are (a) 1 wt. % silica dissolved in poly(*tert*-butyl acrylate), (b) 3 wt. % silica dissolved in poly(*tert*-butyl acrylate), (c) 5 wt. % silica dissolved in poly(*tert*-butyl acrylate), (d) 10 wt. % silica layered in poly(*tert*-butyl acrylate), (e) electrospun polylactic acid cured with poly(*tert*-butyl acrylate) and (f) electrospun poly(ε-caprolactone) cured with poly(*tert*-butyl acrylate).

Table 3-1: Table of translucency values as measured for all the combinations of poly(*tert*-butyl acrylate) tested.

Sample ID	**Translucency (%)**		
	Original	*Stretched*	*Recovered*
A - 1 wt.% Silica dissolved in TBA	88.3 ± 3.7	79.3 ± 3.2	89.3 ± 0.5
B - 3 wt.% Silica dissolved in TBA	84.6 ± 2.1	4.06 ± 0.4	78.7 ± 5.2
C - 5 wt.% Silica dissolved in TBA	89.3 ± 2.3	8.9 ± 7.5	84.6 ± 0.7
D - 10 wt.% Silica layered in TBA	72.3 ± 12.8	15.8 ± 13.8	66.9 ± 12.2
E - Electrospun PLA cured with TBA	93.5 ± 3.1	88.74 ± 2.9	90.2 ± 0.8
F - Electrospun PCL cured with TBA	37.5 ± 0.7	51.7 ± 1.5	36.9 ± 4.7

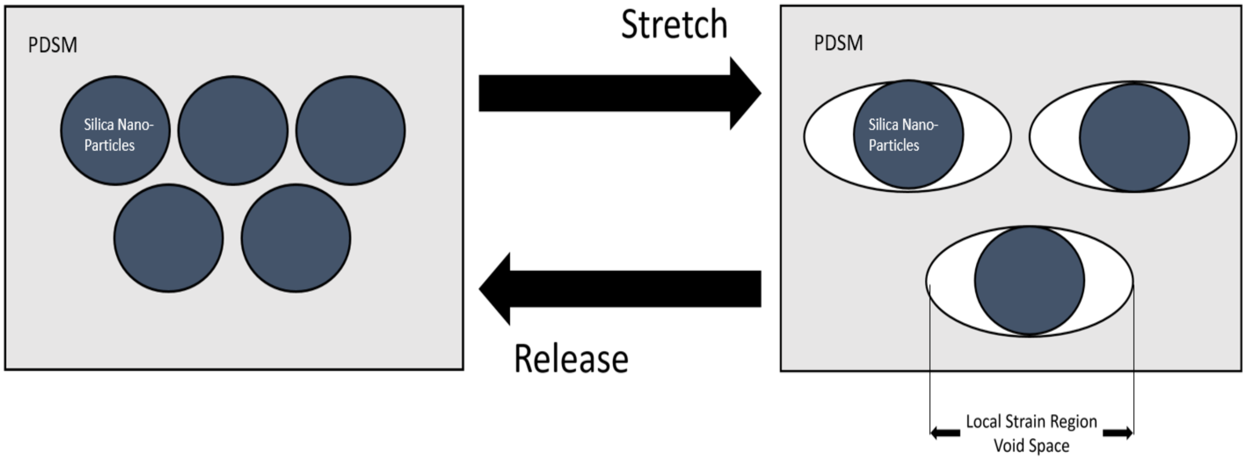

Scheme 3-4: Depiction of mechanistic cause of opacity change of the poly(*tert*-butyl acrylate) with silica nanoparticles. In the stretched state, the poly(*tert*-butyl acrylate) matrix pulls away from the silica nanoparticles, creating void spaces that scatter light.

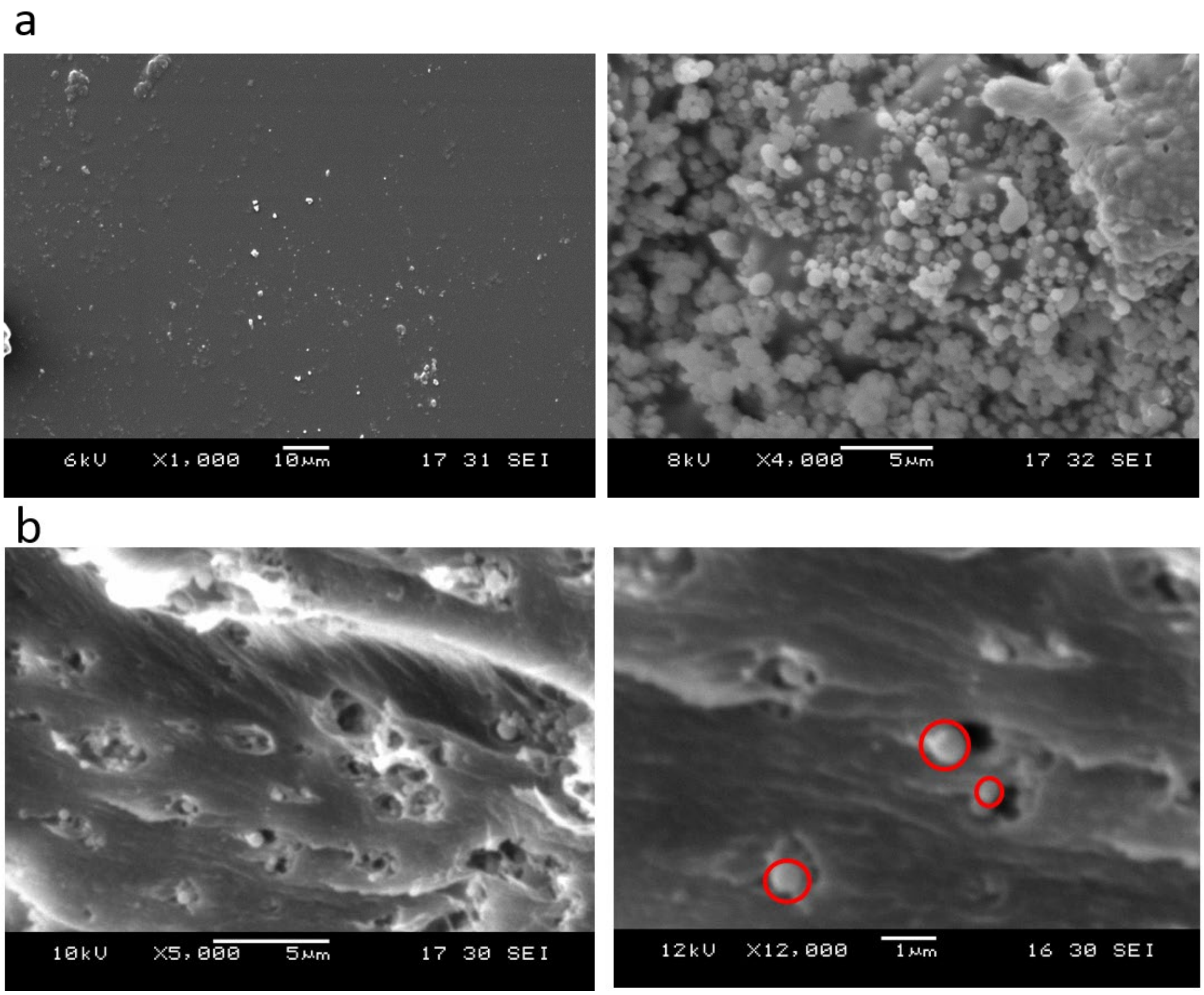

Figure 3-8: SEM images of (a) poly(*tert*-butyl acrylate) with silica nanoparticles as cured and (b) stretched poly(t-butyl acrylate) showing the void spaces created.

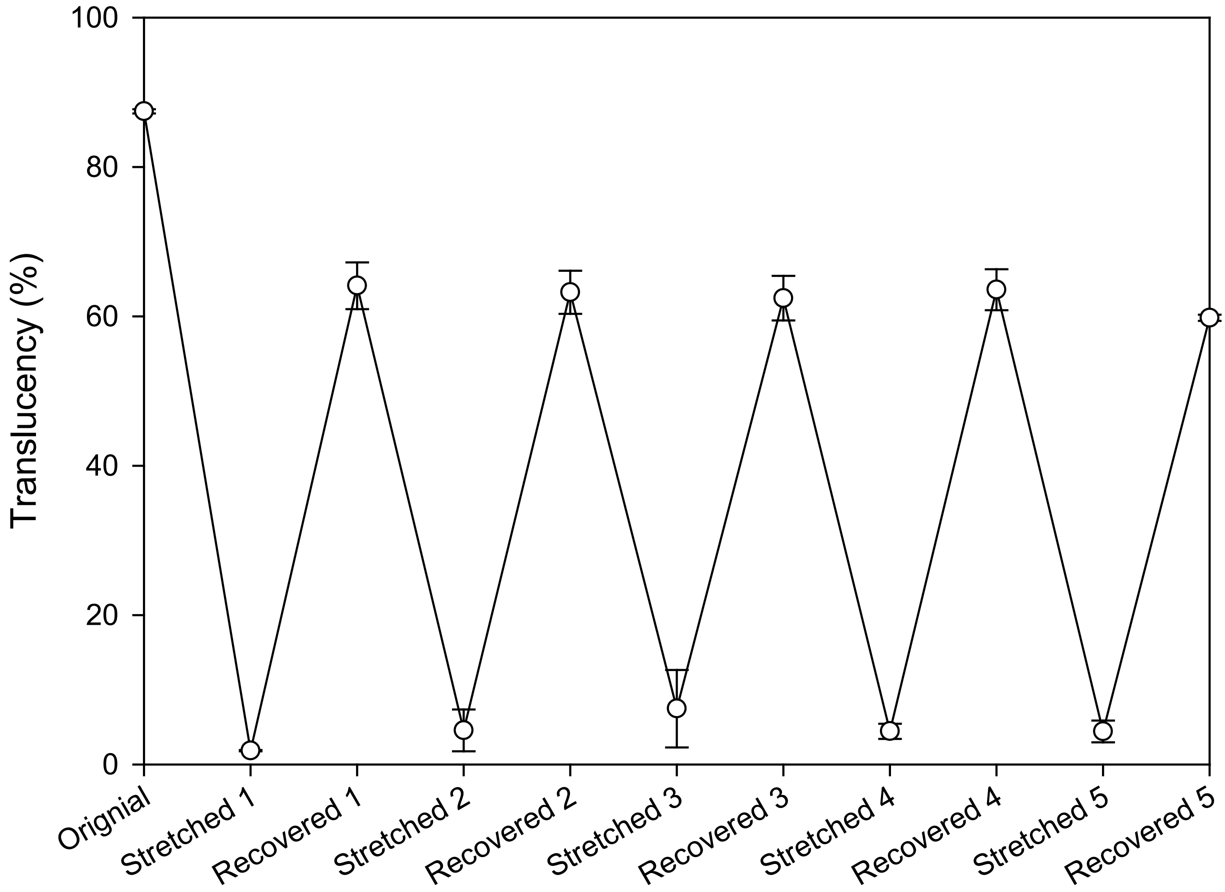

Figure 3-9: Saw-tooth graph showing the measured translucency of 3 wt. % silica nanoparticles in poly(*tert*-butyl acrylate) undergoing a shape memory cycle five times, both in the stretched and recovered states.

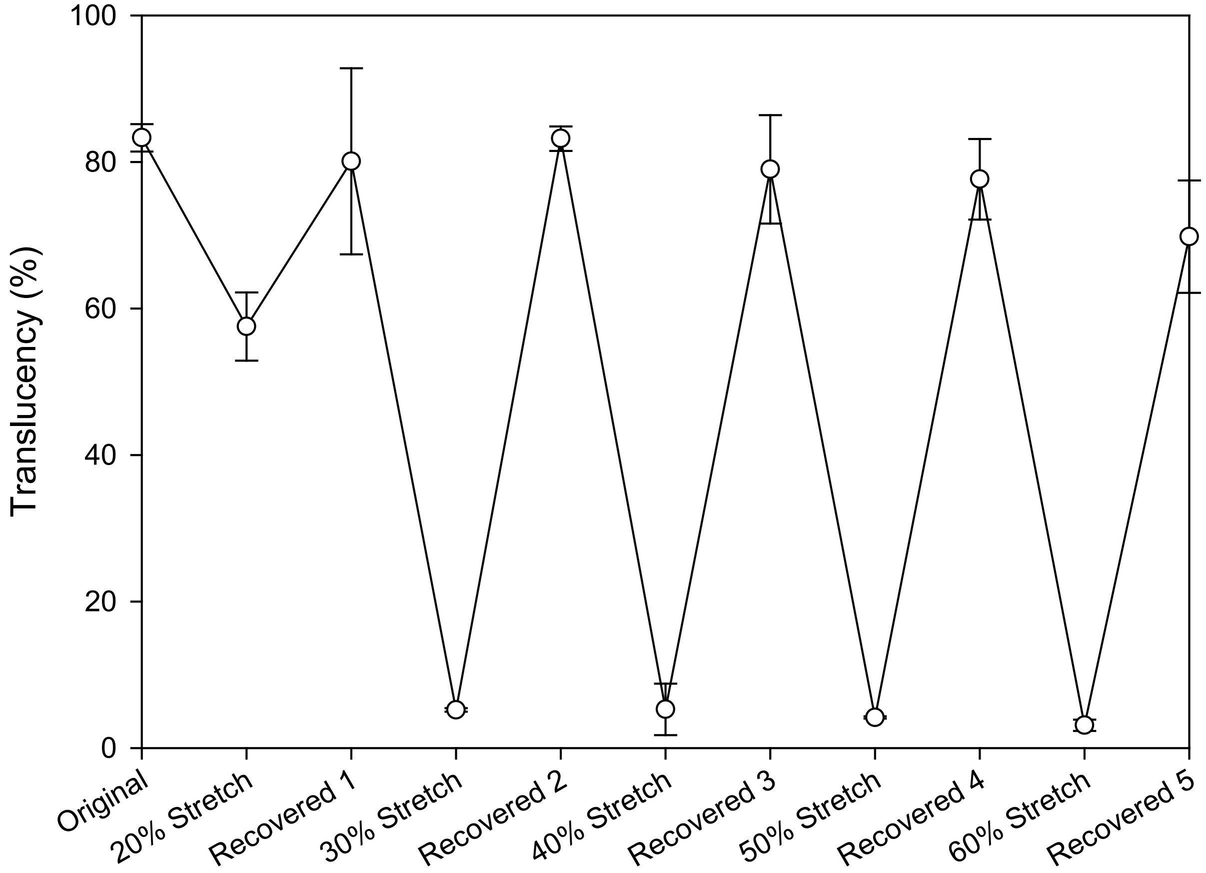

Figure 3-10: Saw-tooth graph showing the measured translucency of 3 wt. % silica nanoparticles in poly(*tert*-butyl acrylate) undergoing a shape memory cycle five times were the amount of strain used is systematically increased, both in the stretched and recovered states.

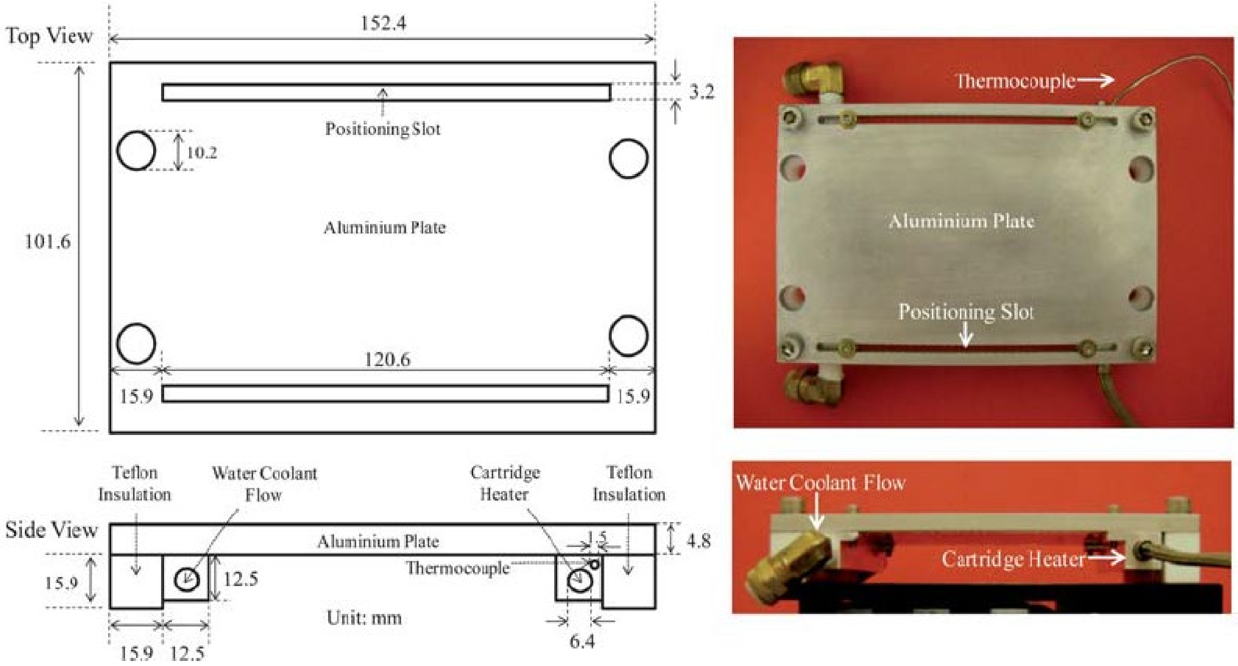

Figure 3-11: Schematic of temperature gradient stage[8] as shown by DiOrio et. al. The same temperature stage was used for this research with the exception of having a solid aluminum top plate.

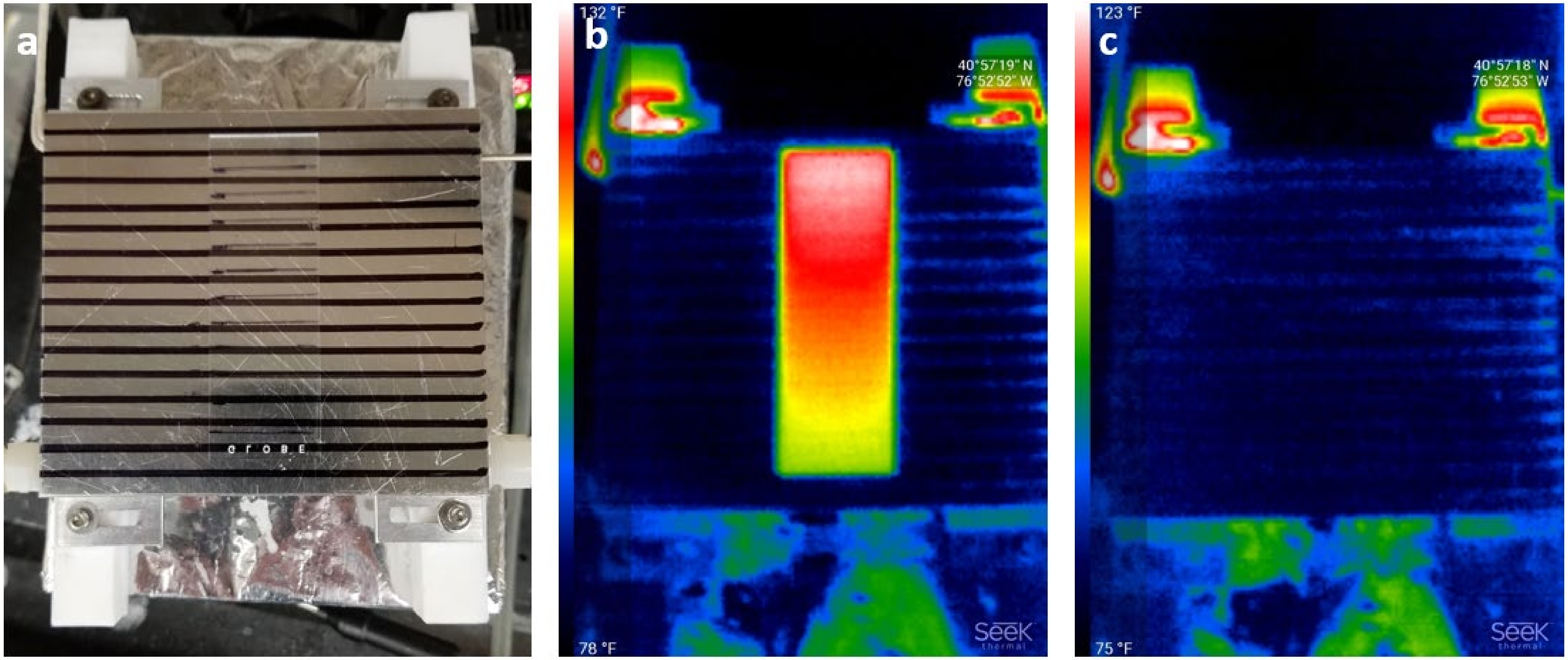

Figure 3-12: Pictures of the (a) setup used to functionally grade the poly(*tert*-butyl acrylate) with 3 wt. % silica nanoparticles (b) thermal image, and (c) thermal image of just the gradient stage.

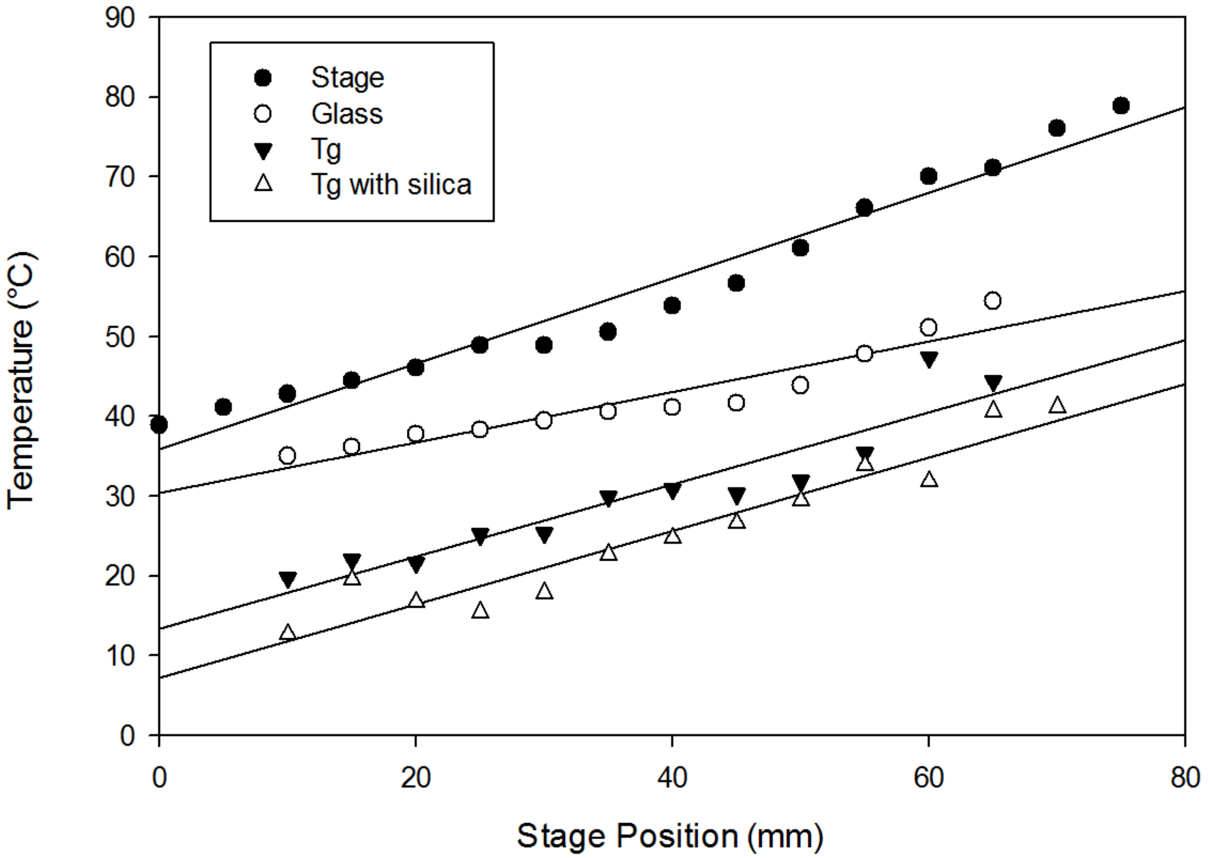

Figure 3-13: Temperature measurements of the functional gradient stage, the glass slide, polymer T_g as measured using DSC without silica and the polymer T_g as measured using DSC with silica.

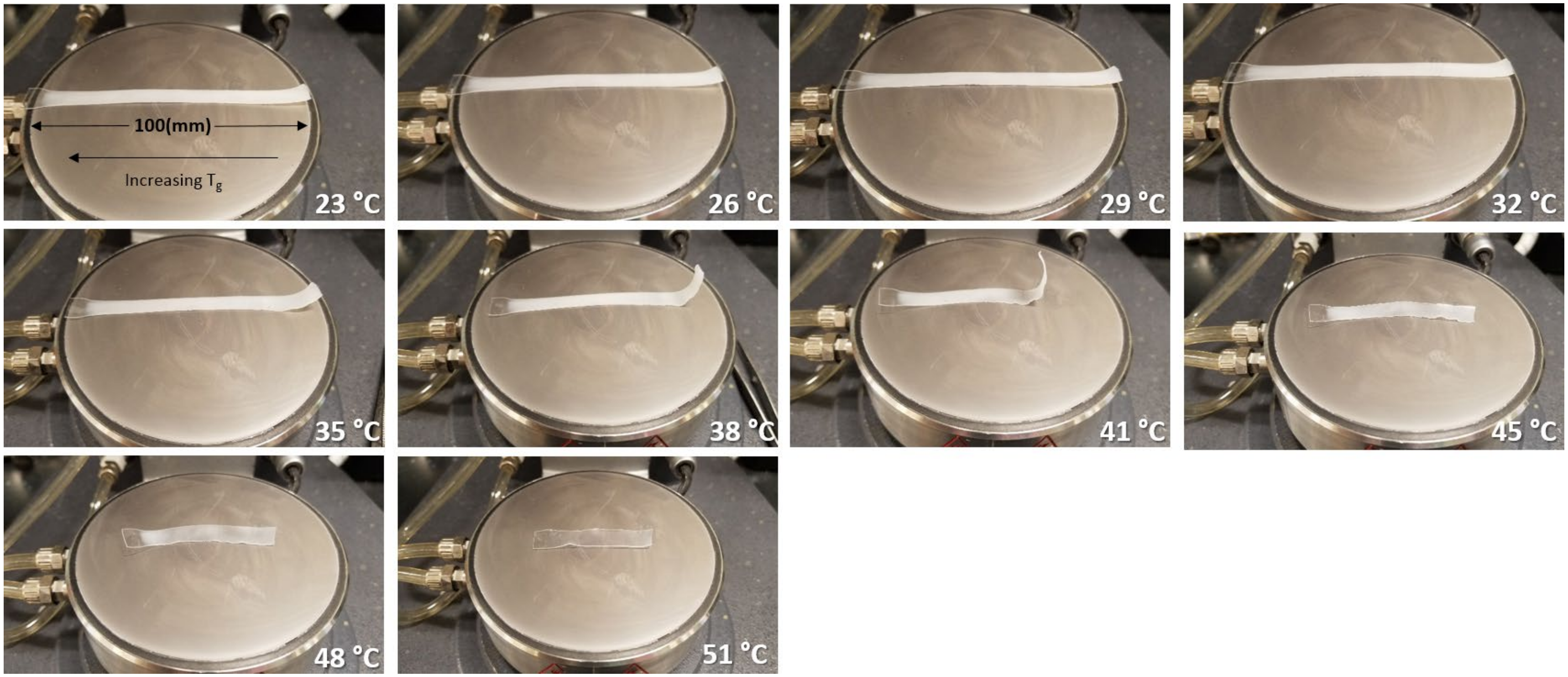

Figure 3-14: Image series showing the progression of shape memory recovery of the stretched poly(*tert*-butyl acrylate) with 3 wt. % silica particles. The sample has a glass transition temperature gradient through the length of the sample, which is increasing from right to left. The farthest left of the sample was intentionally held clear as a method to track recovery progress. Samples where heated using the Peltier plate for the AR-G2 TA rheometer, because it has a precise temperature control, within 0.1 °C and each temperature increment was confirmed using a thermocouple. The sample was allowed to equilibrate at each temperature increment for 5 min.

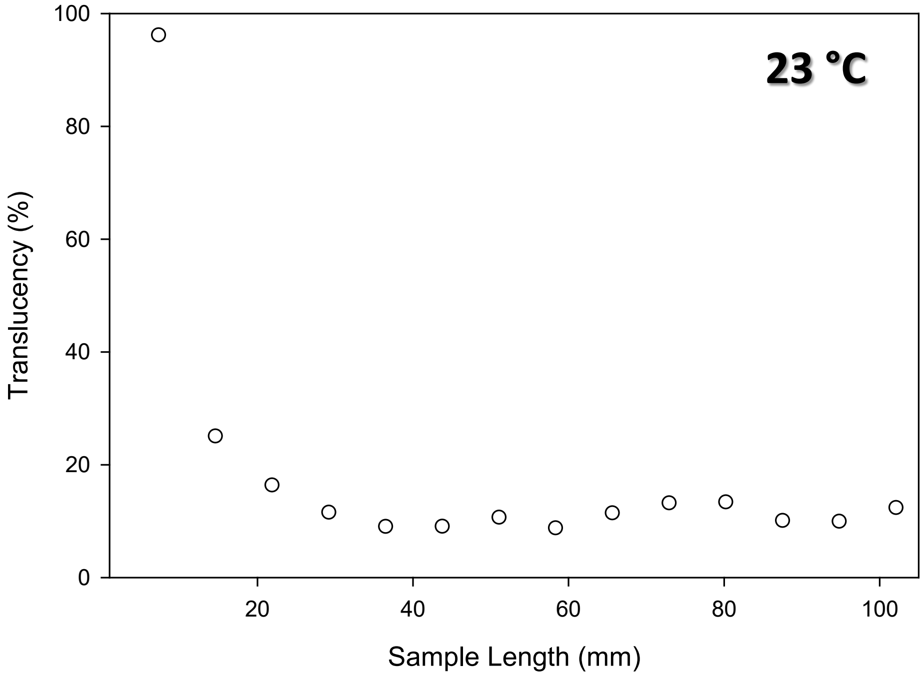
23 °C
Translucency (%)
0
20
40
60
80
100
20
40
60
80
100
Sample Length (mm)

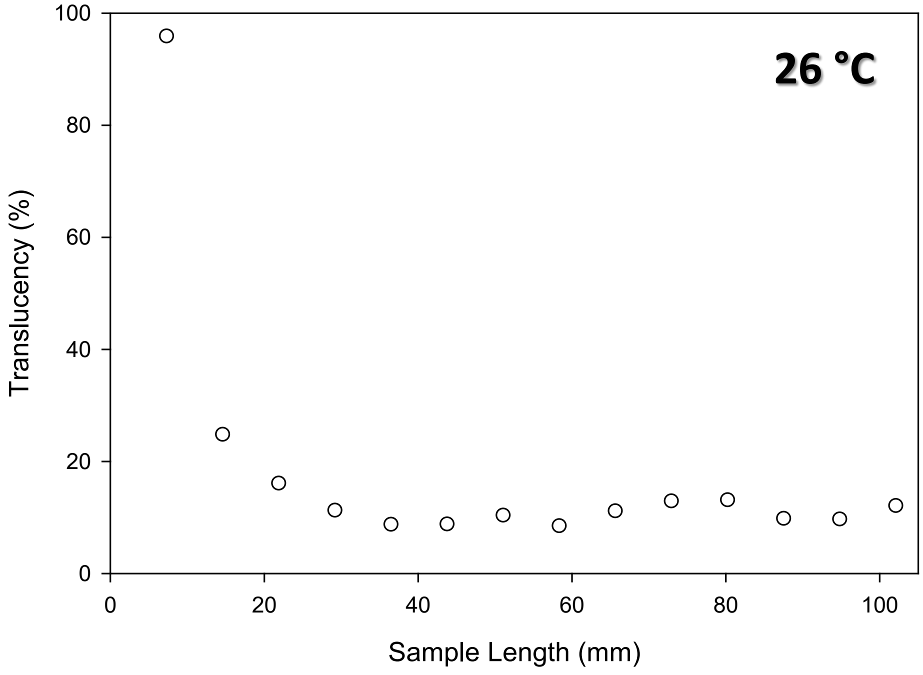
26 °C
Translucency (%)
0
20
40
60
80
100
0
20
40
60
80
100
Sample Length (mm)

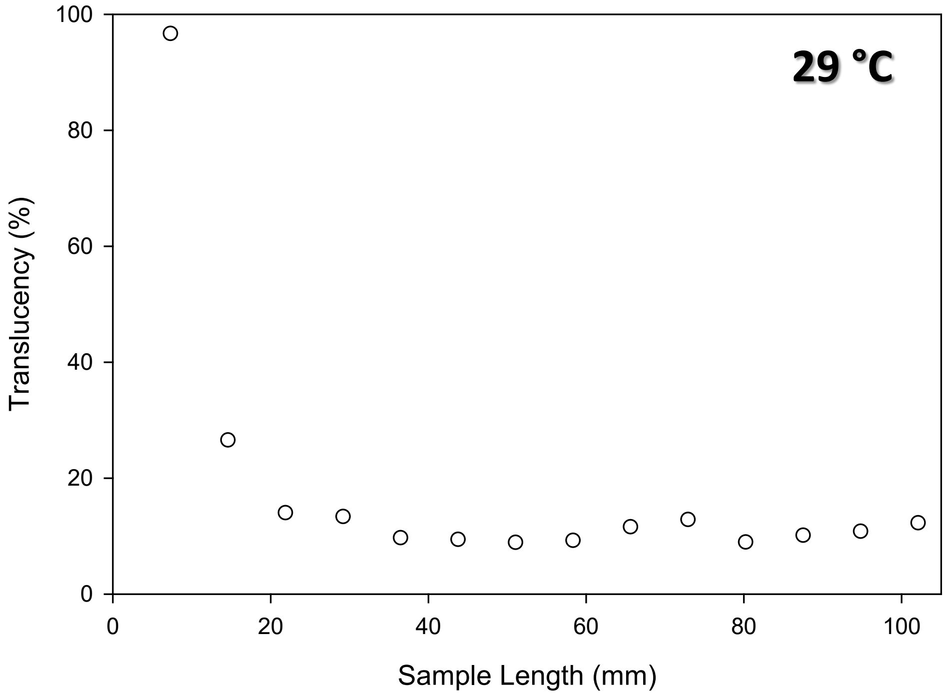
29 °C
Translucency (%)
0
20
40
60
80
100
Sample Length (mm)
0
20
40
60
80
100

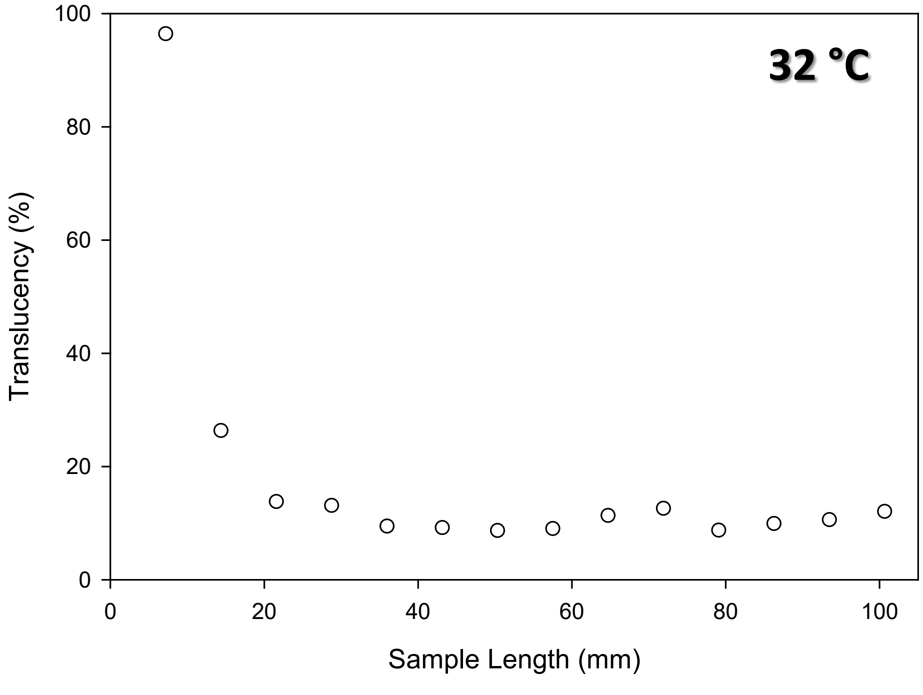
32 °C
Translucency (%)
0
20
40
60
80
100
Sample Length (mm)
0
20
40
60
80
100

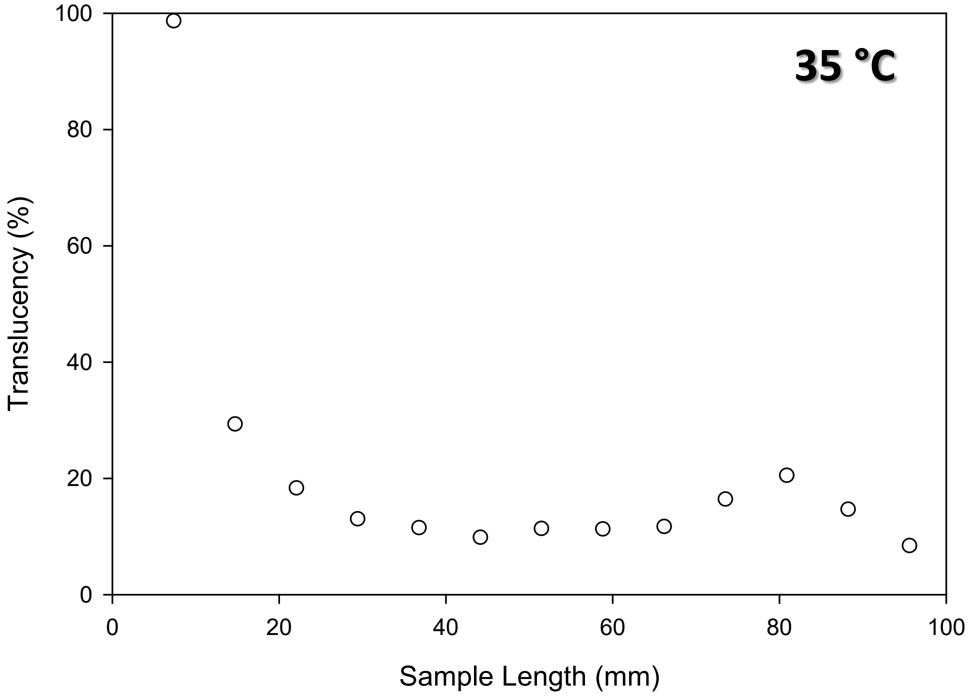
35 °C
Translucency (%)
0
20
40
60
80
100
0
20
40
60
80
100
Sample Length (mm)

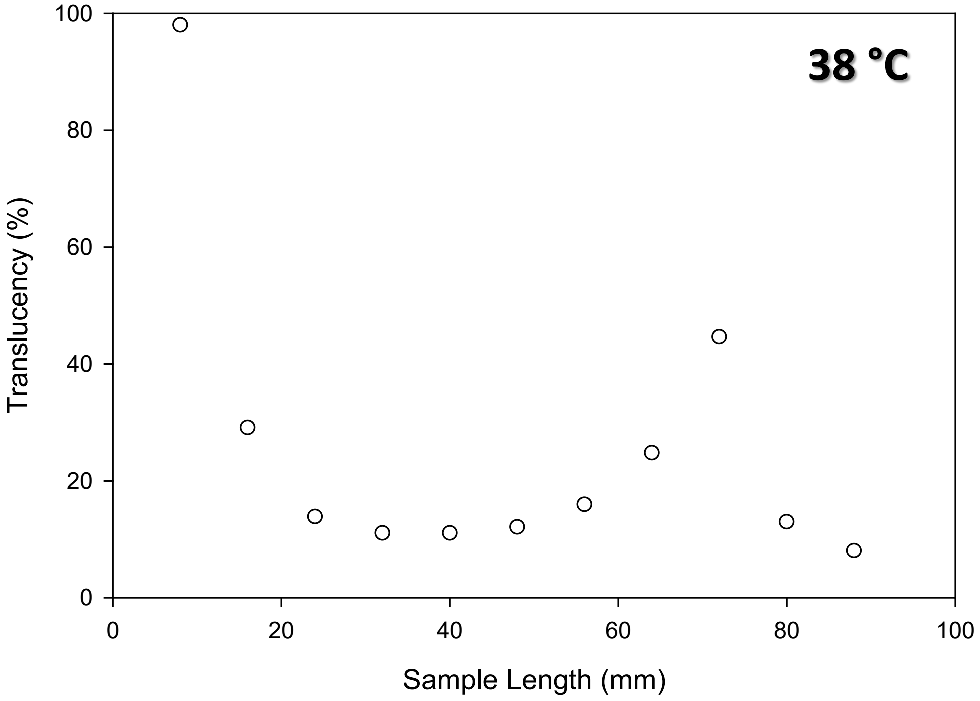
38 °C
Translucency (%)
0
20
40
60
80
100
0
20
40
60
80
100
Sample Length (mm)

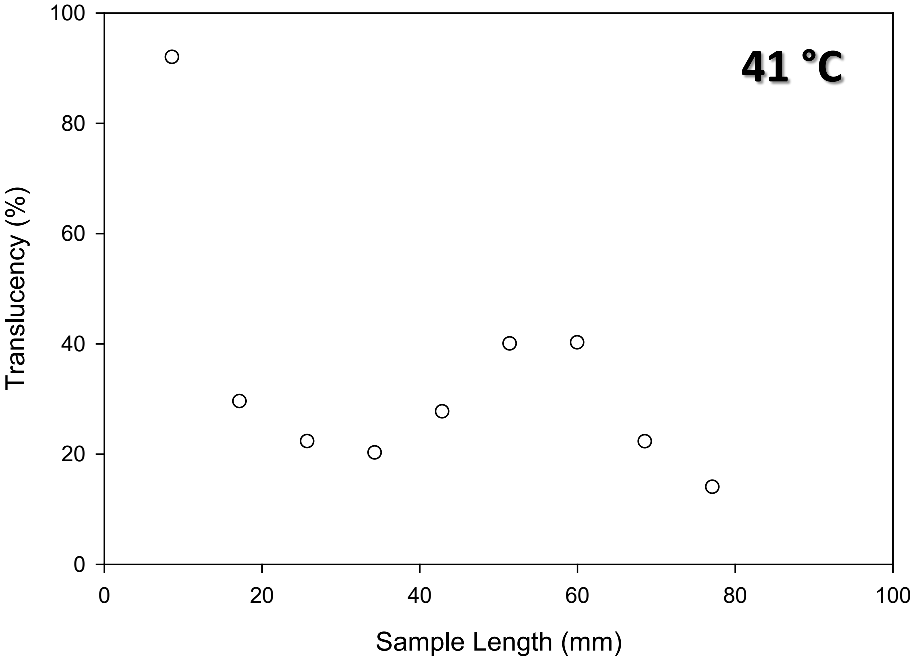
41 °C
Translucency (%)
Sample Length (mm)
0
20
40
60
80
100
0
20
40
60
80
100

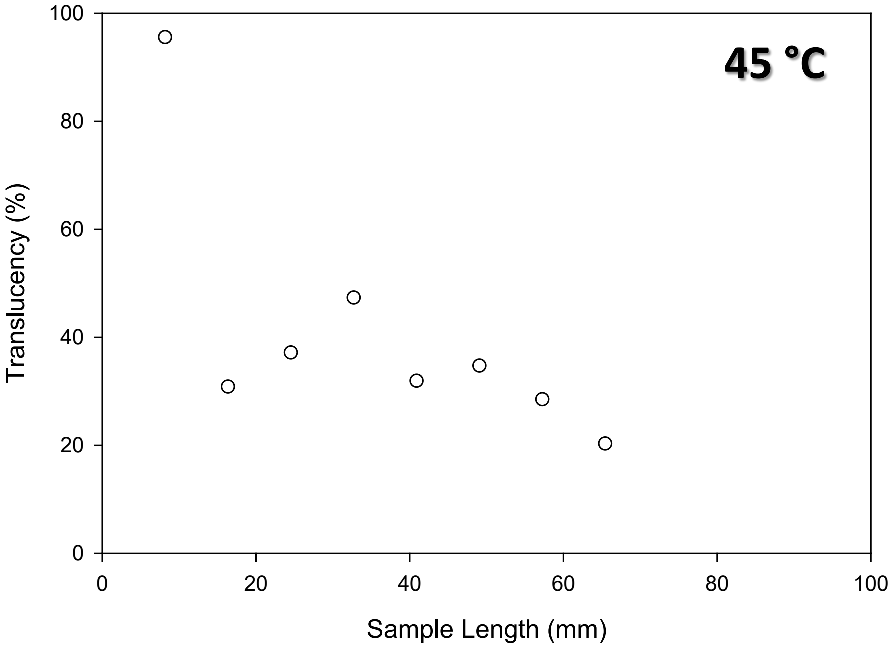
45 °C
Translucency (%)
Sample Length (mm)
0
20
40
60
80
100
0
20
40
60
80
100

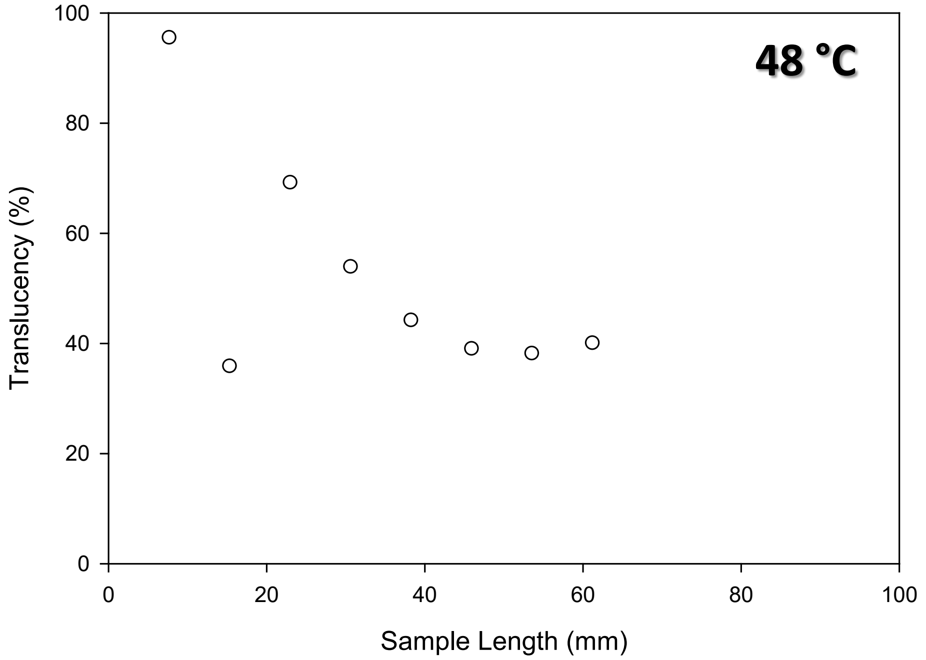

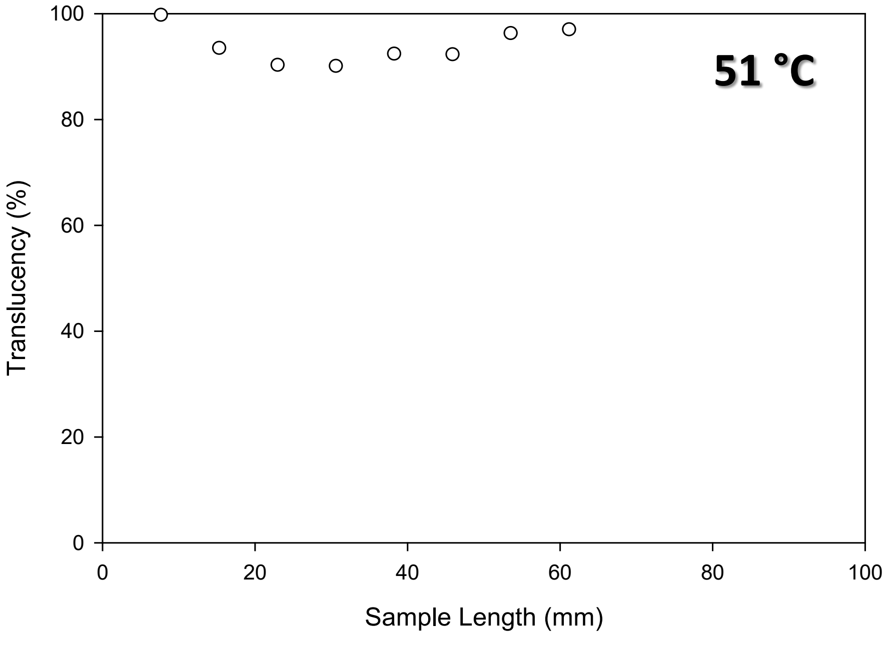

Figure 3-15: Series of graphs showing the translucency measurements of the functionally graded poly(*tert*-butyl acrylate) polymer with 3 wt. % silica nanoparticles. The sequence is quantifying how the sample in **Figure 3-14** is being recovered. The polymer has an increasing glass transition temperature from right to left. As the sample recovers, it also decreases in length, but generally the trend observed is the increasing of optical translucency from right to left as the temperature increase.

Chapter 4. Summary

4.1 Conclusions

The work detailed in this dissertation utilized both electrospun fibers in the development of highly anisotropic materials as well as a thermoset polymer for photo-thermal actuation. The polymers that were selected for generating fiber meshes via electrospinning were selected for their specific thermal and mechanical properties to enable the high anisotropy. **Chapter 2** exploited the fibrous nature of electrospun materials in the development of highly anisotropic trilayer composites. **Chapter 3** used a non-fibrous amorphous thermosetting polymer film incorporated with nanoparticles to achieve a shift in optical transparency through shape memory actuation using a thermal trigger. This work shows the applicability and versatility of electrospinning as a technique to generate nonwoven fibrous meshes as well as using shape memory thermoset polymers as next generation smart materials.

4.1.1 Engineering Anisotropic Electrospun Composites

Chapter 2 detailed the use of aligned poly(methyl methacrylate) and Pellethane fibers in the fabrication of laminated trilayer composites. The rigid nature of the poly(methyl methacrylate) fibers incorporated with the highly elastic Pellethane fibers into a laminate structure was able to effectively mix these polymers together, without either negatively affecting each other. This synergizing of material properties allowed extremely high anisotropy in respect to the Young's and storage modulus for the material. This high anisotropy can be attributed to the large diameter poly(methyl methacrylate) fibers easily separating from each other in the transverse direction. The Pellethane fibers act as a medium holding the poly(methyl methacrylate) fibers together and adding structural rigidity in the transverse direction for the poly(methyl methacrylate) fibers with large fiber diameter. When a stress is applied in the perpendicular direction to the direction of the poly(methyl methacrylate) fibers, the poly(methyl methacrylate) fibers do not resist deformation leaving the Pellethane fibers to deform. When a stress is applied in the fiber direction the poly(methyl methacrylate) fibers bear the load and remain far stiffer than the Pellethane fibers would be on their own.

Increasing the poly(methyl methacrylate) fiber diameters from 6.21µm to 39.29µm caused a positive effect on the anisotropy of the material. There is, however a more complex mechanism involved in the formation of the electrospun poly(methyl methacrylate) fibers. The trilayer structure was the optimal method to incorporate two fundamentally different polymers, for the advantage of high composite anisotropy.

Decreasing the thickness of the Pellethane core layer used in the trilayer composite is also beneficial to the composite anisotropy. This interaction can be explained through microscopic examination of the cross sectional area of the Pellethane present. The thinner the layer of Pellethane present in the trilayer, the less stiff the composite is in the transverse direction. This decrease in stiffness can account for the increase in anisotropy.

4.1.2 Engineering a Thermally Active Optical Shutter

Chapter 3 used a curable amorphous shape memory polymer dispersed with silica nanoparticles to obtain a thermally triggered optical shutter. The innovation here is the ability to obtain a shift in optical opacity through the shape memory cycle. This material is able to be fixed into an optically opaque, temporary state, and upon later heating return it to an optically clear state. This “smart” material could act as a visual temperature sensor for packaging of sensitive products. It was found that this could be cycled, e.g. re-used multiple times, without the diminishing of optical properties. This material is also robust; it can be strained far beyond what is necessary for the optical tansition without any negative effects on the optical properties.

Functional grading of this material was also innovated. Through a method of post curing with a temperature gradient, we were able to control the extent of polymerization spatially. This material allows the addition of functionality to the temperature sensor device, to determine more precisely what temperature, out of a broader range, was reached.

4.2 Future Work

4.2.1 Engineering Anisotropic Electrospun Composites

Anisotropy of soft materials is a material characteristic that is highly sought after because it is a phenomena that occurs naturally in animals. For example in the field of biomimicry making unmanned vehicles that are able to move similarly to an animal, would allow the machine to take advantage of the efficiency, and maneuverability they don't currently have. Bat wings, and fish fins[1] are two examples of materials with high anisotropy. Allowing an unmanned vehicle to fly like that of a bat, could increase the useful deployment in hostile areas as well as potential for camouflaging it from enemy radar.

The trilayer composite developed in **Chapter 2** displayed extremely high anisotropy from the interplay between rigid electrospun poly(methyl methacrylate) and elastic Pellethane fibers. As the next steps in the material development an obvious examination need be given to the poly(methyl methacrylate) fibers and how the morphology changes as the electrospinning solution concentration is increased. It would be prudent to use AFM and other topographical techniques to study how the poly(methyl methacrylate) polymer chains are interacting in the fiber forming process of electrospinning, and what occurs when more, and more poly(methyl methacrylate) polymer chains are added into the fibers. This would allow precise control over not only the overall rigidity of the resulting composite, but also being able to electrospun poly(methyl methacrylate) with other polymers. The interactions between poly(methyl methacrylate) and another polymer fiber is also of concern and the seemingly large electrical charge build up preventing efficient adherence between them.

An interesting off shoot of the current research, using the same materials in the same structure could be as a pressure valve. Using the trilayer as a pressure valve could take advantage of the not only the anisotropy, but the oleophobicity of the two components. Having a strongly oleophobic[2] material (poly(methyl methacrylate)) on the outside, and an oleophillic[3] material on the inside (Pellethane) could allow selective passage. As a valve, the material could be preventing the flow oil, until a pressure is applied. The material will accordion out moving the oleophobic fibers apart, and allowing the inner oleophillic fibers to absorb the oil.

4.2.2 Engineering a Thermally Active Optical Shutter

Soft polymeric based smart materials is highly desired[4]. This type of disposable technology can be used as a value added product to anything that is consumed with a temperature limitation. Having packaging[5] on everything that is purchased that would be able to visually indicate if an unsafe temperature was achieved would be a much welcomed addition.

The poly(*tert*-butyl acrylate) polymer dispersed with silica nanoparticle composite shows the ability to thermally change its optical appearance. This material was functionally graded to achieve a more spatially controlled optical change. To continue this research an interesting adaptation would be the use of nanoparticles with varying size. This should change the size of the void spaces created when the material is stretched, and thus change the color the material changes when stretched. Following this theme we could incorporate the different sized nanoparticles spatially along the length of the polymer, and functionally grade as well. Such a material would have a color shifting temperature sensor, for applications when there is a range of temperature that a product can reach and still be useable.

4.3 References

1. Pavlov, V. V. Dolphin skin as a natural anisotropic compliant wall. *Bioinspiration Ampmathsemicolon Biomim.* **1**, 31–40 (2006).

2. Wang, Y. & Gong, X. Special oleophobic and hydrophilic surfaces: approaches, mechanisms, and applications. *J. Mater. Chem. A* **5**, 3759–3773 (2017).

3. Han, D. & Steckl, A. J. Superhydrophobic and Oleophobic Fibers by Coaxial Electrospinning. *Langmuir* **25**, 9454–9462 (2009).

4. Roy, I. & Gupta, M. N. Smart Polymeric Materials: Emerging Biochemical Applications. *Chem. Biol.* **10**, 1161–1171 (2003).

5. Kerry, J. & Butler, P. *Smart Packaging Technologies for Fast Moving Consumer Goods*. (John Wiley & Sons, 2008).

Appendix Chapter A1. Development of a Hygroscopic Electrospun Polymer Composite.

A1.1 Synopsis:

Self-assembly, or what is colloquially known as 4-D printing[1], is of major interest for application in design of smart systems. The concept is using specific polymers which are 3D printed, then through an external stimuli cause a change in the structure. These materials can be used in biomedical devices, where the ability for the material to change shape on demand allows an improvement in functionality. Drug delivery systems[2,3] can be a viable application for this technology.

The fabrication technique of electrospinning[4] has been utilized for its ability to produce micro sized polymer fibers while integrating them together into a nonwoven sheet. Specifically, the molecular orientation of the polymer molecules within these fibers will be of interest. During this process, elongational forces create a stress that is trapped in the overall polymer fibers once vitrified. For this research, poly (vinyl acetate) (PVAc) polymer fibers will release there stored stress once the material reaches its glass transition temperature. Overall molecular realignment occurs, which causes the fiber mat to shrink. Application of water to these fibers has been shown to selectively plasticize the area and cause a local release of the trapped stress. This, intern, causes a self-folding of the material. Incorporation of a non-water sensitive polymer, poly(ε-caprolactone), into this will decrease the overall amount of actuation. Changing the distribution of and placement of poly(ε-caprolactone) in the composite will allow increased control of the actuation. Electrospun composites of PVAc and poly(ε-caprolactone) and their response to hydration has been studied in detail and characterized.

A1.2 Experimental

A1.2.1 Materials

Poly(ε-caprolactone) (PCL) (Mw = 80,000) pellets were purchased from Sigma-Aldrich. Poly (vinyl acetate) (PVAc) (Mw = 500,000) pellets were purchased from Sigma-Aldrich. N,N-dimethylformamide (DMF), chloroform, and methanol were all purchased from Sigma-Aldrich. All solvents and pellets were used as received.

A1.2.2 Electrospinning Solutions

The electrospinning solution of Poly(ε-caprolactone) contained 15 % w/v and was dissolved in a solution of DMF and chloroform in a 1:4 ratio, which is a modified method from Robertson et al[5]. The PVAc solution contained 15% w/v and was dissolved in a solution of DMF to Methanol 1:4, which was a modified method from Mather et al.[4] Both solutions were stirred continuously for 24 - 36 hours at room temperature to ensure the polymers were completely dissolved and the solution was distributed evenly.

A1.2.3 Electrospinning Equipment

All composites contained within were fabricated using the Spraybase® electrospinning syringe pumps and voltage sources which were integrated into the rotating drum collector with a multi-head emitter as shown in **Scheme A1-1**. For the purposes of this research only 2 emitters will be used. The metallic mandrel is 300 mm in width and 95.6 mm in diameter. The tubing used to connect the syringe pump to the emitter is 1 mm in diameter and 18 gauge emitters were used for both solutions. The collector mandrel was set to -1000 V and to a rotational speed of 2000 rpm. Both of the emitter tips were translated across the width of the mandrel from 60 mm to 190 mm.

A1.2.4 Aligned Bilayer Composite Fabrication

Various composites were made of bilayers where the alignment of the layers was systematically changed. The bilayers made were combinations of anisotropic and isotropic. The composites made as shown in **Figure A1-2, A1-5, A1-8, A1-11** are (isotropic/isotropic), (anisotropic/anisotropic), (isotropic/anisotropic) and (anisotropic/isotropic) respectively. The overall thickness of the fiber sheets as well as the composition ratio of them were held constant at a 50/50 of poly (vinyl acetate) and polycaprolcatone. These composite were made by electrospinning each polymer directly on top of the other.

A1.2.5 Isotropic Dual Electrospinning Composite Fabrication

Composites of increasing amounts of poly(ε-caprolactone) present were fabricated by electrospinning each polymer simultaneously. The composite variables of overall thickness of the fiber sheets as well as the fiber alignment, isotropic for these composites, were held constant.

A1.2.5 Thermal Analysis

Differential Scanning Calorimetry (DSC) (TA Q2000) was used to measure the glass transition and the heat capacity of the neat poly (vinyl acetate) in the dry, hydrated, and post hydrated composites. The process used two heating cycles, where the sample is heated at a rate of 5 °C/min to 100 °C, cooled at 10 °C/min to -50 °C, and then heated at 5 °C/min to 100 °C. The poly (vinyl acetate) content in the neat and composite materials was calculated using the same assumptions and process from Tumbic et al[6]. The following equation **Eq. (A1-1)** was used to calculate all poly (vinyl acetate) content in the composites:

$$w = \left(\frac{\Delta C_p}{\Delta C_{p,neat}}\right) * 100 \tag{A1-1}$$

where w is the weight percent of the poly (vinyl acetate) in the composite, ΔC_p is the heat capacity of the poly (vinyl acetate) in the composite, and $\Delta C_{p,neat}$ is the heat capacity of the neat electrospun poly (vinyl acetate)[5,7]. All heat capacity values were used from the second heating cycle to ensure all samples had equal thermal history.

A1.2.6 Scanning Electron Microscopy

Surface topography of all samples was assessed using the SEM (Jeol JSM-6390LV). All samples were prepared by cutting out a square and adhering it to an SEM stub using carbon tape. All samples were gold-sputter coated for 120 sec in a Denton Vacuum desk IV. The working distance was 10 mm with an accelerating voltage of 10-15 kV.

A1.2.7 Fiber Mat Shrinkage

Unique to poly (vinyl acetate) is the release of trapped stresses, which are created during the process of electrospinning, upon the exposure to water. However, combining into this fibrous sheet a polymer that will not experience that when exposed to water will cause an asymmetric shrinkage, unlike previously observed. The amount of shrinkage experienced by the composite was measured by submerging 25.4 mm square samples in RT DI water. After 24 hours the samples were again measured and the percent shrinkage was calculated using **Eq. (A1-2)**:

$$S = \frac{L_0 - L}{L_0} * 100 \tag{A1-2}$$

Where S is the percent shrinkage, L_0 is the original length (25.4 mm), and L is the length measured after hydrating for 24 hours. For each composite, three samples were used to measure the length along each edge. These values were averaged together, and compared to show not only how much shrinkage occurred, but how asymmetric it is.

A1.3 Preliminary Results

As shown, composite bilayer samples can be made by virtue of changing the rotational speed of the collector mandrel. Using the differential of orientation, stresses can be programmed into the material causing a 2D fibrous sheet to actuate to form a more complex 3D shape at room temperature. A non-affine shape change through hydration and tensile programming is atypical for shape memory composites. This unique behavior as seen in **Figure A1-14, A1-15**, and summarized in **Table A1-1**, can be used for the fabrication of a hydrogel material for drug delivery, or biomedical applications in general. Fiber orientation dependence on fixing and strain induced 3D geometry is a needed progression for this work.

A1.4 References:

1. Khoo, Z. X. *et al.* 3D printing of smart materials: A review on recent progresses in 4D printing. *Virtual Phys. Prototyp.* **10**, 103–122 (2015).

2. Fernandes, R. & Gracias, D. H. Self-folding polymeric containers for encapsulation and delivery of drugs. *Adv. Drug Deliv. Rev.* **64**, 1579–1589 (2012).

3. Guo, W., Li, M. & Zhou, J. Modeling programmable deformation of self-folding all-polymer structures with temperature-sensitive hydrogels. *Smart Mater. Struct.* **22**, 115028 (2013).

4. Mather, P. T., Robertson, J. M., Torbati, A. & University, S. *Water-triggered origami with a polymeric web*. (2015).

5. Robertson, J. M., Birjandi Nejad, H. & Mather, P. T. Dual-Spun Shape Memory Elastomeric Composites. *ACS Macro Lett.* **4**, 436–440 (2015).

6. Tumbic, J., Romo-Uribe, A., Boden, M. & Mather, P. T. Hot-compacted interwoven webs of biodegradable polymers. *Polymer* **101**, 127–138 (2016).

7. Nejad, H. B., Robertson, J. M. & Mather, P. T. Interwoven polymer composites via dual-electrospinning with shape memory and self-healing properties. *MRS Commun.* **5**, 211–221 (2015).

A1.5 Figures, Schemes and Tables

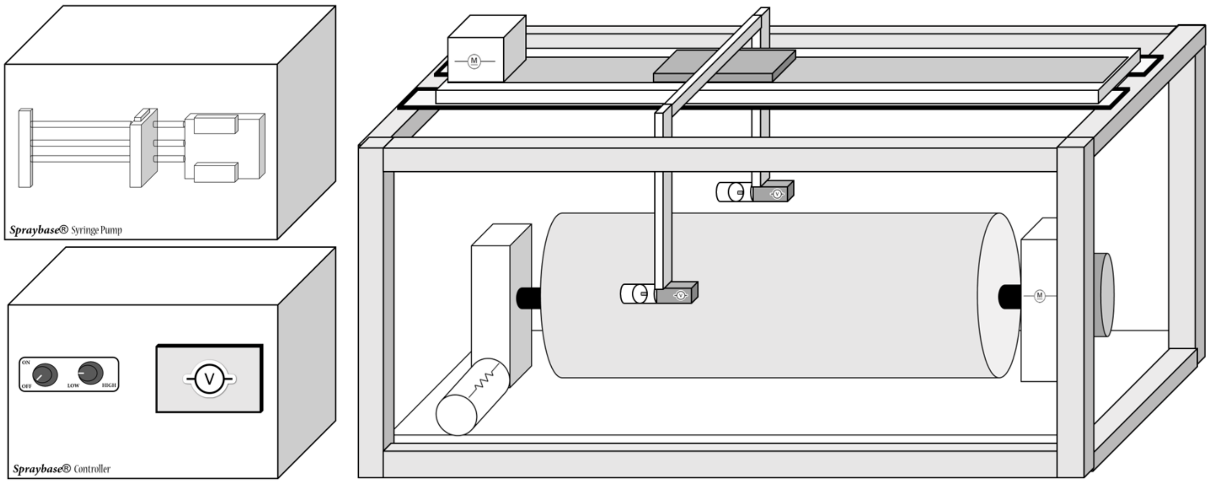

Scheme A1-1: Electrospinning setup used to fabricate samples. This electrospinner is a custom fabrication from the company *Spraybase*.

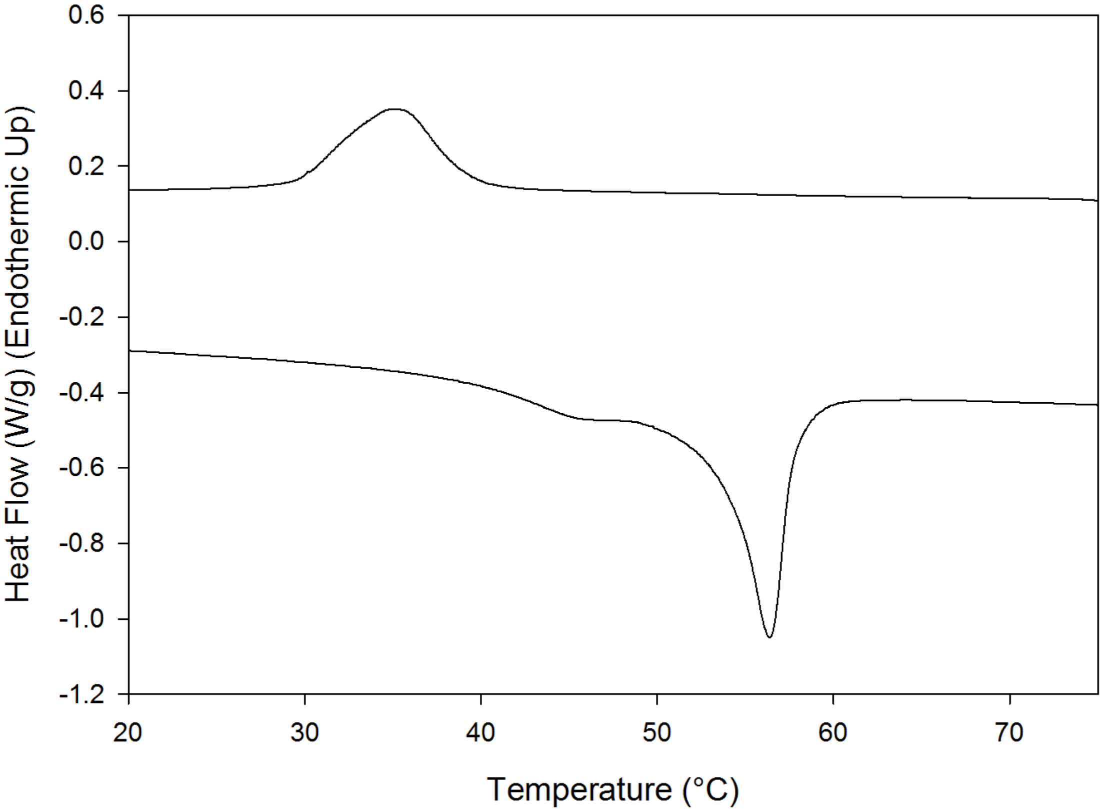

Figure A1-1: DSC trace showing the 1^{st} cooling and second heating for the 50/50 bilayer composites tested. Large melt peak of poly(ε-caprolactone) overlapping with glass transition temperature of poly (vinyl acetate).

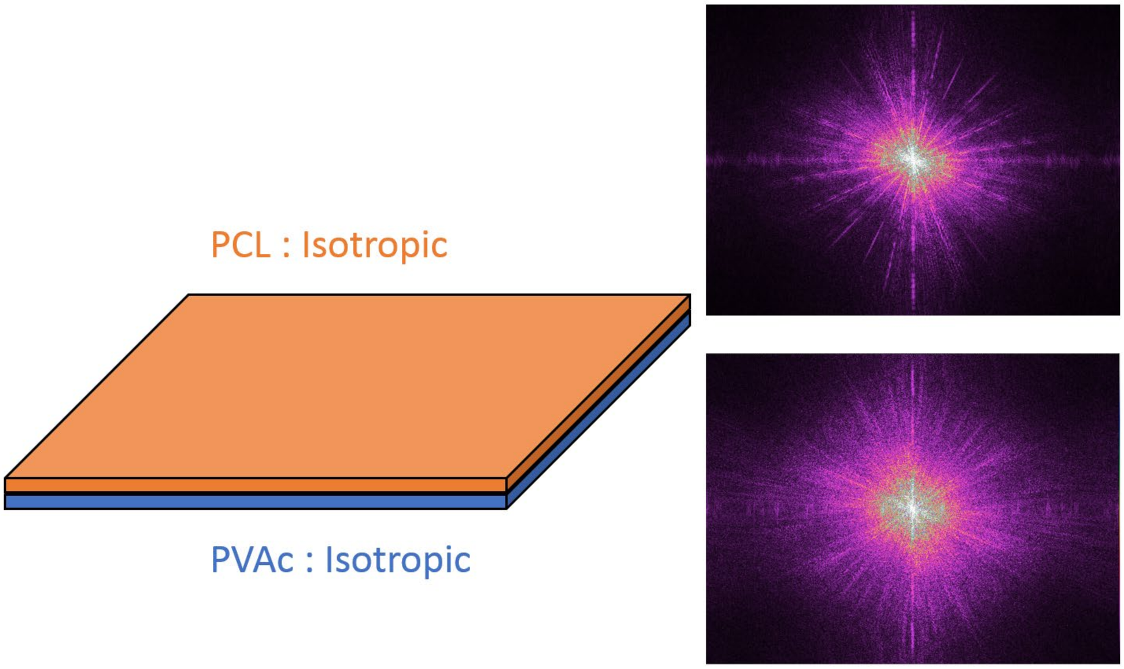

Figure A1-2: Visual representation of electrospun bilayer (left) with Gwyddion analysis of SEM images from the bilayer of the poly(ε-caprolactone) (top right) and the poly (vinyl acetate) (bottom right). The diffraction pattern shows no clear orientation to either layer.

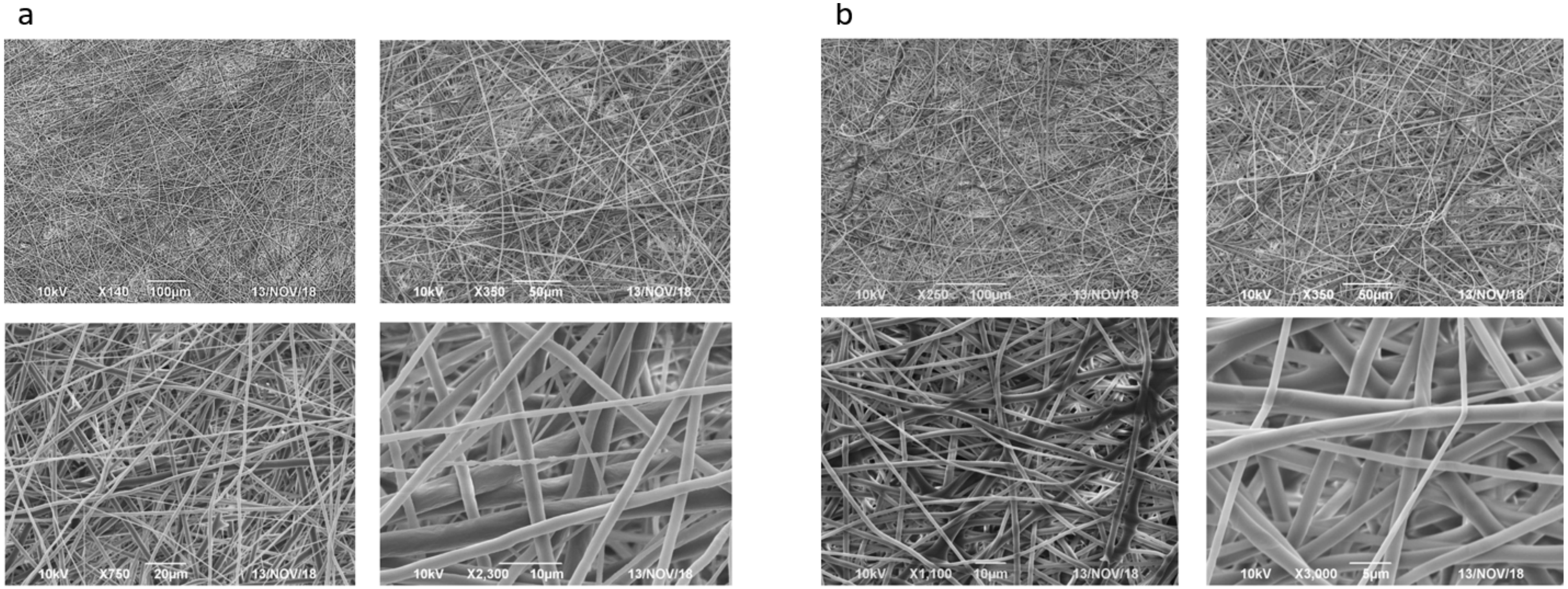

Figure A1-3: SEM images of the electrospun bilayer with (a) poly(ε-caprolactone) and (b) poly (vinyl acetate).

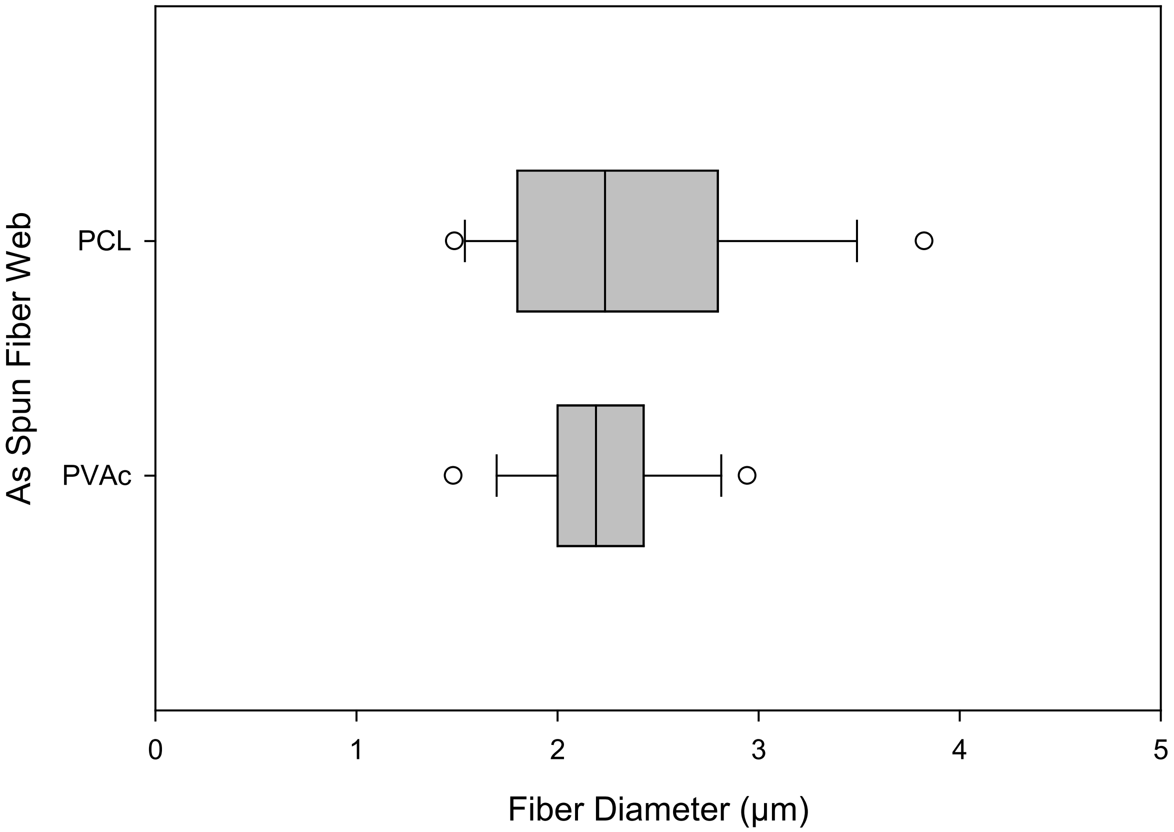

Figure A1-4: Box and whisker plot showing the relative fiber diameter distributions for the bilayer.

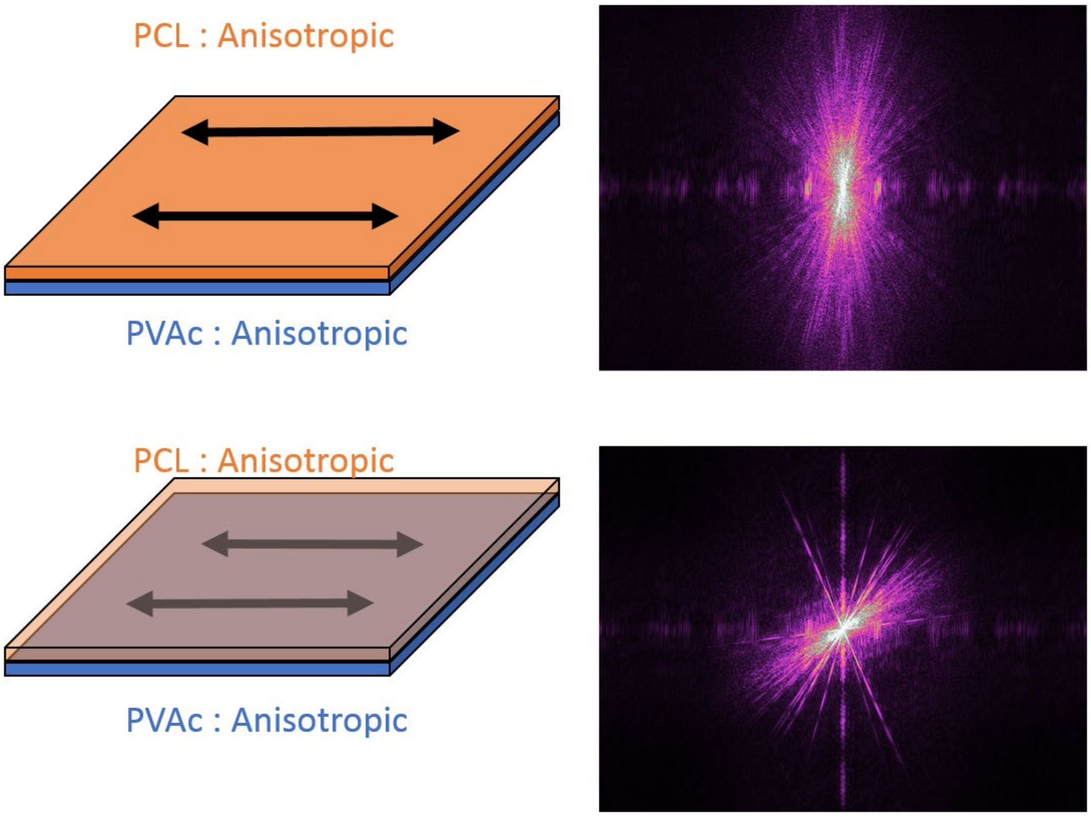

Figure A1-5: Visual representation of electrospun bilayer (left) with Gwyddion analysis of SEM images from the bilayer of the poly(ε-caprolactone) (top right) and the poly (vinyl acetate) (bottom right). The diffraction pattern shows a clear orientation with both layers.

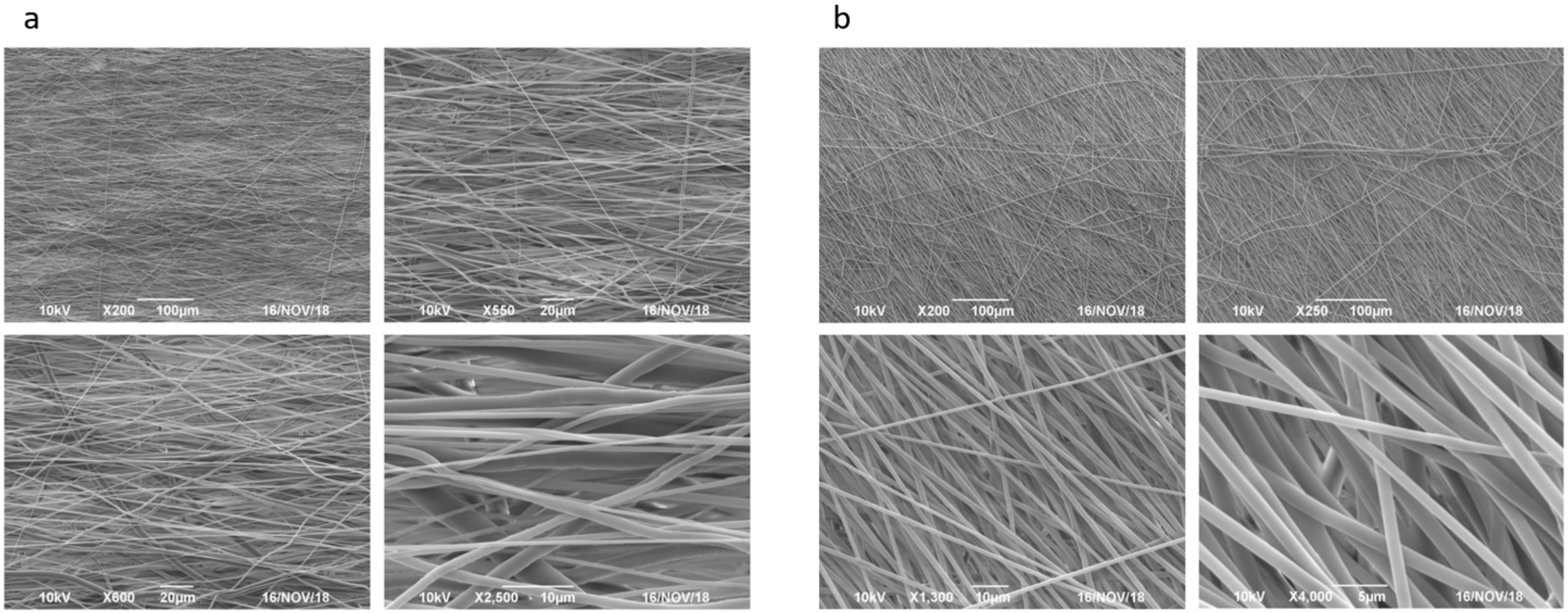

Figure A1-6: SEM images of the electrospun bilayer with (a) poly(ε-caprolactone) and (b) poly (vinyl acetate).

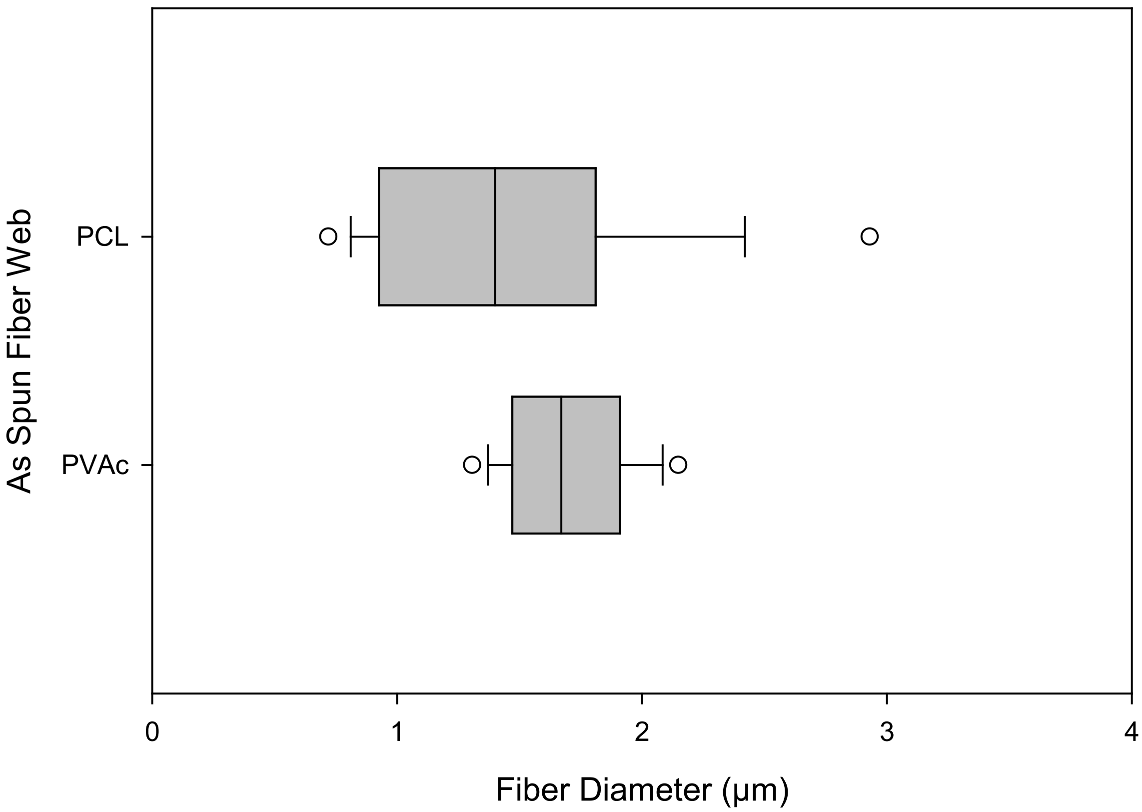

Figure A1-7: Box and whisker plot showing the relative fiber diameter distributions for the bilayer.

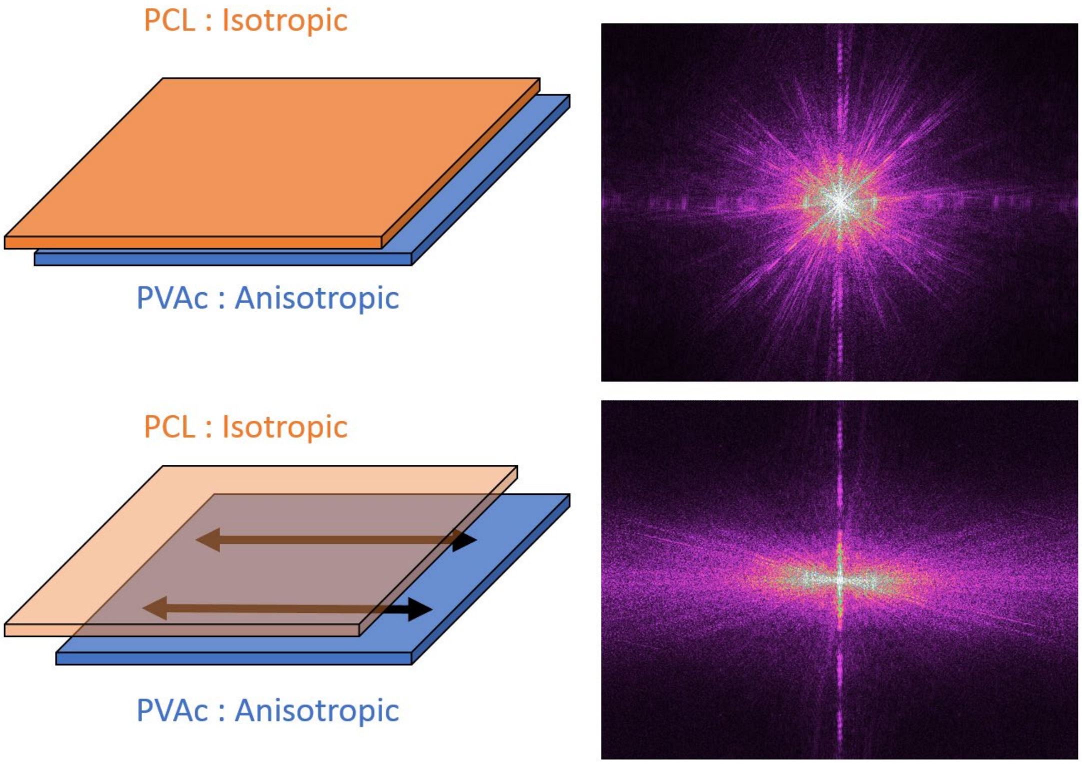

Figure A1-8: Visual representation of electrospun bilayer (left) with Gwyddion analysis of SEM images from the bilayer of the poly(ε-caprolactone) (top right) and the poly (vinyl acetate) (bottom right). The diffraction pattern shows a clear orientation with the bottom layer, but no orientation for the top layer.

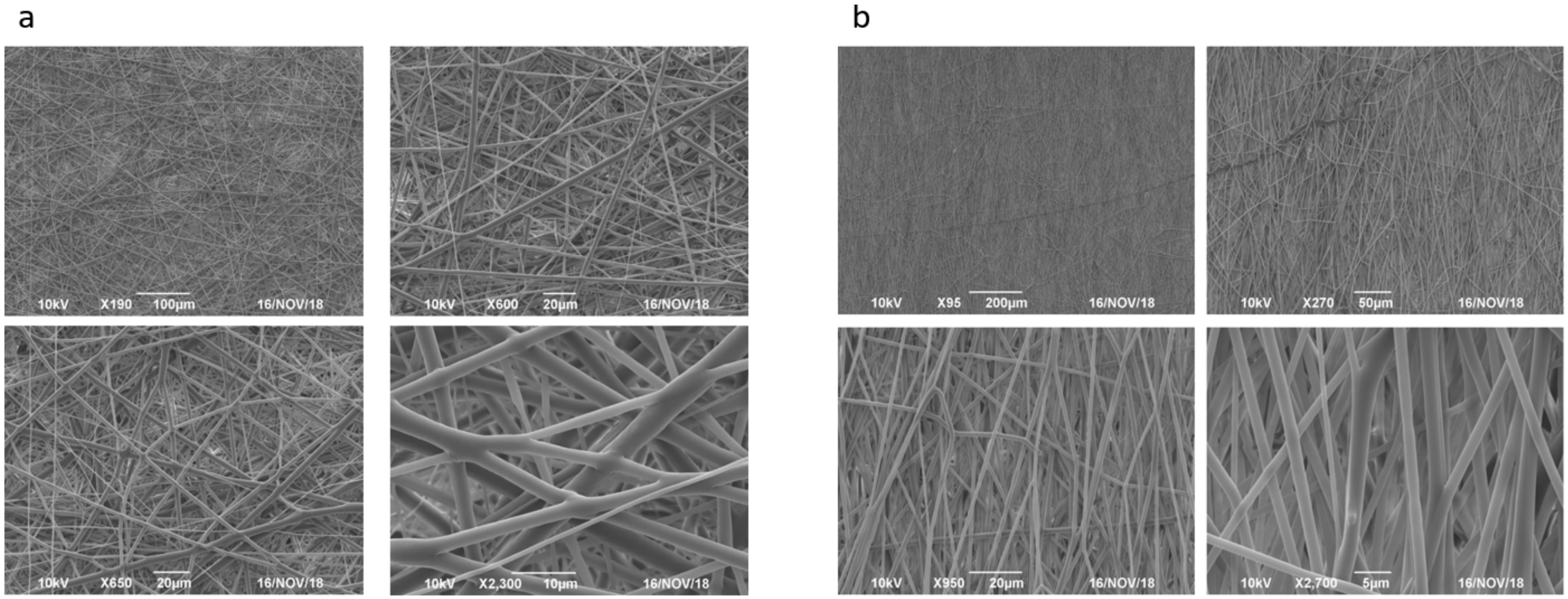

Figure A1-9: SEM images of the electrospun bilayer with (a) poly(ε-caprolactone) and (b) poly (vinyl acetate).

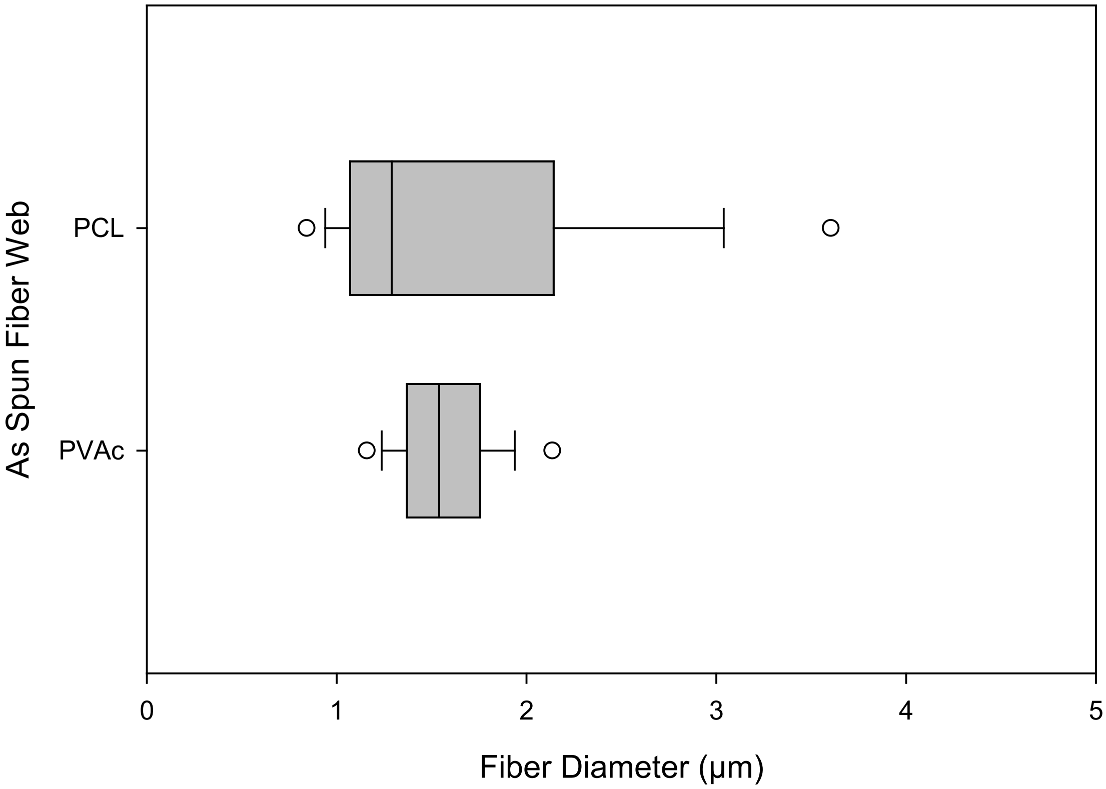

Figure A1-10: Box and whisker plot showing the relative fiber diameter distributions for the bilayer.

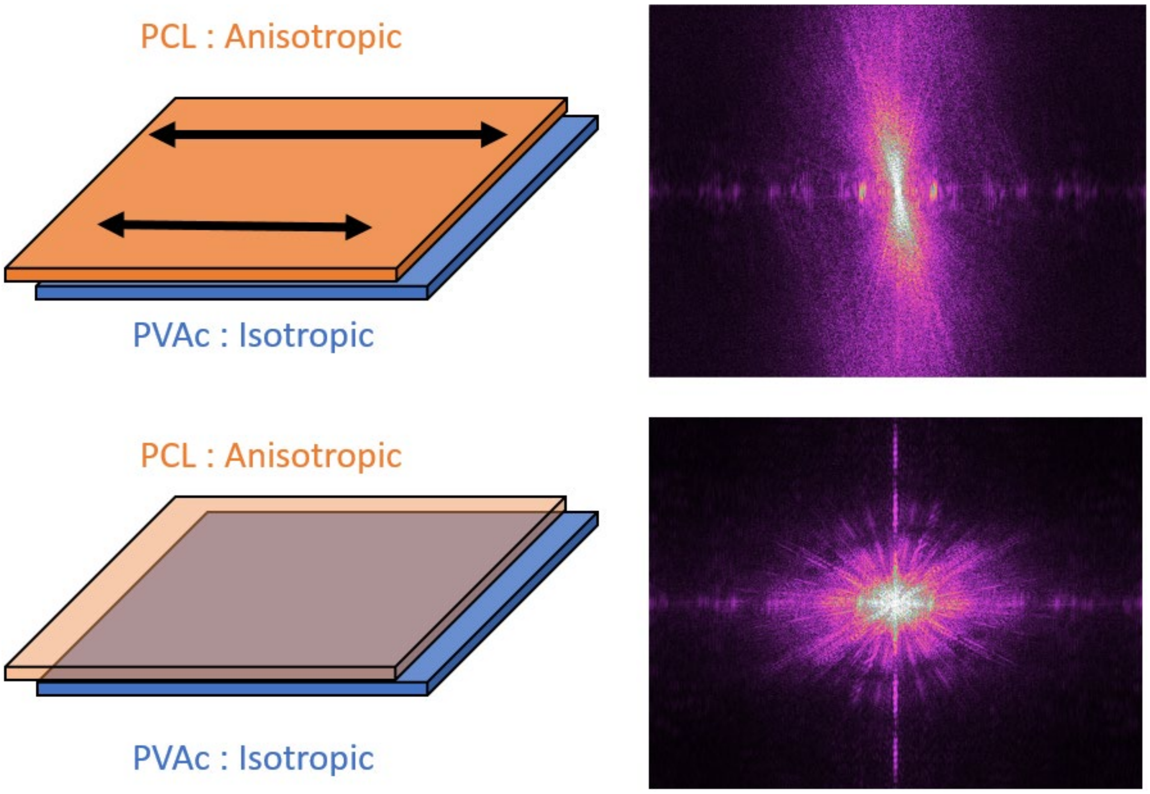

Figure A1-11: Visual representation of electrospun bilayer (left) with Gwyddion analysis of SEM images from the bilayer of the poly(ε-caprolactone) (top right) and the poly (vinyl acetate) (bottom right). The diffraction pattern shows a clear orientation with the top layer, but no orientation for the bottom layer.

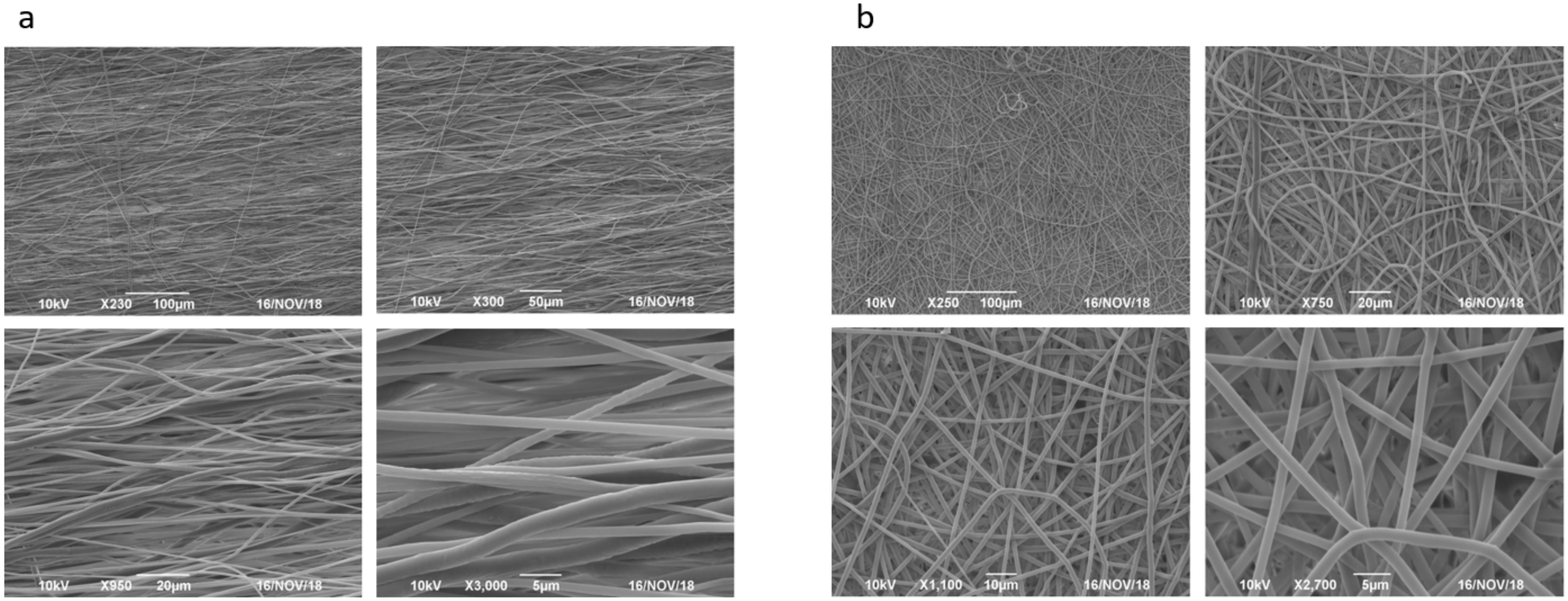

Figure A1-12: SEM images of the electrospun bilayer with (a) poly(ε-caprolactone) and (b) poly (vinyl acetate).

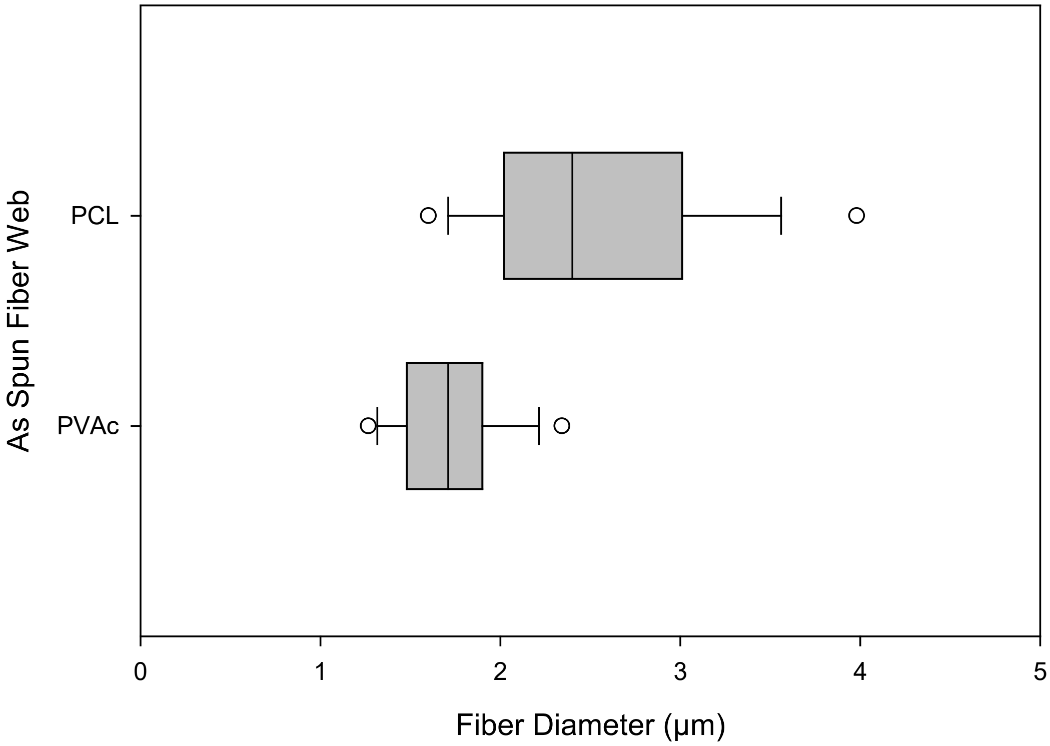

Figure A1-13: Box and whisker plot showing the relative fiber diameter distributions for the bilayer.

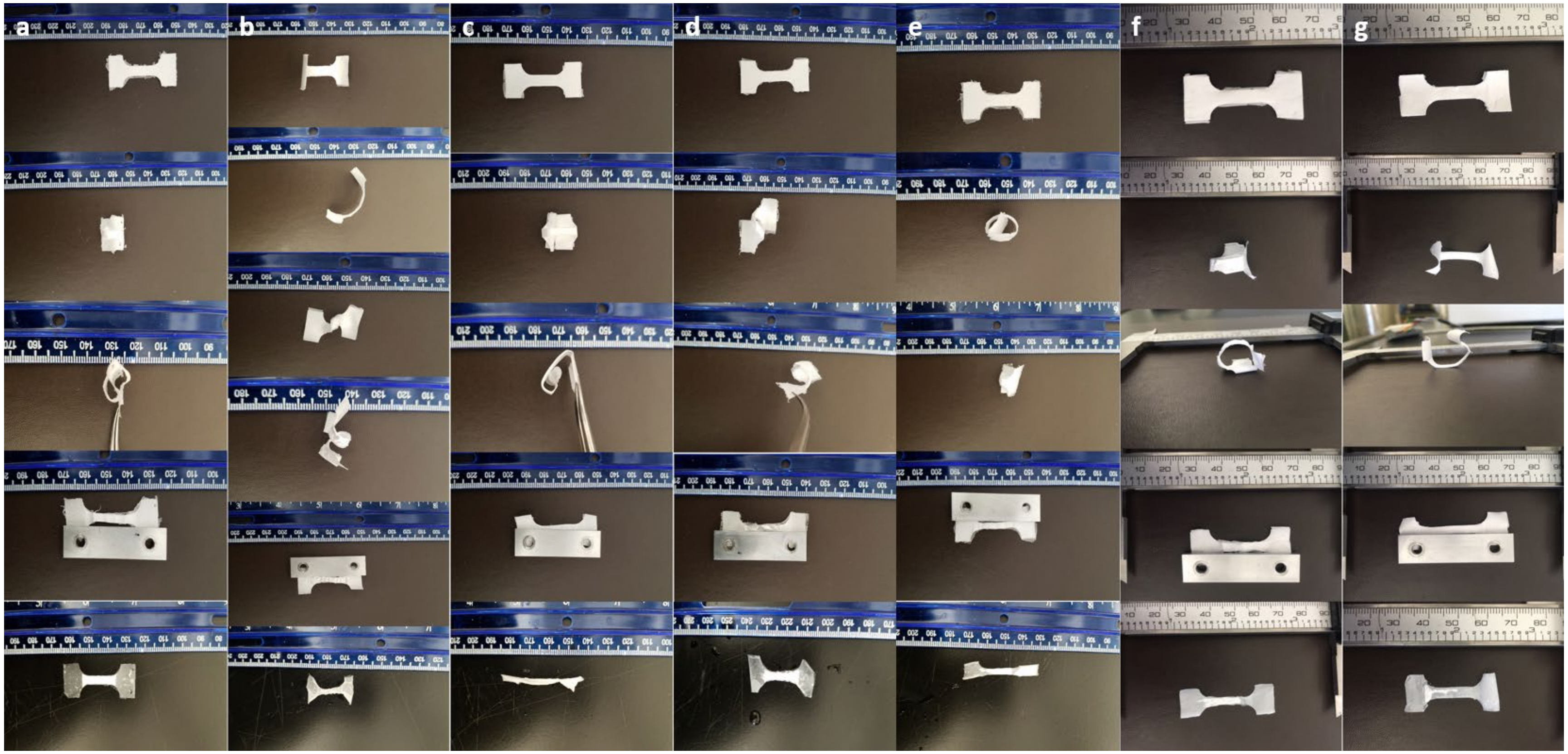

Figure A1-14: Results of manual shape memory testing for each bilayer samples (1st cycle). In general, the series of images follows the following format where the first image is the as spun dog bone, the middle series is showing the dog bone after hydration, 20% strain and being dried under constraint, and the final image is the recovered sample. (a) poly(ε-caprolactone) & poly (vinyl acetate) both isotropic, (b) poly(ε-caprolactone) & poly (vinyl acetate) both anisotropic with tension applied in the 0° fiber direction, (c) poly(ε-caprolactone) & poly (vinyl acetate) both anisotropic with tension applied in the 90° fiber direction, (d) poly(ε-caprolactone) isotropic & poly (vinyl acetate) anisotropic with tension applied in the 0° fiber direction, (e) poly(ε-caprolactone) isotropic & poly (vinyl acetate) anisotropic with tension applied in the 90° fiber direction, (f) poly(ε-caprolactone) anisotropic & poly (vinyl acetate) isotropic with tension applied in the 0° fiber direction and (g) poly(ε-caprolactone) anisotropic & poly (vinyl acetate) isotropic with tension applied in the 90° fiber direction.

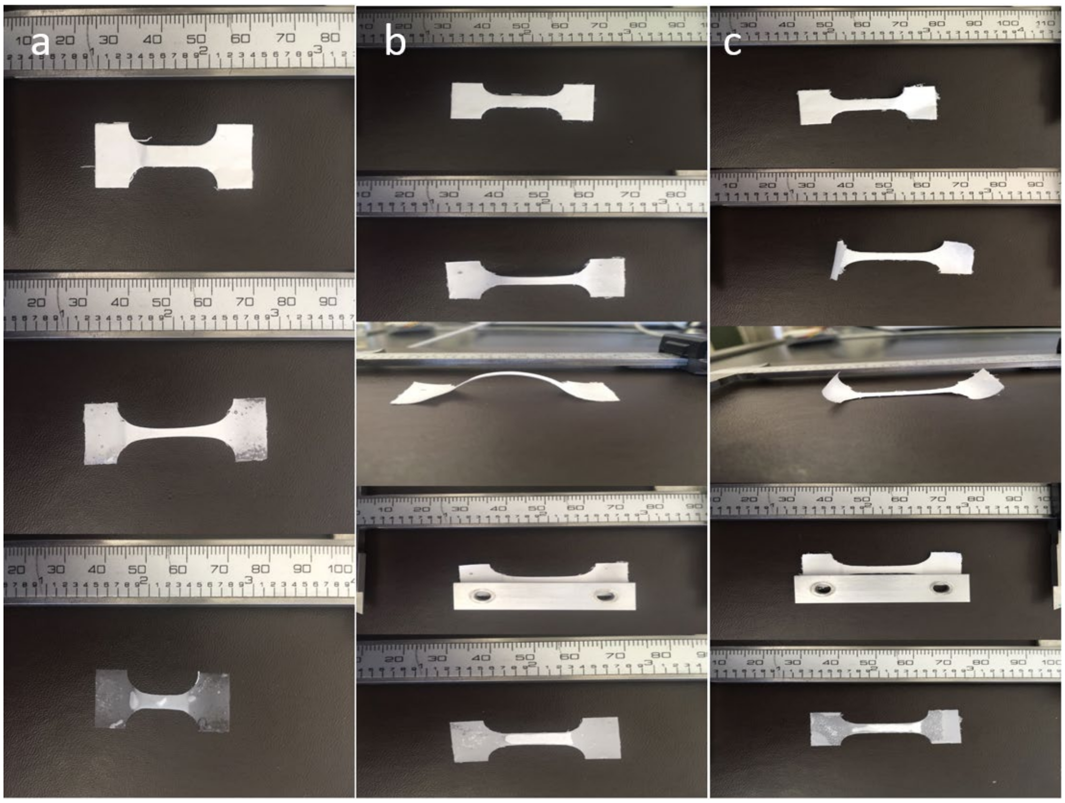

Figure A1-15: Results of manual shape memory testing for each bilayer samples (1st cycle). In general the series of images follows the following format where the first image is the as spun dog bone, the middle series is showing the dog bone after hydration, 20% strain and being dried under constraint, and the final image is the recovered sample. (a) Dual electrospun composite with 25% poly(ε-caprolactone), (b) Dual electrospun composite with 50% poly(ε-caprolactone) and (c) Dual electrospun composite with 75% poly(ε-caprolactone).

Table A1-1: Results of the manual shape memory testing performed on all the electrospun composites of poly(ε-caprolactone) and poly (vinyl acetate).

Bilayer Sample	Fixing Ratio (%)	Recovery Ratio (%)
PCL Isotropic / PVAc Isotropic	72.8 ± 3.13	98.5 ± 13.4
PCL Anisotropic / PVAc Anisotropic (0° Fiber Orientation)	78.9 ± 27.1	177.8 ± 143.31
PCL Isotropic / PVAc Anisotropic (0° Fiber Orientation)	43.6 ± 11.8	321.5 ± 108.8
PCL Anisotropic / PVAc Isotropic (0° Fiber Orientation)	39.8 ± 0.9	40.9 ± 38.9
PCL Anisotropic / PVAc Anisotropic (90° Fiber Orientation)	64.1 ± 4.9	72.6 ± 13.5
PCL Isotropic / PVAc Anisotropic (90° Fiber Orientation)	42.8 ± 11.8	46.6 ± 25.9
PCL Anisotropic / PVAc Isotropic (90° Fiber Orientation)	80.2 ± 9.2	124.7 ± 18.9
Dual Electrospun 25% PCL 75% PVAc	93.3 ± 12.8	113.7 ± 25.6
Dual Electrospun 50% PCL 50% PVAc	82.0 ± 2.1	79.7 ± 4.7
Dual Electrospun 75% PCL 25% PVAc	72.0 ± 12.9	57.8 ± 11.8

Appendix A2. Aligned Electrospun Inversed Trilayer Composites

A2.1 Synopsis.

Please refer to Chapter 2 for an explanation of experiments presented in this appendix.

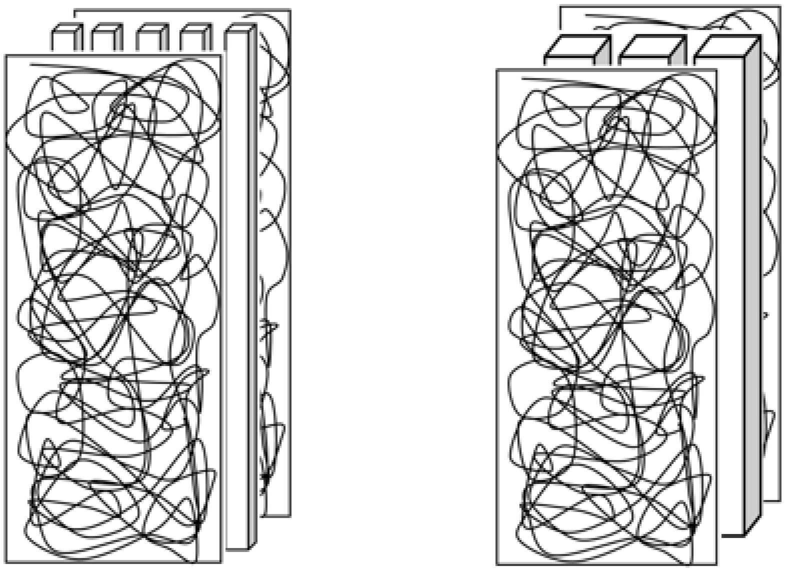

1

2

Scheme A2-1: A depiction of anisotropic electrospun inversed composites, where the Pellethane is on the outer layers. The composites are differentiated by the increasing size of the poly(methyl methacrylate) fibers in the interior. (1) Poly(methyl methacrylate) fibers with average fiber apparent diameter 22.71 ± 6.2 and (2) Poly(methyl methacrylate) fibers with average fiber apparent diameter 39.29 ± 11.7.

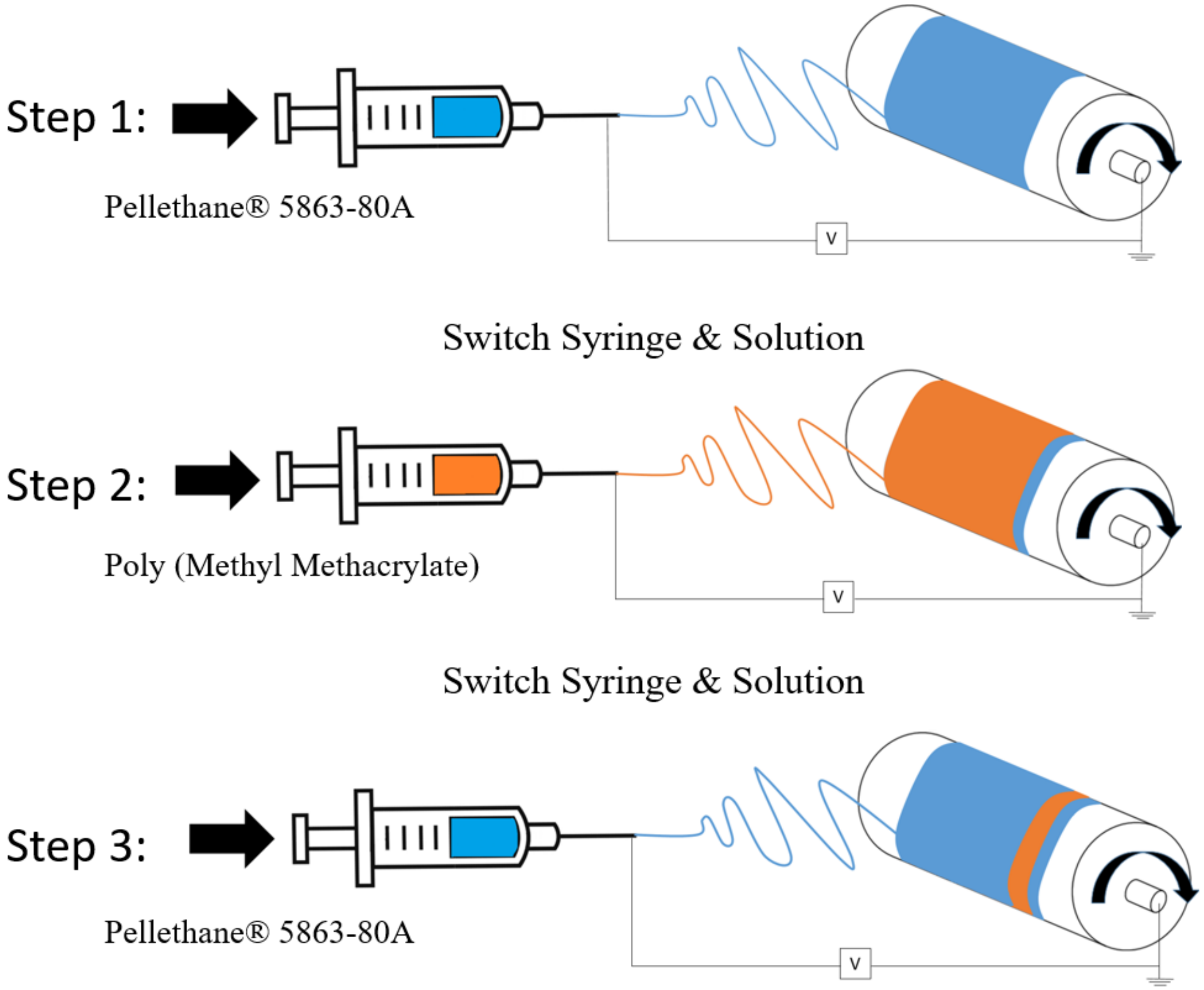

Scheme A2-2: Electrospinning setup used to electrospin aligned inverse trilayer fiber mats of Pellethane (exterior) and poly(methyl methacrylate) (interior). Fabrication begins with electrospinning Pellethane into a singular layer. Switching polymer solutions, the electrospinning is continued with the poly(methyl methacrylate) directly on top of the pervious layer. Finishing off the composite by switching the polymer solution back to the previous Pellethane and electrospinning directly on top of the previous two layers.

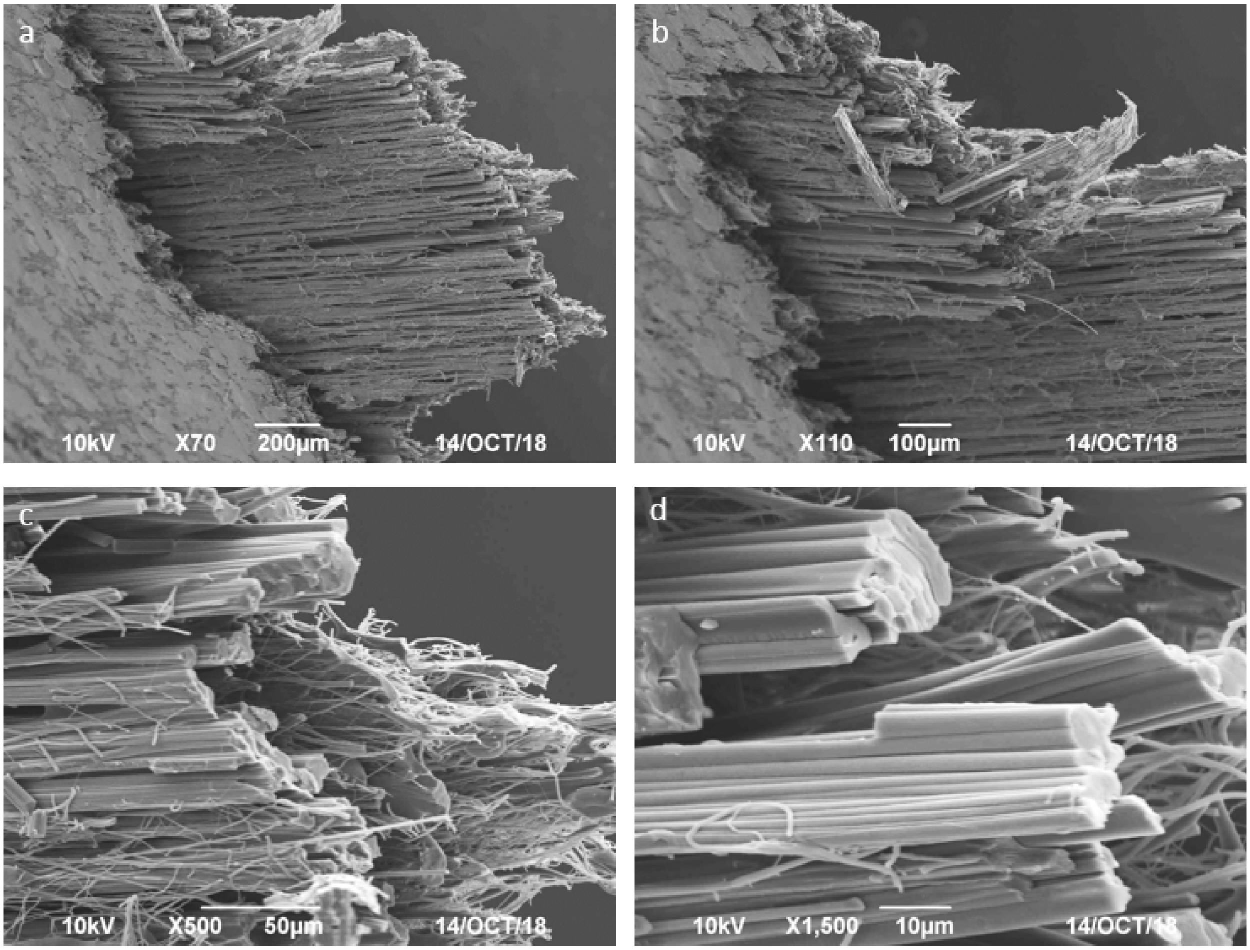

Figure A2-1: SEM Micrographs of electrospun inverse trilayer of the fiber apparent diameter of 22.71 ± 6.2. (a)(b) Shows the exterior layer of Pellethane on top of the large poly(methyl methacrylate) fibers. (c)(d) Shows the poly(methyl methacrylate) fibers close up. The fibers are larger than the Pellethane fibers and solid.

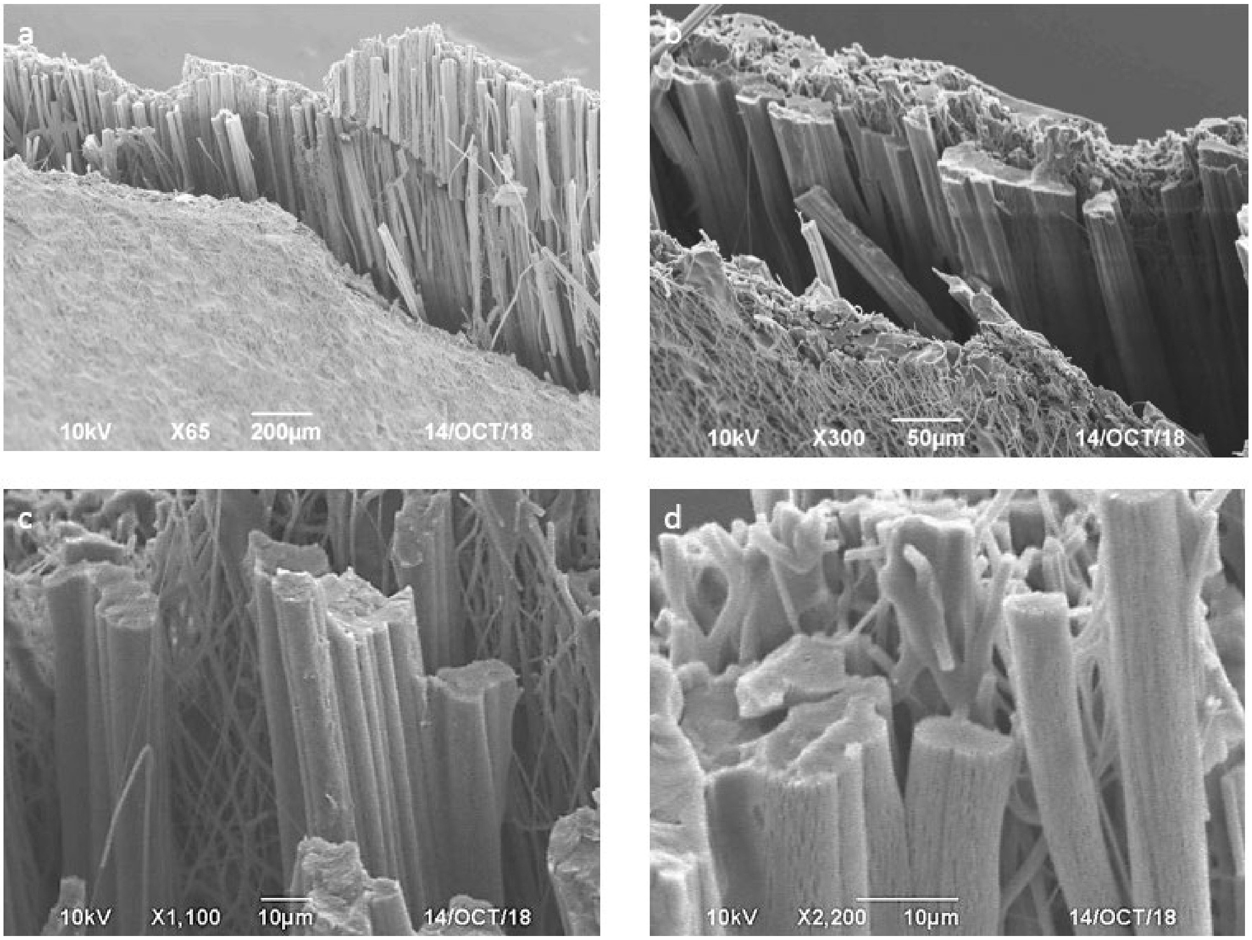

Figure A2-2: SEM Micrographs of electrospun inverse trilayer of the fiber apparent diameter of 39.29 ± 11.7. (a)(b) Shows the exterior layer of Pellethane on top of the large poly(methyl methacrylate) fibers. (c)(d) Shows the poly(methyl methacrylate) fibers close up. The fibers are larger than the Pellethane fibers and solid.

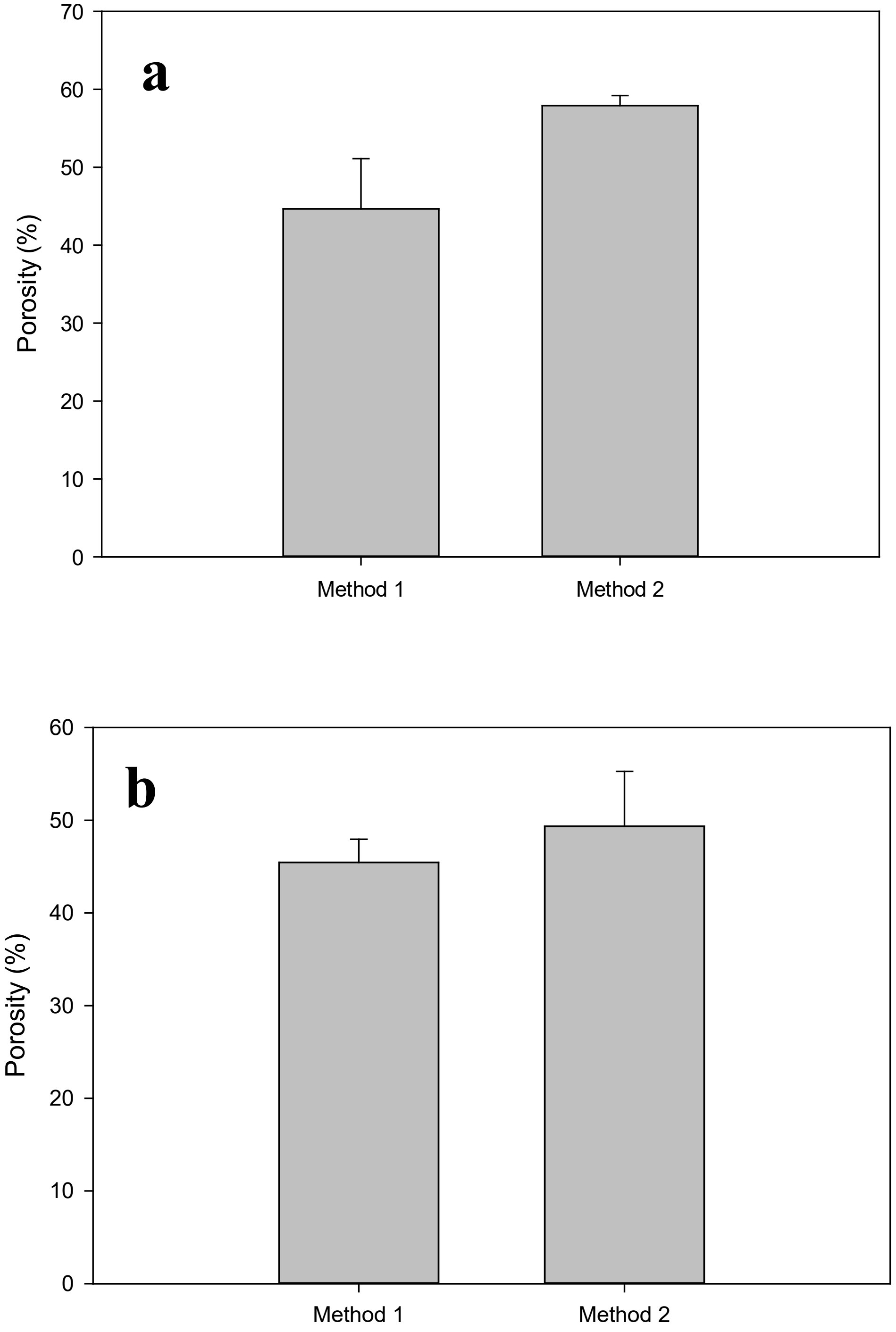

Figure A2-3: Bar charts of the measured apparent porosity (method 1) and porosity (method 2) performed in the same method as shown in **Scheme 2-5** for (a) inverse trilayer with the average fiber apparent diameter of 22.71 ± 6.2 and (b) inverse trilayer with the average fiber apparent diameter of 39.29 ± 11.7.

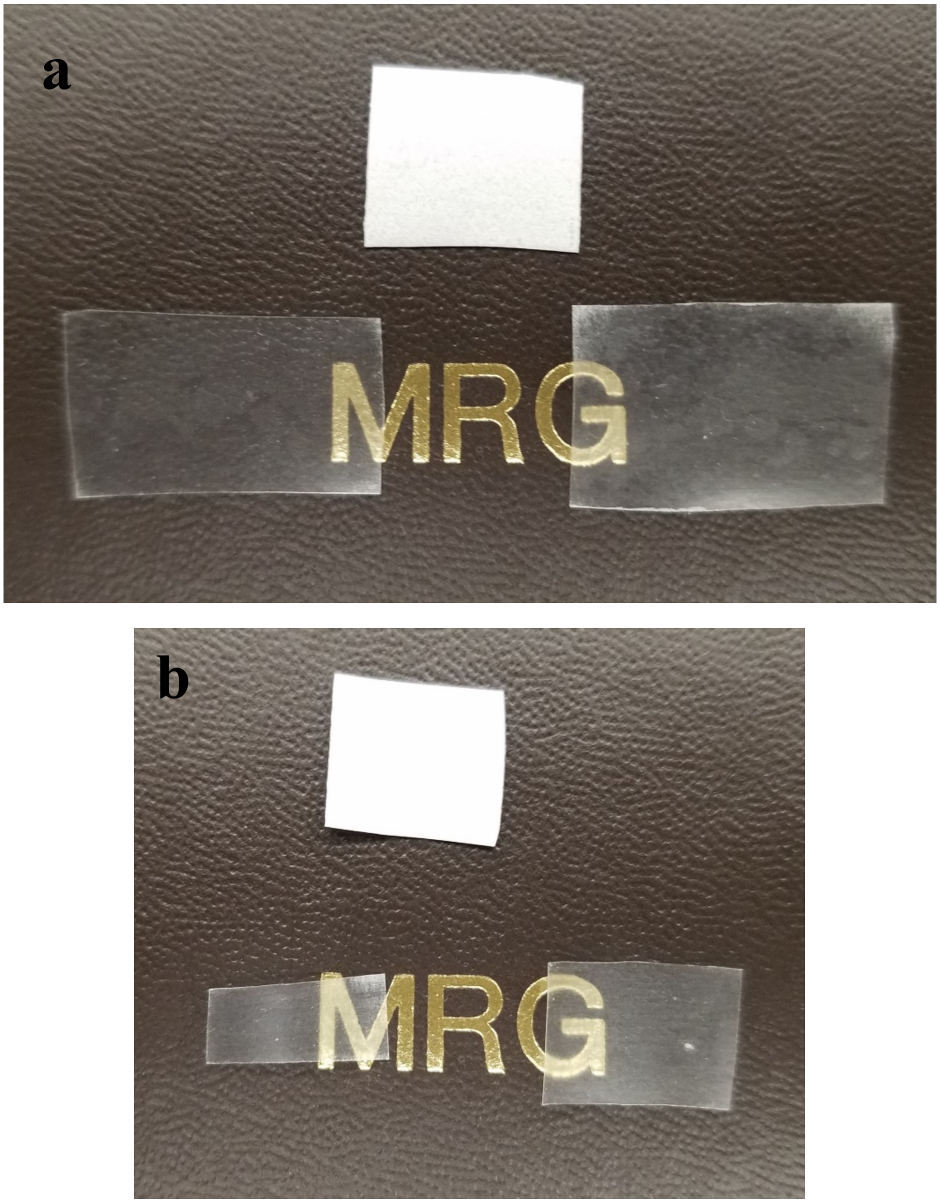

Figure A2-4: Representative images showing the change in physical appearance between the as spun fiber sheet (**a**) and the melted film (**b**) conducted in the same method as in **Scheme 2-5** for (a) inverse trilayer with the average fiber apparent diameter of 22.71 ± 6.2 and (b) inverse trilayer with the average fiber apparent diameter of 39.29 ± 11.7.

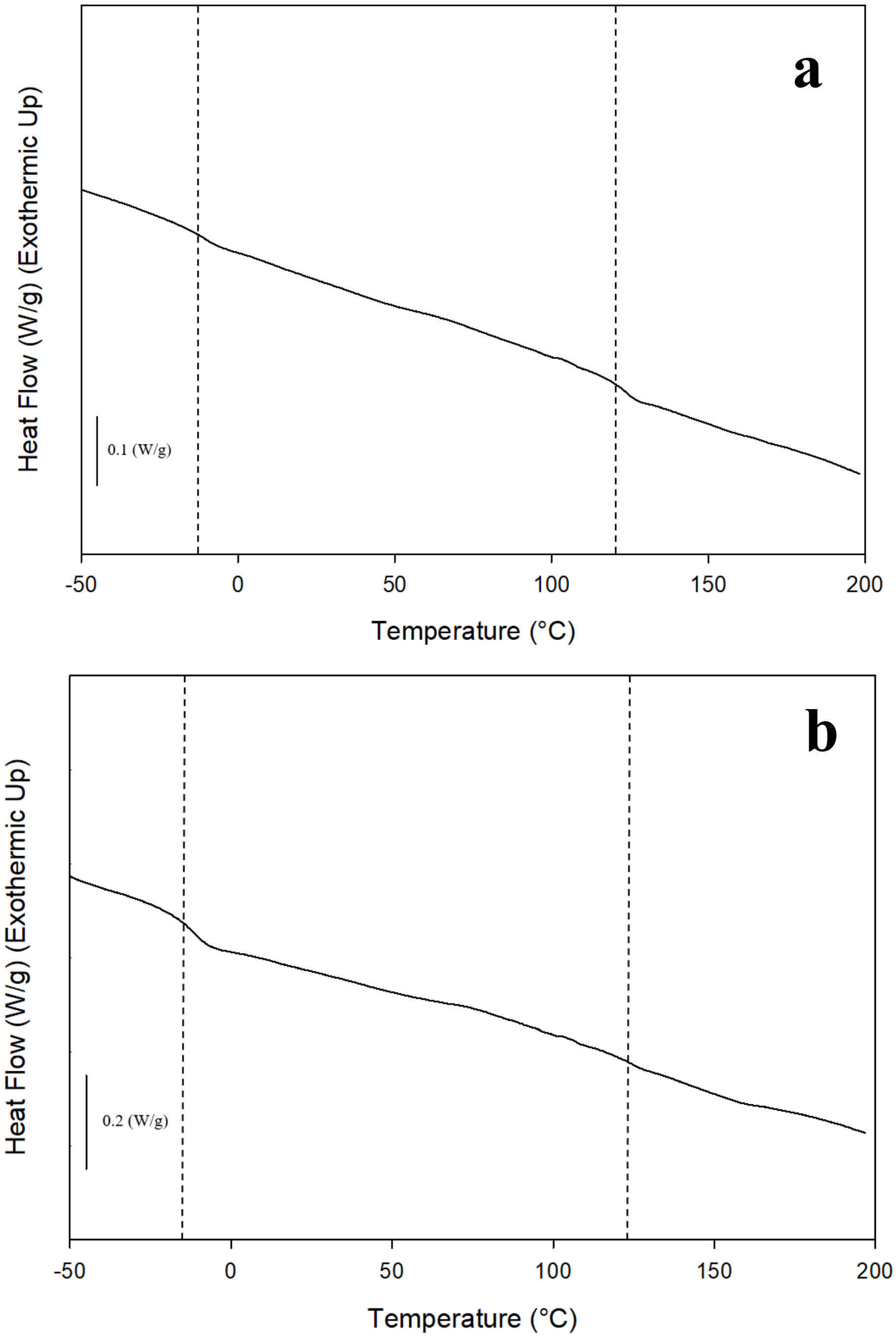

Figure A2-5: DSC of the second heating curves for (**a**) inverse trilayer with the average fiber apparent diameter of 22.71 ± 6.2 and (**b**) inverse trilayer with the average fiber apparent diameter of 39.29 ± 11.7. The measured glass transition temperatures (T_g) for Pellethane is -10 °C and 125°C for poly(methyl methacrylate). Pellethane is a thermoplastic elastomer and has a small melt peak around 155 °C.

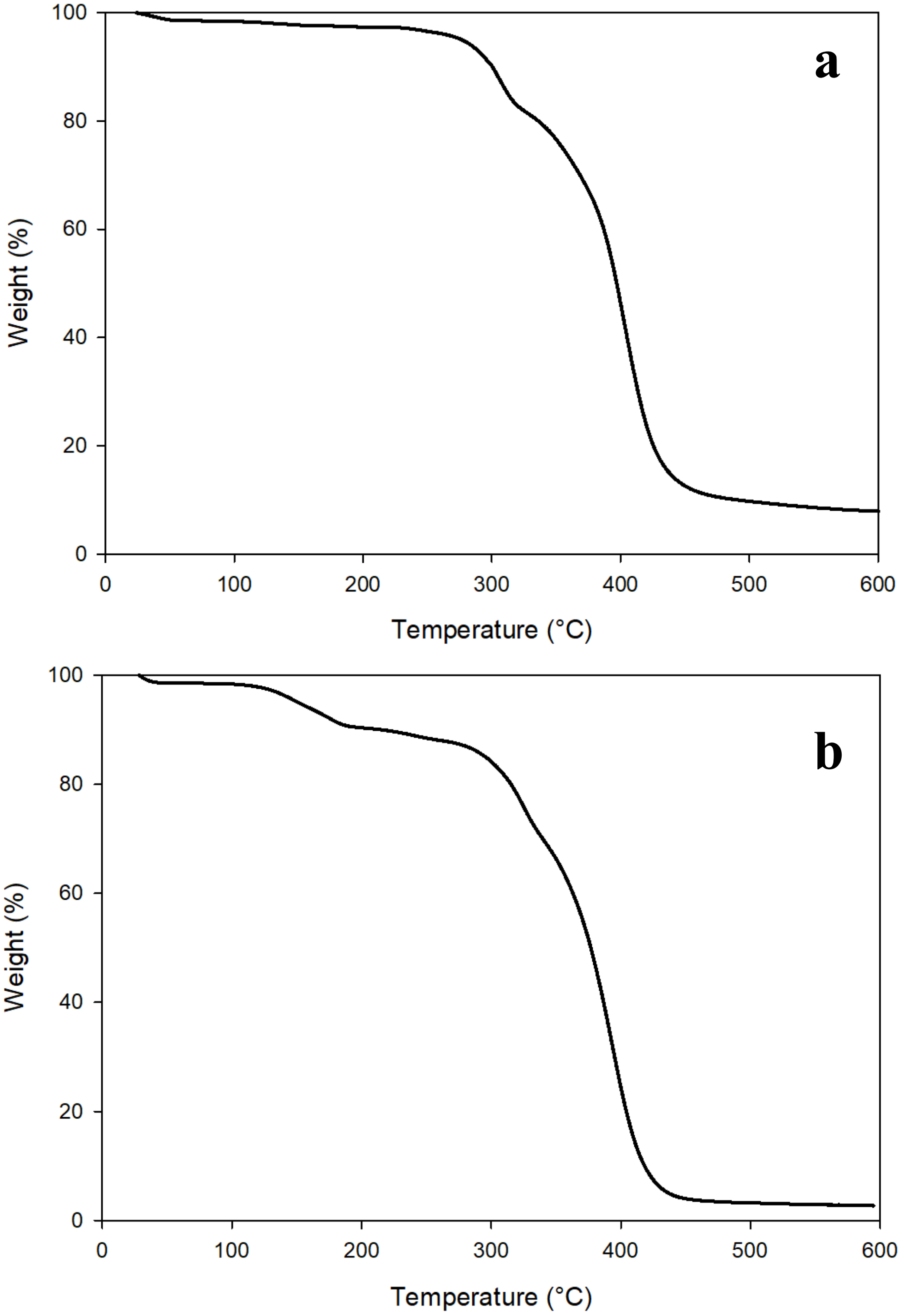

Figure A2-6: TGA mass loss curves as a function of temperature for (a) inverse trilayer with the average fiber apparent diameter of 22.71 ± 6.2 and (b) inverse trilayer with the average fiber apparent diameter of 39.29 ± 11.7.

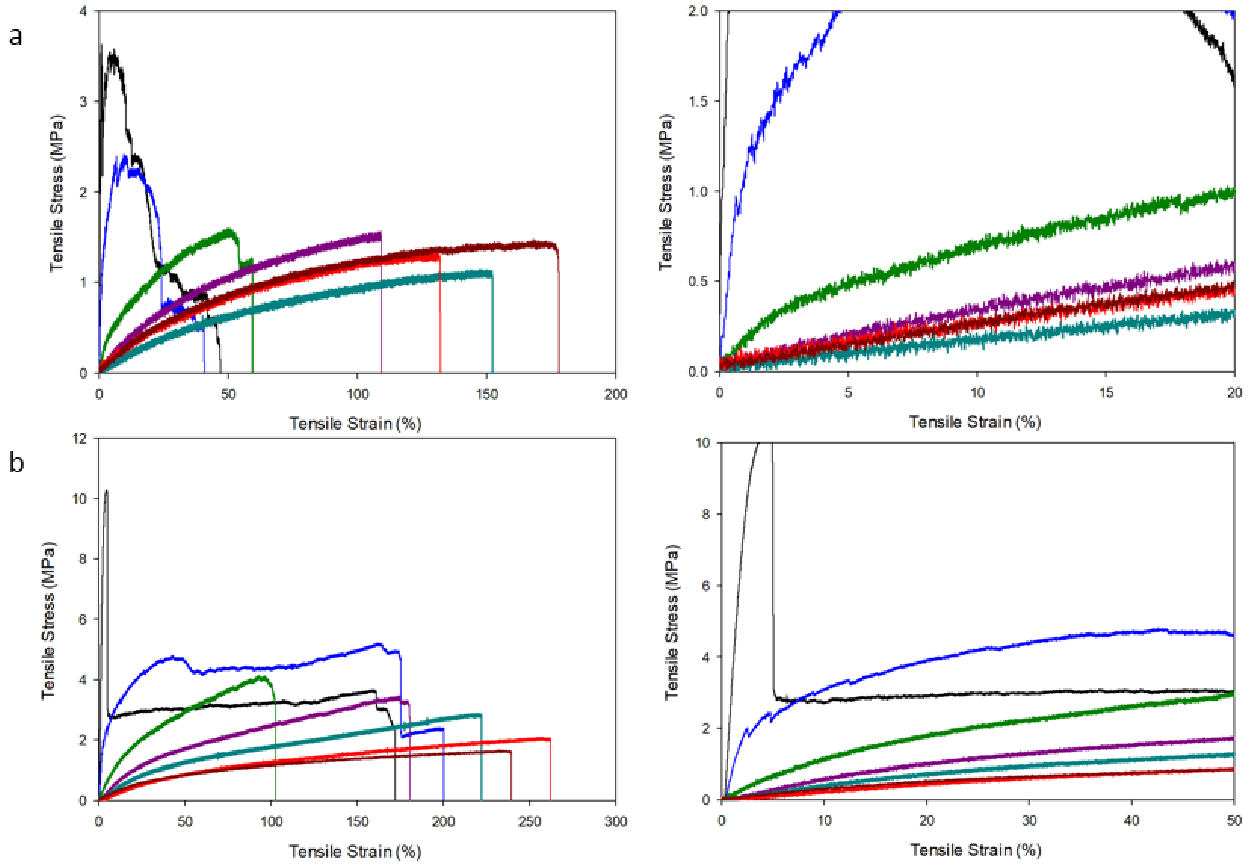

Figure A2-7: Representative stress-strain curves (first column) and magnified view of the elastic deformation (second column) for (a) inverse trilayer with the average fiber apparent diameter of 22.71 ± 6.2 and (b) inverse trilayer with the average fiber apparent diameter of 39.29 ± 11.7. Each graph shows seven distinct fiber orientation angles ($\Delta\theta$) of 0° (black), 15° (blue), 30° (green) 45°(purple), 60° (turquoise), 75° (red) and 90° (brown). All sample curves are an average of n = 5.

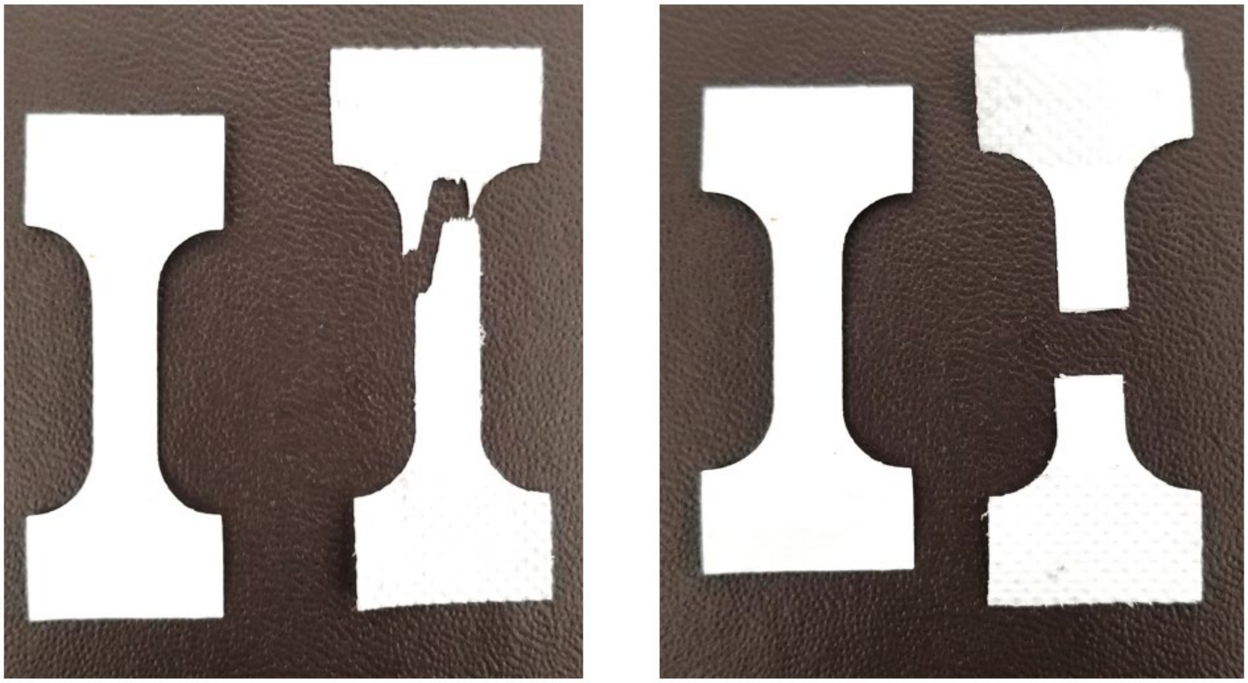

0° Fiber Orientation Angle

90° Fiber Orientation Angle

Figure A2-8: Representative post tensile tested dog bones (right) with pre tensile tested dog bones (left) for the inverse trilayer with the average fiber apparent diameter of 22.71 ± 6.2.

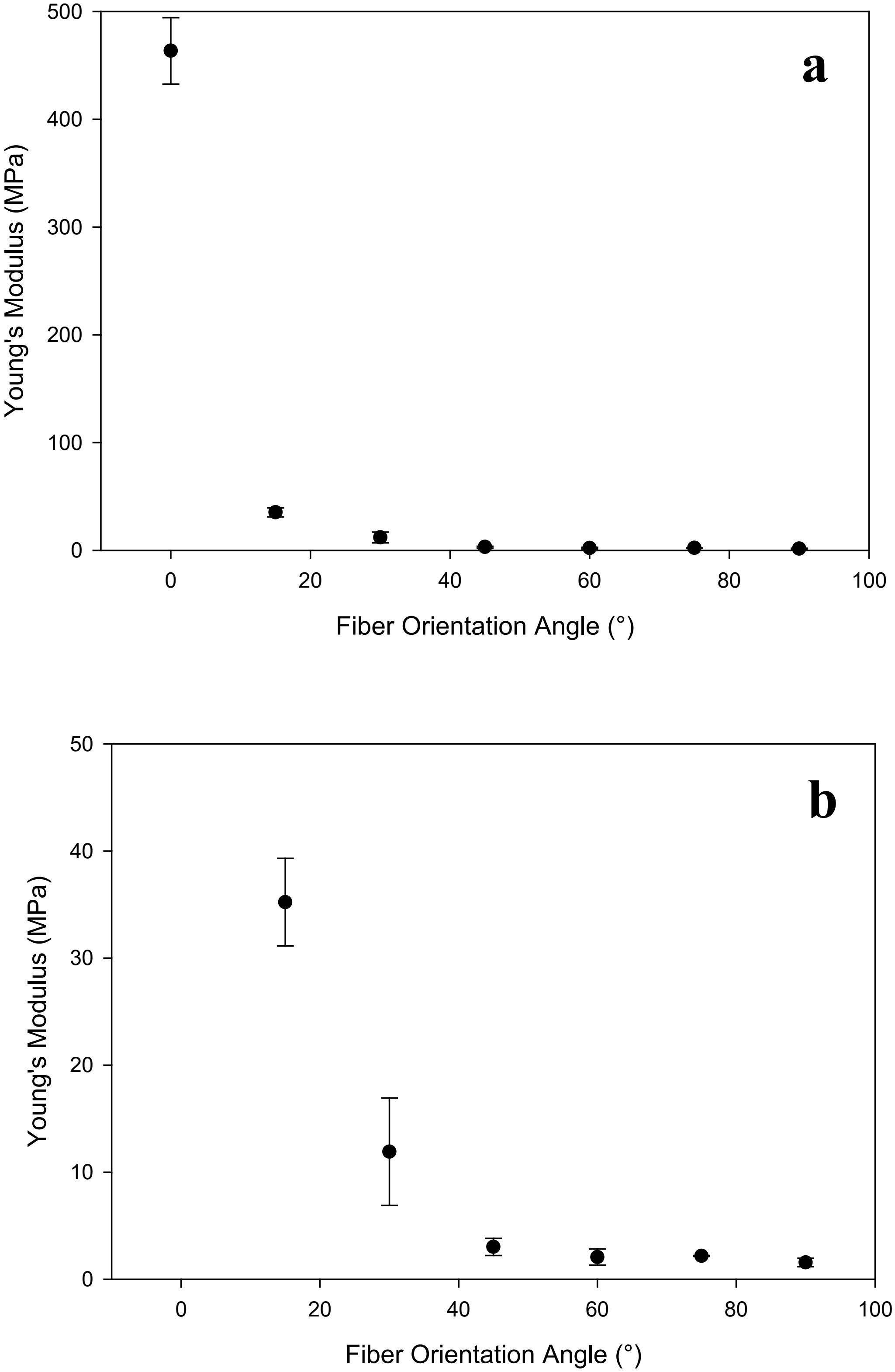
a
Young's Modulus (MPa)
500
400
300
200
100
0
0
20
40
60
80
100
Fiber Orientation Angle (°)
b
Young's Modulus (MPa)
50
40
30
20
10
0
0
20
40
60
80
100
Fiber Orientation Angle (°)

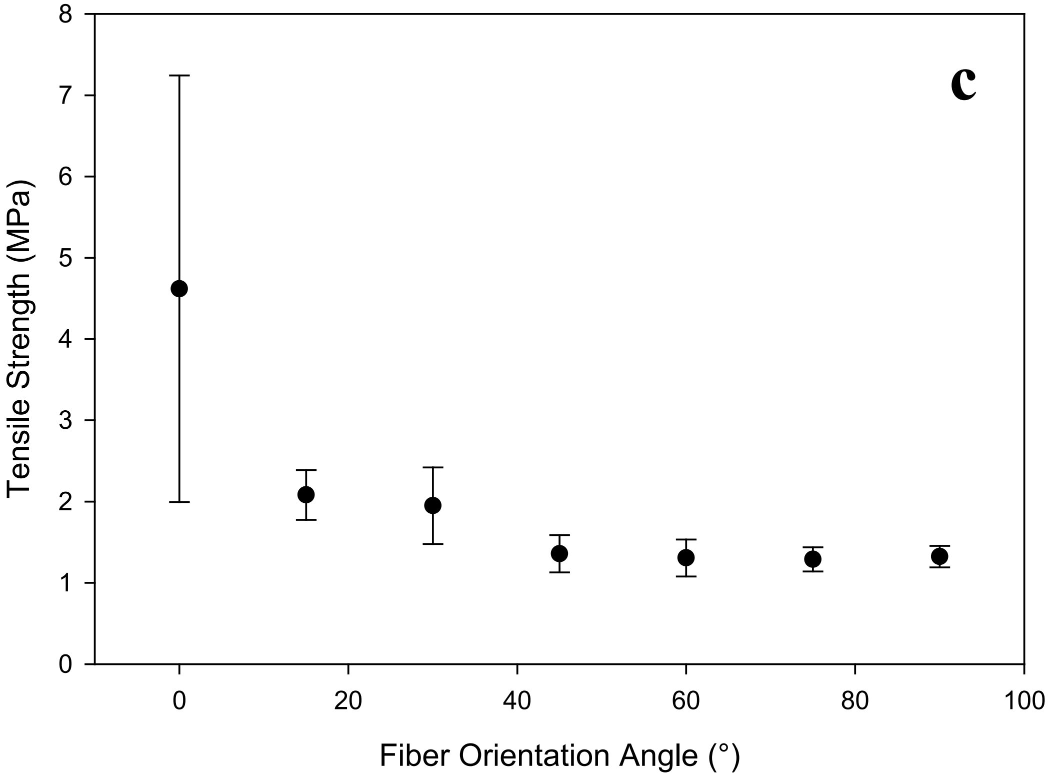
c
Tensile Strength (MPa)
0
1
2
3
4
5
6
7
8
0
20
40
60
80
100
Fiber Orientation Angle (°)

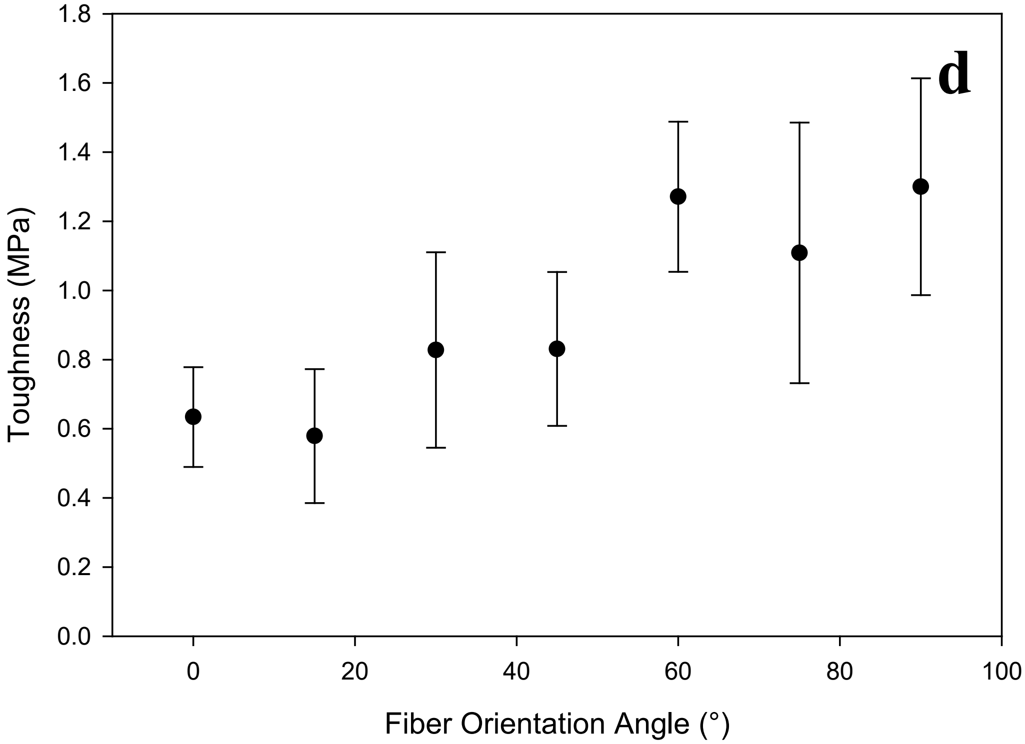
d
Toughness (MPa)
0.0
0.2
0.4
0.6
0.8
1.0
1.2
1.4
1.6
1.8
0
20
40
60
80
100
Fiber Orientation Angle (°)

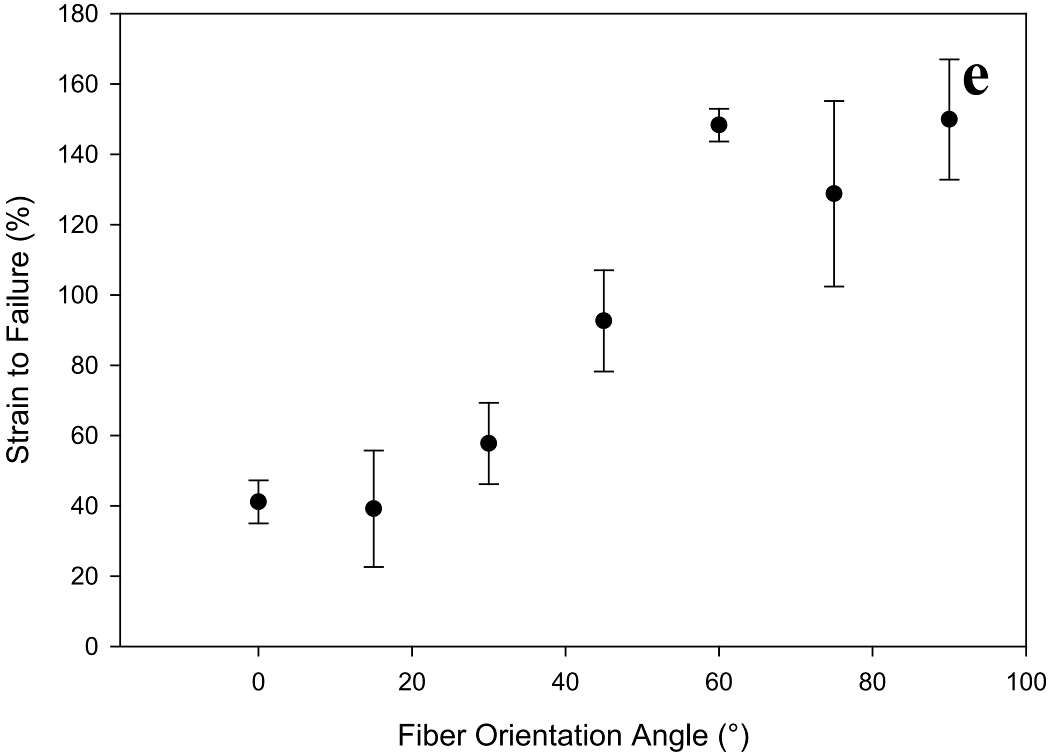

Figure A2-9: Resulting mechanical properties of the electrospun inverse trilayer with the average fiber apparent diameter of 22.71 ± 6.2 from tensile testing as a function of the fiber orientation angle. (a) Young's modulus, (b) magnified view of Young's modulus, (c) tensile strength, (d) toughness and (e) strain-to-failure. All data points are an average of n = 5

Table A2-1: Average Young’s modulus, toughness, tensile strength, and strain to failure for all fiber orientation angles (Δθ) interpreted from the stress strain curves of the electrospun inverse trilayer with the average fiber apparent diameter of 22.71 ± 6.2.

Material Property	**Fiber Orientation Angle [°]**						
	0	*15*	*30*	*45*	*60*	*75*	*90*
Young's Modulus [MPa]	463.58 ± 30.8	35.23 ± 4.1	11.91 ± 5.0	3.03 ± 0.8	2.07 ± 0.8	2.18 ± 0.1	1.57 ± 0.4
Toughness [MPa]	0.63 ± 0.14	0.58 ± 0.2	0.83 ± 0.29	0.83 ± 0.2	1.27 ± 0.2	1.11 ± 0.4	1.30 ± 0.3
Tensile Strength [MPa]	4.62 ± 2.6	2.08 ± 0.3	1.95 ± 0.5	1.36 ± 0.2	1.31 ± 0.2	1.29 ± 0.1	1.32 ± 0.1
Strain to Failure [%]	41.13 ± 6.1	39.18 ± 16.6	57.75 ± 11.6	92.7 ± 14.4	148.32 ± 4.65	128.79 ± 26.4	149.93 ± 17.1

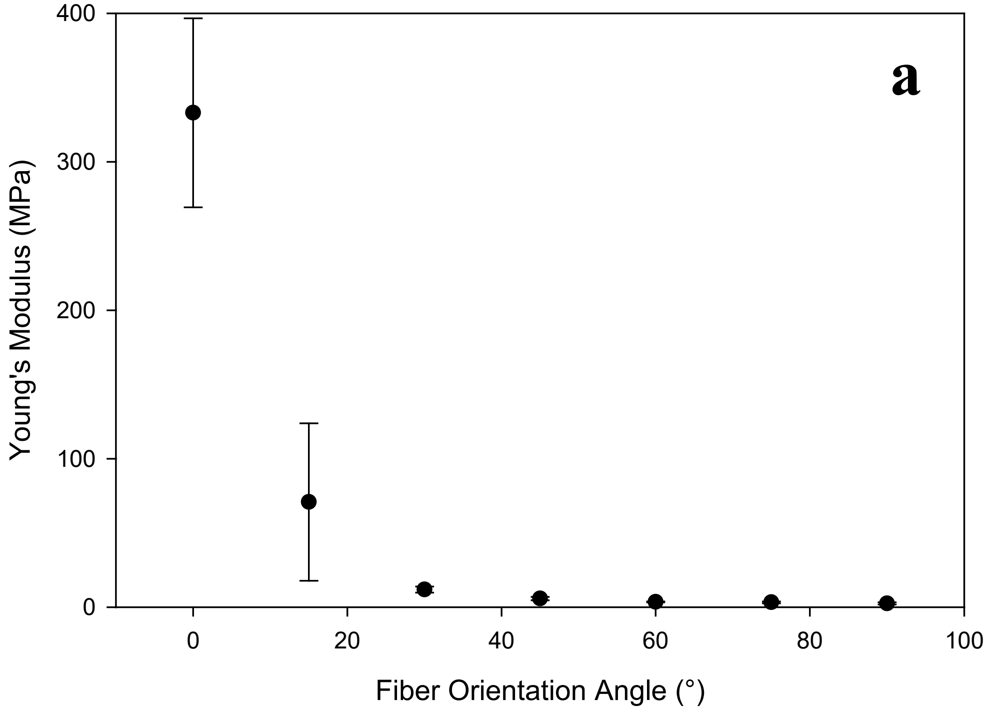
a
Young's Modulus (MPa)
400
300
200
100
0
0
20
40
60
80
100
Fiber Orientation Angle (°)

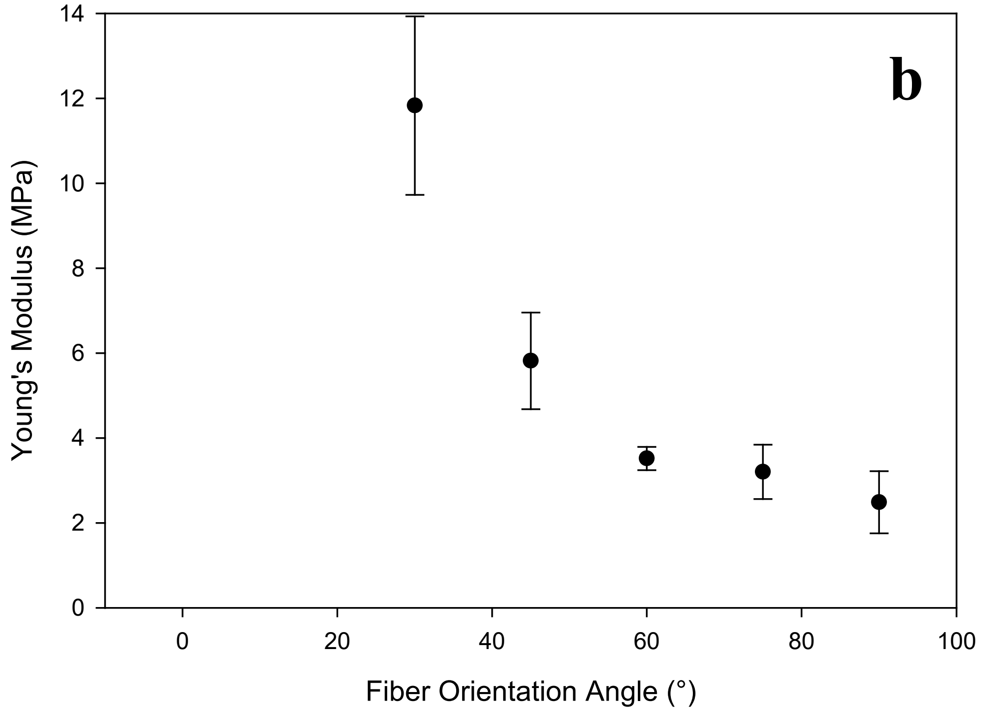
b
Young's Modulus (MPa)
14
12
10
8
6
4
2
0
0
20
40
60
80
100
Fiber Orientation Angle (°)

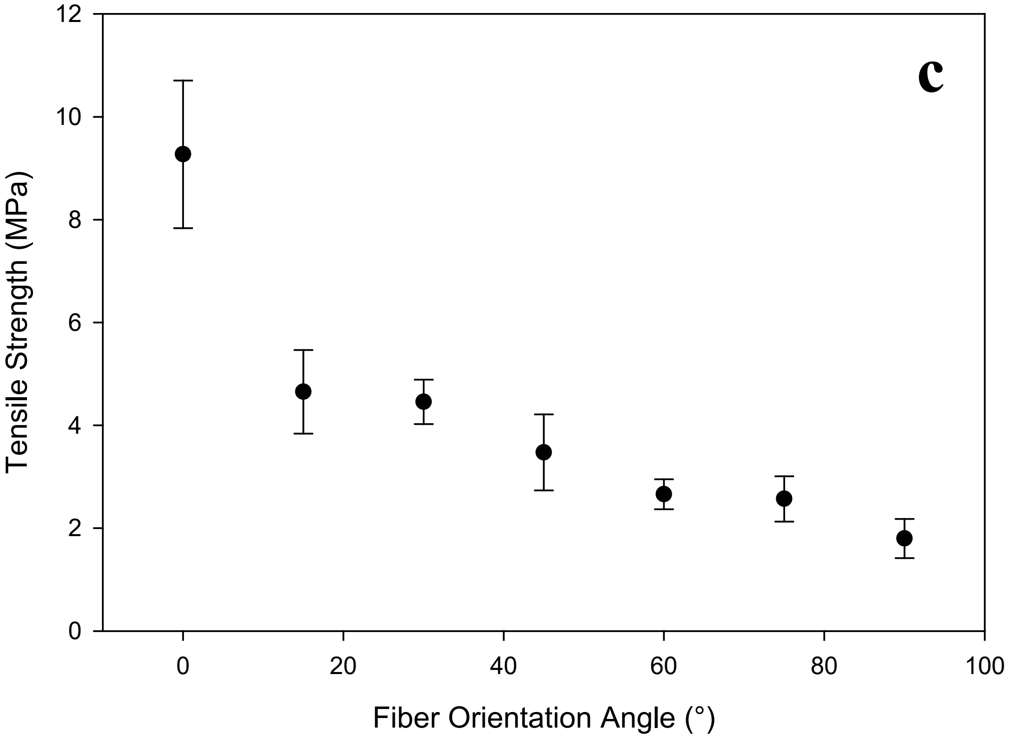
c
Tensile Strength (MPa)
0
2
4
6
8
10
12
Fiber Orientation Angle (°)
0
20
40
60
80
100

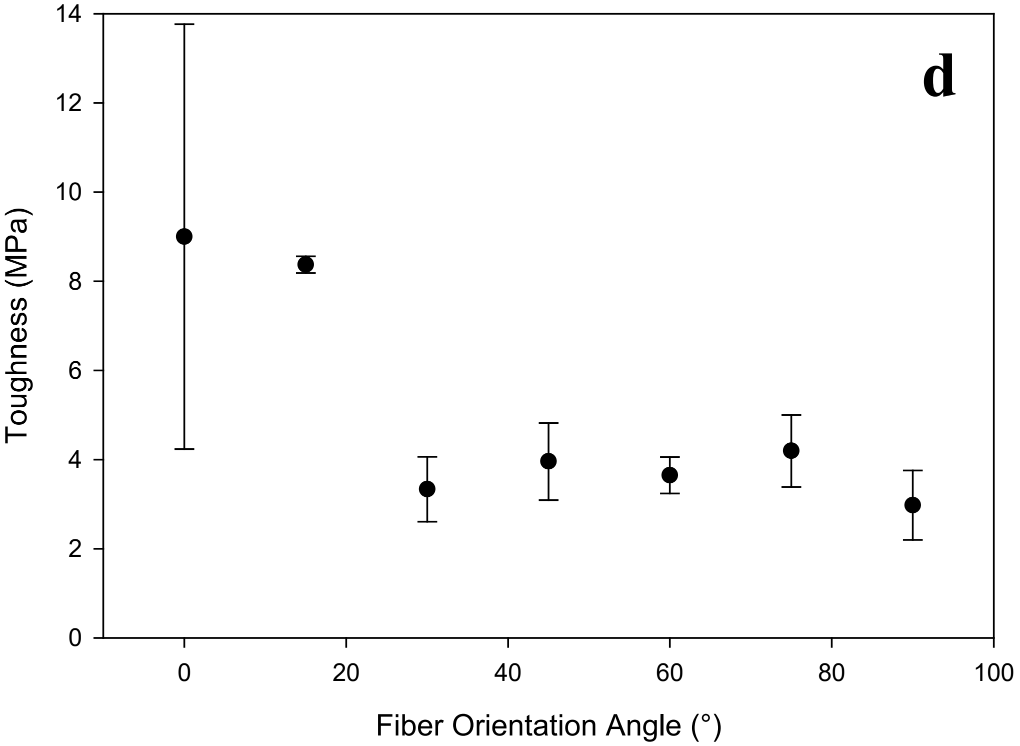
d
Toughness (MPa)
0
2
4
6
8
10
12
14
Fiber Orientation Angle (°)
0
20
40
60
80
100

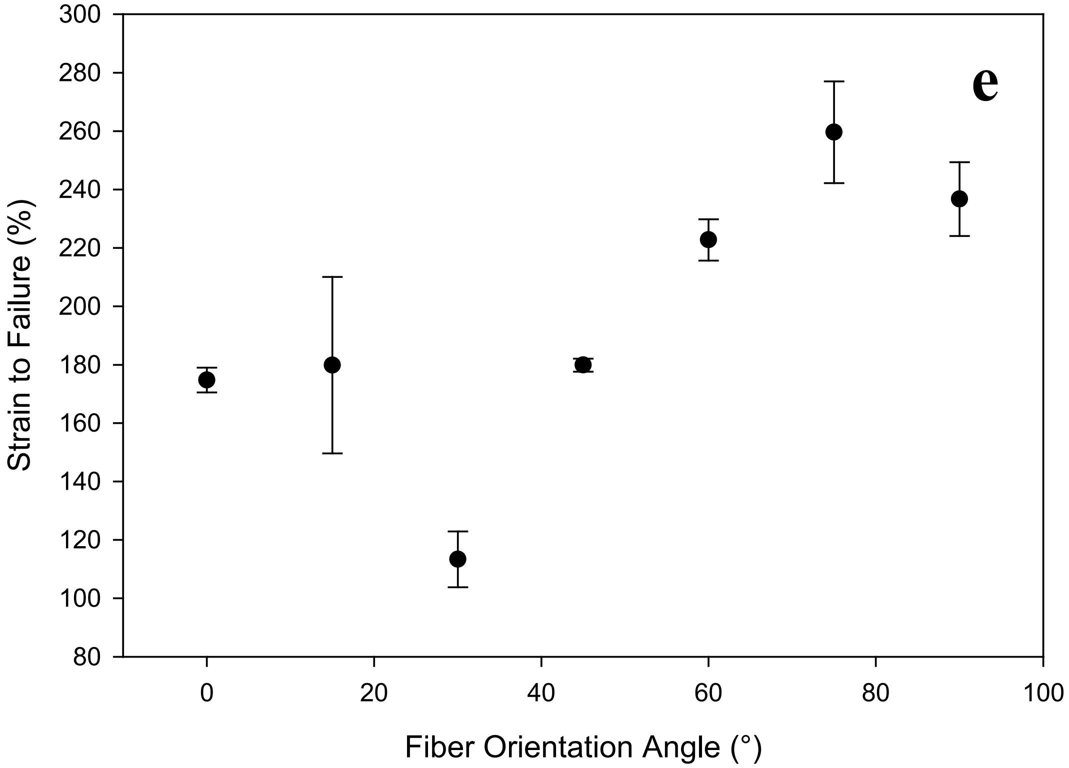

Figure A2-10: Resulting mechanical properties of the electrospun inverse trilayer with the average fiber apparent diameter of 39.29 ± 11.7 from tensile testing as a function of the fiber orientation angle. (a) Young's modulus, (b) magnified view of Young's modulus, (c) tensile strength, (d) toughness and (e) strain-to-failure. All data points are an average of n = 5

Table A2-2: Average Young’s modulus, toughness, tensile strength, and strain to failure for all fiber orientation angles (Δθ) interpreted from the stress strain curves of the electrospun inverse trilayer with the average fiber apparent diameter of 39.29 ± 11.7.

Material Property	**Fiber Orientation Angle [°]**						
	0	*15*	*30*	*45*	*60*	*75*	*90*
Young's Modulus [MPa]	333.11 ± 63.7	70.79 ± 53.0	11.83 ± 2.1	5.82 ± 1.1	3.52 ± 0.3	3.20 ± 0.6	2.49 ± 0.7
Toughness [MPa]	9.00 ± 4.7	8.38 ± 0.2	3.33 ± 0.7	3.96 ± 0.9	3.65 ± 0.4	4.19 ± 0.8	2.98 ± 0.8
Tensile Strength [MPa]	9.27 ± 1.4	4.65 ± 0.8	4.45 ± 0.4	3.47 ± 0.7	2.66 ± 0.3	2.57 ± 0.4	1.79 ± 0.4
Strain to Failure [%]	174.77 ± 4.3	179.83 ± 30.2	113.35 ± 9.6	179.89 ± 2.2	222.76 ± 7.1	259.63 ± 17.4	236.73 ± 12.6

Table A2-3: Anisotropy of the electrospun inverse trilayer with the average fiber apparent diameter of 22.71 ± 6.2 samples quantified as a function of Young's modulus (top) and storage modulus (bottom) in a ratio of the 0° / 90° fiber orientation angles obtained through interpreting the stress-strain curves.

Fiber Orientation Angle [°]	Youngs Modulus [MPa]	Anisotropy
0	463.58	295.27
90	1.57	

Fiber Orientation Angle [°]	$E'_{20\,°C}$ (MPa)	Anisotropy
0	395	313.49
90	1.26	

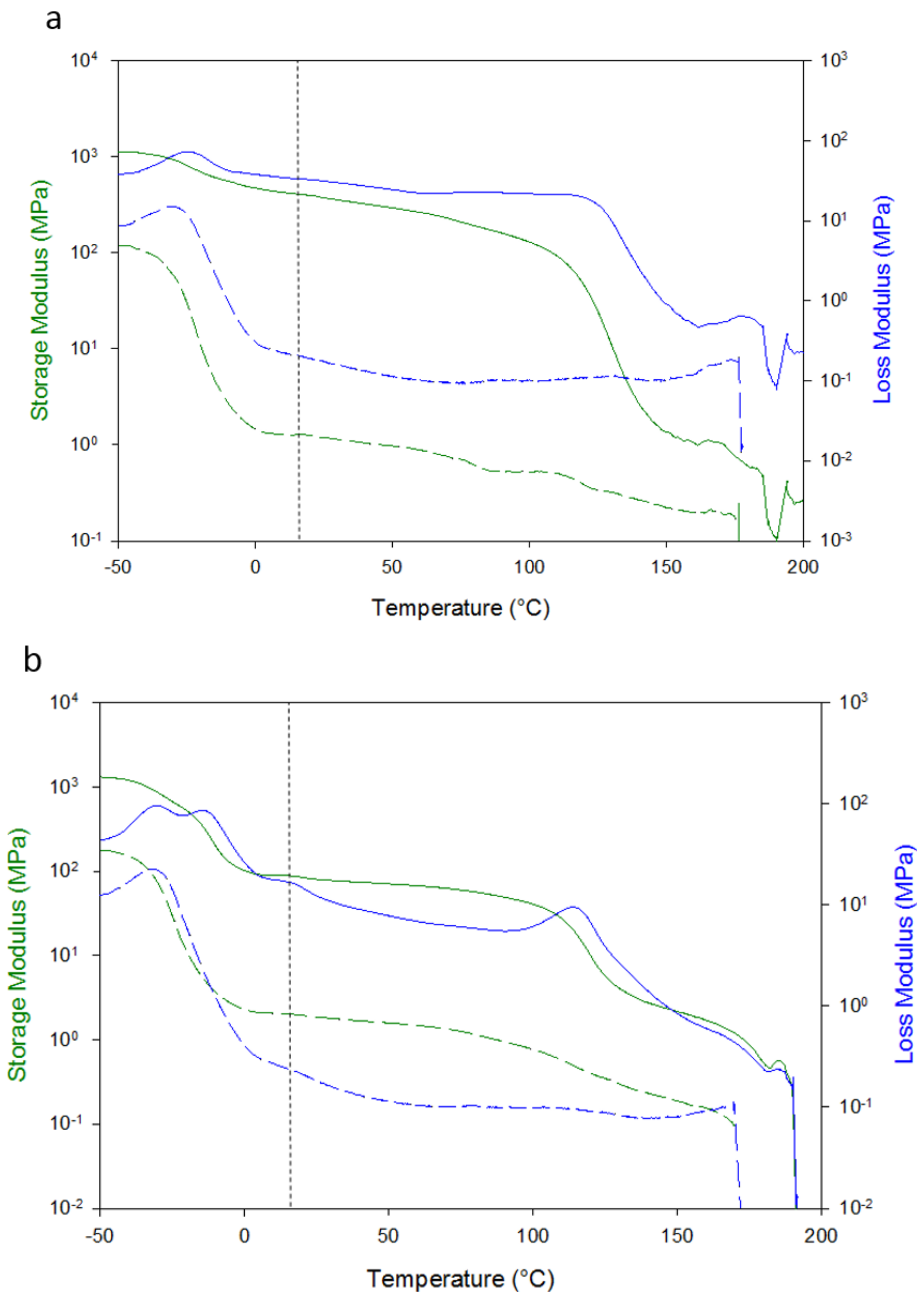

Figure A2-11: Dynamic mechanical analysis of 0° fiber orientation (solid) and 90° fiber orientation (dashed) for (a) inverse trilayer with the average fiber apparent diameter of 22.71 ± 6.2 and (b) inverse trilayer with the average fiber apparent diameter of 39.29 ± 11.7.

Table A2-4: Anisotropy of the electrospun inverse trilayer with the average fiber apparent diameter of 39.29 ± 11.7 samples quantified as a function of Young's modulus (top) and storage modulus (bottom) in a ratio of the 0° / 90° fiber orientation angles obtained through interpreting the stress-strain curves.

Fiber Orientation Angle [°]	Youngs Modulus [MPa]	Anisotropy
0°	333.11	133.78
90°	2.49	

Fiber Orientation Angle [°]	E' $_{20\,°C}$ (MPa)	Anisotropy
0°	84.5	43.56
90°	1.94	

Appendix Chapter A3. Development of an Electrospun Composite with Twisting Actuation.

A3.1 Synopsis

A highly desired soft material application in biomimicry is to replicate twisting actuation, like what is found in the Achilles tendon[1]. Designing a polymer material that will create a torque while being strained has been highly desired. The second aim within this chapter is to use an alteration to the PMMA, Pellethane laminate material discussed above. The change is the orientation of one layer of PMMA fiber to 45°. Doing this will cause an asymmetry in the stress across the material while it is being tensioned, the resulting mechanical deformation will be to twist. Tuning the appropriate variables, we will be able to achieve omni-directional, and well as full reversible twisting of the material.

A3.2 Experimental

A3.2.1 Materials, Electrospinning Solutions & Equipment

Please refer to chapter 2 with the following one exception.

A3.2.2 Pentalayer Fabrication

Fabricating a pentalayer composite will occur in five distinct steps. Step one, electrospinning a layer of isotropic Pellethane using an 80RPM rotational speed of the collector mandrel. Step two, the next layer electrospun directly on to the previous layer of anisotropic poly(methyl methacrylate) using a 2000RPM rotational speed of the collector mandrel. Step three, isotropic Pellethane was electrospun directly on to the previous layers. Step four, a layer of anisotropic poly(methyl methacrylate) was electrospun directly on to the previous layers. Finally step five, a layer of isotropic Pellethane was electrospun onto all the previous.

A3.2.3 Twisting Actuator Fabrication

The twisting actuators were fabricated using a very similar methodology as was discussed in the prior section. For the pentalayer-twisting actuator **Scheme A3-1** first, a PMMA solution was electrospun onto a rotating drum at 2000 rpm. Pellethane was then directly electrospun on the PMMA fiber sheet using a much slower mandrel speed of 100 rpm. This slower rotational speed will cause isotropy in the Pellethane fiber sheet. Finally the bilayer was removed from the mandrel and rotated clockwise, or anti-clockwise 45° then placed back on the mandrel for the final layer of PMMA to be electrospun directly on top. The fabrication of the pentalayer-twisting actuator will again follow a very similar procedure. The addition to this composite is electrospinning isotropic Pellethane first, and last using it to encase the former composite in the Pellethane elastomer.

A3.2.4 Torsion Testing

Quantification of the torsion generated in the twisting actuator samples was done through adaption of the TA Discovery HR-2 Rheometer. Using custom grips **Figure A3-2** for solid samples, dog bones of the same dimensions used from the mechanical testing section were cut. The samples were tested so that one layer of the PMMA fibers were perpendicular to the direction of tension. Using the axial procedure, the sample is pulled to a specified distance while holding the angular velocity to zero and measuring the amount of torque generated. Once the sample reaches the desired length, the program is rerun using compression to measure the amount of torque generated during the slow release of strain. Both experiments can be merged in the rheometer program to generate a desired hysteresis curve.

A3.2.5 Light Microscopy

Determination of PMMA fiber orientation of all twisting actuators was done using the Leica DM2700M light microscope with the Leica DFC450 camera attachment. All samples were imaged as made. The samples were placed on a glass slide and using a 10x magnification, images were taken. All images were analyzed using Gwyddion to accurately determine the angle of PMMA fiber offset as seen in **Figure A3-1**.

A3.3 Preliminary Results & Initial Conclusions

Successful fabrication of an electrospun composite that shows a torsion in response to mechanical strain has been demonstrated. Creating a mulita-layered laminate structure that is able to resist strain asymmetrically is being exploited to achieve this. Building off the research preformed in **Chapter 2**, the sample fabrication techniques and materials were used to achieve this twisting actuation. As shown in **Scheme A3-1** and **Figure A3-1**, changing the fiber orientation angle of one layer of the poly(methyl methacrylate) fibers was sufficient to cause asymmetric deformation resulting in a torsion.

Using custom geometries for the TA Discovery HR-2 Rheometer, we were able to measure the amount of torsion the material will generate during strain. As shown in **Figure A3-2** the material will reversibly generate torque proportional to the amount of strain induced. In general the more strain induced, the more torque the sample will generate until it reaches the materials upper limit. If the sample is rotated about the center axis, we are able to generate torque in the opposite direction, with the same torque strain relationship observed. The omni-directional torque is another key achievement for this work.

A3.4 References

1. van Gils, C. C., Steed, R. H. & Page, J. C. Torsion of the human achilles tendon. *J. Foot Ankle Surg.* **35**, 41–48 (1996).

A3.5 Figures, Schemes and Tables

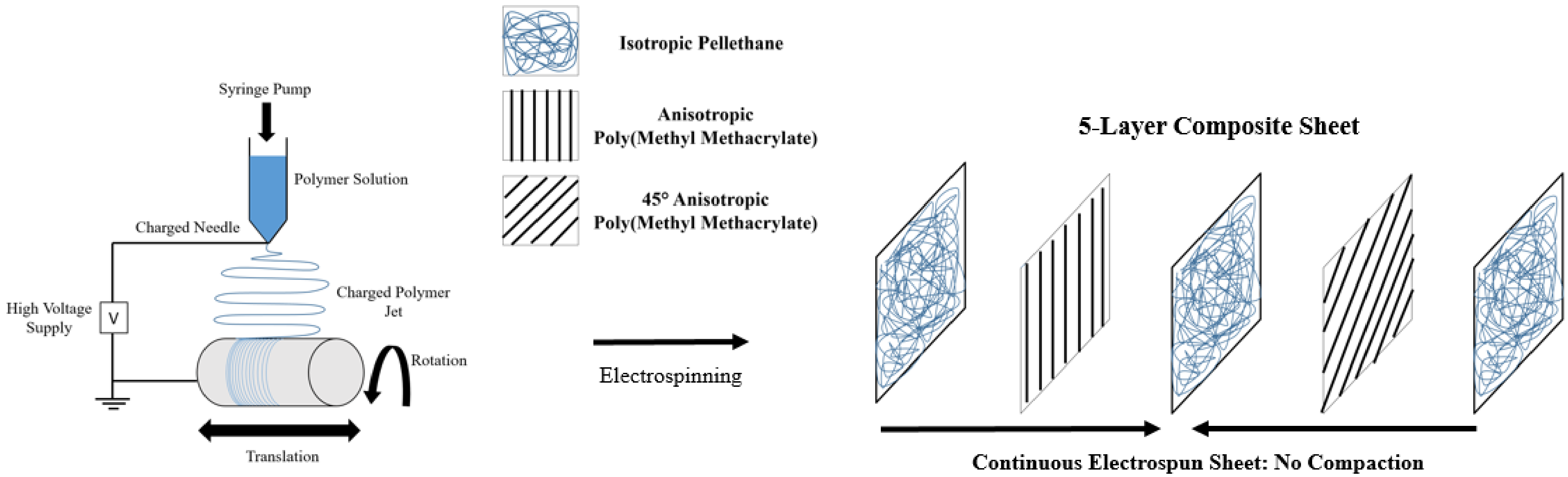

Scheme A3-1: Anisotropic electrospun pentalayer composite fabrication technique where opposing layers of poly(methyl methacrylate) and Pellethane are electrospun in layers. The caveat being one layer of poly(methyl methacrylate) is off shifted to a 45° angle.

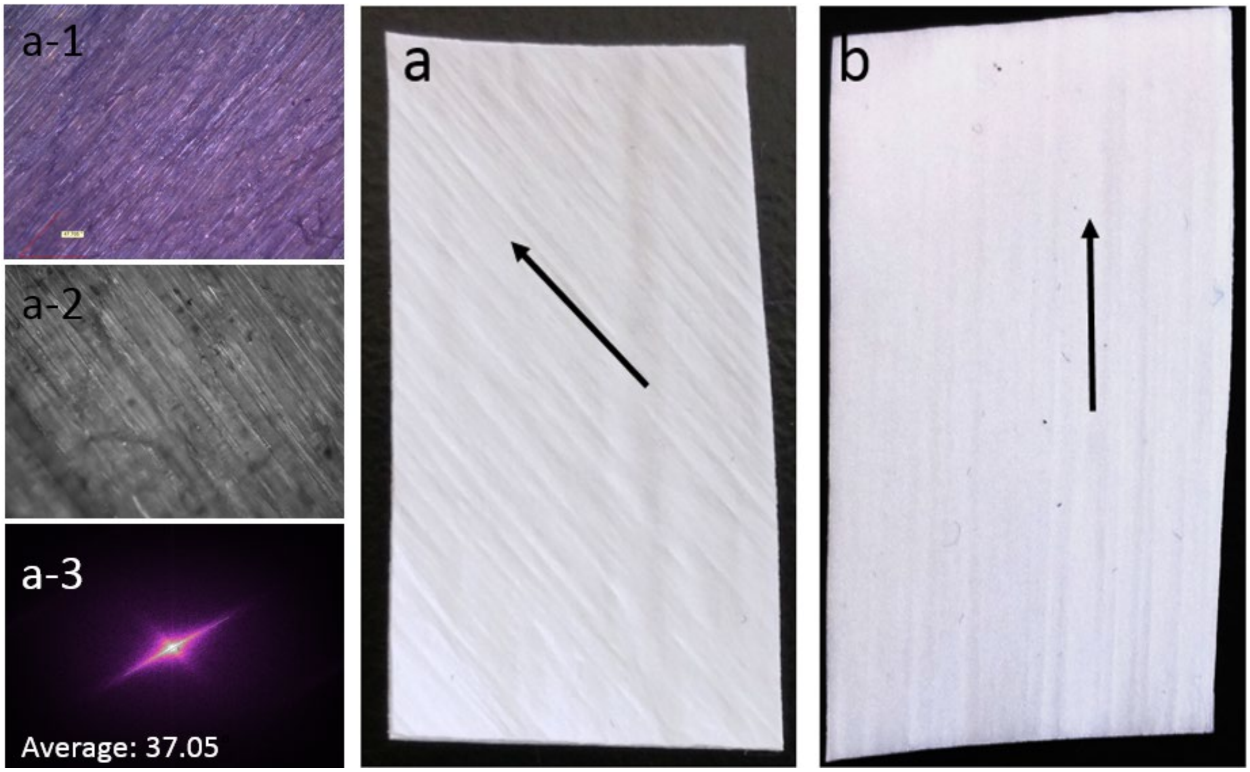

Figure A3-1: Results of the electrospun anisotropic pentalayer composite. (a) Shows a clear fiber orientation angle of 45° on one side of the composite, while on the other side of the same composite (b) there is a 0° fiber orientation angle. Fiber orientation angle fabrication was estimated to be 45° and confirmed to be 37.05° via optical microscope images (a-1),(a-2) and using Gwyddion software for analysis of the images (a-3).

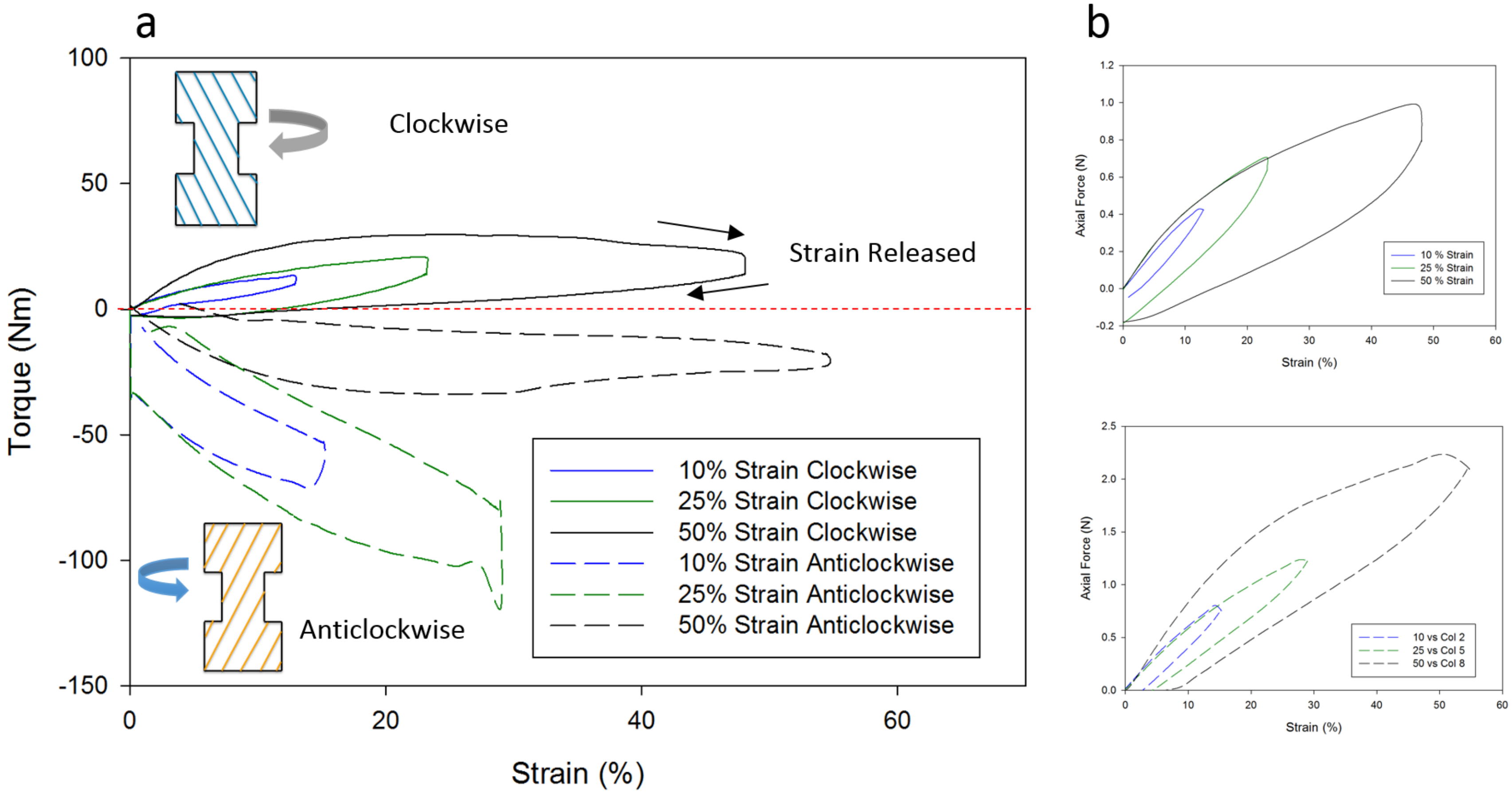

Figure A3-2: Results of torsional testing as done through custom geometry for the TA Discovery HR-2 Rheometer. (a) Dog bone samples were cut and strained, while being allowed to rotate. The amount of torque and axial force generated is proportional to the strain (b).

Appendix Chapter A4. Development of a Core-Sheath Electrospun Composite

A4.1 Synopsis

Two biodegradable polymers were electrospun together and the material properties were quantified for the composites potential application as a cardiac stent[1]. Poly(ε-caprolactone) and poly (lactic acid) were electrospun together in composite blends. The composite with best mechanical properties was determined.

Building off of the prior research, developing of a core-sheath electrospun composite is desired. This continuation is desired for the integration of a drug delivery capability into the potential stent application. Using a biodegradable cardiac stent that can also deliver targeted drugs is the ultimate goal for this work.

A4.2 Experimental

A4.2.1 Materials

Poly (lactic acid) pellets were purchased from Fiber Innovation Technology (FIT) (Grade 6202D). Poly(ε-caprolactone) (MW=80,000 kDa) were purchased from Sigma-Aldrich. Chloroform and N,N-dimethylformamide (DMF) was purchased from Sigma-Aldrich. The PLA pellets were kept in a dry box. All other materials were used as received.

A4.2.2 Electrospinning Solutions

The poly (lactic acid) electrospinning solution was made by dissolving 12 wt. % in a solution containing a 1:5 ratio of DMF: chloroform. A Poly(ε-caprolactone) electrospinning solution was made by dissolving 20 wt. % in a 1:4 ratio of DMF: chloroform. Both solutions were stirred overnight until the polymers were completely dissolved.

A4.2.3 Core-Sheath Electrospinning

A figure of core-sheath electrospinning can be seen in **Figure A4-1**. The poly(ε-caprolactone) polymer was being pumped to the outer nozzle, while simultaneously the poly (lactic acid) was being pumped to the inner nozzle. This makes the resulting core-sheath fiber with poly(ε-caprolactone) on the sheath, with ploy (lactic acid) in the core. The flow rate of poly (lactic acid) was 2.45 mL/hr and the flow rate of poly(ε-caprolactone) was 1.22 mL/hr. The singular voltage at the needle tip was 8.65 kV and the drum voltage was -1000 V.

Perpendicular alignment of the needle tip to the mandrel collector was not appropriate for this method. The preferred needle tip alignment is directly above the collector mandrel.

A4.2.4 Thermal Analysis

Differential Scanning Calorimetry (DSC) (TA Q2000) was used to measure the glass transition and the heat capacity of the neat poly (vinyl acetate) in the dry, hydrated and post hydrated composites. The process used two heating cycles where the sample is heated at a rate of 5 °C/min to 100 °C, cooled at 10 °C/min to -50 °C and then heated at 5 °C/min to 100 °C. The poly (vinyl acetate) content in the neat and composite materials was calculated using the same assumptions and process from Tumbic et al[1]. The following equation **Eq. (A1-1)** was used to calculate all poly (vinyl acetate) content in the composites:

$$w = \left(\frac{\Delta C_p}{\Delta C_{p,neat}}\right) * 100 \qquad \text{(A1-1)}$$

where w is the weight percent of the poly (vinyl acetate) in the composite, ΔC_p is the heat capacity of the poly (vinyl acetate) in the composite, and $\Delta C_{p,neat}$ is the heat capacity of the neat electrospun poly (vinyl acetate)[2,3]. All heat capacity values were used from the second heating cycle to ensure all samples had equal thermal history.

A4.2.5 Scanning Electron Microscopy

Surface topography of all samples was assessed using the SEM (Jeol JSM-6390LV). All samples were prepared by cutting out a square and adhering it to an SEM stub using carbon tape. All samples were gold-sputter coated for 120 sec in a Denton Vacuum desk IV. The working distance was 10 mm with an accelerating voltage of 10-15 kV.

A4.2.6 Embedding Epoxy

Samples were epoxied using a mixture of bisphenol A diglycidyl ether (DGEBA), neopentyl glycol diglycidyl ether (NGDE), and polyoxpropylenediamine (jeffamine D-230) in a 1:2:1 molar ratio. The epoxy was mixed together and applied to the fibrous mat through submersion. Sample were cured at 80 °C for 5 hours.

A4.3 Preliminary Results

A core-sheath electrospun fibrous mat was estimated to have been fabricated. The visual conformation during the electrospinning process, in tandem with the thermal analysis suggest that the core-sheath morphology was obtained. However, visual conformation is still lacking. TEM is the standard method for visual conformation of core-sheath morphology, but was not preformed due to lack of equipment availability.

A4.4 References

1. Tumbic, J., Romo-Uribe, A., Boden, M. & Mather, P. T. Hot-compacted interwoven webs of biodegradable polymers. *Polymer* **101**, 127–138 (2016).

2. Robertson, J. M., Birjandi Nejad, H. & Mather, P. T. Dual-Spun Shape Memory Elastomeric Composites. *ACS Macro Lett.* **4**, 436–440 (2015).

3. Nejad, H. B., Robertson, J. M. & Mather, P. T. Interwoven polymer composites via dual-electrospinning with shape memory and self-healing properties. *MRS Commun.* **5**, 211–221 (2015).

A4.5 Figures, Schemes and Tables

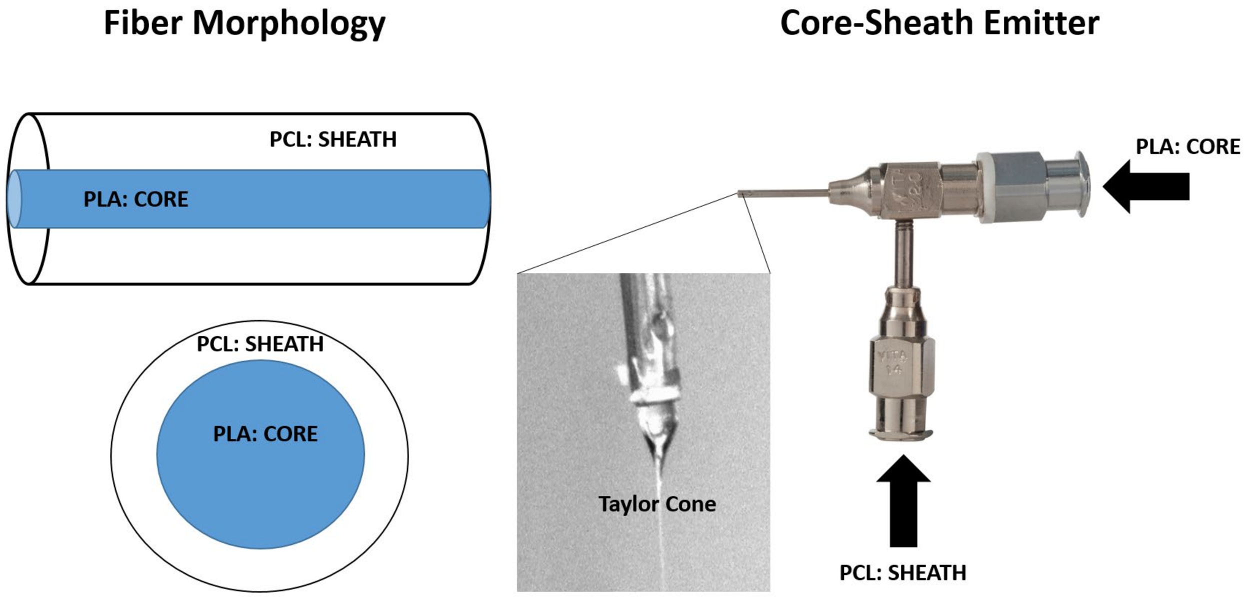

Scheme A1-1: Image of the core-sheath emitter used for electrospinning (right), with an image taken during the electrospinning process showing a good Taylor cone formation (middle) and theoretical core-sheath fiber morphology (left).

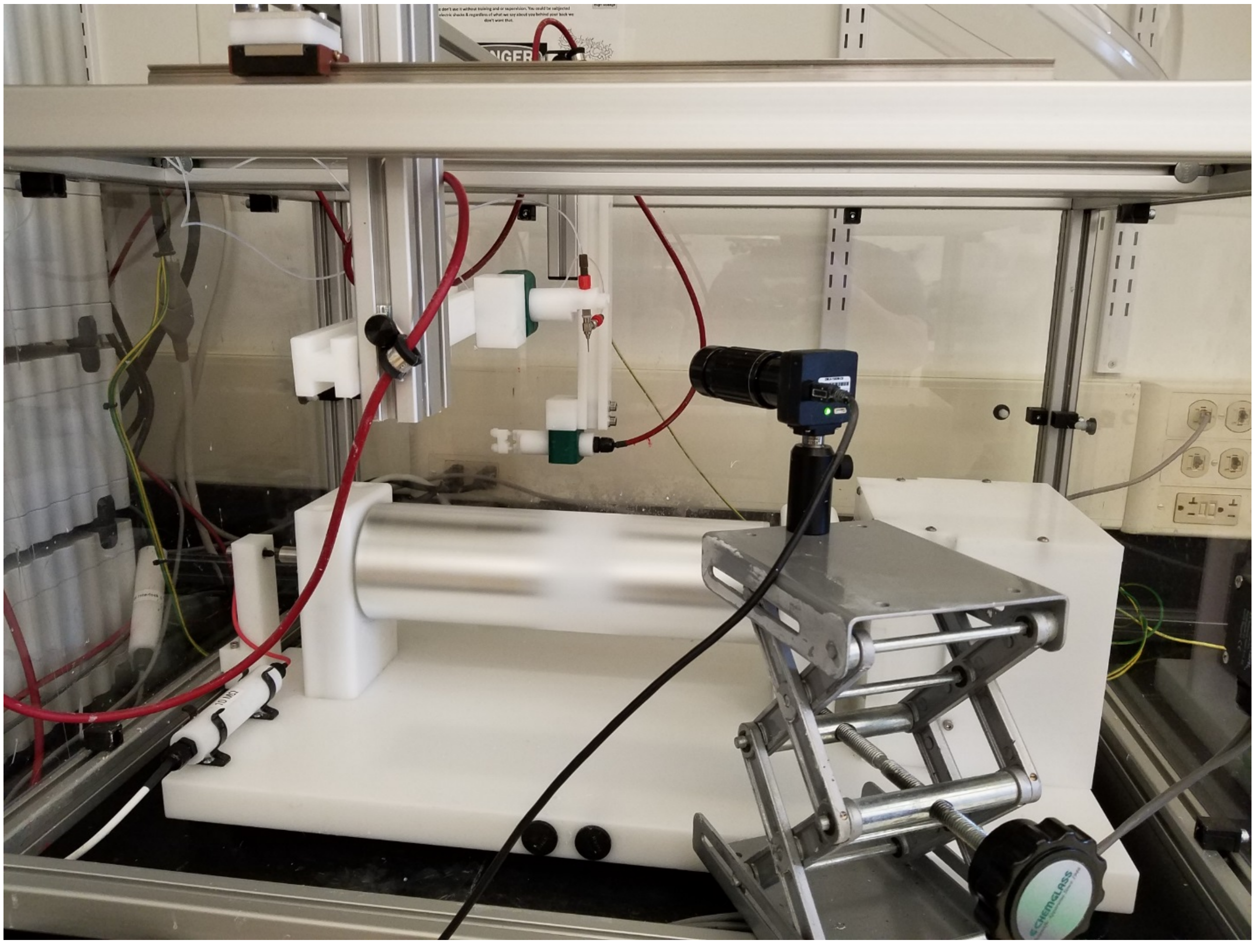

Figure A1-1: Picture of actual core-sheath electrospinning setup used. The core-sheath emitter is suspended above the collector mandrel (spinning) with a camera attached to a scissor jack focused on the emitter tip.

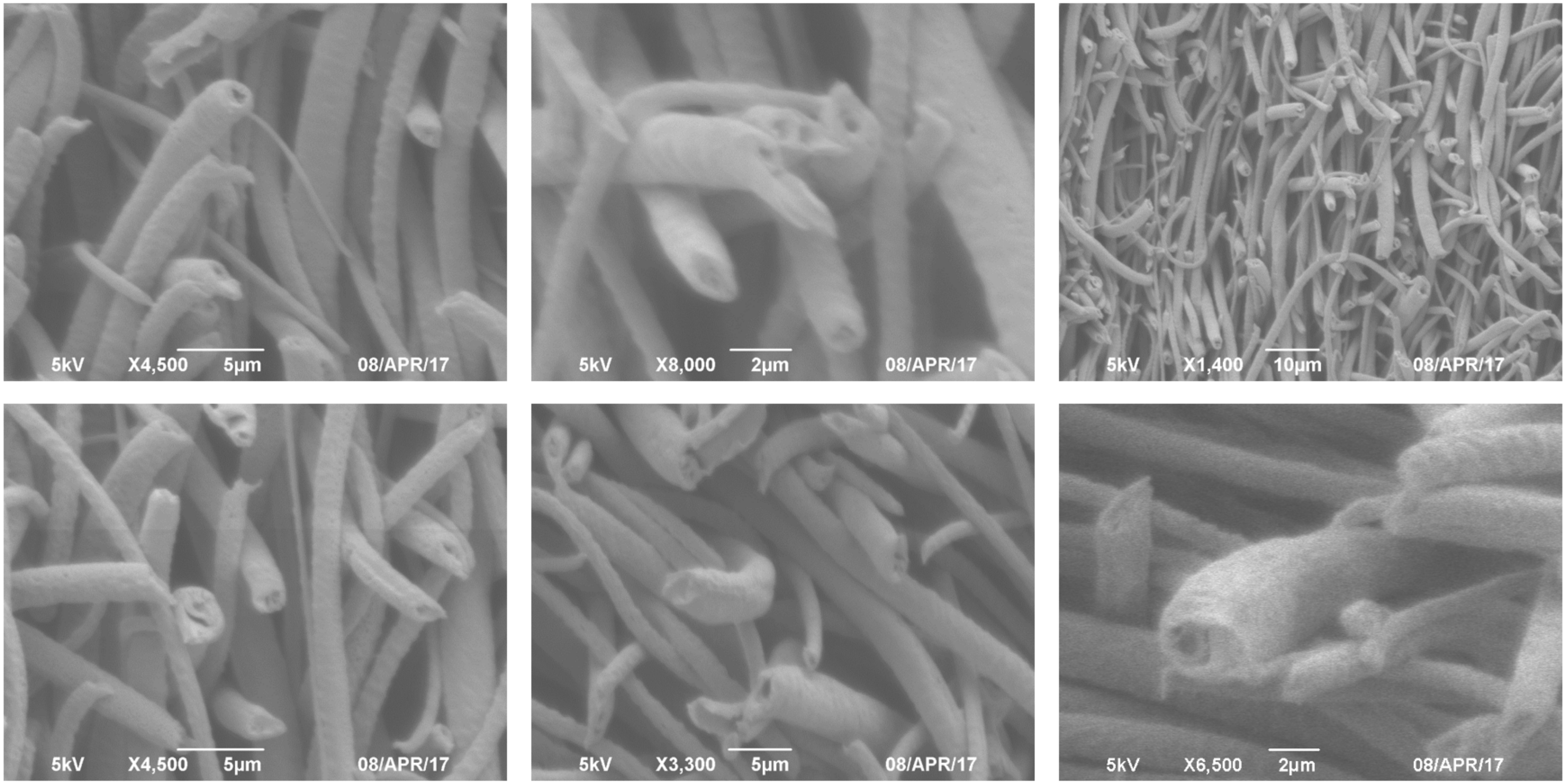

Figure A1-2: A series of SEM images showing the results of electrospinning PCL (sheath) and PLA (core), and the resulting fiber morphology.

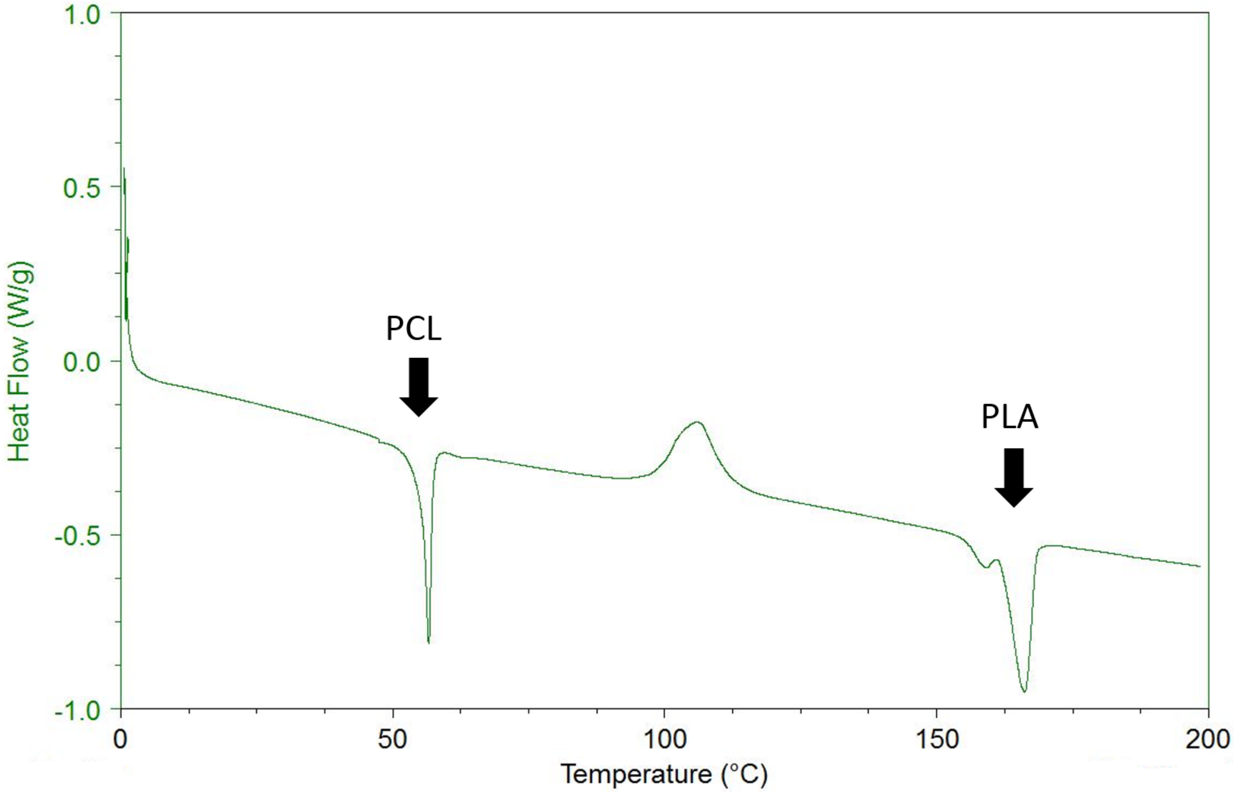

Figure A1-3: DSC thermogram showing compositional analysis of the core-sheath electrospun fibers, where both polymers are identified to be present.

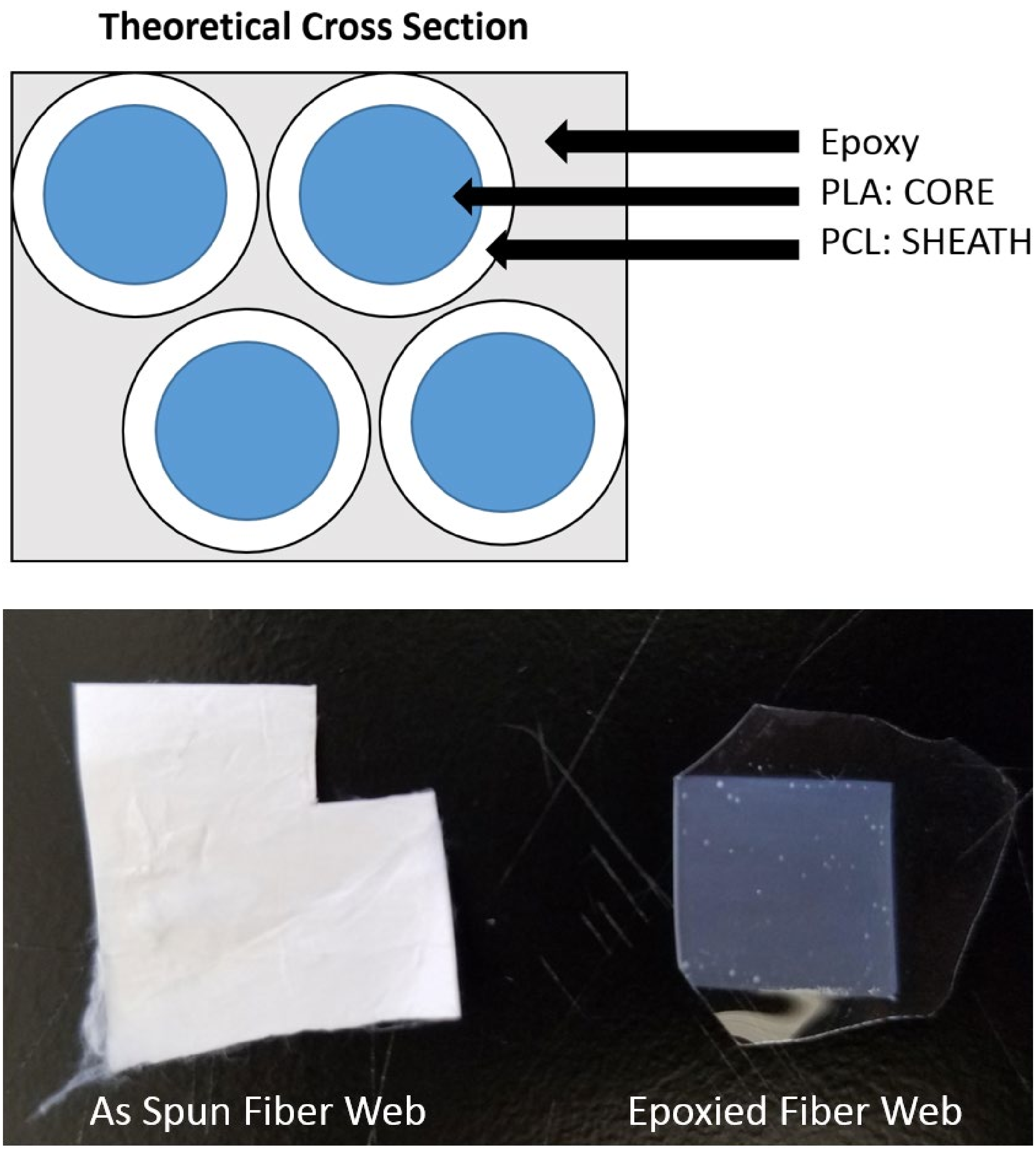

\

Figure A1-4: Theoretical structure obtained of epoxied core-sheath electrospun fibers as seen using SEM (top). Pictures of the electrospun core-sheath fiber web (bottom left) and the epoxied electrospun core-sheath fiber web (bottom right). The clear edges are where there is only epoxy, with the less translucent area being polymer fiber and epoxy.

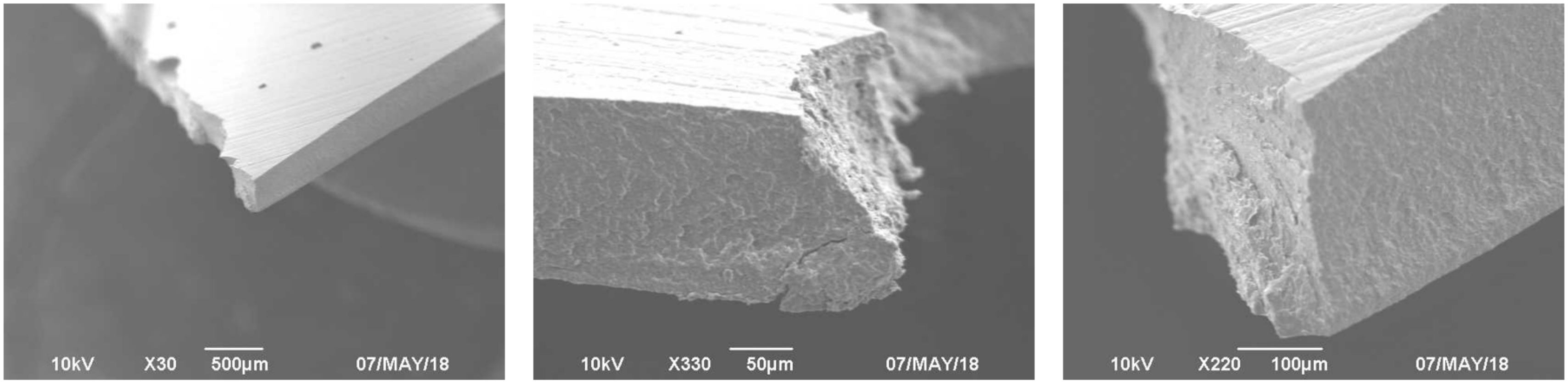

Figure A1-5: SEM images of epoxied electrospun core-sheath fibers. As shown the epoxied sample obscures the fibers so none can be seen.

VITA

NAME OF AUTHOR: Matthew M. Ali

PLACE OF BIRTH: Syracuse, NY, USA

EDUCATION:

B.S. in Paper & Bioprocess Engineering, SUNY College of Environmental Science and Forestry (2010)
M.S. in Paper & Bioprocess Engineering, SUNY College of Environmental Science and Forestry (2013)
Ph.D. in Chemical Engineering, Syracuse University (2019)

SELECTED PUBLICATIONS

Buffington, Shelby L., Justine E. Paul, Matthew M. Ali, Mark M. Macios, Patrick T. Mather, and James H. Henderson. "Enzymatically triggered shape memory polymers." *Acta biomaterialia* 84 (2019): 88-97.